NRSP-2
92-24

VIERS-1 Final Report Phase 3

P. Snoeij
E. van Halsema
J. Vogelzang
S. Waas
S. Zecchetto
H. Janssen
W. Oost
B. Jähne
Ch. Calkoen

BELEIDSCOMMISSIE REMOTE SENSING

BCRS 92-24 MD

VIERS-1 Final Report Phase 3

P. Snoeij
Delft University of Technology
E. van Halsema
Physics and Electronics Laboratory of TNO
J. Vogelzang
Rijkswaterstaat, Tidal Waters Division
S. Waas
University of Heidelberg
S. Zecchetto
C.N.R. Instituto Studio Dinamica Grandi Masse
H. Janssen
W. Oost
Royal Netherlands Meteorological Institute
B. Jähne
Scripps Institution of Oceanography
(on leave from University of Heidelberg)
Ch. Calkoen
Delft Hydraulics

bcrs project OP-1.26 and 1.1/AO-01
bcrs report 92-24

ISBN 90 5411 068 6

June 1993

This report describes a project, carried out in the framework of the National Remote Sensing Programme (NRSP-1 and NRSP-2), under responsibility of the Netherlands Remote Sensing Board (BCRS).
The co-operation with the University of Heidelberg was made possible by a twinning grant from the European Community (contractno. ST2J-0451-C(GDF)).

CIP-GEGEVENS KONINKLIJKE BIBLIOTHEEK, DEN HAAG

VIERS-1

VIERS-1 final report phase 3 / P. Snoeij ... [et al.]. -
Delft : BCRS, Netherlands Remote Sensing Board. - Ill. -
(BCRS report ; 92-24)
BCRS project OP-1.26 en 1.1/AO-01, uitgevoerd in het kader
van het NRSP-1 en NRSP-2) onder verantwoordelijkheid van
de Beleidscommissie Remote Sensing (BCRS). - Met lit.
opg.
ISBN 90-5411-068-6
Trefw.: oceanografie / remote sensing.

Contents

Figures

Tables

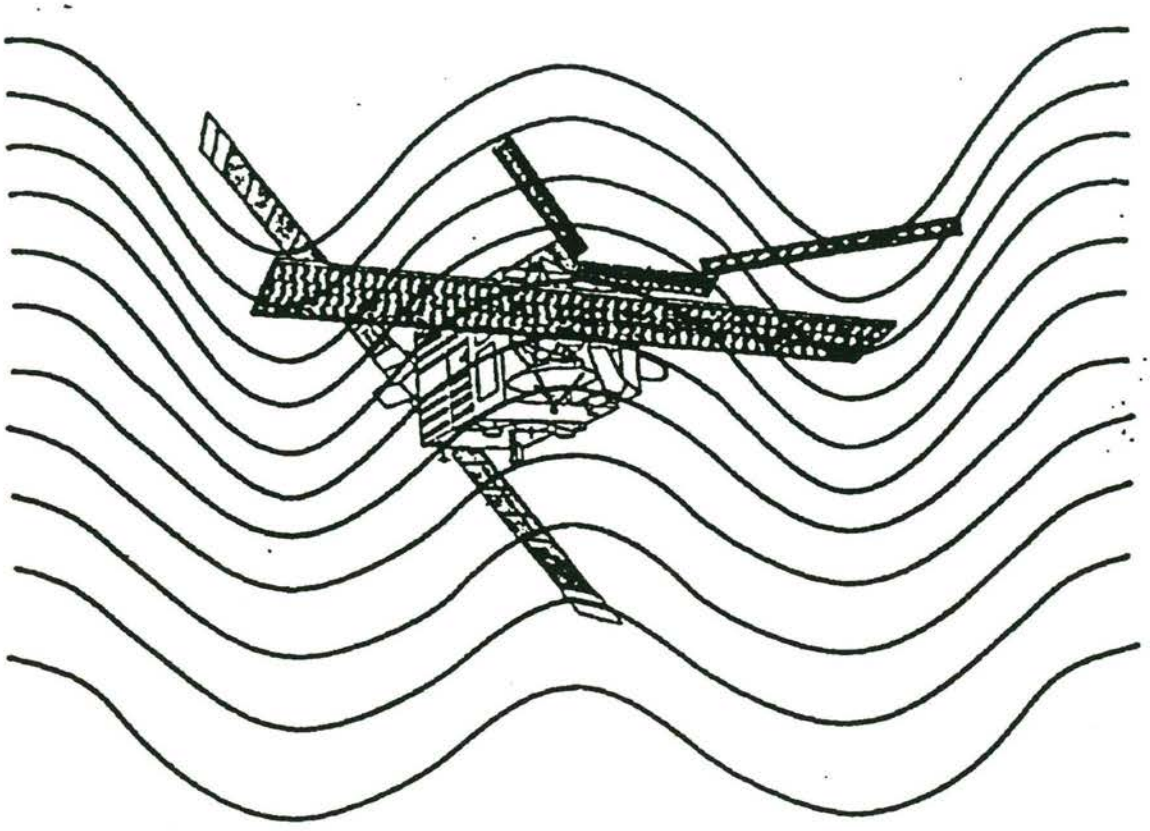

1 Introduction

The presently operational algorithms for extraction of surface wind speed and direction from backscatter measurements are all empirical, based on databases of in situ measurements of both backscatter and wind speed. Analysis of the SeaSat scatterometer database has revealed that these simple models need modification in order to reach the necessary accuracy. The VIERS-1 project is aimed at improvement of the wind extraction algorithms by development of a model, based on physics, which describes the end-to-end process of wind scatterometry. The advantage of a physical model is that the results are not affected by changes in environmental parameters as sea water temperature, air temperature, viscosity etc. Furthermore it may also cover a range of radar frequencies and different polarizations so that it can serve multiple scatterometers.

In order to develop such a model it is essential to gain knowledge on the scattering processes at the water surface. This requires detailed measurement of all parameters involved. The main experimental difficulty is the measurement of the small scale (cm) waves on the ocean surface, which are the main cause of the radar backscatter. The lack of good area-extended measurements of these small scale waves was the main reason to 'return' to the wind/wave flume after ten years of in situ measurements. A five year research program was set up, consisting of two wind/wave flume experiments and one ocean-platform experiment. Special wave measuring equipment for use in the flumes as well as at sea were developed to gain more knowledge on the small scale water waves.

It is generally accepted that the process of microwave backscattering at the ocean surface is not solely dependent on wind and typical radar parameters as polarization, frequency etc.. Other factors as (long) wave spectrum, viscosity, sea water temperature, stability, surface tension also have a significant influence. Radar backscatter models based on a description of the underlying physical phenomena therefore have the potential to provide a better relation between measured microwave backscatter and the surface wind field than the empirical models currently in use.

Recently some first attempts to develop physical backscatter models appeared in the literature see e.g. Plant [85] and Donelan and Pierson [23]. Crucial in these models is the accurate description of the full wave number spectrum of the ocean waves, as this is the link between microwave backscatter and the wind. The spectral density from long waves (several hundreds of meters) down to millimeter waves has to be known. Whereas knowledge on the long waves is readily available, the details of the centimeter and millimeter waves number spectra are quite unknown. The reason for this is mainly the difficulty in performing accurate measurements in the wave number domain of these small waves in the ocean environment.

Fundamental knowledge about the intermediary physical processes which determine the radar backscatter from the ocean surface is at the moment still lacking. To improve the understanding of the interaction between microwaves and water waves the VIERS-1 (Dutch acronym for "Preparation and Interpretation of ERS-1 data") project started in 1986 with the preparation of two wind/wave tank experiments and an ocean tower experiment, while airborne scatterometer data became available through the participation in different ESA windscatterometer campaigns.

The VIERS-1 project is carried out in a cooperation between the Royal Netherlands Meteorological Institute (KNMI), Delft Hydraulics, the Laboratory for Telecommunication and Remote Sensing Technology of the Delft University of Technology, the University of

Heidelberg, the Physics and Electronics Laboratory of TNO (FEL-TNO), and Rijkswaterstaat, Tidal Waters Division.

Financial support for the contribution of the Dutch institutes is provided by the Netherlands Remote Sensing Board (BCRS), the German contribution has been made possible by a grant of the State Baden Wurttemberg and the European Community.

In the VIERS-1 team all disciplines involved in wind scatterometry are present: meteorology, oceanography, microwave technology, and microwave remote sensing. Experiments in wind/wave tanks have the advantage over ocean environment that detailed measurements can be performed with relatively little effort. Above that, conditions can be controlled and precisely reproduced, so that the effect of varying only one parameter at the time can be studied. The disadvantage is however that a wind/wave tank is an artificial surrounding and some scaling effects may occur. In order to control these effects, a phased approach was adopted:

1. An experiment in a large indoor, well equipped wind/wave facility (100x8x0.8 m^3) of Delft Hydraulics in Delft;
2. An experiment in the much larger Delta tank (250x5x5 m^3) where full-scale oceanic waves can be generated;
3. An ocean-based platform experiment.

The Delft facility is excellently suited for detailed studies of microwave backscattering from waves in the capillary region. This tank was mainly used for studying wind-generated waves. In section 2 the short-wave spectral model will be discussed and compared with the wave measurements made in the Delft facility. In section 3 an introduction will be given to some backscatter models, while in section 4 these models will be compared with wind, wave and microwave measurements performed in the Delft facility.

In the Delta tank almost real size waves can be generated with significant wave heights of up to 3 meters. Of this tank 150 meters were covered with a wind tunnel roof, specially constructed for this experiment. The Delta tank is much better suited for studying the effects of long waves on short gravity and capillary waves. In section 5 an overview of the measurement campaign will be given, the influence of the larger waves on the wind will be determined and the modulation of the backscatter due to the large waves will be given.

Finally, the tower based experiment was used as a final check on the validity of the tank experiments with respect to the possible influences of scaling effects. Along with the increase in size of the facility, new measurement equipment had to be developed. In section 6 an overview of the field experiment will be given, the wind, wave and backscatter measurement equipment is discussed and some results will be presented.

2 Calculations of short-wave spectra

In a previous progress report only a brief description of the short-wave model was given. Here we will discuss the model (called Testwa) in considerable detail and also confront it with measured short-wave spectra.

2.1 Physics of gravity-capillary waves

In water wave theory there are basically three spectra to describe a stationary and homogeneous wave field: the one-dimensional variance spectra in frequency and wavenumber domain, E(f) and F(k), and the two-dimensional wavenumber spectrum ψ(k) (Note that in the backscattering models this function is denoted by W(k)). The latter two are related by:

$$F(k) = \int_{-\pi}^{\pi} \psi(\vec{k}) dk \tag{2.1}$$

If $<\eta^2>$ denotes the variance, the spectra are normalized in such a way that

$$\int\int \psi(\vec{k})\, d\vec{k} = \int_0^{\infty} kF(k)dk = \int_0^{\infty} E(f)df = <\eta^2> \tag{2.2}$$

If the wave field is linear (i.e. the superposition principle applies), then the spectra E and F can be related by the dispersion relation.

$$E(f) = k\frac{dk}{df}F(k) = \frac{2\pi k}{v_g}F(k) \tag{2.3}$$

The group speed is denoted by $v_g = d\omega/dk$. If non-linear effects are present the relation no longer applies. For the sake of simplicity we will assume that it is also valid for slightly non-linear waves.

For deep-water gravity waves the energy per unit area, e, is proportional to the variance: $e = \rho g <\eta^2>$. For capillary waves a similar proportionality applies, but now for the variance of the gradient field: $e = \rho T<(\nabla\eta)^2>$, where T is surface tension. One may introduce the energy density of the wave field $\mathcal{E}$ according to:

$$\mathcal{E}(\vec{k}) = \frac{\omega^2}{k}\psi(\vec{k}) \tag{2.4}$$

The integral of $\mathcal{E}$ over all wavenumbers is proportional to the total energy of the wave field per unit area.

$$\rho \int\int \mathcal{E}(\vec{k})\, d\vec{k} = \rho g <\eta^2> + \rho T <(\nabla\eta)^2> \tag{2.5}$$

The energy balance equation is an equation for $\mathcal{E}$. For deep water and in the absence of currents it reads:

$$\frac{\partial \mathcal{E}}{\partial t} + \vec{v}_g \cdot \frac{\partial \mathcal{E}}{\partial \vec{x}} = S \tag{2.6}$$

S describes all kinds of energy exchange processes. As long as the term S is not specified, one still has an exact equation. Note that the energy balance equation introduces a space and time dependence for $\mathcal{E}$. This is not in conflict with the homogeneity and stationarity of the wave field as long as one demands these properties to vary on time and space scales that are small compared to the scales on which $\mathcal{E}$ varies.

Next we assume that the energy exchanges are additive. This is a valid assumption in a perturbative approach [72]. Hence S can be described as a sum of three terms, that encompass the processes of wind input, non-linear wave interactions and energy dissipation.

$$S = S_{in} + S_{nl} + S_{dis} \tag{2.7}$$

Consider the situation in which a constant wind blows over a body of water. In the stationary case the first term in the energy balance equation vanishes. For waves 'in the tail' of the spectrum the advection term can also be neglected. Due to viscosity short waves can not be advected over distances on which the spectrum varies. We conclude that the energy balance for short waves simplifies according to:

$$S_{in} + S_{nl} + S_{dis} = 0 \tag{2.8}$$

This is the basic equation for the energy balance of short waves.

2.1.1 Source terms

We will subsequently discuss the different source terms and describe how they are modeled in the Viers-1 module.

2.1.1.1 Wind input

From Miles' theory on wave growth it follows that the wave amplitude grows exponentionally. Hence the wind input should be of the following form.

$$S_{in} = \beta\mathcal{E} \tag{2.9}$$

The growth rate β may only depend on wind speed, wavenumber and angle between wind and wave vectors.

There are several expressions for β 'on the market'. A formula that is supposed to apply to high-frequency waves ($\leq$ 20 Hz) has been proposed by Plant [85].

$$\beta = \delta\omega\frac{u_*^2}{c^2}R(\chi) \tag{2.10}$$

Here u_* is the friction velocity of the wind, c the phase speed of the generated wave and χ the angle between wind and wave vectors ($-\pi/2 \leq \chi \leq \pi/2$). The dimensionless constant δ has a numerical value of the order 0.04 ± 0.02.

For the directional dependence Plant takes $R(\chi) = \cos\chi$. Scale arguments of Miles suggest a $\cos^2$ dependence. Phillips [82] takes the general form $R(\chi) = \cos^{2p}(\chi)$. For the Viers-1 module the precise form of $R(\chi)$ is immaterial as we will take a directional average later on.

Donelan and Pierson [23] contend that (2.10) is inaccurate if $U_{10}/c \leq 1.2$. They favor an expression based on measurements by Larson and Wright. For 3-cm Bragg waves this means that Plant's expression becomes inaccurate if $U_{10} \leq 25$ cm/s. Hence for scatterometric applications it should be a valid formula.

2.1.1.2 Dissipation

Dissipation of wave energy occurs due to viscosity of water, breaking and bottom friction. Hence (assume additivity)

$$S_{dis} = S_{vis} + S_{br} + S_{bot} \tag{2.11}$$

On deep water bottom friction can be neglected.

In the Testwa model only viscous damping is taken into account. For a monochromatic wave one can show that the amplitude decreases exponentially due to viscous damping [75]. For a linear wave field this means that the source term S_{vis} is given by

$$S_{vis} = -4\nu k^2 \mathcal{E} \tag{2.12}$$

Where ν is the kinematic viscosity of water.

Donelan and Pierson [23] also take dissipation due to wave breaking into account. This means that their spectra will fall off faster than corresponding Testwa spectra.

2.1.1.3 Non-linear interactions

There is discussion whether the term S_{nl} is of much importance for gravity-capillary waves. Donelan and Pierson [23] do not take non-linear interactions into account. Kitaigorodskii [65] and also Phillips [82], however, stress the importance of non-linear interactions.

There exist exact expressions for three and four-wave interactions, but we do not use them because they would require very time-consuming calculations. For three-wave interactions there is an additional problem of a singular factor. In Testwa simplified expressions are chosen. They will be derived in what follows.

First note that the non-linear interactions conserve total energy (and hence only can redistribute energy).

$$\iint S_{nl} \vec{dk} = 0 \tag{2.13}$$

Assume now that the interactions are local in k space (i.e. only waves with practically the same k interact). S_{nl} can then be written as the divergence of an energy flux.

$$S_{nl} = -\frac{\partial}{\partial \vec{k}} \cdot \vec{T}(\vec{k}) \tag{2.14}$$

Where T(k) is the energy flux.

On dimensional grounds and in analogy with Kolmogorov's treatment of turbulence we write the energy flux as

$$\vec{T}(\vec{k}) = \vec{k}\mathcal{E}\tau_{NL}^{-1} \tag{2.15}$$

Where τ_{NL} is a typical time for non-linear interactions. If one uses this in the previous expression one gets

$$S_{nl} = -\frac{1}{k}\frac{\partial}{\partial k}(k^2\mathcal{E}\tau_{NL}^{-1}) \tag{2.16}$$

The next step is to find an expression for τ_{NL}. The action density N is introduced for convenience.

$$N = \frac{\mathcal{E}}{\omega} \tag{2.17}$$

Consider the evolution of the action density under the influence of three and four-wave interactions.

$$\frac{\partial}{\partial t}N(\vec{k}) = I_3(\vec{k}) + I_4(\vec{k}) \tag{2.18}$$

The 'collision integral' for four-wave interactions is given by [36,37]

$$\begin{aligned} I_4(\vec{k}_1) = \int d\vec{k}_2 \int d\vec{k}_3 \int d\vec{k}_4 \; | \; Q^2_{\vec{k}_1,\vec{k}_2,\vec{k}_3,\vec{k}_4} \; | \; \delta(\vec{k}_1 + \vec{k}_2 - \vec{k}_3 - \vec{k}_4)\delta(\omega_{k_1} + \omega_{k_2} - \omega_{k_3} - \omega_{k_4}) \\ \times \{(N(\vec{k}_1) + N(\vec{k}_2))N(\vec{k}_3)N(\vec{k}_4) - (N(\vec{k}_3) + N(\vec{k}_4))N(\vec{k}_1)N(\vec{k}_2)\} \end{aligned} \tag{2.19}$$

Also for three-wave interactions can one write down the corresponding collision integral [20,61].

$$\begin{aligned} I_3(\vec{k}_1) = 4\pi \int d\vec{k}_2 \int d\vec{k}_3 \, | V^2_{-\vec{k}_1,\vec{k}_2,\vec{k}_3} | \, \delta(\vec{k}_2 + \vec{k}_3 - \vec{k}_1)\delta(\omega_2 + \omega_3 - \omega_1) \\ \times \{N_2N_3 - (s_3N_2 + s_2N_3)s_1N_1\} \end{aligned} \tag{2.20}$$

Where N_2=N(k_2) en s_2=sign(k_2), etc.. Note that the factor $\delta(\omega_2+\omega_3-\omega_1)$ gives rise to a singularity.

The typical time for non-linear interactions is defined as

$$\tau_{NL}^{-1} = \frac{I_3(\vec{k}) + I_4(\vec{k})}{N(\vec{k})} \tag{2.21}$$

If we now assume[1] that the largest contribution to the integrals I_3 en I_4 comes from the region where all k-vectors are practically equal, $k_1 \approx k_2 \approx k_3 \approx k_4$, then the following approximation applies (cf. [65]).

$$I_4(\vec{k}) \simeq |\ Q\ |^2 N^3(\vec{k}) \frac{k^3}{v_g} \tag{2.22}$$

$$I_3(\vec{k}) \simeq |\ V\ |^2 N^2(\vec{k}) \frac{k}{v_g} \tag{2.23}$$

Because $|Q_{k,k,k,k}|^2 \sim k^6$ and $|V_{-k,k,k}|^2 \sim \omega k^3$ and because N can be expressed in ψ, one thus finds

$$\tau_{NL}^{-1} = \omega \frac{c}{v_g}(\alpha_3(k^4\psi) + \alpha_4(k^4\psi)^2) \tag{2.24}$$

Where α_3 and α_4 are dimensionless "coupling constants", that still may depend on c/v_g. Note that this equation gives the first two terms of an expansion in the dimensionless function $B(k)=k^4\psi(k)$. B is what Phillips calls "degree of saturation".

With the aid of this expression the non-linear source term can be written as

$$S_{nl} = \frac{1}{k}\frac{\partial}{\partial k}\frac{c^4}{v_g}[\alpha_3(k^4\psi)^2 + \alpha_4(k^4\psi)^3] \tag{2.25}$$

This result can be interpreted as follows. From the two assumptions about the non-linear interactions, locality in k space and an energy flux uniform in all directions, it immediately follows (on dimensional grounds) that S_{nl} can be expanded as

$$S_{nl} = \frac{1}{k}\frac{\partial}{\partial k} c^3 \sum_{n=3}^{\infty} \beta_n B^{n-1} \tag{2.26}$$

The n-th term in this expansion gives the n-wave contribution.

For gravity waves three-wave interactions are insignificant. Hence the coupling constant α_3 should have the property $\alpha_3(c/v_g) \rightarrow 0$ as $c/v_g \rightarrow 2$. This does not apply to α_4; both for gravity and capillary waves it may be unequal zero.

2.1.2 Energy balance

In the previous part all different source terms have been discussed. Taking everything together, one arrives at the following energy balance.

$$\frac{\partial}{\partial k}\varepsilon(k) = \frac{\gamma c^3}{\omega k} B \tag{2.27}$$

The energy flux $\varepsilon(k)$ is given by

$$\varepsilon(k) = \frac{c^4}{v_g}(\alpha_3 B^2 + \alpha_4 B^3) \tag{2.28}$$

[1] For four-wave interactions this is the usual assumption [65], for three-wave interactions it is certainly wrong because always two capillary waves interact with one gravity wave.

The coefficient γ is defined as

$$\gamma = \delta\omega\frac{u_*^2}{c^2}R(\chi) - 4\nu k^2 \tag{2.29}$$

It gives the net effect of wind input and viscous damping.

A simplification of the energy balance may be achieved by assuming a factorized wavenumber spectrum.

$$\psi(\vec{k}) = F(k)f(\chi) \tag{2.30}$$

With $\int_{-\pi}^{+\pi} f(\chi)d\chi = 1.$

In this way the angular dependence is eliminated. For the directional distribution f one often takes $\cos^2$. Donelan en Pierson [22,23], however, adopt sech^2.

For the one-dimensional wavenumber spectrum the energy balance equation explicitly reads:

$$\frac{\partial c^4}{\partial k v_g}[\bar{\alpha}_3(k^4F)^2 + \bar{\alpha}_4(k^4F)^3] = \frac{\bar{\gamma}c^3}{\omega k}(k^4F) \tag{2.31}$$

with

$$\bar{\alpha}_3 = \alpha_3\int_{\pi}^{\pi} f^2(\chi)d\chi \quad \bar{\alpha}_4 = \alpha_4\int_{-\pi}^{\pi} f^3(\chi)d\chi \tag{2.32}$$

$$\bar{\gamma} = \bar{\delta}\omega\frac{u_*^2}{c^2} - 4\nu k^2 \quad \bar{\delta} = \delta\int_{-\pi/2}^{\pi/2} f(\chi)R(\chi)d\chi \tag{2.33}$$

If one transforms to the frequency spectrum E, the new equation becomes:

$$\frac{\partial}{\partial k}c^2 v_g(\alpha_1 S^2 + \alpha_2 S^3) = \bar{\gamma}\frac{cv_g}{k^2}S \tag{2.34}$$

With

$$S = \frac{\omega}{2\pi}k^2E \quad \alpha_1 = \bar{\alpha}_3 \quad \alpha_2 = \frac{v_g}{c}\bar{\alpha}_4 \tag{2.35}$$

The energy balance written in this form is the starting point for the program Testwa.

As already stipulated this simplified energy balance is only valid for waves in the spectral tail, say for $k \geq k_0$ (k_0 far from the peak: $k_0 \gg k_p$). In order to get a unique solution, a boundary condition at $k=k_0$ has to be imposed. Obviously one needs the energy flux from the spectral peak to the tail.

$$\varepsilon(k_0) = \varepsilon_0 = c_0^2 v_{g0}(\alpha_1 S_0^2 + \alpha_2 S_0^3) \tag{2.36}$$

If necessary one can express S_0 in the spectral value E_0.

The following form of the energy balance clarifies the physical picture.

$$\frac{\partial}{\partial\omega}c^2 v_g(\alpha_1 S^2 + \alpha_2 S^3) = \bar{\delta} u_*^2 \frac{S}{k} - 4\nu c S \tag{2.37}$$

The left-hand side is the spectral energy flux, whereas the right-hand side is the sum of the energy supply by the wind and viscous damping.

2.1.3 Quasi-linear effect

The wind source term as we have given it previously, represents the input by a stationary logaritmic wind profile. If one, however, assumes that the windgenerated waves have an effect on the wind profile (feedback), then the wind profile is no longer stationary and it will adapt to the wave field. The effective wind input changes as a result. In the following we will calculate the effective wind input in the one-dimensional case under certain assumptions.

In Miles' theory of wave generation by wind one finds for the growth rate

$$\beta = -\pi\epsilon c \mid \chi_c \mid^2 \frac{W_c''}{|W_c'|} \tag{2.38}$$

Here ε is the ratio of air and water density. The wind profile $U_0(z)$ is hidden in W, where $W=U_0 - c$. The index c denotes that the quantity should be evaluated at the critical height z_c. The critical height is determined by the condition W=0. The quantity χ is the normalized vertical component of the wave-induced air speed. χ satisfies the Rayleigh equation.

$$[W(\frac{\partial^2}{\partial z^2} - k^2) - W'']\chi = 0 \tag{2.39}$$

with boundary conditions $\chi(0)=1$ and $\chi(\infty)=0$.

According to scale arguments of Miles the growth rate should be of the following form.

$$\beta = \delta\omega(\frac{u_*}{c})^2 \tag{2.40}$$

with $\delta=\delta(c/u_*, gz_0/u_*^2)$ and z_0 a typical roughness length. Note that in Plant's expression δ is a constant.

Calculations by P. Janssen [60] show that the wind profile is changed by the feedback of the waves. It changes according to

$$\frac{\partial}{\partial t}U_0 \mid_{\text{waves}} = D_W \frac{\partial^2}{\partial z^2}U_0 \tag{2.41}$$

D_W is the wave-induced diffusion coefficient, which is proportional to the wave spectrum [62].

$$D_W(z) = \frac{\pi c^2 k^3}{|c - v_g|} \mid \chi^2 \mid F(k) \tag{2.42}$$

The variables k, c and v_g via the resonance condition $U_0(z)=0$ have to be expressed in z.

The growth rate is determined by two factors, the curvature of the wind profile at the critical height and the factor $|\chi_c|^2$. If one assumes that due to feedback only the curvature changes significantly then it follows

$$\delta = -\delta_0 z_c \frac{U_{0c}''}{U_{0c}'} \tag{2.43}$$

δ_0 is the growth rate without wave feedback.

By the resonance condition $U_0(z)=c$ heights are coupled to wavenumbers (or frequencies). This implies that one can interpret β not as a function of ω but as a function of z. It follows

$$\beta(z) = -\pi \epsilon c(z) \mid \chi \mid^2 \frac{U_0''}{U_0'} \tag{2.44}$$

With this relation $|\chi|^2$ can be eliminated. Using the resonance condition one arrives at

$$D_W = -\frac{U_0'}{U_0''} \frac{\delta}{\epsilon} \frac{u_*^2}{U_0} \frac{v_g}{|c - v_g|} S \tag{2.45}$$

Here S is given by

$$S = \frac{c}{v_g} k^4 F = \frac{\omega}{2\pi} k^2 E \tag{2.46}$$

The wind profile is determined both by the turbulent stress and the wave-induced stress.

$$\frac{\partial U_0}{\partial t} = \frac{1}{\rho_a} \frac{\partial}{\partial z} \tau_{turb} + D_W \frac{\partial^2 U_0}{\partial z^2} \tag{2.47}$$

With ρ_a the air density.

For the turbulent stress often a "mixing-length" model is assumed.

$$\tau_{turb} = \rho_a \ell^2 \mid \frac{\partial U_0}{\partial z} \mid \frac{\partial U_o}{\partial z} \tag{2.48}$$

Where the "mixing length" l is given by $l = \kappa z$ (κ is the Von Kármán constant, $\kappa \approx 0.4$).

For a stationary profile one gets the following condition.

$$-\frac{\delta}{\epsilon} \frac{u_*^2}{U_0} \frac{v_g}{|c - v_g|} S \frac{\partial U_0}{\partial z} + \frac{\partial}{\partial z} \ell^2 \mid \frac{\partial U_0}{\partial z} \mid \frac{\partial U_0}{\partial z} = 0. \tag{2.49}$$

From this equation one can derive

$$\frac{z U_0''}{U_0'} \mid_{z=z_c} = -1 + \frac{\delta}{2\kappa\epsilon} \frac{u_*^2}{c} \frac{v_g}{|c - v_g|} \frac{S}{\ell U_0'} \tag{2.50}$$

The first term on the right-hand side gives the contribution of the unperturbed wind profile, whereas the second gives the correction due to the quasi-linear effect. If the correction is small, one may calculate lU_0' with a logaritmic profile, hence $lU_0' = u_*$.

We thus find for the Plant and Wright constant

$$\delta = \frac{\delta_0}{1+\Delta} \qquad \Delta = \frac{\delta_0}{2\kappa\epsilon}\frac{u_*}{c}\frac{v_g}{|c-v_g|}S \tag{2.51}$$

The growth rate becomes

$$\beta = \frac{\delta_0}{1+\Delta}\omega\left(\frac{u_*}{c}\right)^2 \tag{2.52}$$

Hence the quasi-linear effect quences the wind input to a certain extent.

The conclusion from the computation given above is that the quasi-linear effect can easily be incorporated by replacing the Plant and Wright constant by its renormalized value.

2.2 Testwa

The physical principles that lie at the basis of the energy balance equation have now been sketched. In the following we will go into the details of the implementation of the energy balance equation in the Testwa program.

2.2.1 The energy balance revisited

Testwa has to solve the following equation

$$\frac{\partial}{\partial k}\varepsilon(k) = \gamma\frac{cv_g}{k^2}S \tag{2.53}$$

The net growth rate γ is given by (quasi-linear effect included)

$$\gamma = \frac{\delta_0}{1+\Delta}\omega\left(\frac{u_*}{c}\right)^2 - 4\nu k^2 \tag{2.54}$$

The exact expression for Δ is only valid if $\Delta \ll 1$. It appears, however, that Δ has a singularity for waves with $c = v_g$. We assume that this singularity will be neutralized by other processes not taken into account. Therefore we do not implement the singular expression derived before, but use an "effective" expression given by

$$\Delta = Q\frac{\delta_0}{\kappa\epsilon}\frac{u_*}{c}S \tag{2.55}$$

Q is a constant of order 1.

The validity of this effective expression is limited, not only by cutting the singularity, but also because at large u_* there are waves with $\Delta \approx 1$. A prudent approach to the quasi-linear effect is first calculate spectra with Q=0, and next, if fine-tuning is necessary, do the same with $Q \neq 0$.

One may also regulate the singularity by replacing $1/|c-v_g|$ by $1/|c-v_g| + 0.01$. In that case one doesn't need to introduce the tuning parameter Q.

The energy flux ε is defined as

$$\varepsilon(k) = c^2 v_g(\alpha_1 S^2 + \alpha_2 S^3) \tag{2.56}$$

We recall that the coupling constants α_1 and α_2 may depend on c/v_g (or, in terms of frequencies, on the ratio f/f_{3W}, with $f_{3W}=1/2\pi\{g\sqrt{(g/\{2T\})}\}^{1/2}$. This dependence has not been fixed yet.

For the four-wave interactions Testwa uses a constant α_2.

$$\alpha_2 = T_4 = \text{constant} \tag{2.57}$$

For three-wave interactions α_1 is modeled such that $\alpha_1 \rightarrow 0$ for gravity waves.

$$\alpha_1 = T_3 \frac{\pi}{16}[\tanh(\Sigma(x-1)) + 1] \tag{2.58}$$

With $x = f/f_{3W}$ and T_3 and Σ two constants. T_3 is a measure for the strength of the interactions, Σ is a measure for the width of the transition region of α_1 (from minimal to maximal).

The choice for α_1 is ad hoc, typical for an engineering approach. Fundamental justification is hard to give, there is however evidence that it is not that bad. ISG measurements by Jähne [50] show a distinct viscous cut off at k=1000 1/m. This means for the three-wave interactions that resonant triplets containing capillary waves with $k \geq 1000$ do not exist. This implies that also waves with $k \leq 70$ ($f \leq 4$ Hz) are not represented in the triplets. The transition point in the expression for α_1 is at f_{3W} (7 Hz), which is of the same order of magnitude.

2.2.2 The boundary condition

In order to impose the boundary condition one needs to know the energy flux ε_0 from the spectral peak to the tail. The parameter ε_0 is determined by the structure of the peak, which itself depends on fetch and friction velocity. If one wants the gravity-capillary spectrum as a function of fetch and friction velocity, one first has to determine ε_0 as function of fetch and friction velocity.

In Testwa this problem is solved by assuming that the peak of the spectrum is known up to $f=f_0$. Requiring continuity of the spectrum at $f=f_0$ one automatically obtains ε_0.

How far should f_0 lie from the peak frequency f_p? This question cannot be answered within our theory. Therefore f_0 has to be treated as a tuning parameter. There is, however, the condition that the spectra may not differ very much if f_0 is large enough.

For $f \leq f_0$ the spectrum is parameterized by the JONSWAP expression [39]. The spectral parameters (α, γ, δ, f_p) depend on fetch wind speed. The following parameterization, based on measurements both at sea and in the laboratory, were obtained in JONSWAP.

$$\hat{f}_p = \frac{u_*}{g} f_p = 1.107 \hat{a}^{-0.33} \tag{2.59}$$

$$\alpha = \min(0.05, 0.57(2\pi \hat{f}_p)^{1.5}) \tag{2.60}$$

$$\gamma = \max(1, 1 + 9(1 - (\frac{0.00608}{\hat{f}_p})^2)) \tag{2.61}$$

$$\sigma = 0.08 \tag{2.62}$$

$\hat{a}$ is the dimensionless fetch: $\hat{a} = gx/u_*^2$.

Testwa is developed in order to calculate spectral densities of gravity-capillary waves. For the peak one thus has to rely on a parameterization like the one given above. An alternative method is to calculate the peak by the standard wave model WAM. In WAM there are 25 frequency bins from 0.0418 till 0.4117 Hz. For f_0 one could take the last WAM bin (f_0=0.4117). It is a longer term objective of VIERS to couple Testwa and WAM.

It has to be noted at this point that the JONSWAP parameterization is not universally valid. From the VIERS experiment in Delft it turned out that JONSWAP was not accurate in the laboratory. Hence a special peak parameterization had to be developed.

2.2.3 Description of the program

The program Testwa calculates at given friction velocity and fetch the following quantities: 1D frequency spectrum E(f), 1D wavenumber spectrum F(k), and Phillips' saturation parameter B(k). The spectral data is stored in the arrays indicated in table 2-1. Between different parts of the program the arrays are transported by the common block /SPECTRA/. The array dimension is: ML = 100.

Table 2-1 Testwa arrays

Array	Description	Dimension
FR	frequency grid	ML
XK	wavenumber grid	ML
ET	1D frequency spectrum	ML
PSI1	1D wavenumber spectrum	ML
BSAT	saturation parameter	ML

Testwa has a 'peak' and a 'tail' module: the subroutines GWAMOD and GRACAW.

GWAMOD generates a frequency grid with the grid parameters FR1 and DELF. FR1 is the frequency of the first grid point and DELF is the relative increase in the frequency of the next grid point (on a logaritmic scale the grid points are equidistant).

GWAMOD also calculates the frequency spectrum for the peak and initializes the frequency

spectrum for the tail. The calculation of the peak can be done in different ways depending on the circumstances. The most important factor is whether the fetch or effective fetch is known.

The fetch is well defined in the laboratory or at sea when a constant wind is blowing from the shore (JONSWAP). In this case one can either use the JONSWAP parameterization or a special laboratory one.

At sea the fetch will in general be unknown. Then there are two options to generate a spectral peak.

The first option is to assume that the sea is fully developed. One can then either use a Pierson-Moskowitz spectrum [84] or a JONSWAP spectrum [38] with $x'=10^7$ (at this point the wave growth saturates, see [39]). A third possibility is to take a Toba spectrum and cut it off at the peak.

The second option is to use forecast or analyzed WAM spectra.

The subroutine GRACAW recalculates the tail of the spectrum. First the tail domain is determined. It is set by the parameter FST: the tail starts at FST times peak frequency. The original value of FST is 2, but it turned out that values 3 and 4 give better results. Subsequently GRACAW calculates at every frequency point the corresponding wavenumber according to the dispersion relation. In this way the wavenumber grid XK is generated. Finally GRACAW solves the energy balance equation supplemented by the boundary condition for the energy flux. En passant the wavenumber spectrum PSI1 and the saturation parameter BSAT are calculated.

2.2.4 Tuning

A number of Testwa parameters has not been specified yet. In table 2-2 we give a listing.

Table 2-2 Parameters in the energy balance

Parameter	Name in Testwa	Description	Type
ν	XNUW	kinematic viscosity of water	empirical constant
δ	DELPW	Plant and Wright constant	empirical constant
κ	XKAPPA	Von Kármán constant	empirical constant
T_4	T4	strength four-wave interactions	tuning parameter
T_3	T3	strength three-wave interactions	tuning parameter
Σ^3	WIDTH	width three-wave interactions	tuning parameter
f_0	FST * FP	match frequency	tuning parameter
ε_0	EPS0	energy flux from peak	input parameter
u_*	USTAR	friction velocity	input parameter
Q	QL	quasi-linear effect	fine-tuning parameter

There are three kinds of parameters:

- the empirical constants, which have a fixed value,
- the tuning parameters, which need an assigned value,
- the input parameters, the value of which has to be determined.

The empirical constants ν, δ_0 and κ have the values: $1.22\ 10^{-6}$, 0.05 en 0.4.

Two of the four tuning parameters, FST and WIDTH, are not critical (i.e. the results do not sensitively depend on their exact values.

FST determines the starting point of the spectral tail. Originally FST had the value 2, but if the peak is located at a very small frequency one may need higher values.

WIDTH is a typical smoothing parameter: the smaller WIDTH, the sharper the transition between gravity (no three-wave interactions) and capillary waves (non-zero three-wave interactions). For WIDTH=0 one has a step function that gives rise to a discontinuity in the spectrum. If turns out that WIDTH=4 gives a transition that is sufficiently smooth.

The two parameters T3 and T4 may be determined in such a way that calculated spectra are as close as possible to measured ones.

QL is a fine-tuning parameter, the value of which may be taken zero in lowest order.

2.3 Calculated versus measured spectra

The essential part of Testwa is the subroutine GRACAW, which calculates the spectral tail. As we want to test the performance of GRACAW, we have to make sure that GWAMOD generates the right peak. This implies different versions of GWAMOD for laboratory and sea.

2.3.1 Laboratory spectra (90m fetch)

In the Delft experiment a great number of wave spectra were obtained. A subset (Lobemeier wire spectra) was used to determine the optimal value of the tuning parameters. The Lobemeier spectra were measured at a fetch of approximately 90m and at friction velocities 0.132 till 1.013 m/s. The frequency range is 0 till 17.58 Hz. The spectra are reliable up to 10 Hz.

The following peak parameterization were obtained.

$$\hat{f}_p = 0.731\hat{a}^{-0.325} \tag{2.63}$$

$$\alpha = \min(0.05, 0.24\hat{f}_p) \tag{2.64}$$

$$\gamma = 9.6 \tag{2.65}$$

$$\sigma = 0.16 \tag{2.66}$$

$\hat{a}$ is the dimensionless fetch: $\hat{a} = gx/u_*^2$.

The main difference with JONSWAP is that the Phillips constant α is about a factor 10 smaller, whereas the width σ peak is a factor 2 larger.

As figures 2-1 and 2-2 show, Testwa is able to generate satisfactory spectra over the full wind range. The coupling constants have been set as T3=70 and T4=140. We have also plotted corresponding LSG spectra.

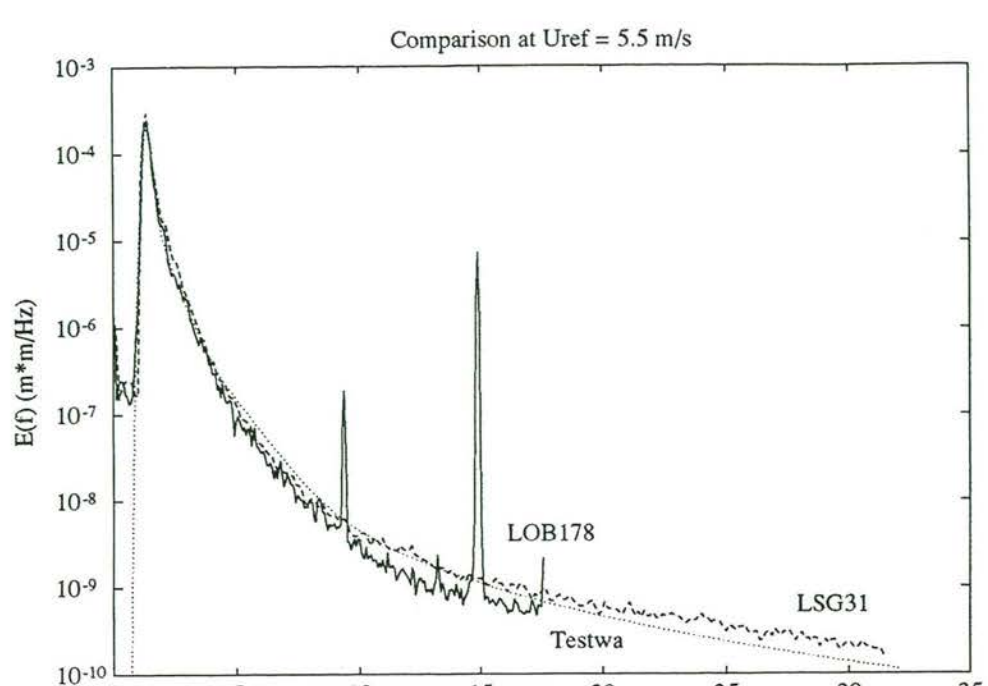

Figure 2-1 Testwa compared with measurements, Uref = 5.5 m/s, 90 m fetch

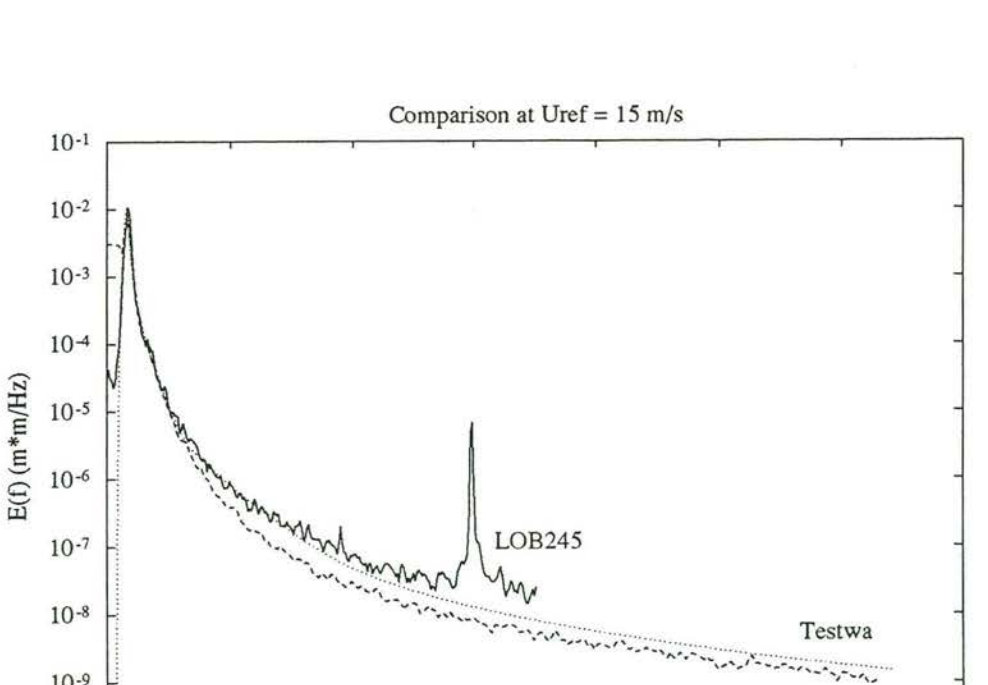

Figure 2-2 Testwa compared with measurements, Uref = 15 m/s, 90 m fetch

2.3.2 Laboratory spectra (30m fetch)

Having set the tuning parameters with the 90m fetch spectra, Testwa was tested against the 30m fetch spectra. The performance of Testwa turns out to be satisfactory. See figures 2-3 and 2-4.

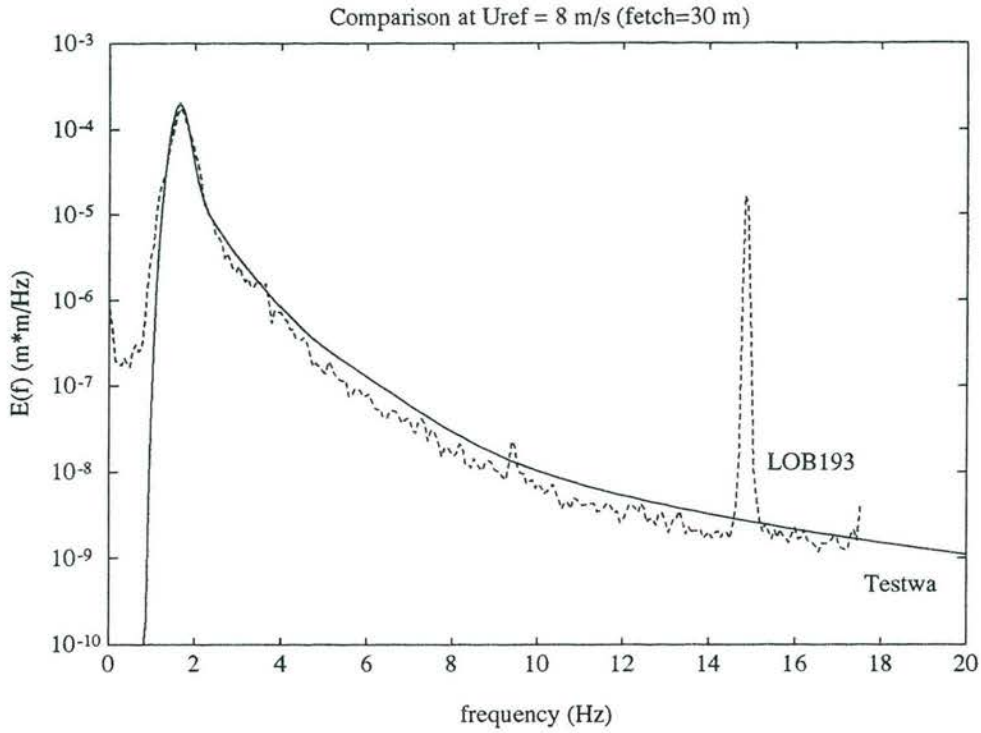

Figure 2-3 Testwa compared with measurements, Uref = 8 m/s, 30 m fetch

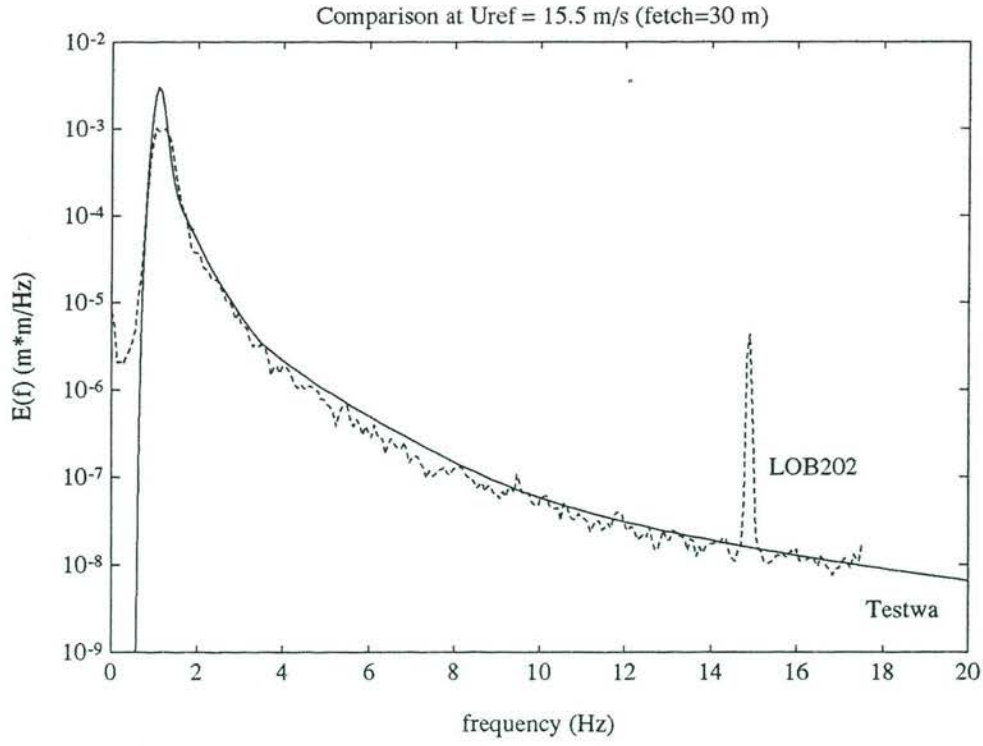

Figure 2-4 Testwa compared with measurements, Uref = 15.5 m/s, 30 m fetch

2.3.3 Sea spectra

There are few measurements of gravity-capillary waves at sea. The Lobemeier spectra obtained at "meetpost Noordwijk", turned out only to be reliable up to 2 Hz. We therefore tested Testwa against a parameterization given by Stolte [97]. Stolte measured sea spectra at "Forschungplattform Nordsee" and obtained for constant winds ($U_{10} \leq 8$ m/s) the following parameterization ($0.8 < f < 8$ Hz)

$$E(f) = \alpha g^2 (2\pi)^{-4} f^{-n} \tag{2.67}$$

$$n = 5.25 - 0.199 U_{10} + 0.00962 U_{10}^2 \tag{2.68}$$

$$\log \alpha = -2.90 + 0.306 U_{10} - 0.0185 U_{10}^2 \tag{2.69}$$

In figure 2-5 we compare a Stolte spectrum at 6m/s with a Testwa spectrum at u_*=0.25 m/s and find that the differences remain within acceptable limits. The peak used by Testwa is a Toba parameterization, $E(f) = \tau g u_* f^{-4}$. At MPN we find a Toba constant of $\tau = 2.5\ 10^{-4}$ in fair agreement with values reported previously [99].

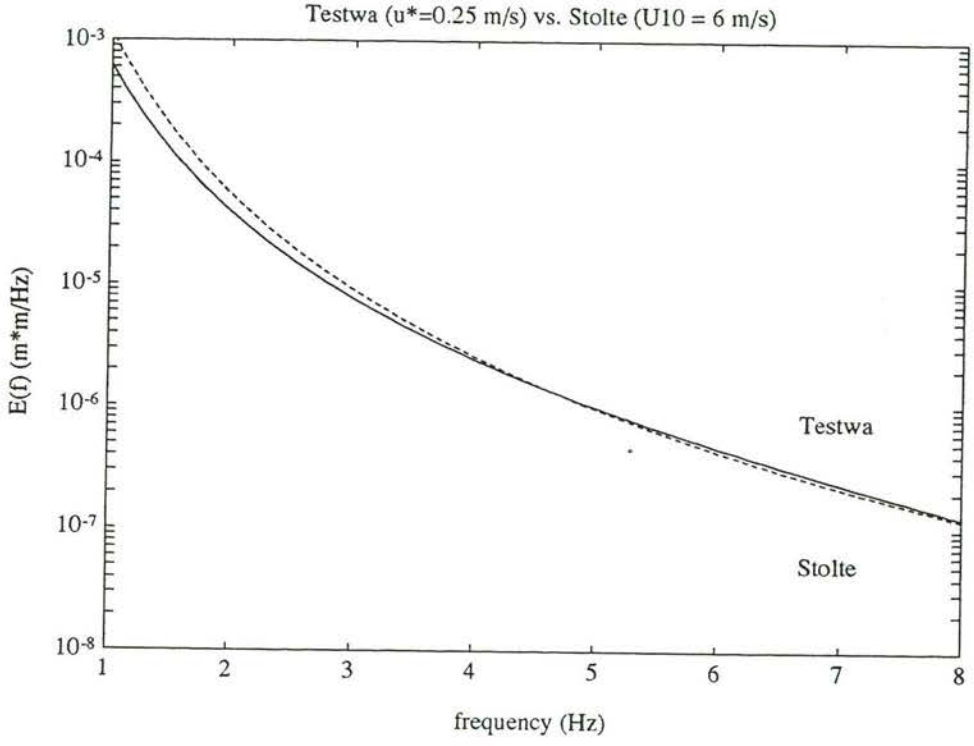

Figure 2-5 Testwa (u_*= 0.25 m/s) compared with Stolte (U_{10} = 6 m/s)

2.3.4 Discussion

On the basis of these tests we conclude that Testwa is quite capable to generate reliable spectra if the coupling constants for 3- and 4-wave interactions are given appropriate values (T3=70, T4=140). It turns out, however, that these values are quite high: T3 and T4 are an order of magnitude larger than one would expect from estimates based on the exact wave mode equations. An obvious reason for this enhancement is that T3 and T4 are *effective* coupling constants. Not only the nonlinear interactions contribute to these constants, but also

processes that are not taken explicitly into account. Examples of these latter are e.g. wave breaking and wave-shear current interactions. Overestimation of the wind input is another possible cause for the spurious enhancement of the coupling constants.

The actual cause for the enhanced nonlinear interactions is hard to identify. Even if it can be found the next question, how to implement the additional process into the short-wave model, is far from trivial. Therefore, for the time being we have to contend ourselves with our effective theory. Although it may not encompass all relevant processes, it does produce realistic short-wave spectra.

3 Sea-surface scattering models

3.1 Introduction

Over the last twenty years a lot of research has been conducted on the topic of radar backscattering from the ocean surface. Although it is still not possible to obtain exact analytical solutions to the problem of scattering from the ocean surface, approximate solutions have been obtained.

In the VIERS project three of these approximate solutions or -models- have been compared. The models are: a two-scale model, the full-wave model, developed by Bahar and the Integral Equation Model from Fung.

The excellent data acquired in the Delft wind/wave flume experiment, and especially the detailed wave spectra, permitted a comparison of these models based on realistic water surface characteristics. The results of this comparison are presented in chapter 4.

In this chapter the basics of each of the models will be outlined. In paragraph 3.2 an overview over the models is presented partly based on an excellent introduction to backscattering from sea surfaces by Valenzuela [101]. The more interested reader may then proceed to sections 3.3-3.6 (and Appendix A) where more details will be given on the models.

3.2 Overview of microwave backscattering models

It is well known that in e.m. theory the electric field $\vec{E}$ and the magnetic field $\vec{H}$, in a domain V enclosed by a simple surface S may be determined by the Stratton-Chu integral equations if the surface fields are known:

$$\vec{E}(\vec{r}) = \vec{E}_i(\vec{r}) - \oint\left\{ i\omega\mu_0(\vec{n}\times\vec{H})G + (\vec{n}\times\vec{E})\times\nabla G + (\vec{n}\cdot\vec{E})\nabla G\right\} d\vec{S} \qquad (3.1)$$

$$\vec{H}(\vec{r}) = \vec{H}_i(\vec{r}) - \oint\left\{ i\omega\epsilon_0(\vec{n}\times\vec{E})G - (\vec{n}\times\vec{H})\times\nabla G - (\vec{n}\cdot\vec{H})\nabla G\right\} d\vec{S} \qquad (3.2)$$

where the index i denotes the incident field. Here ϵ_0 and μ_0 are the electric permitivity and magnetic permeability of the medium, ω is the angular frequency of the incident e.m. radiation, G is the Green's function,

$$G = \exp(ik_oR) \,/\, 4\pi R \qquad (3.3)$$

with k_0 the wavenumber of the e.m. radiation, R the distance from the observation point $\vec{r}$ to the scattering point on the surface $\vec{r'}$, $\vec{n}$ is the unit vector normal to the surface and ∇ is the gradient vector operator.

In the case that the surface fields in the integrands are known, the scattered field can be determined, because by definition:

$$\vec{E}_S = \vec{E} - \vec{E}_i \qquad (3.4)$$

and

$$\vec{H}_S = \vec{H} - \vec{H}_i \tag{3.5}$$

From these fields then the backscattered power P_s and the radar cross section can be determined by:

$$P_s = \tfrac{1}{2}\Re < \vec{E}_S \times \vec{H}_S^* > \tag{3.6}$$

and

$$\sigma = \lim_{R\to\infty} 4\pi R^2 < |\vec{E}_S|^2 > / |\vec{E}_i|^2 \tag{3.7}$$

Here $\vec{H}_S^*$ is the complex conjugate of the scattered magnetic field $\vec{H}_S$ and < ... > denotes the ensemble average.

For a perfectly conducting surface

$$\vec{n} \times \vec{E} = 0 \tag{3.8}$$

and

$$\vec{n} \cdot \vec{H} = 0 \tag{3.9}$$

it can be shown that the integral equations (3.1) and (3.2) decouple and that the magnetic field satisfies

$$\vec{n} \times \vec{H}(\vec{r}') = 2\vec{n} \times \vec{H}_i(\vec{r}') - 2\vec{n} \times \int_{\vec{S}} (\vec{n} \times \vec{H}) \times \nabla G \, dS \tag{3.10}$$

where $\vec{r}'$ is on the surface S under the condition that $\vec{r}' \neq \vec{r}$. Equation (3.10) is also known as the surface current integral equation and it is the starting point for most of the approximate scattering theories such as the small perturbation method or the Kirchhoff approximation. In the following paragraphs the approximations used in the derivation of the formulas for the scattering cross sections will be briefly explained.

3.2.1 The Small Perturbation Method (SPM)

Rice [86] was the first to apply perturbation theory to the scattering of e.m. waves from perfectly conducting surfaces. Doing this he obtained the explicit first- and second-order scattered fields for both HH and VV polarization.

In perturbation scattering theory the surface is supposed to be slightly rough, which means that it must satisfy the conditions: $|k_0\xi| \ll 1$ and $|\nabla\xi| \ll 1$. Thus the surface excursions must be small compared to the incident e.m. wavelength and also the surface slopes must be small.

In SPM theory the small-scale roughness of the surface is 'replaced' by effective currents on the mean surface. In Rice's approximation this mean surface had to be flat, but this was later

extended by Mitzner [77] to arbitrarily shaped mean surfaces. The surface fields are then expanded in a series

$$\vec{H} = \vec{H}^{(0)} + \vec{H}^{(1)} + \vec{H}^{(2)} + \ldots \tag{3.11}$$

$$\vec{E} = \vec{E}^{(0)} + \vec{E}^{(1)} + \vec{E}^{(2)} + \ldots \tag{3.12}$$

where

$$\vec{E}^{(0)}, \vec{H}^{(0)} \tag{3.13}$$

are the surface fields when the small scale roughness is absent and

$$\vec{E}^{(i)}, \vec{H}^{(i)} \tag{3.14}$$

are the higher-order fields dependent on powers of the amplitude ξ.

Mizner [77] derived expressions for the first- and second order fields. In first order

$$\vec{n} \times \vec{E}^{(1)} = -\vec{n} \times \left\{ \Delta(\vec{n} \times \vec{E}^{(0)}) \nabla_T \xi + \xi \left[\Delta \left(\frac{\partial \vec{E}^{(0)}}{\partial n} \right) \right] \right\} \tag{3.15}$$

$$\vec{n} \times \vec{H}^{(1)} = -\vec{n} \times \left\{ \Delta(\vec{n} \times \vec{H}^{(0)}) \nabla_T \xi + \xi \left[\Delta \left(\frac{\partial \vec{H}^{(0)}}{\partial n} \right) \right] \right\} \tag{3.16}$$

where $\Delta(...)$ denotes the discontinuity of the quantity at the mean surface, $\vec{n}$ is the unit normal to the mean surface and ∇_T is the transverse gradient operator. Hence the first order fields are linear functions of the surface elevation ξ.

Using these approximated fields one can then derive the well known formulae for the backscatter cross-section per unit area (see e.g. Ulaby et al [100])

$$\sigma_0^{(1)}(\theta)_{pol} = 8\pi k_0^4 \cos^4\theta \, |g_{pol}^{(1)}|^2 [W(\vec{k_b}) + W(-\vec{k_b})] \tag{3.17}$$

where W(,) is the two-dimensional wave-number spectral density of the surface, θ is the incidence angle, $k_o=2\pi/\lambda$ is the radar wavenumber, $|k_b|=2k_o\sin\theta$ is the Bragg wavenumber, $\arg(k_b)$ is the radar look direction and $g^{(1)}_{pol}$ are the first order polarization dependent scattering coefficients:

$$g_{HH}^{(1)}(\theta) = \frac{(\epsilon_r - 1)}{[\cos\theta + (\epsilon_r - \sin^2\theta)^{1/2}]^2} \tag{3.18}$$

$$g_{VV}^{(1)}(\theta) = \frac{(\epsilon_r - 1)\left[\epsilon_r(1+\sin^2\theta) - \sin^2\theta\right]}{\left[\epsilon_r \cos\theta + (\epsilon_r - \sin^2\theta)^{1/2}\right]^2} \tag{3.19}$$

Here ε_r is the complex relative dielectric constant. It should be noted here that the definition of the normalization of the two-dimensional wave-number spectral density function $W(\vec{k})$ differs in literature. The normalization used here is:

$$< \xi^2 >= \sigma^2 = \iint W(\vec{k})\, d\vec{k} \tag{3.20}$$

thus the spectrum W is normalized on the surface variance. Valenzuela [101] uses a normalization equal to 4 times the surface variance. Other authors like e.g. Fung [24]use a factor $1/2\pi$. Care should be taken when calculating Bragg backscattering with (3.17) that the spectral density W is normalized in the right way.

3.2.2 The Two-Scale model (TSc).

It has been known for some time that the polarization ratio (the ratio of the cross section for vertical and horizontal polarization) decreases, for large angles of incidence, as the ocean becomes rougher with wind speed. To account for this effect, Wright [113] formulated for the first time what was called a *composite-surface scattering model.*

In this model the sea is assumed to be composed of an infinite number of slightly rough patches. The net back-scattered power is an average, of the backscattered power from a single rough patch, over the distribution of slopes of the dominant waves of the ocean.

When this type of model is combined, for small incidence angles, with a low frequency approximation as e.g. the physical optics approximation then we speak of a two-scale model.

In one of the earlier reports on the VIERS experiment [14] an implementation of a two-scale model was used which was based on work done by Donelan and Pierson [23]. It turned out that this model had a number of shortcomings which were:

- at high wind speeds the VV prediction of the model was much larger than the measured cross sections,
- the model exaggerates the difference between VV and HH polarized scatter,
- the model had two rather arbitrarily chosen cut-off parameters;one wavenumber k_c which separates the long wave and short wave spectrum and an angular cut-off for the SPM contribution to the backscattering for incidence angles $\theta_c < 18^o$,
- the model backscatter at small incidence angles highly depends on the choice of the angular cut-off parameter θ_c, that shields a model singularity at zero incidence angle,
- the model provides no means to explain the upwind/downwind difference, other than by assuming an asymmetry in the waves.

Actually the 'two-scale' model reported was a 'one-scale' model, since the contribution from physical optics was not taken into account. This was done on purpose because the influence of the ad-hoc cut-off parameter in the low incidence angle region (see the third shortcoming) overruled the contribution of the physical optics.

Donelan and Pierson [23] chose their separation of scales cut-off parameter k_c at $k_b/40$, with k_b the Bragg wavenumber given by $k_b = 2k_o\sin\theta$. This was not a good choice for the tank data since the dominant wave in the tank has a much larger wavenumber than at sea, sometimes even beyond $k_b/40$. Since there was no physical reasoning for the choice of this pa-

rameter, a rather arbitrary choice was made for k_c = 36 rad/m. In one of the hindsight observations in the second VIERS report [14, p. 21]) it was mentioned that the cut-off could perhaps better have been chosen a little higher.

With these shortcomings in mind, ways were sought to come to solutions of the problems. This was done in the following ways:

- by determining the separation of scales cut-off parameter k_c in a more or less physical way,
- by removal of the angular cut-off wavenumber which had to shield the model singularity at nadir incidence,
- by improvement of the integration algorithm,
- by adding the physical optics contribution.

An improved version of the two-scale model is described in section 3.3.

3.2.3 The "Holliday" model (HSW).

Starting point for the derivation of their scattering model by Holliday, St-Cyr and Woods [41] are the Maxwell equations (3.1) and (3.2). Assuming a perfectly conducting surface these equations decouple and they come to the surface integral equation (3.10). In this equation they substitute in the second term on the right hand side the *incident* field instead of the local field. This can be thought of as a first step in an iterative solution of the integral equation. Furthermore they use the following well known approximation for the gradient of the Green's function:

$$\nabla^{(1)} G(\vec{r}_0, \vec{r}_1) = \frac{i}{4\pi} \frac{\exp(ik_o r_0)}{r_0} \exp(-i\vec{k}_o \cdot \vec{r}_1) \vec{k} \left[1 + O\left(\frac{1}{k_o r_0}\right) \right] \qquad (3.21)$$

With these approximations they find a simple way of calculating the radar backscatter cross section. This solution of the surface current integral equation is also known as the "Kirchhoff" solution.

For small incidence angles and in the limit $k_0 \rightarrow \infty$ this solution is equal to the well known physical optics specular reflection formula, see e.g. Valenzuela [101].

For high incidence angles or small mean square wave heights, a solution is found which resembles more or less the SPM or Bragg solution, with this difference, that it shows no polarization dependence. To include a polarization dependence higher order terms from the second iteration should be added.

For the interested reader more details will be given in section 3.4 on the derivation of the "Holliday" model and especially a fast numerical way to calculate the radar backscatter from the ocean surface assuming a k^{-4} wave spectrum for the small scale waves.

3.2.4 The IEM model by Fung and Pan (IEM).

In the previous section recent developments of microwave backscattering theory have been described as performed by Holliday et al [41]. The approximation of Holliday et al leads to,

what is known also as the Kirchhoff approximation. A similar result was obtained earlier by Beckmann and Spizzichino [11] and Sancer [89].

It was believed to be (and still is) a valid solution to the backscattering from random rough surfaces, like the sea surface, at small angles of incidence.

At large angles of incidence, the first-order solution of the small-perturbation theory seemed to predict the results better, especially with regard to the polarization characteristics. The Kirchhoff solution does not show any polarization difference at all, which is in contradiction to the observations.

More recently Fung, at the university of Texas, published a number of articles on scattering from random rough surfaces also based on approximation of the Integral Equation (Fung and Pan [26], Pan and Fung [81], Fung and Chen [27], Chen and Fung [16]. In this work they also simplify the surface current equation, however, where Holliday uses a zero-th order approximation for the surface current, Fung et al use a higher order approximation. The most important consequence of this is that this theory unites the Kirchhoff approximation on one hand and the small perturbation method on the other. Thus with one theory the backscattering over the whole range of incidence angles can be described. This means that a solution is found which is probably also valid for the intermediate region where neither Kirchhoff nor SPM are applicable.

In order to be able to solve the surface current equation, Fung and Pan apply some simplifications in (3.10). They argue that several terms in (3.10) will cancel for a random surface and further that higher order slope terms will contribute much less than first order slope terms and thus can be neglected. With these and some other 'intuitive simplifications they come to a new approximation. The simplifications lead to a restriction on the validity of the model which is examined in a separate paper for specific surface statistics [81]. They find:

$$\cos^2\theta \frac{(k_o\sigma)^2}{(k_oc)^{1/2}} \exp\left\{-[2k_oc(1-\sin\theta)]^{1/2}\right\} \ll 1 \qquad (3.22)$$

where θ is the incidence angle, k_0 the wavenumber, σ the surface standard deviation, c is equal to 0.459 l and l is the autocorrelation length. Since the autocorrelation length is not known most of the time, it is impossible to verify this condition under realistic circumstances.

Further details of the results of their calculations and comparisons with our measurements will be presented in section 3.5.

3.2.5 The "full wave model" by Bahar (BAH).

In the derivation of what Bahar [4] calls the "full wave model" he follows a different approach than Holliday and Fung. Bahar starts with the conversion of the Maxwell equations into a set of coupled first-order differential equations for the wave amplitudes. The solution of these coupled differential equations is then approximated in an iterative way. First the first order solution is obtained by neglecting the transmission and reflection scattering coefficients. Then the first order solutions are substituted again in the differential equations and so a second order solution is found. These solutions are then used in the complete expansion for the electro-magnetic fields to obtain the desired scattered radiation fields. Hereby the steepest descent method was used. For more details on the derivation of this theory, the reader is referred to [2,3,4,5,6].

The solution reached thus far is only valid for small surface slopes. In order to extend the solution to problems of scattering by two-dimensional rough surfaces with arbitrary slopes, the rough surface is regarded as a continuum of elementary surfaces of varying slope and height rather than a continuum of horizontal elementary surfaces of varying height. The contribution to the total scattered field from an inclined elementary surface is obtained from the standard solution after making the appropriate coordinate transformation. In this way the restrictions of the maximum slope of the rough surface are removed while full use can be made of the relatively easy to use solution of the full-wave approach.

The basic equations of this model are described in section 3.6.

3.3 An improved two-scale model.

In the initial VIERS two-scale model, the following integration was performed over the long wave slopes:

$$\sigma^o_{pol,TSc} = \int_{-\infty}^{\infty} P(\tan\psi, \tan\delta)\tilde{\sigma}^o_{pol}\, d\vec{s} \tag{3.23}$$

where

$$\begin{aligned} \tilde{\sigma}^o_{pol} &= G_{pol}(k_0, \vec{s}; \theta, \ldots) \times W(k_b), && \text{for } \theta > \theta_c \ (= 18^\circ) \\ \tilde{\sigma}^o_{pol} &= 0.0 && \text{elsewhere} \end{aligned} \tag{3.24}$$

and ψ, δ are the tilt angles of the surface facet with respect to the normal in and perpendicular to the plane of incidence respectively. In words (3.23) reads: the radar backscatter σ^o_{pol} can be found by integrating the backscatter $\tilde{\sigma}^o_{pol}$ of the facets tilted in a plane with angles ψ and δ times the probability P(tanψ, tanδ) that the water surface is tilted in that direction. The backscatter $\tilde{\sigma}^o_{pol}$ is determined by SPM and is proportional to the wave spectrum W(k,α) evaluated at the Bragg wavenumber k_b. The function G_{pol} is given by Bragg theory, see Valenzuela [101].

In this integration an artificial cut-off is introduced for local incidence angles below 18°. This empirical determined angular cut-off turned out to be necessary in order to shield off a model singularity at nadir incidence angles which would otherwise 'blow-up' the backscatter predictions below incidence angles of approximately 30 degrees. Numerical integration using standard techniques over a function with a discontinuity as described above introduces rather large errors (O(1 dB)) which can only be avoided when the amount of integration points is increased. This has the disadvantage of reducing the speed of the program.

A better approach is the one described by Brown [13]. He splits the surface into a low and a high frequency part via the splitting parameter k_c:

$$W(k,\alpha) = W_L(k,\alpha) + W_H(k,\alpha) \tag{3.25}$$

with

$$\begin{aligned} W_L(k,\alpha) &= W(k,\alpha) \quad k < k_c \\ &= 0. \quad\quad\quad k \geq k_c \\ W_H(k,\alpha) &= W(k,\alpha) \quad k \geq k_c \\ &= 0. \quad\quad\quad k < k_c \end{aligned} \tag{3.26}$$

SPM or better: the composite-surface scattering is only applied to the high wavenumber region i.d $k > k_c$ and physical optics is applied to the low frequency part of the spectrum. The two contributions to the backscattering are then summed:

$$\sigma^o_{pol,TSc} = \sigma^o_{PO} + \sigma^0_{pol,SPM} \tag{3.27}$$

This summing of the composite-surface contribution and the physical optics contribution was first done by Barrick and Peake [9]. To do this one must make the assumption that the large scale roughness and the small scale roughness are not correlated. It is well known that this assumption is violated for the ocean surface since the small scale waves are modulated by the long, gravity waves. However the impact of this modulation on the applicability of the theory has never been sorted out in detail, to our knowledge.

The contribution from physical optics can be written as:

$$\sigma^o_{PO} = \frac{|R(0)|^2 \sec^4\theta}{2s_{a,w}s_{c,w}} \exp\left(\frac{\tan^2\theta}{2s_L^2}\right) \exp\left(-4k_0^2\sigma_H^2\right) \tag{3.28}$$

see e.g. Donelan and Pierson [23]. The term $\exp(-4k_0{}^2\sigma_H{}^2)$ in (3.28) gives a correction to the physical optics contribution due to the effect of small scale waves, $\sigma_H{}^2$ is the surface variance of the high frequency part of the wavenumber spectrum, defined in (3.37). A condition for the applicability of (3.28) is:

$$4k_o^2\cos^2\theta\sigma_L^2 \gg 1 \tag{3.29}$$

The surface variance of the low frequency part of the wavenumber spectrum $\sigma_L{}^2$ is defined in a similar way as $\sigma_H{}^2$ (3.37). The long wave slope variances in downwind and crosswind directions, $s^2_{a,w}$, $s^2_{c,w}$ respectively, are obtained from the long wave spectrum W_L as follows:

$$\begin{aligned} s^2_{a,w} &= \int_0^{2\pi}\int_0^{k_c} k^3\cos^2(\alpha-\alpha_w)W_L(k,\alpha)dkd\alpha \\ s^2_{c,w} &= \int_0^{2\pi}\int_0^{k_c} k^3\sin^2(\alpha-\alpha_w)W_L(k,\alpha)dkd\alpha \end{aligned} \tag{3.30}$$

where α_w is the wind direction with respect to North. In case of an elliptical variation with respect to the azimuth angle, the slope variance $s_L{}^2$ in the plane of incidence can be shown to equal:

$$s_L^2 = \frac{s^2_{a,w}s^2_{c,w}}{s^2_{c,w}\cos^2(\alpha_r-\alpha_w)+s^2_{a,w}\sin^2(\alpha_r-\alpha_w)} \tag{3.31}$$

where α_r is the radar look direction with respect to North. For the more realistic azimuth dependence of the wave spectrum: $[1+2a_2\cos 2(\alpha-\alpha_w)]/2\pi$ (see eq. 4.2), s_L^2 will be determined later in this report (see eq. 4.7).

$|R(0)|^2$ in (3.28) is the reflection coefficient at normal incidence, depending on the microwave frequency via the relative dielectric constant ε_r:

$$|R(0)| = |0.65(\epsilon_r - 1) / (\sqrt{\epsilon_r} + 1)^2| \tag{3.32}$$

The factor 0.65 in this last equation is based on a correction of the standard reflection coefficient as specified by Valenzuela [101]. The factor is necessary because the remaining short scale disturbances of the water surface reduce the cross section as given by physical optics.

The contribution of the composite-surface scattering model is calculated differently from the way it was done in the initial VIERS model. As mentioned before, the SPM approximation is only applied to the high frequency part of the ocean spectral density spectrum $W(k,\alpha)$. So the wavespectrum W(..) in (3.24) is replaced by the high wavenumber wavespectrum $W_H(..)$. Since the integrand is zero for wavenumber below the cut-off k_c, the artificial angular cut-off θ_i is not necessary anymore. However the numerical integration problem still remains, because also the new integrand displays a discontinuity. It can be solved by splitting of the integral in two parts and an adjustment of the integration intervals (see [13]).

Assuming small angles ψ and δ so that $\sin\psi \approx \tan\psi$ and $\sin\delta \approx \tan\delta$ and knowing that the integrand in the integration is equal to zero for $|k| < k_c$ we can approximate the integral in (3.23) by re-defining the integration limits and splitting the integration in two pieces as follows:

$$\sigma^o_{pol,SPM} = \sigma^o_{pol,I} - \sigma^o_{pol,II} \tag{3.33}$$

with:

$$\begin{aligned} \sigma^o_{pol,I} &= \int_{-\infty}^{+\infty}\int_{-\infty}^{+\infty} P(\tan\psi,\tan\delta)\,\tilde{\sigma}^o_{pol}\,d\tan\psi\,d\tan\delta \\ \sigma^o_{pol,II} &= \int_{a_0}^{a_1}\int_{a_2}^{a_3} P(\tan\psi,\tan\delta)\,\tilde{\sigma}^o_{pol}\,d\tan\psi\,d\tan\delta \end{aligned} \tag{3.34}$$

where:

$$\begin{aligned} a_0 &= (-k_c - 2k_o\sin\theta) / 2k_o\cos\theta \\ a_1 &= (+k_c - 2k_o\sin\theta) / 2k_o\cos\theta \\ a_2 &= -k_c / 2k_o \\ a_3 &= +k_c / 2k_o \end{aligned} \tag{3.35}$$

Within these integration limits, the integrand is continuous and smooth and thus the numerical integration does not encounter the difficulty anymore which was seen before. The approximations made in the derivation of (3.34) are acceptably small for the type of application we are talking of.

3.3.1 The choice of the cut-off wavenumber k_c.

Of course, a very important parameter in the two-scale model is the separation wavenumber k_c. This wavenumber separates the scales between the two approximating theories, in our case the physical optics and the composite surface theory. In the original VIERS model this so-called cut-off parameter was more or less arbitrarily chosen at a fixed value of k_c=36 rad/m.

However there are some guidelines which can be used to determine the cut-off parameter.

For instance, Bahar, Barrick and Fitzwater [7] investigate the specification of the wavenumber for the spectral splitting k_c in their article. They perform this investigation by applying a special two-scale version of the full wave approach model (see also section 3.6) to rough surface backscattering. Since the full wave approach is not restricted by the limitations of perturbation theory, it is possible to examine the sensitivity of the computed values for the backscatter to large variations in the value of the splitting wavenumber k_c. They conclude that a good choice of the cut-off wavenumber is determined by the parameter

$$\beta = 4k_o^2\sigma_H^2 \tag{3.36}$$

The surface variance of the high frequency part of the wavenumber spectrum σ_H^2 is defined as follows:

$$\sigma_H^2 = \int_0^{2\pi}\int_{k_c}^{\infty} W_H(k,\alpha)k\,dk\,d\alpha \tag{3.37}$$

For application with the full wave approach Bahar et al find that $\beta \approx 1$ is an optimal choice. Optimal means in this context that the cross section variation with the actual choice of k_c is negligible and that the computation of the Full Wave Approach model can be executed in an efficient way. The choice for $\beta = 1$ means that the wave number cut-off parameter k_c must be chosen in such a way that the short wave variance is approximately equal to:.

$$\sigma_H^2 \approx 1 / (4k_o^2) \tag{3.38}$$

In an earlier study using a two-scale model similar to the one used in the VIERS model, Brown [13] finds a different optimal value for the parameter β. He argues that the cut-off parameter must be chosen such, that for the high wavenumber region the Small Perturbation Theory could be applied whereas for the low frequency region the physical optics approximation should be applicable. He then finds an optimal value for $\beta \approx 0.1$, which is much smaller than the value given by Bahar et al and which means that k_c will be much larger.

The reason for the difference is that the full wave approach takes into account higher order approximations than the perturbation method. As a consequence it can handle surfaces with a larger roughness than SPM.

Since we discuss here the application of a two-scale model with for the high frequencies the small perturbation approximation, it is more appropriate to adapt the value of $\beta \approx 0.1$ as found by Brown. However, in practice it turns out that this value is too small. Under circumstances of a rough surface (medium to high wind speeds) the cut-off parameter k_c will be larger than the Bragg wavenumber for moderate to high incidence angles. This leads to an underestimation of the backscatter cross section.

On the other hand, in a recent publication Fung, Li and Chen [28] have investigated the first order perturbation method and found that the range of validity could be up to $\beta \approx 0.5$. This value leads to much lower cut-off wavenumbers and hence the above mentioned problem does not arise.

It turns out that in a comparison with our data (see section 4) $\beta \approx 0.13$ gives an optimal result. So for the purpose of the VIERS model the separation wavenumber k_c was determined using this value.

3.4 The Holliday model for microwave scattering

Holliday, St-Cyr and Woods [41] solve the surface current integral equation simply by putting $\vec{H} = \vec{H}_i$ (zeroth iteration). In case of an infinite footprint (or a footprint that is large compared to the longest waves present), they find for the normalized radar cross section σ^0:

$$\sigma^0 = 2\frac{k^4}{k_{oz}^2}\Gamma(-2\vec{k}_H) \tag{3.39}$$

with

$$\vec{k_o} = (k_{ox}, k_{oy}, k_{oz}) = (\vec{k}_H, k_{oz}) \tag{3.40}$$

the wavenumber of the incoming microwave radiation and Γ given by

$$\Gamma(-2\vec{k}_H) = \frac{1}{2\pi}\int_{-\infty}^{\infty}\int_{-\infty}^{\infty}\exp(-2i(k_{ox}x + k_{oy}y)F(x,y)dxdy \tag{3.41}$$

where

$$F(x,y) = \exp[-4k_{oz}^2\{\phi(0,0) - \phi(x,y)\}] \tag{3.42}$$

The autocorrelation function ϕ is defined as:

$$\phi(x,y) = \int_{-\infty}^{+\infty}\int_{-\infty}^{+\infty} W(k_x, k_y)\cos(k_x x + k_y y)dk_x dk_y \tag{3.43}$$

where W is again the two-dimensional wave number spectrum. The reader is referred to Holliday, St-Cyr and Woods [41] for a clear derivation of these equations.

The model defined by equation (3.39) till (3.43) is also known as the Kirchhoff approximation for a rough surface. It includes the effects of long waves in a natural way, but there is no polarization dependence. Polarization enters when the first iteration of the surface current equation is taken into account. Therefore this model is restricted to small incidence angles ($\theta < 30°$).

In their article, Holliday, St-Cyr and Woods [41] evaluate these equations numerically applying FFT techniques. To obtain good accuracy, a fine grid in both position and wavenumber is necessary. For short radar wave lengths (which require a high resolution in space) and/or high wind speeds (which require a fine resolution in wave number space to

describe the peak of the wave spectrum accurate enough) the dimension of the FFT's easily grows beyond today's computer capacities. Even when the long-wave part of the spectrum is treated numerically (see the Appendix of the paper by Holliday et al [41]), the calculation of the cross section still requires too much time for our purposes.

Given a specific shape of the two-dimensional wave number spectrum W it is possible to speed up the calculation of the autocorrelation function $\phi(x,y)$, the first step in the calculation of the cross section. The price paid here, is that the tail of the spectrum should resemble the specific shape of the parameterization.

In the following it will be summarized how the radar cross section can be calculated accurately and fast for a specific quadropole spectrum. The calculation is especially focused on the calculation of the function Γ since this function also features in the model by Fung and Pan (section 3.5) and the Full Wave Approach model by Bahar (section 3.6). Through the efficient calculation of Γ one is able to implement all of these models in an efficient and accurate way.

3.4.1 Numerical calculation of the function Γ

First, assume that the wave spectrum W is separable into a radial part, W_r, and an angular part, W_a, as is the case in many parameterizations:

$$W(k_x, k_y) = W_r(k)W_a(\alpha) \tag{3.44}$$

where α is the angle in the horizontal plane. When we define:

$$U(r,\alpha) = \phi(0,\alpha) - \phi(r,\alpha) \tag{3.45}$$

then, using Jacobi-Anger expansion, one can show that (see Appendix A.1):

$$U(r,\alpha) = A_0[N - R_0(r)] - 2\sum_{m=1}^{\infty}(-1)^m A_{2m} R_{2m}(r)\cos(2m\alpha) \tag{3.46}$$

where

$$\begin{aligned} N &= \int_0^{\infty} W_r(k)k\,dk \\ R_n(r) &= \int_0^{\infty} kW_r(k)J_n(kr)dk, \qquad n \geq 0 \\ A_n &= \int_0^{2\pi} W_a(\alpha)\cos(n\alpha)d\alpha, \quad n \geq 0 \\ B_n &= \int_0^{2\pi} W_a(\alpha)\sin(n\alpha)d\alpha, \quad n > 0 \end{aligned} \tag{3.47}$$

here $J_n(kr)$ stands for the Bessel function of the integer order n. For the simple angular distributions, which are normally used for the wind wave spectra, only the first few coefficients survive. For instance for a cosine-squared distribution one finds: $A_0=1$ and $A_2=0.5$, all other angular coefficients are equal to zero.

The radial coefficients are not so easy to calculate. For some classes of radial spectra, it will be shown that they can be calculated analytically. Here only the results of this derivation will be presented. The interested reader is referred to Appendix A.2.

Several forms of the radial spectrum with a k^{-4} asymptotic behavior were considered. A spectrum that appeared to be particularly suitable for analytic integration is the so-called octupole spectrum

$$W_r(k) = B\frac{k^4}{k_p^8+k^8} \tag{3.48}$$

with k_p and B parameters determining the peak position and the strength, the peak being located at $k=k_p$. It can be shown (see Appendix A.2) that the radial coefficients for this spectrum are given by

$$R_{2n}(r) = \frac{i\pi B}{4k_p^2}\sum_{j=1}^{4}\exp\{-i\pi(2j-1)/4\}H_{2n}^{(1)}[k_p r\exp\{i\pi(2j-1)/8\}] \tag{3.49}$$

In Appendix A.2 it is shown that the expansion for the radial coefficients in (3.49) converges rapidly. Only the first two or three terms contribute. The factor N in (3.46) and (3.47)becomes:

$$N = \pi\sqrt{2}\frac{B}{8k_p^2} \tag{3.50}$$

when evaluated for the spectrum given in (3.44).

With the determination of the radial coefficients $R_{2n}(r)$ and the angular coefficients A_{2m} and N, the description of the function $U(r,\alpha)$ is complete. Please note that this function is, except for a constant factor $-4k_{ox}^2$ the argument of the exponential function F(x,y), (3.42) . The desired function $\Gamma(k_x,k_y)$ is the Fourier transform of this function F(x,y). It is possible to calculate Γ using an FFT algorithm. However, since Γ is evaluated only at $k = -2k_H$, the "Bragg" wavelength, it is still better to develop a dedicated numerical integration procedure. Especially, because as mentioned before, for realistic circumstances the dimensions of the FFT become very large. Note that both Γ and $U(r,\alpha)$ are both real quantities, so the complex exponential in (3.41) reduces to a cosine. This cosine factor can be written as:

$$\cos(2\vec{k}_H\cdot\vec{x}) = \cos(k_{ox}x)\cos(k_{oy}y) - \sin(k_{ox}x)\sin(k_{oy}y) \tag{3.51}$$

Now the function U is symmetrical under the transformation $x \rightarrow -x$ and $y \rightarrow -y$, causing the sine terms in (3.51) to vanish. Therefore (3.41) becomes

$$\Gamma(-2\vec{k}_H) = \frac{1}{2\pi}\int_{-\infty}^{\infty}\cos(k_{ox}x)dx\int_{-\infty}^{\infty}\cos(k_{oy}y)\exp[-4k_{oz}^2U(r,\alpha)]dy \tag{3.52}$$

It depends on the azimuth direction α whether or not the factor $\cos(k_{ox}x)$ or $\cos(k_{oy}y)$ is modulated by the exponential or not. In the upwind/downwind directions ($\alpha = 0, \pi$), the factor $\cos(k_{ox}x)$ is modulated; in the crosswind directions ($\alpha = \pi/2, 3\pi/2$) the factor $\cos(k_{oy}y)$ is modulated.

In these cases the modulated factor is integrated first using a three-point Gauss quadrature formula over each period of the cosine:

$$\int_{-\pi}^{+\pi} f(z)\cos(z)dz \approx w_0[f(0) - 0.5f(z_1) - 0.5f(-z_1)] \tag{3.53}$$

with

$$w_0 = 2\pi / (\pi^2 - 6) \tag{3.54}$$

and

$$z_1 = \pm\sqrt{2\pi^2 - 12} \tag{3.55}$$

This procedure is continued until the contribution of a block is smaller than a given relative error times the total integral. The second integral is evaluated with an open Romberg algorithm. To smooth the integrand, the transformation

$$\int_0^{\infty} f(z)dz = \int_0^1 \frac{f[\log(t)/c]}{ct}dt \tag{3.56}$$

is applied with $c=|k_H|$.

For azimuth angles near 45° both cosine factors in (3.52) are modulated by the exponential. In those cases both integrations are performed with the cosine quadrature formula (3.53).

This dedicated numerical procedure yields precision in the cross section of about 0.1 dB or better, depending on the azimuth angle. To obtain such a precision using an FFT requires at least four times oversampling of the Bragg wavenumbers and thus leads to unacceptably large transforms.

3.5 The Fung integral equation model.

The approximations done by Fung et al lead to the following expression for the normalized radar cross section [28]:

$$\sigma^o_{pp} \approx \frac{k_o^2 \exp(-2k_o^2\sigma^2\cos^2\theta)}{2}\sum_{n=1}^{\infty}\frac{W_N^{(n)}(2\vec{k}_h)}{n!}(k_o^2\sigma^2\cos^2\theta)^n \times \left\{2^{2n}|f_{pp}|^2\exp(-2k_o^2\sigma^2\cos^2\theta) \pm 2^n\Re(f_{pp}^* F_{pp})\exp(-k_o^2\sigma^2\cos^2\theta) + \frac{|F_{pp}|^2}{4}\right\} \tag{3.57}$$

Here σ^2 is the surface variance of the *full* surface. In (3.57) the plus sign of the second term is for VV polarization and the minus sign is for HH polarization. So the second terms causes a polarization difference. $W_N^{(n)}$ is the normalized roughness spectrum of the surface related to the *n*th power of the surface correlation function ϕ_N by Fourier transform as follows:

$$W_N^{(n)}(-2\vec{k}_h) = \frac{1}{2\pi}\int_{-\infty}^{+\infty}\exp[-j(k_{ox}x + k_{oy}y)]\phi_N^n(x,y)dxdy \quad (n = 1,2,\ldots) \tag{3.58}$$

The autocorrelation function used here is a normalized autocorrelation function i.e. $\phi_N(0,0) = 1$. It is thus related to the a.c. function $\phi(x,y)$, used by Holliday as follows:

$$\phi_N(x,y) = \frac{\phi(x,y)}{\phi(0,0)} \quad \text{and} \quad \sigma^2 = \phi(0) \tag{3.59}$$

In (3.57) the following coefficients occur:

$$\begin{aligned} f_{vv} &= \frac{2R_{\parallel}}{\cos(\theta)} \\ f_{hh} &= \frac{-2R_{\perp}}{\cos(\theta)} \\ F_{vv} &= 2\frac{\sin^2(\theta)}{\cos(\theta)}\left[\left(1-\frac{\epsilon_r\cos^2(\theta)}{\epsilon_r-\sin^2(\theta)}\right)(1-R_{\parallel})^2+\left(1-\frac{1}{\epsilon_r}\right)(1+R_{\parallel})^2\right] \\ F_{hh} &= 2\frac{\sin^2(\theta)}{\cos(\theta)}\left[4R_{\perp}-\left(1-\frac{1}{\epsilon_r}\right)(1+R_{\perp})^2\right] \end{aligned} \tag{3.60}$$

where $R_{\parallel}$ *and* $R_{\perp}$ are the Fresnel reflection coefficients for vertical and horizontal polarized waves, respectively, given by:

$$\begin{aligned} R_{\parallel} &= \frac{\epsilon_r\cos\theta-\sqrt{\epsilon_r-\sin^2\theta}}{\epsilon_r\cos\theta+\sqrt{\epsilon_r-\sin^2\theta}} \\ R_{\perp} &= \frac{\cos\theta-\sqrt{\epsilon_r-\sin^2\theta}}{\cos\theta+\sqrt{\epsilon_r-\sin^2\theta}} \end{aligned} \tag{3.61}$$

In case of a surface with small $k_o\sigma\cos\theta$, the summation in (3.57) reduces to the first term effectively. The condition mentioned here is the prime condition for the application of the small perturbation approach, which leads to the well known small perturbation scattering theory, better known as the theory of 'Bragg' backscattering. It can be easily shown that for this condition, (3.57) reduces to the 'Bragg' backscattering equations. For simplicity let us apply (3.57) to a perfectly conducting surface:

$$\begin{aligned} R_{\parallel} &= 1 \\ R_{\perp} &= -1 \\ \epsilon_r &= -\infty i \end{aligned} \tag{3.62}$$

This simplifies the equations for f_{pp} and F_{pp}. It can then be shown quite easily that the first, and significant, term in the summation in (3.57) reduces to:

$$\begin{aligned} &VV\text{: } 8k_o^4(1+\sin^2\theta)^2\,\sigma^2 W_N^{(1)}(2\vec{k_h}) \\ &HH\text{: } 8k_o^4(\cos^4\theta)^2\,\sigma^2 W_N^{(1)}(2\vec{k_h}) \end{aligned} \tag{3.63}$$

which is exactly the same as the results derived from the first-order small-perturbation theory (3.17), except for a factor of 2π which is 'hidden' in the definition of $W_N^{(1)}$.

Using the expansion:

$$\exp(x) = \sum_{n=0}^{\infty} \frac{x^n}{n!} \tag{3.64}$$

one can re-write the expression given by Fung in a form similar to the notation used by Holliday.

One then finds:

$$\sigma^o_{pol} = \frac{k_o^2}{2}\{ |f_{pol}|^2 \Gamma(-2\vec{k}_h) + \Re(f^*_{pol} F_{pol}) \exp(-k_{oz}^2\sigma^2)\Gamma'(-2\vec{k}_h) + \frac{|F_{pol}|^2}{4}\exp(-k_{oz}^2\sigma^2)\Gamma''(-2\vec{k}_h)\} \tag{3.65}$$

with

$$\begin{aligned} \Gamma'(-2\vec{k}_h) &= \frac{1}{2\pi}\int_{-\infty}^{+\infty}\int_{-\infty}^{+\infty} \exp\{-2i(k_{ox}x + k_{oy}y)\}\exp[-2k_{oz}^2 U(r,\alpha)]dxdy \\ \Gamma''(-2\vec{k}_h) &= \frac{1}{2\pi}\int_{-\infty}^{+\infty}\int_{-\infty}^{+\infty} \exp\{-2i(k_{ox}x + k_{oy}y)\}\exp[-k_{oz}^2 U(r,\alpha)]dxdy \end{aligned} \tag{3.66}$$

The functions Γ' and Γ'' can be evaluated using the same efficient numerical procedure as for Γ, with the small modification in the integrand as listed above.

For an ideal conducting surface

$$|f_{HH}|^2 = |f_{VV}|^2 = \frac{4}{\cos^2\theta} \tag{3.67}$$

and the first term in the approximation (3.65) is identical to the model by Holliday, see (3.39) in section 3.4. The second and third term do give slight modifications, the strength of which is dependent on the factor $\exp(-k_{oz}^2\sigma^2)$ in which σ^2 is the surface variance.

In the form of (3.65), the model can be computed in a way very similar to the way described in section 3.4 for the Holliday model. For an octupole spectrum (3.48), the function U(r,α) can be replaced with the expansion given in (3.46), with the coefficients given in (3.47). The calculation of the normalized backscattering cross section can then be performed as described in section 3.4.1, with the integrand now consisting of three terms instead of only one term. The total amount of computing time has increased a little, but this is insignificant to the other advantages of this new model. The integration method described in section 3.4 can be applied similar as to this model.

3.6 The unified full wave approach.

Considering the inaccuracies of the two-scale model and awaiting the solution of the present problems with the model by Fung (see later), a third model for the microwave backscattering of the water surface was studied. This method was developed by Bahar and is called the full wave approach [4,5,6,7].

Like the model by Fung and Chen, this model accounts for both small perturbation scattering and specular point scattering in a self-consistent manner. Thus contrary to e.g. two-scale models, it is not necessary to decompose the surface into two surfaces with small and large roughness scales. Therefore, the transition between both ranges of validity is quite smooth.

The principal elements of the 'full-wave approach' as listed by Bahar [4] are:

- Complete expansion of the fields into vertically and horizontally polarized waves. The complete spectrum of the waves consists of the radiation fields and the surface and the lateral wave terms.
- Imposition of exact boundary conditions at the irregular interface between two media characterized by complex electromagnetic parameters ε and μ.
- Use of Green's theorems to avoid term by term differentiation of the complete expansions.
- Conversion of Maxwell's equations into rigorous sets of coupled first-order differential equations for the wave amplitudes.
- Use of a variable coordinate system that conforms with the local features of the rough surface.

There are no restrictions on the height or slope of the rough surface, and both upward and downward scattering of the incident fields are accounted for in the analysis. The effects of shadowing can also be included. These features make the model applicable for the purpose of the VIERS model. It will be shown in the following, that the numerical implementation of the model again resembles the implementation of the Holliday model and thus use can be made of the efficient code for a k^{-4} spectrum.

The basic equation of the model is:

$$\sigma^o_{pol} = I_{pol}(\vec{n}^f, \vec{n}^i) Q(\vec{n}^f, \vec{n}^i) \tag{3.68}$$

where $\vec{n}^i$ *and* $\vec{n}^f$ are unit vectors in the directions of the incident and scattered wave normals, respectively. For backscattering

$$\vec{n}^f = -\vec{n}^i \tag{3.69}$$

I_{pol} is given by:

$$I_{pol} = \frac{k_o^2}{\pi} \int \left| \frac{D_{pol}(\vec{n})}{\vec{n} \cdot \vec{a}_z} \right|^2 P_2(\vec{n}^f, \vec{n}^i | \vec{n}) p(\vec{s})\, d\vec{s} \tag{3.70}$$

where n is the unit vector normal to the rough surface, a_z is the unit vector in the z(vertical)-direction, D_{pol} are reflection coefficients as given by eq. 29 in [5]. $p(s)$ is the probability density function for the slopes s. $P_2(n^f, n^i | n)$ is the probability that a point on the rough surface is both illuminated and visible. This function accounts for shadowing effects at high incidence angles (larger than 70 degrees). For the purpose of the VIERS model such a shadowing function is not necessary and thus $P_2 = 1$.

The function Q:

$$Q = \int_{-\infty}^{+\infty} (\chi_2 - |\chi|^2) \exp[-2i(k_{ox}x + k_{oy}y)]dxdy \tag{3.71}$$

is the two-dimensional Fourier transform of $(\chi_2 - |\chi|^2)$. Here χ and χ_2 are the characteristic and joint characteristic functions for the surface height h. For the moment it is assumed that the probability density function for the surface height is jointly Gaussian. Thus:

$$\begin{aligned} |\chi(k_{oz})|^2 &= \exp(-4k_{oz}^2\sigma^2) \\ \chi_2(k_{oz}) &= \exp[-4k_{oz}^2\{\phi(0,0) - \phi(x,y)\}] = F(x,y) \end{aligned} \tag{3.72}$$

So for the case of backscattering and assuming a Gaussian surface height distribution

$$\begin{aligned} Q &= 2\pi\Gamma(-2\vec{k}_h) - \int_{-\infty}^{+\infty} |\chi|^2 \exp[-2i(k_{ox}x + k_{oy}y)]dxdy \\ &\approx 2\pi\Gamma(-2\vec{k}_h) \end{aligned} \tag{3.73}$$

The approximation in (3.73) is valid for our purposes since the Fourier Transform of $|\chi|^2$ only yields a DC-component which does not contribute to off-nadir backscattering.

Thus the evaluation of the radar backscatter using this model can be done in three steps:

- Calculate function Q with the numerical code developed for the 'Holliday' model (3.52) using (3.47).
- Calculate the polarization dependent function I_{pol} by integrating over the surface slopes (3.70).
- Multiply the outcomes (3.68).

3.7 Conclusions

In this chapter an overview was given on some of the presently available approximations for the backscattering from rough ocean surfaces. An efficient algorithm was developed to obtain cross sections using the more complicated "Holliday", "Fung" and "Bahar" models. In chapter 4 these approximate theories will be evaluated by applying them to parameterized wave spectra as acquired during the 'Delft' experiment in 1990.

4 The experiment in the Delft flume, results and conclusions

4.1 Summary of experimental data.

The first VIERS experiment, conducted in 1988 in the Delft wind-wave flume yielded data which were excellently suited for a verification of the radar backscatter models. For this purpose, one needs detailed knowledge of the water surface at which the scattering takes place, as well as good radar backscatter measurements. Both elements are available in the data set.

A lot of attention was paid to the acquisition of high quality, detailed measurements of the water surface. Both, conventional and sophisticated new wave measurement devices were deployed. Among these are, high frequency wave wires, a laser slope gauge and the imaging slope gauge. For a description of these instruments the reader is referred to [14].

4.1.1 The Microwave measurements

Performing backscatter measurements in the Delft wind/wave tank at a short distance requires an illuminated spot large enough to accommodate a collection of independent scatterers, which leads to the requirement of a two-way illuminated spot of at least 0.5 meter diameter. This has implications on the antenna size and the overall system realization. Due to space limitations within the Delft wind/wave tank the measurement distance was limited to 4.22 meter and only one antenna with a diameter of 1.2 meter or less could be used. Because of the fact that the measurements must be extrapolated to larger distances a curvature of the phase-front must be avoided. This means that the antenna pattern must have a flat phase-front at the measurement distance, while the antenna pattern must fulfill the requirement of a two-way illuminated spot of at least 0.5 meter diameter. Three possible solutions exist for the choice of the antenna :

- a small antenna (object in the far field),
- a focused antenna (object in the near field),
- a large (reflector) antenna (object in the near field).

The far field requirement yields an antenna diameter of less then 0.12 meter for a one way illuminated area of one meter diameter at a distance of 4.22 meter. The phase distribution, however, has a variation which is much more than 180 degrees over an one meter spot. So only near field measurements are possible in the Delft wind/wave tank setup. Using a focused antenna would result in a plane wavefront at the measuring distance, in this case, however, the illuminated area would be much smaller than the requirement. In the near field the radiation is nearly parallel to the antenna axis, so a flat phase distribution can be expected. However, the amplitude distribution shows a large variation as a function of the distance from the antenna. The amplitude and phase distributions can be adjusted using different patterns for the feed antenna. A computer program was developed based on the theory presented by R.C. Hansen and L.L. Bailin [35] to calculate the amplitude and phase distributions for different antenna-distance combinations. As a result a 1.1 meter parabolic reflector antenna with an uniform aperture illumination was chosen.

Four different types of measurements have been performed on the antenna system:

- reflection measurements of the feed antenna,
- far field pattern measurements of the feed antenna,
- near field measurements of the antenna system in a flat plane,
- near field measurements of the antenna system in a cylindrical plane.

The first two types of pattern measurements were done in the Delft University of Technology Chamber for Antenna Tests (DUCAT), the last one were carried out at the Physics and Electronics Laboratory TNO (FEL-TNO) as a verification of the measurements performed in DUCAT.

- reflection measurements of the feed antenna.
  The feed antenna consists of a waveguide with a square cross-section of 9.5 x 9.5 mm² filled with a dielectric material. The feed is capable of handling two polarizations. The reflection measurements were carried out using an automatic network analyzer. Both ports (one for horizontal and one for vertical polarization) were measured. The ports don't have an identical frequency behavior, so two slightly different operating frequencies were chosen for the scatterometer, one for each polarization. The return loss of the feed is rather high so special care has to be taken to avoid saturation of the receiver.
- far field measurements of the feed.
  In DUCAT it is possible to measure the amplitude of the EM field of an antenna in eight different axes using an automatic measurement setup. The results shows a negligible frequency dependence of the pattern within the used frequency band.
- near field phase and amplitude measurements of the antenna system in DUCAT.
  Using an HP8410B network analyzer the planar phase and amplitude response of the parabolic reflector with the feed antenna were measured in DUCAT. The measurements are in good agreement with the theoretically calculated amplitude and phase responses. In figures 4-1 and 4-2 the calculated and measured planar amplitude pattern respectively planar phase pattern are given.

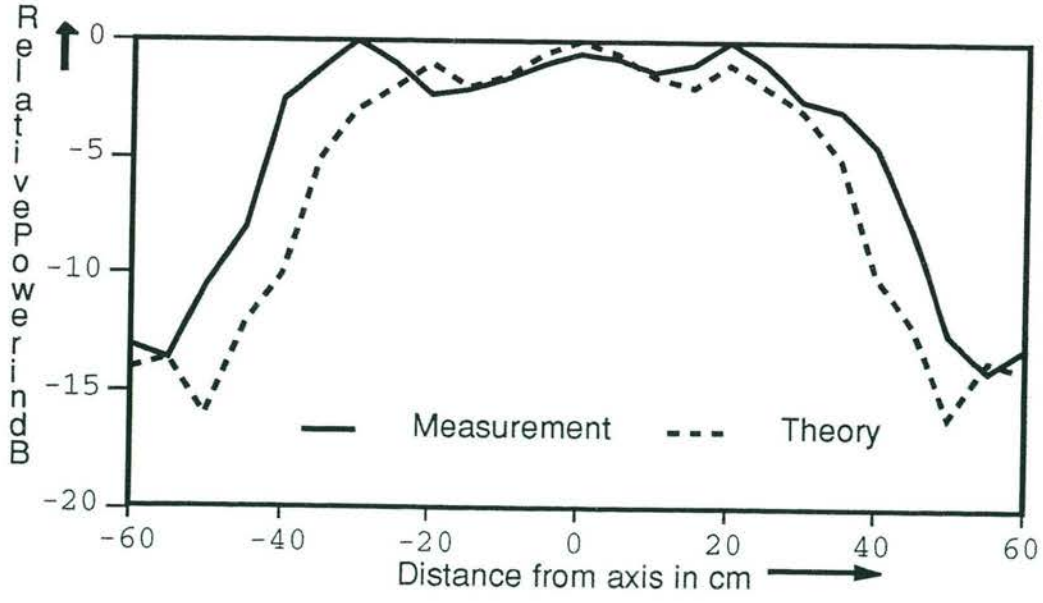

Figure 4-1 Planar amplitude pattern

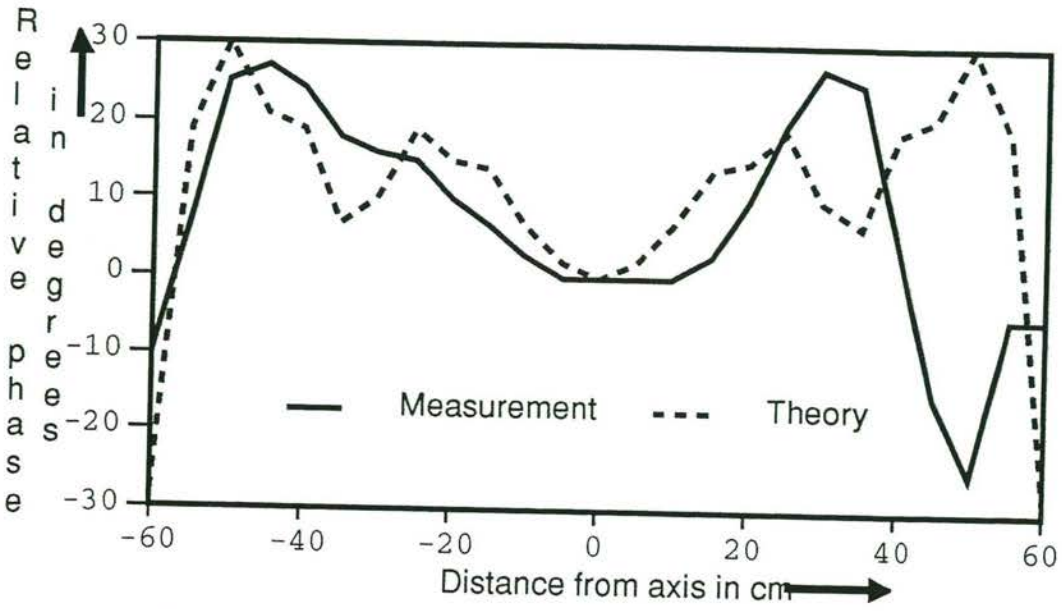

Figure 4-2 Planar phase pattern

- near field measurements at FEL-TNO.
  The measurements were performed in a cylindrical plane. The spill-over lobes are at +110° and -110° and 30 dB below the main lobe. The pattern has also been measured over a frequency range of 1 GHz and shows a very broadband behavior, the calculated and measured spherical gain pattern are given in figure 4-3.

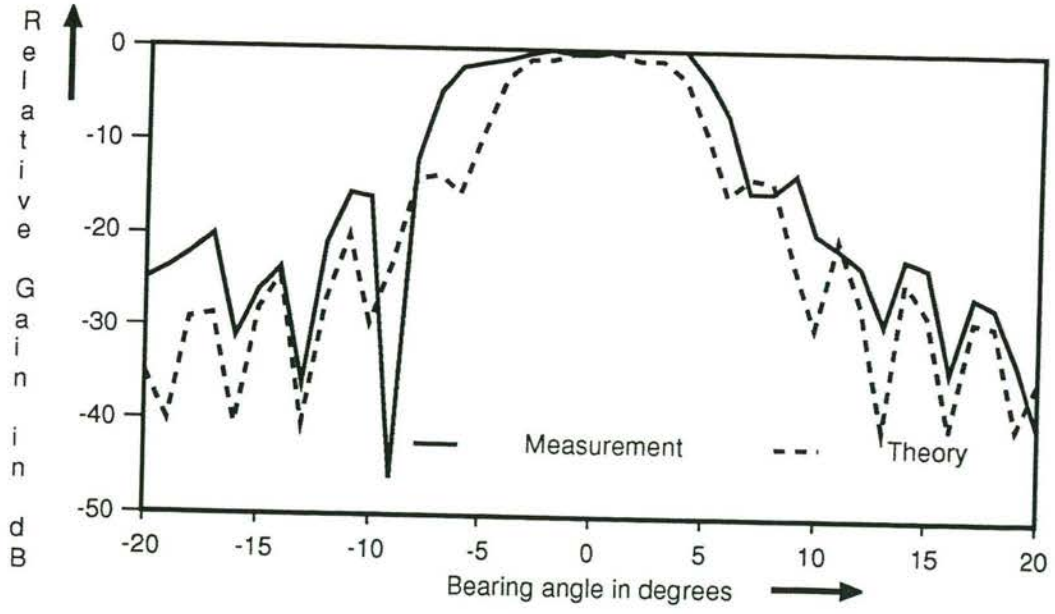

Figure 4-3 Spherical gain pattern

The theoretically calculated responses are in good agreement with the measurements and it has been possible to design and construct an antenna with a flat amplitude and phase response at the measurement distance of the scatterometer for the Delft experiment.

The instrumental principles to be applied in scatterometer realization are basically the same as those used in radar, the differences mainly concern the way in which the information is collected. In the experiments the microwave backscatter measurements were performed with a FM-CW X-band scatterometer. Some characteristics of this system are listed in table 4-1.

Table 4-1 Specifications of the X-band FM/CW scatterometer

Radar type	FM/CW
Frequency	9.6 GHz
Frequency modulation	triangular, 300 MHz sweep
Polarization	HH or VV
Range resolution	0.5 m
Operating range	4.2 m
Antenna	one parabolic dish, 1.1 m diameter
Footprint	0.6 x 0.6 m
Phase error over footprint	< 15 degrees
Azimuth angle	0 - 180 degrees
Incidence angle	24.5 - 60 degrees

4.1.2 The Wave measurements

Since the wave field plays such an important role, we give here a short overview of the measuring devices and the methods used to process the data. During the Delft wind-wave flume campaign the wave field was measured with the help of three devices:

- a high frequency wave wire (sample frequency 35.2 Hz, reliable up to about 10 Hz).
- a laser slope gauge (LSG) measuring along and crosswind slopes (sampling frequency 1000 Hz, subsampled to 62.9 Hz).
- an imaging slope gauge (ISG) from which a 2-dimensional wave number spectrum can be obtained for wave number values between 26.5 and 1600 m^{-1}.

Wave measurements have been made for wind velocities U_{10} between 2.6 and 20 m/s.

4.1.3 The ISG and scatterometer results

All radar backscattering models used need information from the two-dimensional wave number spectrum of the water waves. This information can be obtained in a number of ways. The first way we went was to analyze the data from all wave sensors and to try to extract the wave number spectrum. This was the approach used in [14]. The advantage of this approach is that errors in individual sensors become less important. This was considered important, because initially it was thought that especially the ISG measurements were not very accurate. A problem with this method is, that the -more conventional- wave measuring instruments, the wave wire and the laser slope gauge, perform point measurements and thus yield frequency spectra rather than wave number spectra. The way to circumvent this prob-

lem is to estimate the wave number spectrum from these frequency spectrum by assuming that all waves were propagating with speeds given by the dispersion relation:

$$c_w = \sqrt{(g / k_w + Tk_w) \tanh k_w d} \qquad (4.1)$$

Where k_w is the wavenumber of the long wave, d is the water depth and T is the ratio of the surface tension and the water density.

It is well known that the assumption made above cannot be simply applied for this purpose, since the speed of the small scale waves is modulated by the orbital motions of the long waves. However it was assumed that in the Delft flume, the orbital motions were sufficient small for this effect to be neglected. In a later analysis it turned out that the spectra obtained this way were quite different from the direct observations performed by the Imaging Slope Gauge, the reason for this being, probably, that the assumption about the orbital motions is not valid.

Table 4-2 Results of the radar measurements during the Delft experiment

Dependence on the wind speed, θ=45°; α=0°				Dependence on the incidence angle, u*=0.367 m/s; α=0°		
u_*	U_{10}	σ°_{HH}	σ°_{VV}	θ	σ°_{HH}	σ°_{VV}
0.069	2.64	-29.1	-26.1	24.5	-5.4	-5.8
0.103	3.89	n.a.	n.a.	30	-8.1	-8.3
0.140	5.17	-26.1	-22.5	35	-11.5	-9.9
0.183	6.58	-21.7	-17.8	40	-12.9	-11.4
0.246	8.52	-17.4	-13.2	45	-15.4	-11.7
0.367	10.96	-14.7	-11.6	50	-17.1	-12.4
0.490	13.45	-13.2	-10.6	55	n.a.	n.a.
0.670	16.19	-11.9	n.a.	60	-22.1	-15.1
0.900	18.7	-9.6	-8.7			

In the approach taken here, only the data from the Imaging Slope Gauge is used for the evaluation of the wave number spectra. The information from the other sensors is only used to determine the peak frequencies of the spectra. It should be re-called that the limited footprint of the ISG did not permit measurements of the dominant wave under all wind conditions. Above wind speeds of a few meters per second, the wave-length of the dominant wave becomes larger than the ISG footprint. The residual calibration error in the ISG data is estimated at about 0.4-0.6 dB. The random error when taking samples from the ISG spectrum is around 0.35 dB, when averaging over a 3x3 data window. This means that the overall error in the ISG data is estimated at around 0.9-1.0 dB, which is more accurate than the approach with all three sensors. The data processing of the ISG data necessary to prepare the spectra to be used in the backscattering models is described in section 4.2. Table 4-2 summarizes the conditions and results of the radar measurements in the Delft wind/wave flume for the incidence and wind speed dependence series.

4.2 Processing of the wave data

In order to compare model calculations with the backscatter measurements a number of preparations were performed. The ISG data from Bernd Jähne were acquired under slightly different circumstances than the radar backscatter measurements because, in the analysis of the original ISG data acquired during the March 1988 experiment it turned out that the illumination time used for the ISG was too long. This resulted in a motion-defocussing of the short waves. It was therefore decided to use data acquired in a second experiment in November 1988 in which a chopper was used in front of the ISG camera leading to shorter illumination times and thereby canceling these motion effects. However, no simultaneous radar measurements were performed in November and the circumstances under which the data were acquired were slightly different from the measurements in March. Since the wind speeds during the second experiment were measured using the same calibrated equipment as during the first experiment, the new wind speed data could be related to the old data. Using these wind speeds, the ISG spectra were interpolated to match the wind speeds during which the radar data were taken.

In order to do so, all ISG spectra were read into the software program "MATLAB" [76]. A cubic spline was used to calculate the backscatter saturation coefficients at the desired friction velocities. The original wind speeds did not exceed considerably the range of wind speeds of the second experiment and so the interpolated data show no artifacts caused by the interpolation schedule.

Table 4-3 Friction velocities as used in the November and March experiment

Reference wind speed U_r (m/s) Nov. 1988	Reference wind speed U_r (m/s) Mar. 1988	Friction velocity u_* (m/s) Nov. 1988	Friction velocity u_* (m/s) Mar. 1988
	2.19		0.069
2.12		0.073	
3.08		0.100	
4.20		0.140	
	3.96		0.140
	5.15		0.183
5.62		0.205	
	6.63		0.246
6.78		0.296	
	8.37		0.367
9.06		0.424	
	10.48		0.490
	12.97		0.670
12.4		0.722	
	16.35		0.900

The ISG spectra as delivered by Jähne were in a log(k) versus α grid, with 64 wavenumbers with equidistant logarithmic scale and 40 angles between -87.5 and 87.5 degrees. To make them suitable for use in a digital two-dimensional Fast Fourier Transform, the spectra were

re-gridded onto a symmetric 128x128 grid running from k_x,k_y: -1585 ... +1585 rad/m. The re-gridding was performed using a spline interpolation routine. Because of the rather course digitization in the original (log(k), α) frame at small wavenumbers, some small artifacts showed up after this re-gridding. These artifacts occur far away from the Bragg wave numbers and thus their influence on the backscattering calculations is small. Figure 4-4 shows an example of an interpolated ISG spectrum from Bernd Jähne.

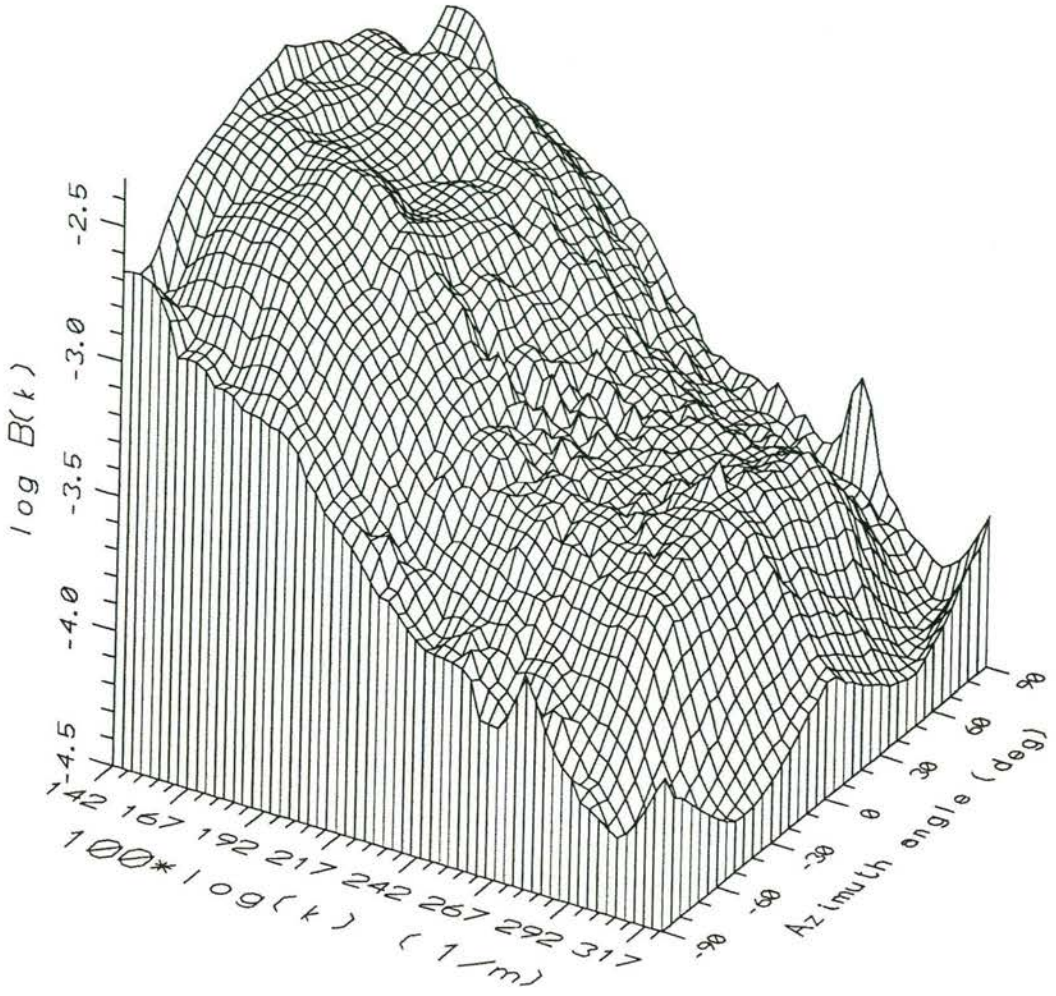

Figure 4-4 Example of an ISG spectrum as measured in the Delft wind/wave flume. u_*=0.367 m/s, 100 meter fetch.

The x-axis represents the logarithm of the wavenumber, starting at log(26.5) rad/m till log(1585) rad/m. The corresponding range in wave length is 23.7 till 0.4 cm. The y-axis represents the propagation direction of the waves with respect to the upwind direction, along the vertical axis the logarithm of $W(k,\alpha)*k^4$ is plotted. Plotting the spectral density this way has the advantage, that an equilibrium k^{-4} spectrum shows no dependence along the k-axis. Indeed it can be seen in fig. 4-4 that the plot is quite constant along the k-axis (i.e. resembles a k^{-4} spectrum) around wavenumbers of 200--300 rad/m. This is the 'Bragg' regime for the TU-Delft X-band scatterometer at moderate incidence angles.

4.2.1 Parameterization of the wavespectra

As explained in section 3.4.1 the new backscattering models can be made to work very efficiently on wave data of a specific (octupole) shape. The spectra as measured by the ISG resemble the general shape of this parameterization very well, especially around the Bragg wavenumbers, the most important region for backscattering. For this reason, the spectra were parameterized using a spectrum of the following form:

$$W_p(k,\alpha) = \frac{B\ k^4}{2\pi k_p^8 + k^8} \cdot [1 + 2a_2 \cos(2(\alpha - \alpha_w))] \qquad (4.2)$$

The parameters B and a_2 can directly be obtained from the ISG data. The peak wave number of the spectrum, k_p could only be obtained via the point measurements by the LWG and LSG. The following parameterization was obtained for the peak frequency:

$$f_p = 0.731 \cdot \frac{g}{u_*}\left(\frac{gx}{u_*^2}\right)^{-0.325} \qquad (4.3)$$

where g is the gravity constant (9.81 m/s^2) and x is the fetch in meters. Then the peak wavenumber can be obtained by using the deep-water dispersion relation:

$$k_p = \frac{(2\pi)^2}{g} f_p^2 \qquad (4.4)$$

Table 4-4 Parameters of the ISG wave spectra in the Delft experiment

u_*	B	k_p	a_2
0.069	$7.69\ 10^{-4}$	15.3	0.027
0.103	$5.26\ 10^{-4}$	11.54	0.058
0.140	$1.91\ 10^{-3}$	9.31	0.171
0.183	$4.30\ 10^{-3}$	7.72	0.277
0.246	$8.27\ 10^{-3}$	6.28	0.321
0.367	$1.96\ 10^{-2}$	4.74	0.310
0.490	$3.42\ 10^{-2}$	3.87	0.282
0.670	$4.59\ 10^{-2}$	3.11	0.224

The expression for deep water waves is valid for wave lengths up to approximately twice the water depth. Otherwise a correction with a factor $\tanh(k_w d)$ has to be applied. The results of these parameterizations are listed in table 4-4.

To check whether the parameterization used is acceptable, figure 4-5 shows the quotient of the original spectral data and the parameterization.

Figures 4.5 - 4-12 represent the results of the parameterization of the spectra for all 8 wind speeds listed in table 4-4. The contour plots show contour lines for the function $10*\log10(W_{isg}/W_p)$.Contour lines are plotted with steps of 0.5 (dB) between -6 and +6 dB.

The first plot, figure 4-5 clearly shows two dominant wave peaks. The parameterized spectrum does not follow the spectrum around these peaks and thus they show up in the contour plot. From this figure, it should be concluded that for the very low wind speeds in the flume, the parameterization is not valid. This should be kept in mind when interpreting the results.

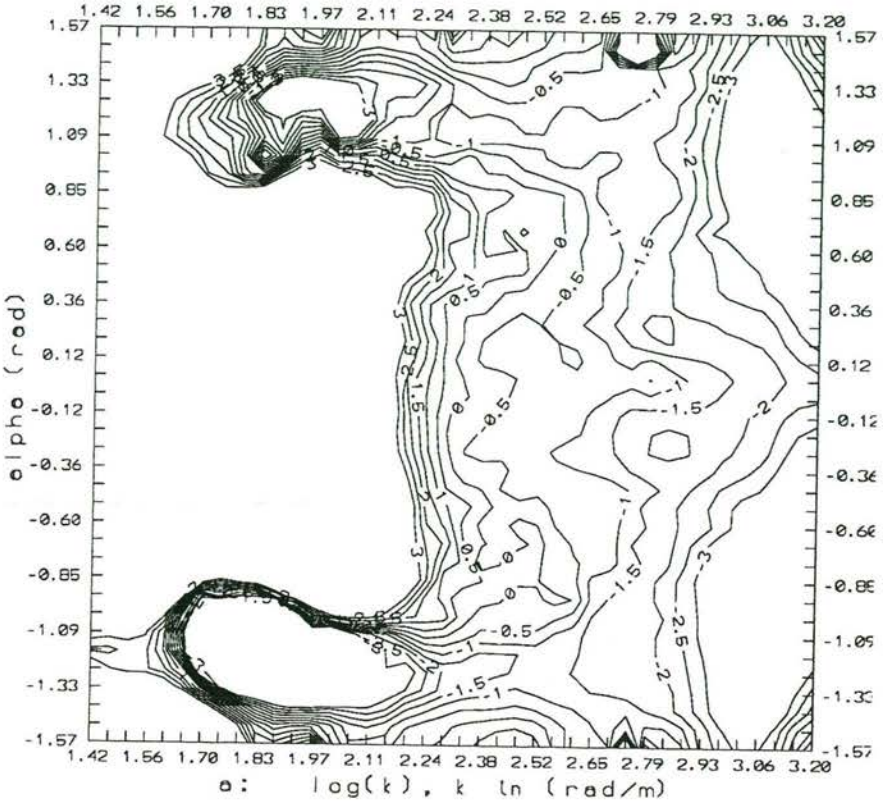

Figure 4-5 Contour plots of the quotient between measured and parameterized wave spectra, $u_* = 0.069$ m/s.

Figure 4-6, taken at a friction velocity of 0.103 m/s shows a better result, at least the angular dependence is much better as can be seen from the nearly vertical contour lines. Two noise peaks show up in the data near cross wind conditions at log(k)=2.8. These do not influence the data analysis. The overall error in the parameterization at this wind speed is about 2 dB.

In a later stage the parameterization has been improved, however this correction has not been applied yet to the data presented in this report.

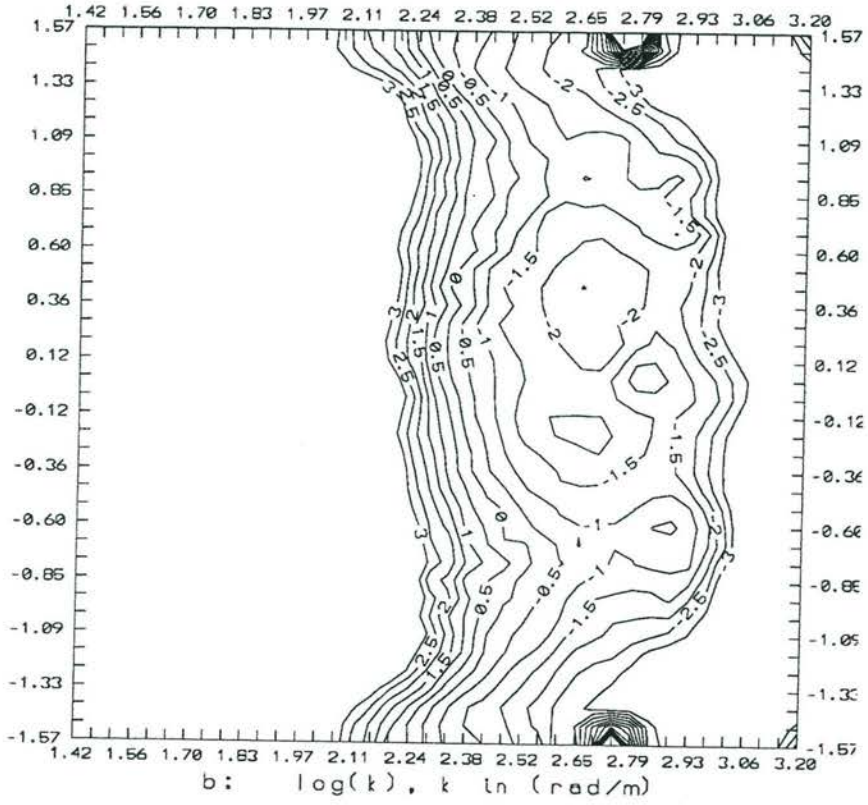

Figure 4-6 Contour plots of the quotient between measured and parameterized wave spectra, $u_* = 0.103$ m/s.

From friction velocities of 0.140 m/s and higher the data shows increasingly better resemblance to the parameterized spectrum. Over the range of the X-band Bragg waves (log(k)=2.2-2.5) the difference is generally less than 1-1.5 dB. The sharp cut-off of the measured spectrum at wavenumbers above 900 rad/m is, of course, not followed by the parameterization. The influence of these short waves on the radar cross section is small though.

It can also be seen that the angular dependence assumed in the parameterized spectra is valid for the short, Bragg resonant waves, but not for the larger, near-gravity waves in the flume. The influence of this discrepancy is considered acceptable for the flume data.

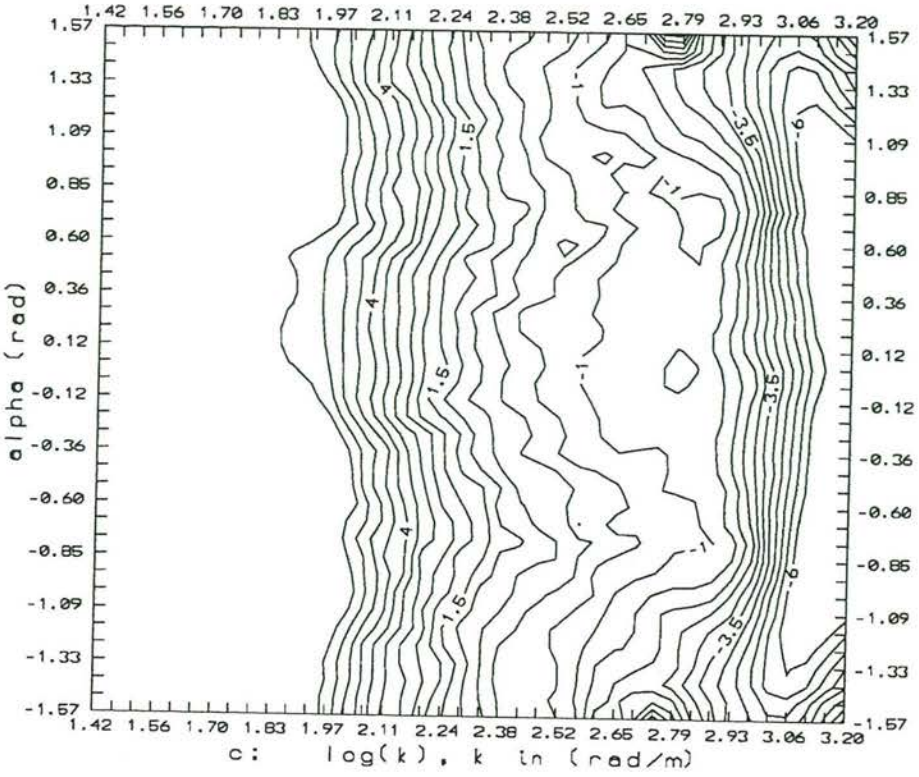

Figure 4-7 Contour plots of the quotient between measured and parameterized wave spectra, $u_* = 0.140$ m/s.

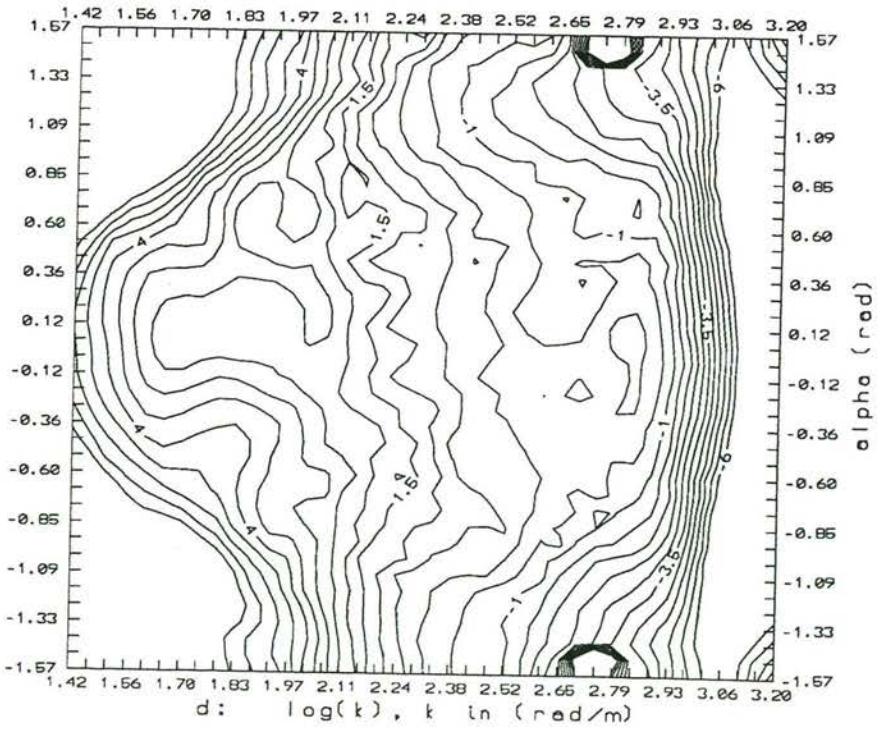

Figure 4-8 Contour plots of the quotient between measured and parameterized wave spectra, $u_* = 0.183$ m/s.

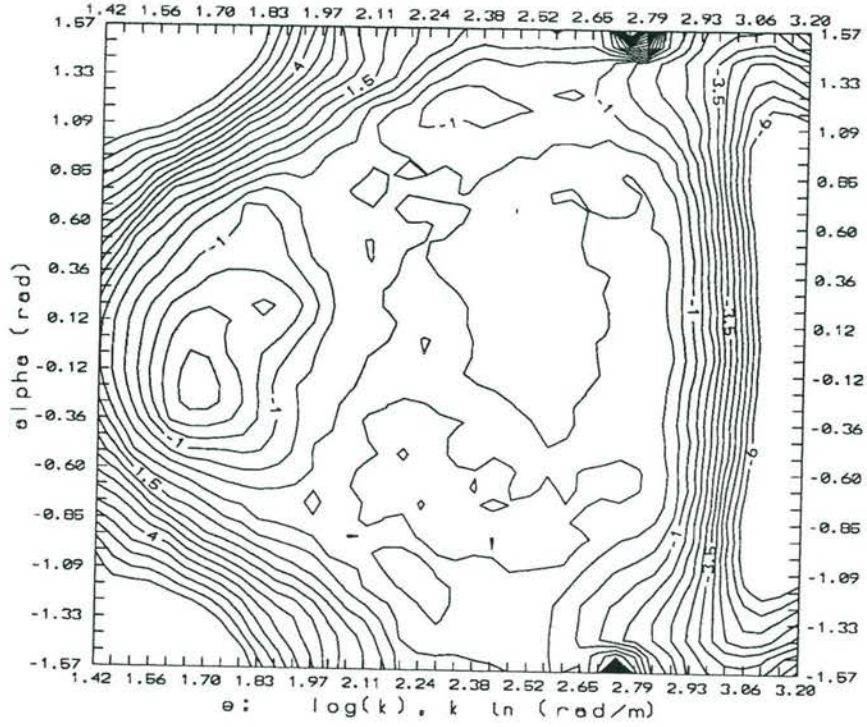

Figure 4-9 Contour plots of the quotient between measured and parameterized wave spectra, $u_* = 0.246$ m/s.

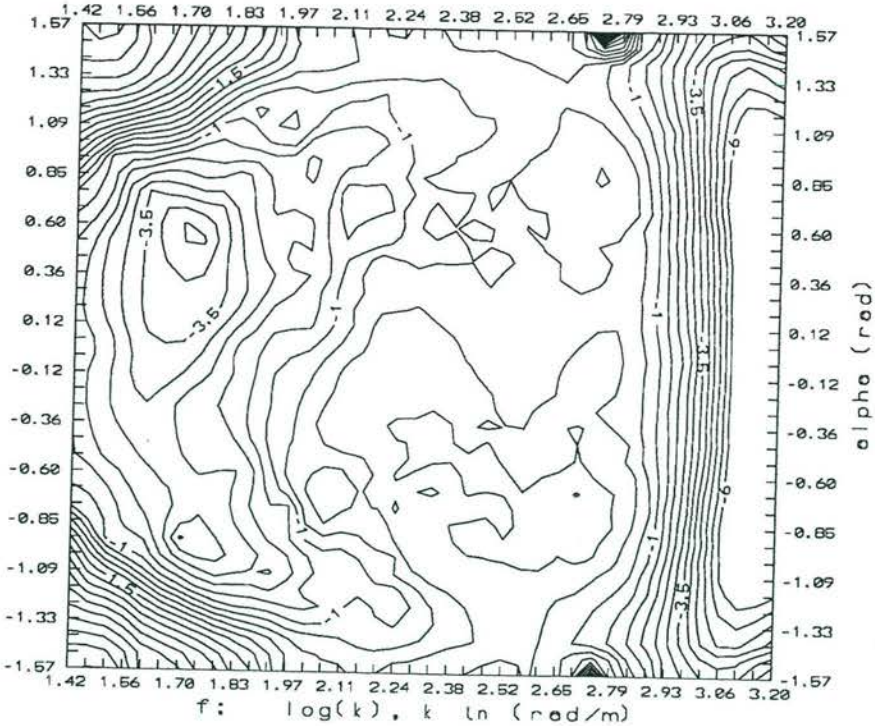

Figure 4-10 Contour plots of the quotient between measured and parameterized wave spectra, $u_* = 0.367$ m/s.

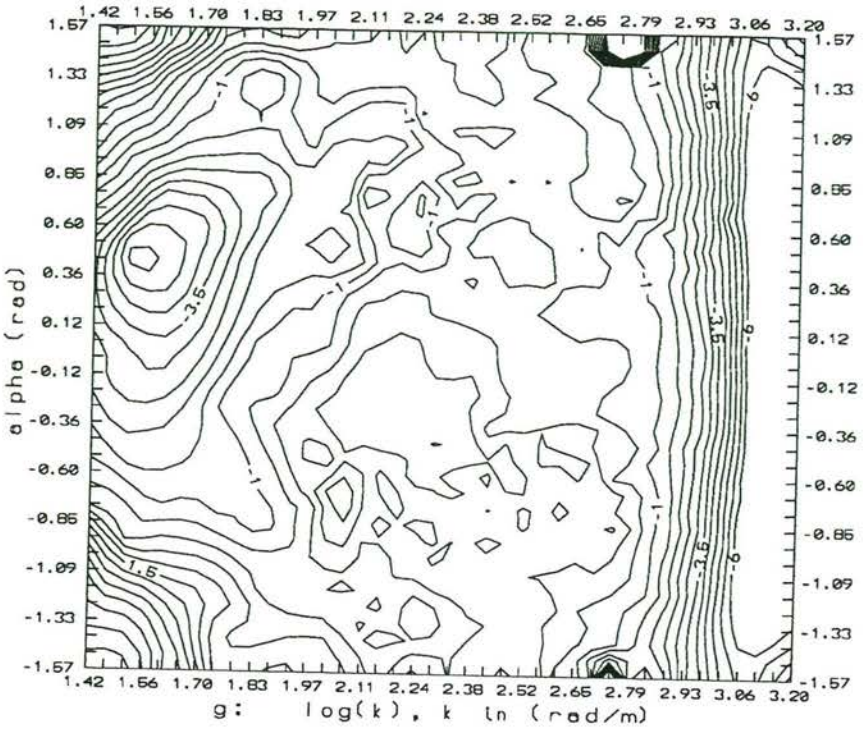

Figure 4-11 Contour plots of the quotient between measured and parameterized wave spectra, $u_* = 0.490$ m/s.

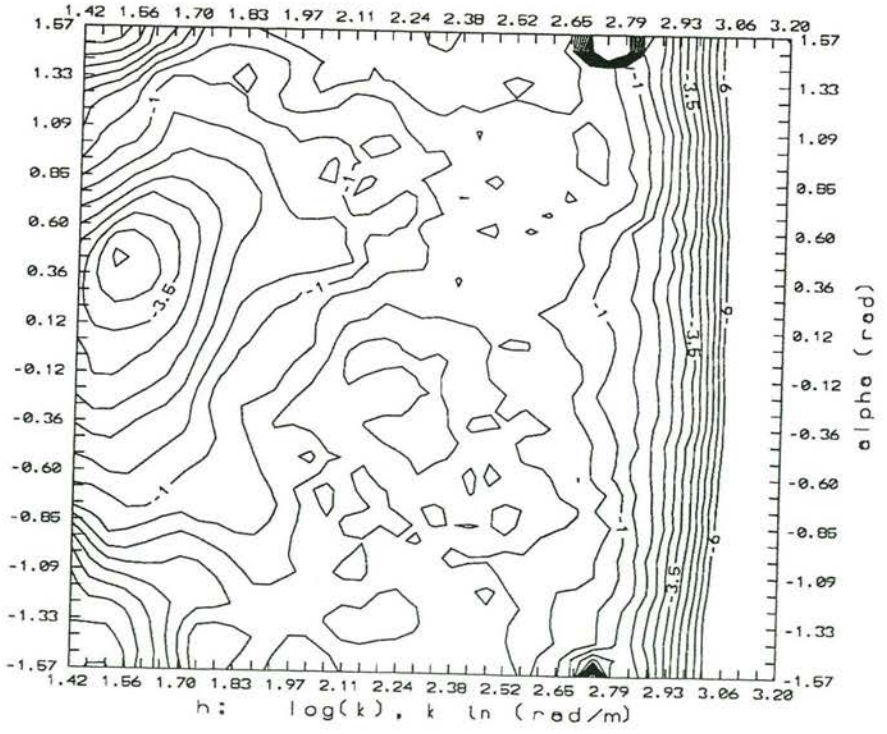

Figure 4-12 Contour plots of the quotient between measured and parameterized wave spectra, $u_* = 0.670$ m/s.

4.3 Implementation of the backscattering models

4.3.1 The two-scale model

The comparison between models and observations was done primarily using the parameterized spectra. For these spectra, the cut-off wavenumber was determined using several values of β. It can be shown that the high frequency surface variance σ_H^2, (3.37) can be approximated with:

$$\sigma_H^2 \approx \frac{B}{2k_c^2} \tag{4.5}$$

So for a given β the cut-off parameter can be easily determined as

$$k_c = \sqrt{\frac{2k_o^2 B}{\beta}} \tag{4.6}$$

The other parameters to be determined for the two-scale model are the slope variances in- and perpendicular to the plane of incidence (s_L^2 respectively s_C^2). Using the parameterized wavenumber spectrum (4.2) one can show that

$$\begin{aligned} s_L^2 &= \frac{B}{16}\ln\left(\frac{k_c^8+k_p^8}{k_p^8}\right)\left[1 + a_2\cos\left(2(\alpha_r - \alpha_w)\right)\right] \\ s_C^2 &= \frac{B}{16}\ln\left(\frac{k_c^8+k_p^8}{k_p^8}\right)\left[1 - a_2\cos\left(2(\alpha_r - \alpha_w)\right)\right] \end{aligned} \tag{4.7}$$

The along and cross wind long wave slope variances $s_{a,w}^2$ and $s_{c,w}^2$, necessary for the determination of the physical optics contribution (3.28) can easily be determined from (4.7) by substitution of α_r by α_w. Using these expressions, the two-scale model is defined except for the final value of the parameter β. As mentioned above, β indirectly determines the cut-off wavenumber k_c. It has been argued, that β should not exceed ≈ 0.5 and should not be less than 0.1. In figures 4-13 and 4-14 the incidence angle dependence of the backscatter σ° is plotted as a function of the incidence angle for both copolar measurements.

The spectrum used was the parameterization of the wavenumber spectrum for a friction velocity of $u_* = 0.367$ m/s (see table 4-4). The radar was pointed in the upwind direction. Figure 4-13 shows the results for horizontal polarization and figure 4-14 for vertical polarization. The values for β are listed in the figure.

β has the largest effect at small incidence angles. For as well HH as VV polarization small values of β show the best results. Still rather large differences occur at small incidence angles. These differences can be caused by two effects. First of all the effective Fresnel coefficient R(0) in (3.32) might be too large. This will be discussed later. Secondly, the accuracy of the parameterization used can be of influence at small incidence angles. This might lead to an overestimation of the backscatter cross section by the model.

Figure 4-15 shows the polarization difference, expressed in dB's, between HH and VV polarization as a function of incidence angle for different values of the parameter β, with a friction velocity of $u_* = 0.367$ m/s, the radar was pointed in the upwind direction. All curves show a very similar behavior with respect to the measurements, except for an offset. This offset is minimal for the curve with $\beta = 0.07$ and is within the measurement accuracy (1 dB).

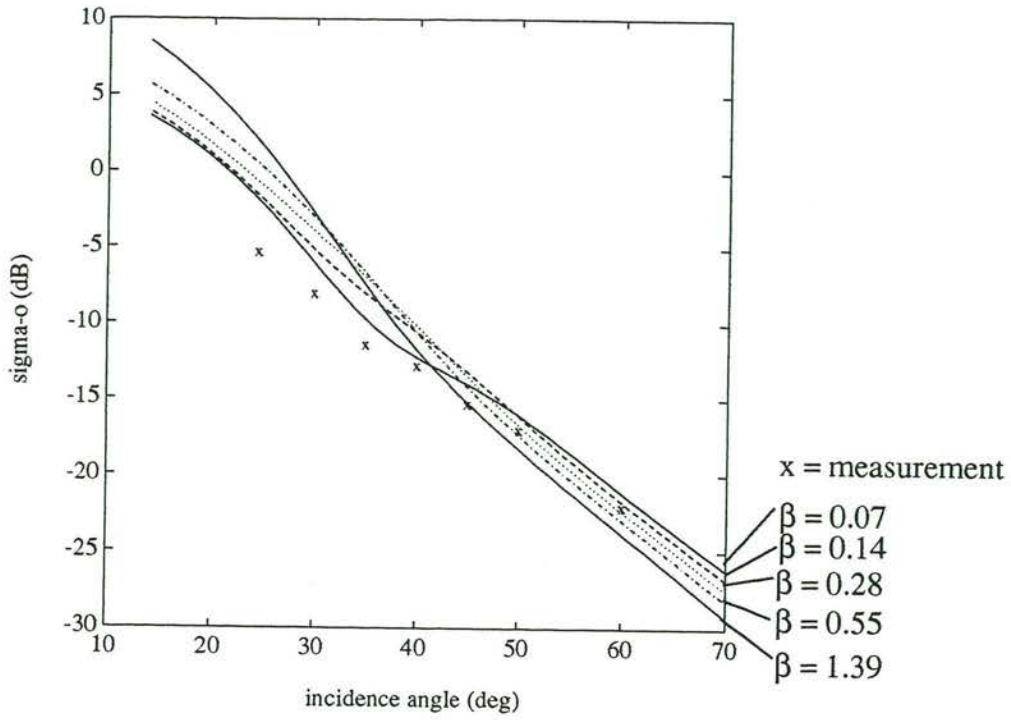

Figure 4-13 Incidence angle dependence of the backscatter for HH polarization

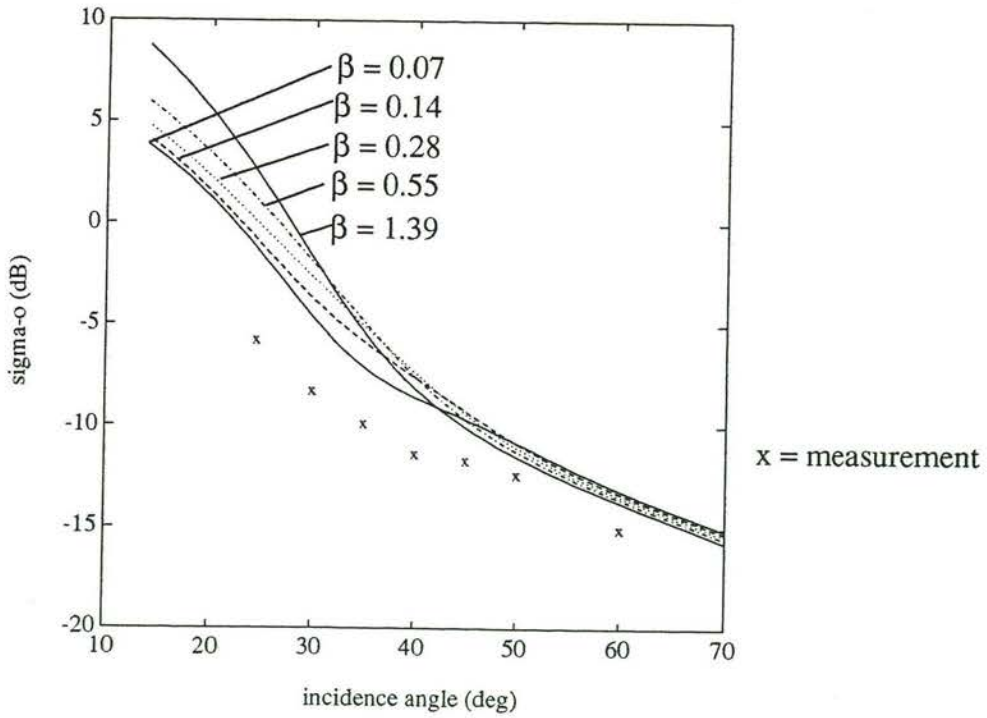

Figure 4-14 Incidence angle dependence of the backscatter for VV polarization

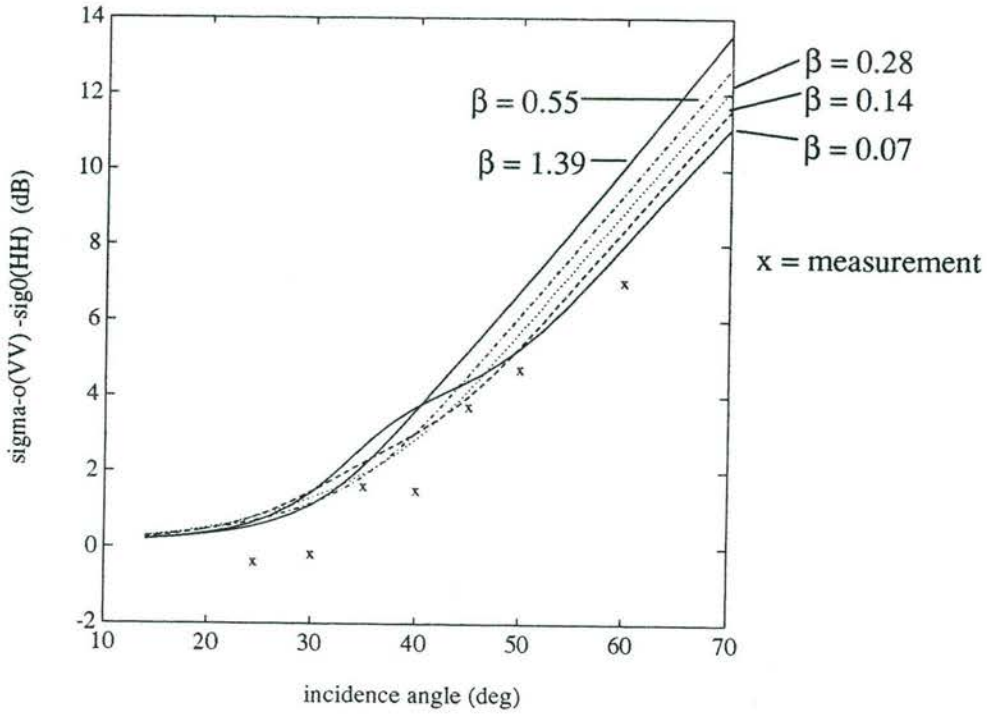

Figure 4-15 Polarization ratio in dB as a function of incidence angle

Based on the comparison of model calculations and the measurements the parameter β was set at a value of 0.07. In all of the model calculations with the two-scale model presented here, this value of β was used.

4.3.2 The IEM model

The basic function Γ in the evaluation of the backscatter according to the IEM model of Fung was evaluated using the method described in section 3.5. As mentioned before, use can be made of the efficient algorithm developed for the Holliday model (section 3.4.1). However, one parameter still has to be determined here and that is the pre-factor in front of the second and third term in the model:

$$\exp(-2k_{oz}^2\sigma^2) \tag{4.8}$$

Here σ^2 is the total surface variance. k_{oz} is the vertical component of the incident radar wavenumber, in our case k_{oz} will have a value between 182 and 100 rad/m for incidence angles of 24.5 till 60 degrees and a radar wavenumber of ~201 rad/m. For small values of σ^2, the exponential factor will be approximately 1, for large values it will approach zero. The influence of this factor is, that it weighs the influence of the second and third term in the calculation of the radar backscatter of the IEM model (3.65). So for large σ^2 the influence of these terms will approach zero and the model will be identical to the Holliday or Kirchhoff model. For small values of σ^2 the influence is largest. It should be noted here that the polarization dependence in the model is caused by the second term in (3.65). So the polarization dependence decreases with increasing σ.

To get some idea of this parameter σ^2, it can be shown that for the adopted spectrum:

$$\sigma^2 = \frac{\sqrt{2}\pi B}{8k_p^2} \tag{4.9}$$

For our spectrum, $B=1.96\cdot10^{-2}$ and $k_p=4.74$, so $\sigma^2=4.84\cdot10^{-4}$ and $\exp(-2k^2_{oz}\sigma^2)=3.2\cdot10^{-9}$. So one can see that the parameter becomes indeed very small, which means that the polarization dependence is (much) smaller than in the case of SPM or Bragg theory. One can also learn from (4.9) that the exponential pre-factor is, via the surface variance, strongly dependent on the peak wavenumber of the spectrum. At sea, this peak wavenumber is much smaller than in the wind/wave flume. This leads to much larger surface variances and hence to much smaller pre-factors. In practice this means, that for a realistic sea-spectrum the polarization difference disappears for all incidence angles. Such a strong coupling between surface variance and polarization ratio is not realistic.

Because of the importance of the polarization dependence for the radar backscattering at higher incidence angles, this matter has been taken up with the authors of the model. In their first response they mention that the surface variance should be calculated only for those waves with wavelengths shorter than the footprint size. This is reasonable, because longer waves are not illuminated and thus cannot contribute to the scattering in this way. Longer waves do tilt the total surface of course, thereby causing 'tilt' modulation. Applying this restriction to the measurements in the 'Delft' wind/wave flume, the model comes up with a small polarization difference. This polarization difference shows a dependence on wind speed (read: surface variance) which is similar to the measurements.

So at first sight the problems seemed to be solved. However, when applied to the ERS-1 (footprint 25 km) the method used above cannot be used again, because all waves are illuminated and thus contribute to the scattering. This finding was discussed with A.K. Fung. He acknowledged the problem and mentioned that the solution will have to be found in the fact that the long waves do not contribute to the scattering in the same way as the short waves. Thus the wave spectrum should be cut-off at some point. However, where and how to cut-off this spectrum is a point which is still under investigation.

4.3.3 The Full Wave Approach model

The evaluation of the Full Wave Approach model by Bahar [2,3,4,5,6,7], can be performed efficiently for the octupole spectrum (3.48) by using the code developed for the Holliday model to calculate the function Γ which is identical to function Q in (3.68), except for a factor 2π. The function I_{pol} can be calculated by evaluation of (3.70). The integration here is over the slopes of the waves. However, not only over the long wave slopes, as for the two-scale model, but over all slopes:

$$\begin{aligned} s_x^2 &= \int_0^{2\pi}\int_0^{\infty} k^3\cos^2(\alpha)W(k,\alpha)dkd\alpha \\ s_y^2 &= \int_0^{2\pi}\int_0^{\infty} k^3\sin^2(\alpha)W(k,\alpha)dkd\alpha \end{aligned} \tag{4.10}$$

In practice, the integral over k is not evaluated until infinity, but to some wavenumber k_m, well beyond the Bragg wavenumbers.

In our case we chose a value of k_m = 1100 rad/m since at that wavenumber the wave spectrum starts to fall off much steeper than k^{-4} and thus the parameterization is not valid beyond that point. Also waves with a wavenumber larger than 1100 rad/m contribute less to the slope variance because of this. With the octupole spectrum (3.48), the expressions for s_x^2 and s_y^2 are similar to the equations for the two-scale model (4.7) except with k_c replaced by k_m.

4.4 Results of the Delft experiment

4.4.1 Incidence angle dependence

The results of the calculation of the incidence angle dependence of the radar cross section are summarized in table 4-5.

Table 4-5 Incidence angle results of experiment and model calculations

	experiment		SPM		TSc		HSW	IEM		BAH	
θ (deg)	σ°_{VV} (dB)	σ°_{HH} (dB)	σ°_{VV} (dB)	σ°_{HH} (dB)	σ°_{VV} (dB)	σ°_{HH} (dB)	σ° (dB)	σ°_{VV} (dB)	σ°_{HH} (dB)	σ°_{VV} (dB)	σ°_{HH} (dB)
24.5	-5.8	-5.4	-3.5	-6.1	-1.3	-1.9	+1.8	-0.3	-0.3	+2.1	-1.1
30	-8.3	-8.1	-6.4	-10.2	-4.6	-6.1	-2.1	-4.1	-4.2	-1.3	-5.7
35	-9.9	-11.5	-8.3	-13.6	-7.1	-9.8	-5.3	-7.3	-7.3	-4.0	-9.7
40	-11.4	-12.9	-9.9	-16.5	-8.6	-12.3	-8.0	-10.0	-10.1	-6.2	-13.3
45	-11.7	-15.4	-11.2	-19.4	-9.6	-14.1	-10.2	-12.2	-12.3	-8.0	-16.7
50	-12.4	-17.1	-12.4	-22.3	-10.8	-16.1	-12.2	-14.2	-14.2	-9.7	-19.9
55			-13.4	-25.4	-12.0	-18.5	-13.6	-15.6	-15.7	-11.1	-22.9
60	-15.1	-22.1	-14.4	-28.6	-13.2	-21.2	-14.9	-16.8	-17.0	-12.7	-26.0
65			-15.5	-32.1	-14.2	-23.8		-17.1	-17.5	-14.2	-29.1
70			-16.7	-36.2	-15.1	-26.2		-16.6	-18.1	-15.9	-32.2

The calculations were performed using a parameterized spectrum of the shape given by (4.2), with B= $1.96 \cdot 10^{-2}$, a_2 = 0.321 and k_p = 4.74. This is the best fit parameterization for the conditions under which the radar backscatter measurements were taken at u_*=0.367 m/s.

In figure 4-16 the dependence on the incidence angle is plotted for each of the models and the measurements for HH and VV polarization. The measurements are indicated with the symbol. The dotted line is the backscatter as calculated with the IEM model, the drawn line represents the SPM model, dash-dotted the BAH model and dotted the IEM model. The HSW model does not show any incidence angle dependence and is not represented in this graph. For small incidence angles, the IEM model converges to the HSW model.

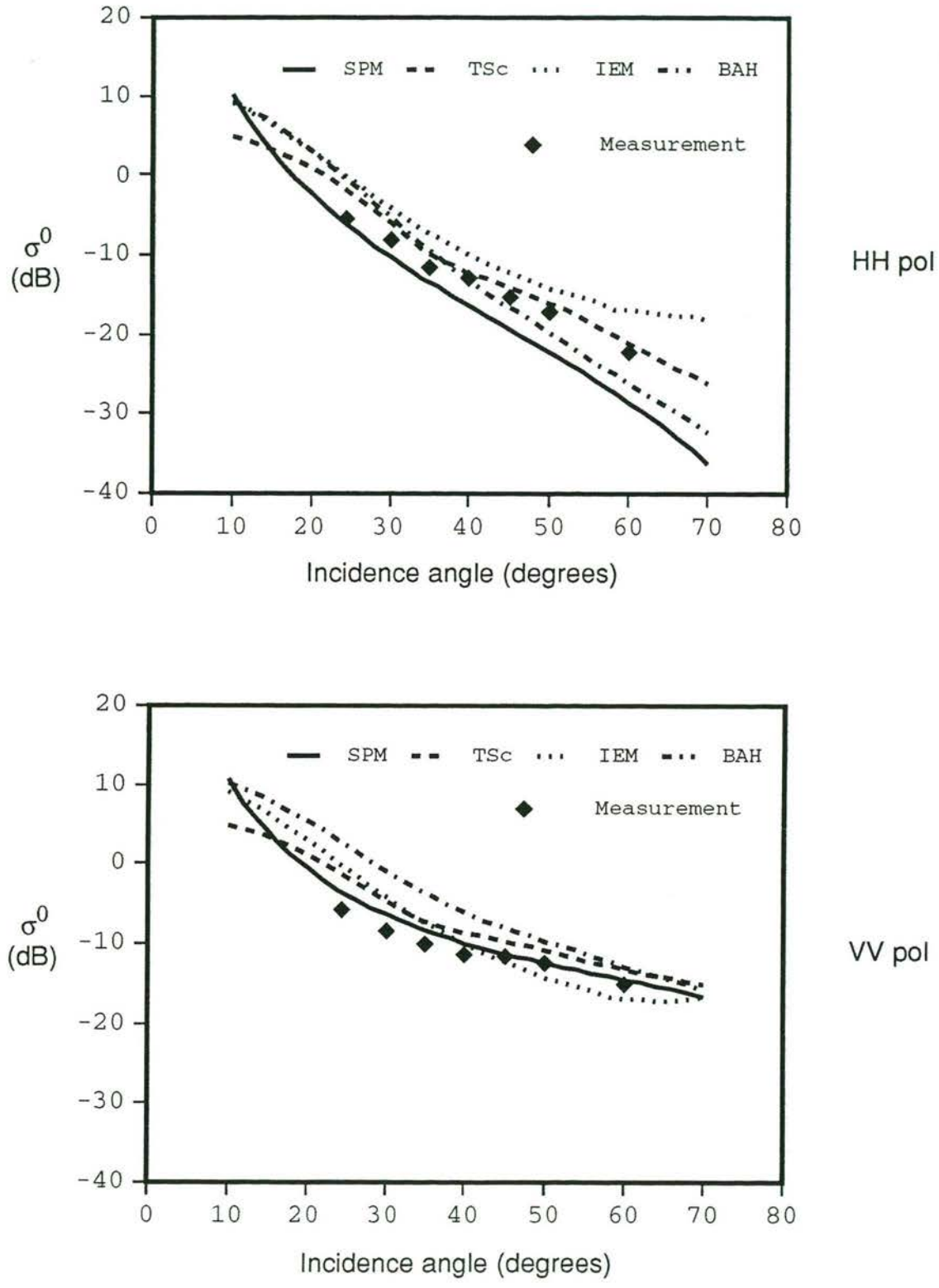

Figure 4-16 Incidence angle dependence for HH and VV, u_*=.367m/s, upwind

4.4.1.1 HH-polarization

It is well known that for HH polarization the influence of tilting becomes much more pronounced. Thus it is interesting to see how the different models compare with the observations for HH polarization. For the ERS-1 scatterometer this is less important since it operates only in VV polarization. However, an accurate physical model should predict correct cross sections in VV as well as HH polarization (and even in VH and HV, but that is outside the scope of this project).

At small incidence angles all models except SPM again overpredict the cross section. For moderate incidence angles the best results are obtained with the TSc and BAH model, the SPM model underpredicts and the IEM model overpredicts the cross-section. For large incidence angles the models diverge, the differences being more than 10 dB at 70 degrees. This is a disappointing result. Both sophisticated models, IEM and BAH show large discrepancies with the observations. SPM underpredicts the cross section as was to be expected. Only the TSc model gives good results in this regime.

Whereas the authors of the IEM and BAH models claim that the influence of long waves is taken into account in their models, the results are quite different. Furthermore, the predicted cross sections differ by more than 2 dB from the measurements and thus cannot be explained with inaccuracies in the measurements. Again, of all models, the TSc model gives the best results, but is not accurate enough at small incidence angles.

4.4.1.2 VV-polarization

The incidence angle dependence at VV can be split up in three parts. For small incidence angles (10-30 degrees), the IEM and Bahar model outcome agree quite well with each other. The TSc model gives slightly smaller results. This is caused by the implementation of an effective reflection coefficient (3.32) rather than the theoretical value of 1. The SPM model is not applicable in this region.

The differences between the models and the measurements is quite large and systematic: the models overestimate the backscatter with 2-5 dB. Although, it can never be excluded that some errors exist in the measurements, it is at this moment considered very unlikely that the errors in the measurements could be much more than the indicated 1 dB. It is more likely that, as was already observed by Barrick [9], the reflection coefficients at these small incidence angles are not a simple constant. The effect of the reflection coefficient can be observed by comparison of the TSc model with the IEM and Bahar models. Without the use of the effective reflection coefficient, the TSc model gives nearly identical results as the IEM and Bahar models.

In the second region, moderate incidence angles between 30 and 50 degrees, the SPM, TSc and IEM model agree very well with each other and with the measurements. Since the incidence dependence in this region is very small for VV, the influence of tilting by long waves is limited and thus the cross section can also be approximated with SPM. Strange enough, the Full Wave Approach model BAH disagrees significantly, overpredicting the cross section with approximately 5 dB.

For the high incidence angles the models split up. Of the four models the TSc model agrees best with the measurements. SPM and BAH overpredict the cross sections and IEM underpredicts.

Overall, the comparison is best for the TSc model, with the restriction that in the present form it overpredicts the cross section for incidence angles smaller than 30 degrees. The BAH model disagrees with the observation over the whole range of angles.

4.4.2 Dependence on the friction velocity

The results for the wind dependence of the models are summarized in table 4-6. The wind parameter used is the friction velocity u_*. It is assumed that the friction velocity is more directly related to the radar backscatter from the waves, since it represents the momentum transfer from the air into the water.

Table 4-6 Friction velocity results of experiment and model calculations

	experiment		SPM		TSc		HSW	IEM		BAH	
u_* (m/s)	σ°_{VV} (dB)	σ°_{HH} (dB)	σ°_{VV} (dB)	σ°_{HH} (dB)	σ°_{VV} (dB)	σ°_{HH} (dB)	σ° (dB)	σ°_{VV} (dB)	σ°_{HH} (dB)	σ°_{VV} (dB)	σ°_{HH} (dB)
0.069	-26.1	-29.1	-27.2	-35.4	-27.1	-35.2	-27.9	-26.5	-35.5	-27.1	-35.5
0.103			-28.6	-36.8	-28.6	-36.7	-29.3	-27.9	-36.8	-28.5	-36.7
0.140	-22.5	-26.1	-22.2	-30.4	-22.1	-30.0	-22.8	-21.9	-28.5	-22.0	-30.2
0.183	-17.8	-21.7	-18.0	-26.2	-17.8	-25.2	-18.5	-18.6	-22.2	-17.5	-25.7
0.246	-13.2	-17.4	-14.9	-23.1	-14.3	-20.7	-14.9	-16.2	-17.3	-13.5	-21.9
0.367	-11.6	-14.2	-11.2	-19.4	-9.6	-14.1	-10.2	-12.2	-12.3	-8.6	-16.7
0.490	-10.6	-13.2	-9.0	-17.2	-8.2	-12.1	-6.7	-8.7	-8.7	-3.6	-12.3
0.670		-11.9	-8.0	-16.2	-6.2	-9.7	-5.0	-7.1	-7.1	-1.6	-9.9
0.900	-8.7	-9.6									

These results are also shown in figure 4-17 for HH and figure 4-18 for VV polarization, respectively. In these figures the symbols represent resp: points=measurements, drawn line=SPM model, dashed line=TSc model, dash-dotted=BAH model and dotted=IEM model.

The description of the data can be found in [14]. Here we shall focus merely on the comparison of data and model calculations. One can observe that for VV polarization and low friction velocities, the cross section is quite accurately predicted by all models. This is not strange, since at these small wind speeds the backscatter at 45 degrees is mainly Bragg backscatter. All models reduce to Bragg backscattering under these circumstances. The growth of backscatter with windspeed is followed quite accurately by the SPM, TSc and IEM models. For some reason, the BAH model overestimates the backscatter for VV polarization severely at friction velocities above 0.25 m/s. Models and data compare well for the other models within the accuracy.

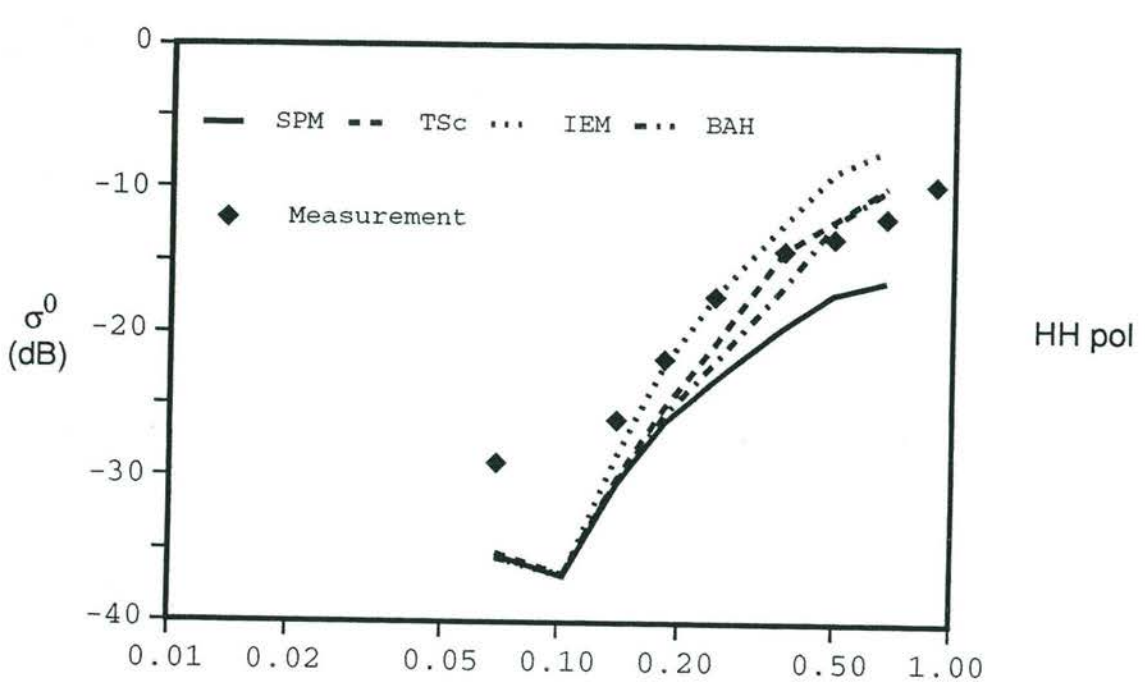

Figure 4-17 Friction velocity dependence experiment and models, HH pol.

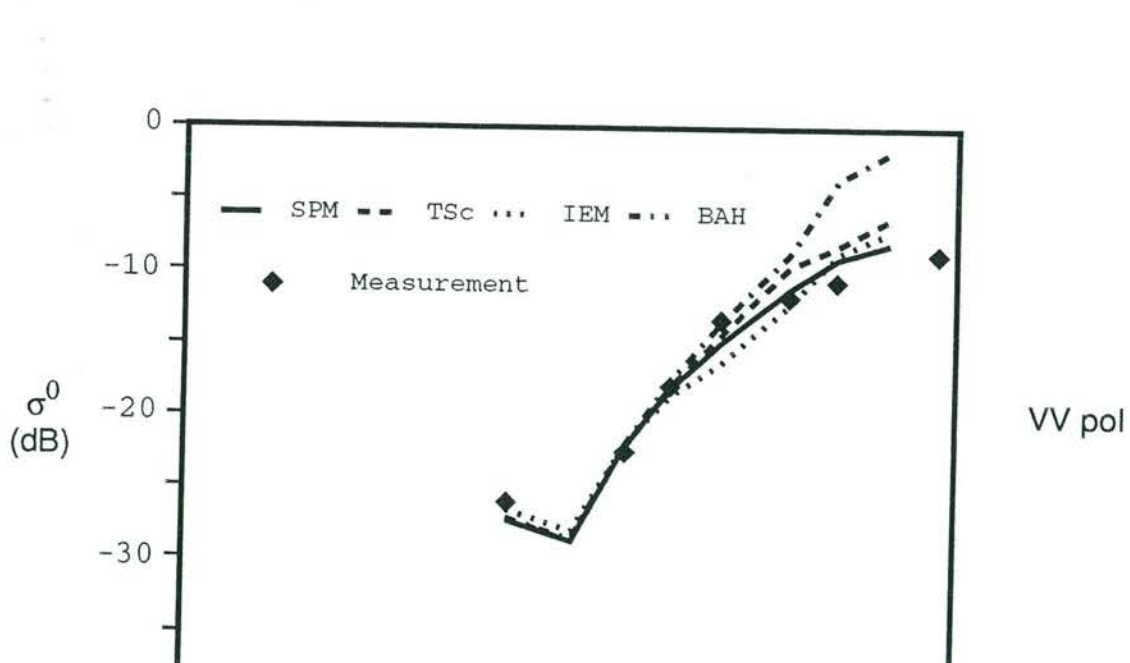

Figure 4-18 Friction velocity dependence experiment and models, VV pol.

For HH polarization a large difference is observed for very small wind speeds. All models, following Bragg backscatter, predict levels which are approximately 5-6 dB below the observed data. In this case it is believed the data could be faulty. At these low wind speeds the backscatter is quite low, especially at HH polarization. It is possible that the noise level exceeds the signal level and thus leads to an overestimation of the backscatter. At a slightly higher wind speed the models compare much more favorably with the data. For intermediate wind speeds, with friction velocities between 0.15 and 0.40 m/s most models, with the exception of the BAH model,underestimate the cross section. Beyond the point of wave breaking (at a friction velocity of approximately 0.25 - 0.30 m/s) the IEM and TSc model get closer to the observations, cross over and for high wind speeds overestimate the cross sections. The BAH model gives too high values for all wind speeds above 0.25 m/s as at VV polarization. The SPM model shows over the whole range of observed friction velocities an underestimation.

4.5 Discussion, selection of preferred model.

In the previous sections a comparison has been shown between four different models (SPM, TSc, IEM and BAH) and the measurements performed in the Delft wind wave flume. The essential input for the backscattering model, the wavenumber spectrum, was obtained directly from measurements with the Imaging Slope Gauge. In order to make the ISG spectra suitable for input into the models they were interpolated with respect to wind speed and regridded onto a equidistant (k_x, k_y) grid (see section 4.2). After that a parameterization of the spectra was made using the octupole spectrum (4.2). By doing this, use could be made of a very efficient algorithm (see section 3.4.1) for the calculation of the backscattering using the IEM and BAH model. The two-scale model TSc can work as well with the raw spectra. However to make a fair comparison between the models, also the two-scale model calculations were based on the *parameterized* spectra.

For the TSc model one important parameter has to be set. This is the separation parameter k_c between the long wave part of the spectrum and the short wave part. In contrast to an earlier version of the VIERS model this parameter was determined on a more or less physical basis. The main restriction to k_c was that is should be chosen in such a way, that the composite scattering model could be applied to the short wave part of the water surface. At the same time, the long wave part of the waves had to fulfill the restriction for the physical optics scattering theory. The optimal solution was found by choosing:

$$k_c = \sqrt{\frac{2k_o^2 B}{\beta}} \quad \text{with} \quad \beta = 0.07 \tag{4.11}$$

It was found that the IEM model by Fung and Pan gives very small polarization differences as soon as the surface variance became larger than $\approx 10^{-2}$ m^2. This is a very small surface variance for the ocean. The problem with the model was discussed with the authors, but no readily available solution was provided. According to A.K. Fung [28] the scattering from the long waves should be different from the short waves. It might even be necessary to cut-off the wave spectrum to exclude the long waves entirely. This option was not tried out in the context of this project. The problem will be forwarded again to A.K. Fung.

Two comparisons were made between model calculations and observed cross sections: the dependence on the incidence angle (section 4.4.1) and the dependence of the friction veloc-

ity (section 4.4.2). With regard to the incidence angle dependence, good results were obtained with the SPM-, TSc- and IEM model for VV polarization and moderate incident angles. The BAH model overpredicts the cross section significantly in this region. For small incidence angles all models predict much higher cross sections than measured. It is probable that for these small incidence angles the reflection coefficient R(0) used in the models is too large. Several effects are known to modify the reflection coefficient: small scale roughness, slicks and foam. The implementation of corrections for these phenomena is one thing that remains to be done. Until that time we will have to work with the present models. It will be interesting to see how the results at small incidence angles compare with the ERS-1 data. To study this it is recommended to gather ERS-1 data sets with wind fields that do not show significant changes in speed and direction over the full swath of the ERS-1 scatterometer. It such a case the wind/wave module of the VIERS model should give similar results for each of the footprints, whereas the radar backscatter should change according to the incidence angle.

Overall, for VV-polarization, the ERS-1 polarization, best results were obtained with the modified two-scale model.

For HH-polarization the results were quite similar. Again at small incidence angles the models show an overshoot. For medium to high incidence angles the best comparison is shown by the TSc model. The BAH model performs better at HH- than at VV polarization, but the decrease of backscatter with incidence angle is steeper for this model than the observed measurements. The HH cross sections by the IEM model are too large for all incidence angles. This can be manipulated by the introduction of a long wave cut-off in the wave spectrum supplied to the IEM model. This would decrease the total surface variance of the spectrum and thus decrease the above mentioned term $\exp(-k^2_{oz}\sigma^2)$ which plays an important role in the polarization dependence of this model. Since we have no good physical reason to cut-off the wavenumber spectrum, we did not exercise this type of manipulation. It is clear that the HH cross sections calculated by simple Bragg or SPM are too small.

The conclusion with respect to the incidence dependence is, that of the models which were compared, the modified two-scale gives the best comparison with the data. At small incidence angles none of the models follows the data. Part of the difference may be attributed to the differences between the parameterization of the ISG data and the real spectrum, and another part must be found in a wrong prediction of the models. The reflection coefficient R(0) used in the models at these small incidence angles should be corrected for effects of surface slicks, small scale waves and foam.

At 45 degrees incidence angle the dependence on the wind speed is shown in figure 4-17 and 4-18. The models predict the observations quite well for VV polarization. The exception is again the BAH model which overpredicts the cross section at the higher friction velocities. At HH-polarization the differences are much larger. For very low wind speeds the observed radar cross section is much larger than the model prediction. This might be an artifact of the data. At high incidence angles the models all show an increase with wind speed which is generally larger than the observed dependence. The SPM model underpredicts the cross section severely. The other models are slightly better, but none shows a real good comparison with the observations.

It is obvious that the influence of the long waves, which is much more pronounced in HH-polarization, is still difficult to model. It was hoped that the new models, based on the integral equation (BAH, IEM) would solve this problem. But, as can be shown from the comparison here, this seems not to be the case. In all of the comparisons the two-scale model

follows the observations as accurate or even more accurate than these models. Also at small incidence angles, where the two-scale model suffers the transition between the composite and physical optics approximation, the new models show no better results.

So it is concluded that for the purpose of the VIERS project, the best choice at the moment is still a two-scale model. The presently available model gives good results for VV-polarization, however, care should be taken at incidence angles below 30 degrees. The behavior of the model at small incidence angles should be checked against ERS-1 observations. Furthermore the influence of small waves, foam and slicks on the reflection coefficient should be incorporated in the model. This remains to be done.

Meanwhile it is hoped that the problems with the IEM model can be solved in the near future. This model can be extended to include third order surface statistics. It has been shown that this inclusion permits the prediction of upwind/downwind ratio's. All of the models considered sofar predict equal upwind/downwind ratio's. In order to be able to predict accurate wind directions with the ERS-1, the upwind/downwind asymmetry will have to be added in an artificial way at the moment. In the VIERS model, this will be done by the addition of a correction based on the observations by the ERS-1 (empirical correction).

5 The 'de Voorst' experiment, results and conclusions.

5.1 Introduction

The Delta tank at the "de Voorst" establishment of Delft Hydraulics, where the second experiment took place, is a unique facility. With its length of 240 meter and a water depth of 5 meter (or more) it is large enough to study waves with a length of up to about 10 meter without significant distortion due to bottom effects.

Although the Delta tank has an advanced computer controlled hydraulic system for wave generation, it has no wind facility, whereas wind is essential for the experiment. We were forced to build a hood over the facility in order to circumvent this problem. The hood we build was 150 meter long and the distance between water surface and hood was 3.4 m. Two large ventilators, place at the end of the hood provided wind speeds up to 10 m/s.

Table 5-1 lists some of the conditions under which the measurements were performed.

Table 5-1 Instrumental and environmental conditions 'de Voorst' experiment

Wind speed (PA)	4-10 m/s
Wave height	0 - 1 m
Wave spectrum	monochromatic and JONSWAP
Wave length (monochr.)	11 m
Air temperature	2.5° - 20° C
Water temperature	7.8° - 9.2° C
$T_{air} - T_{water}$	-6.2° .... 12.2° C
Distance PA - water	0.4 - 1.4 m
Scatterometer	X-band FM/CW
Distance scat - water	28 m
Incidence angle	45 deg.
Look direction	upwind, downwind

Backscatter measurements were done with an X-band FM/CW scatterometer at a fixed incidence angle of 45° looking either in upwind or downwind direction. A pressure anemometer [79] was used to measure the mean wind vector as well as the vertical momentum flux. The wave slope was measured simultaneously at the radar footprint. The wave structure was measured by a so-called Reflective Slope Gauge [48]. Furthermore a wave wire was used to measure the wave spectrum up to approximately 15 Hz.

5.2 Shear stress and large waves

At the VIERS-1 symposium in 1990 a new kind of wind profile was introduced for use in a wind-wave flume, intended to be used for the interpretation of turbulence measurements made during the "de Voorst" experiment. The model and its results are described in [80]. Basic assumptions are a linear relation between momentum flux and height (a direct consequence of a constant pressure gradient along the flume) and a mixing length

$$\ell = \kappa \frac{z(H-z)}{H^2} \tag{5.1}$$

in which κ is the von Kármán constant, H the total height of the flume and z the vertical distance to the water surface. The model produced a very satisfactory relation with the data. Another step has recently been attempted, viz. to calculate the difference in momentum flux above the crests and the troughs of the mechanically produced large waves. This may lead to more information about the position of the small waves (which are mainly responsible for both the roughness and the radar backscatter) with respect to the long ones. Knowledge of the modulation of the small waves by the large ones is essential for an adequate understanding of the radar backscatter, as aimed for in the VIERS-1 program. In a flume the effects of the large waves are

- a variation in the effective height (distance water to ceiling) of the flume
- a movement of the lower boundary, due to the orbital velocity of the waves.

Both effects are indicated in figure 5-1.

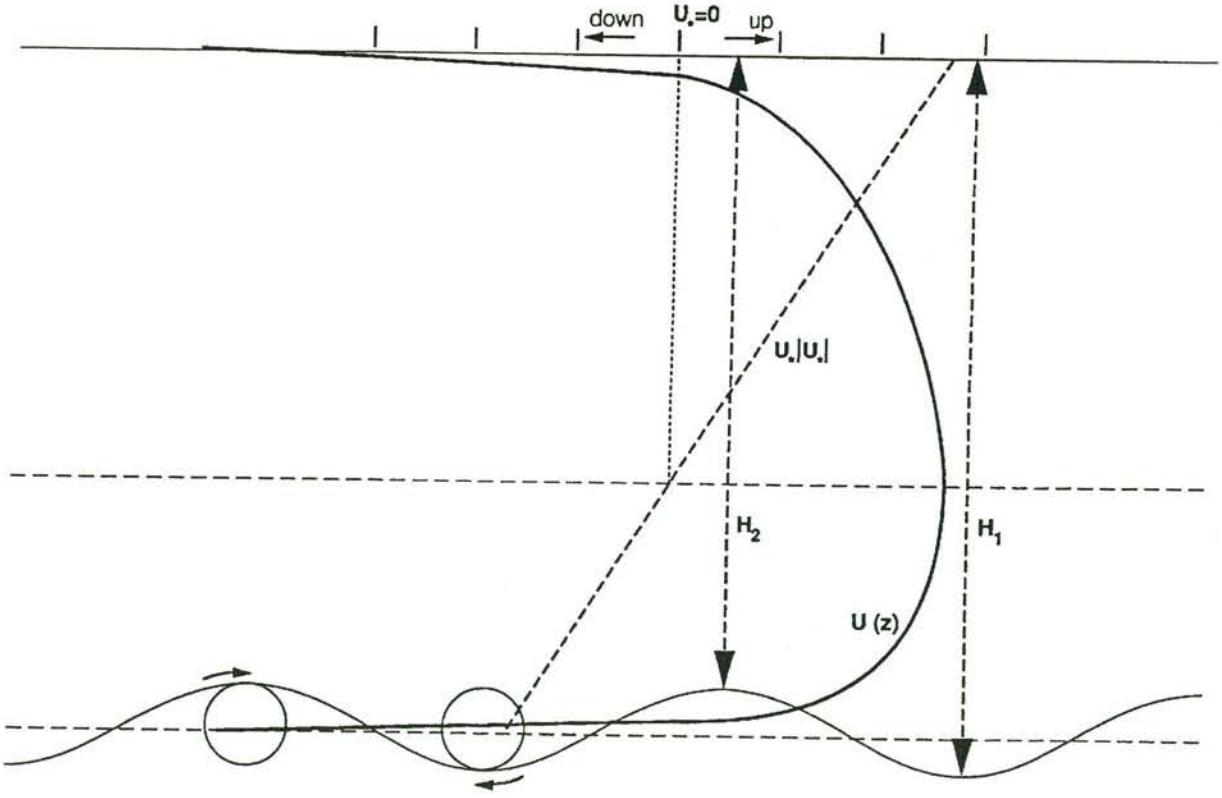

Figure 5-1 Effects of large waves in a flume

To simplify the calculation, the waves are divided in an "upper" and "lower" part, with the crossing of the undisturbed level as the criterion. For the two parts effective values were calculated. The maximum value of the orbital velocity at the wave surface is given by

$$V_{orb,\,max} = \frac{H\pi}{T} \tag{5.2}$$

(H is the wave height, T its period), its horizontal average value over half a period by

$$\overline{V_{orb}} = \frac{2}{\pi} V_{orb,\,max} = \frac{2H}{T} \tag{5.3}$$

Due to the viscous sublayer in the atmosphere near the watersurface the horizontal velocity in the atmosphere at the lowest point of the turbulent regime in the tunnel is not equal to the (average) orbital velocity. In [109] a model is presented for the relation between the velocity u_l of the surface and the resulting friction velocity u_*

$$\frac{1}{\kappa} \ln\left(\frac{u_\star}{u_\ell}\right) + \frac{u_\ell}{u_\star} = 5.1 \tag{5.4}$$

leading to

$$\frac{u_\ell}{u_\star} \approx 11.1 \tag{5.5}$$

The effect of the moving boundary will be strongest near the water surface, so the linear relation between u_* and z of the earlier model is replaced by

$$u_\star \mid u_\star \mid = D(h - z)^2 + Az + B \tag{5.6}$$

The boundary conditions are

$$DH^2 = u_{\star,o} \mid u_{\star,o} \mid \qquad u_{\star,o} = u_{\star,\ell} \,/\, 11.1 \tag{5.7}$$

the suffix 0 indicating a quantity at the boundary of the turbulent regime. This leads us to

$$u_\star = \{D(H - z)^2 + Az + B\}^{1/2} = \kappa \frac{z(H-z)}{H} \frac{dU}{dz} \tag{5.8}$$

if we again make the earlier mentioned assumption for the mixing length. The wind speed profile can then be calculated from

$$U = \frac{H}{\kappa} \int \frac{z(H-z)}{\{D(H-z)^2 + Az + B\}^{1/2}} dz \tag{5.9}$$

which, like the profile given in [80], can be found by analytic integration. The physically unrealistic results of the calculations made so far indicate, however, a not yet located error in the data handling. We expect to rectify this in the near future.

5.3 Modulation of the microwave backscatter by long waves

An analysis has been made on the modulation of the microwave backscatter by long, monochromatic waves of constant wave length (11 m.) and varying height (0 - 1 m.). Wave slope signals were measured by means of the Reflective Slope Gauge at approximately the same footprint as the microwave measurements. A time synchronization of 40 ms was achieved between both types of measurements. A correction has been applied for the small (0.25 m) misalignment between the footprint of the LSG and the center of the scatterometer footprint.

The radar backscatter is lowest around 0-90 degrees, i.e. between the trough and the down-going zero crossing of the wave. Maxima are found between the up-going zero-crossing (180 degrees, minimal local incidence angle) and the crest.

Table 5-2 Backscatter modulation depth and phase.

u_* m/s	Wave ampl. m_{pp}	Pol.	mod. dB	max. angle deg.	min. angle deg.
.355	1.0	HH	20	220	15
.32	0.6	HH	12.5	245	15
.34	0.6	VV	5	215	0
.30	0.3	HH	6.25	175	30
.30	0.3	VV	3	185	65

'mod.' is the difference of the backscatter level between maximum and minimum in dB's. 'max' indicates the phase angle at which the backscatter reaches its maximum, 'min': the minimum.

Table 5-2 lists the approximated modulation and the phase angles for the maximum and the minimum for the 5 cases analyzed so far. The magnitude of the modulation is much larger for HH polarization than for VV polarization, as could be expected on the basis of tilt modulation. The minimum shifts from 0 degrees (VV, 0.6 meter wave) to 70 degrees (VV, .30 meter wave), which means the minimum shifts towards the trough with decreasing tilt modulation, probably under influence of hydrodynamic and other types of modulation (e.g. wind-induced).

A preliminary comparison has been made with the tilt modulation model. It has been assumed that the short wave spectrum falls off as k^{-4}. A different coefficient has some influence on the amount of tilt modulation but the best fit was obtained with a coefficient of -4. A correction has been made for the varying footprint size due to the tilting of the long waves. The model curves were fitted to the measured data around a phase angle of 180 degrees.

The 'tilt' modulation model gives a good qualitative and quantitative description of the modulation especially for the HH polarized signals at phase angles between 0 and 180 de-

grees. Above 180 degrees the HH data is generally underestimated by the tilt model, indicating that other types of modulation (e.g. hydrodynamic modulation) are of importance there.

For VV polarization, the tilt modulation is much smaller than for HH polarization, therefore the effects of hydrodynamic modulation become more visible as the hydrodynamic modulation is polarization independent. The tilt modulation model underestimates the total modulation in the microwave backscatter. Inclusion of hydrodynamic modulation does give some improvement, especially for the small amplitude cases. The effect of the shift of the minimum backscatter toward 70 degrees is qualitatively predicted by the combined tilt/hydrodynamic model. For the small amplitude wave VV-polarized measurement even quite good quantitative agreement is reached with inclusion of hydrodynamic modulation. More single wave data will have to be analyzed before any conclusions can be drawn on the value of these models. The simple tilt modulation describes the magnitude of the total modulation of the radar backscatter rather well, but especially around the crest sometimes more backscatter is measured than can be explained by tilting alone.

In the near future we will process more of the data acquired. Especially the data with the scatterometer looking downwind/downwave will be further analyzed. These data are interesting because the tilt modulation at down wind will shift over 180 degrees whereas the hydrodynamic and wind/wave modulation stays the same.

Wind/wave interaction was observed in the data acquired by means of the Pressure anemometer. These signals remain to be analyzed.

6 The VIERS-1 field experiment, first results

6.1 Introduction

The VIERS-1 field experiment took place from November 12 until December 6, 1990 at 'Meetpost Noordwijk' (MPN), a research platform 5 sea miles off the Dutch coast, near the coastal resort of Noordwijk, owned and operated by Rijkswaterstaat (figure 6-1).

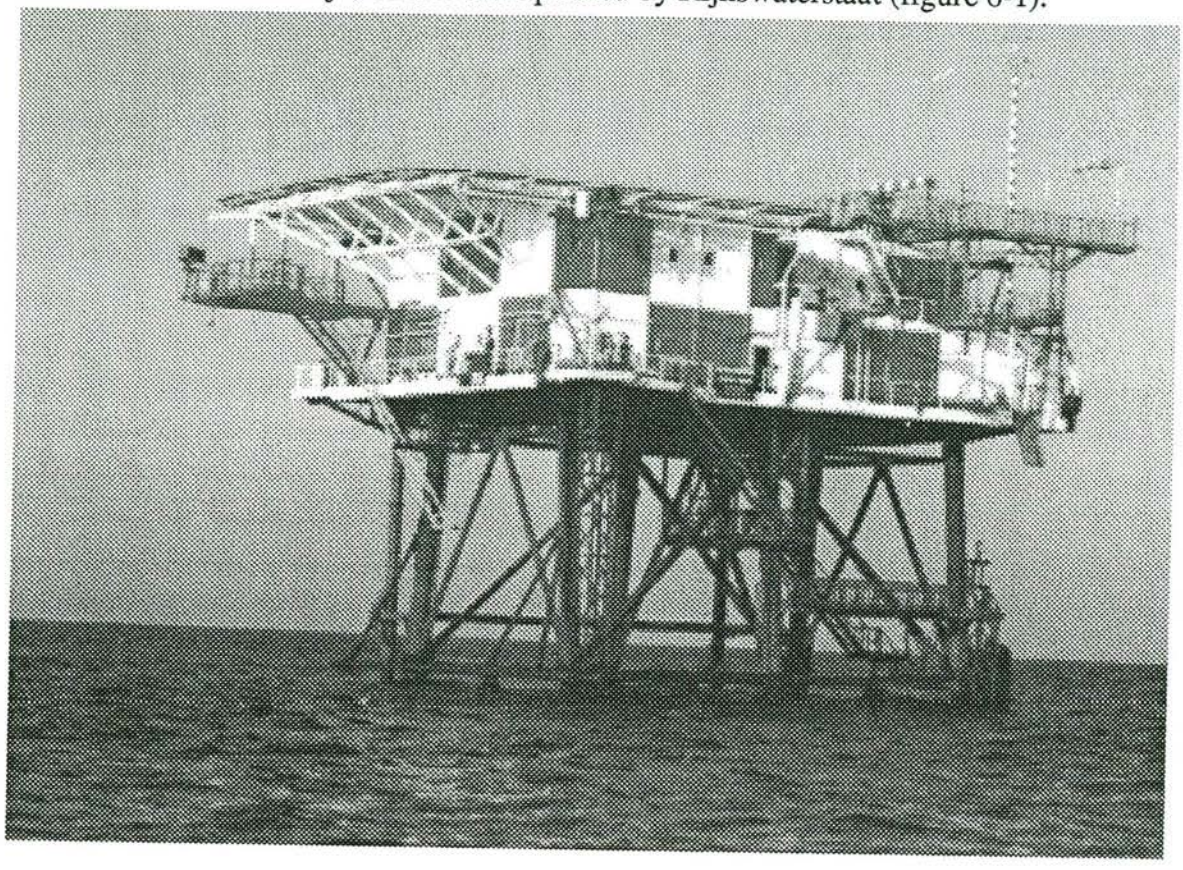

Figure 6-1 Measuring Platform Noordwijk

Participating organizations were

1. Royal Netherlands Meteorological Institute (KNMI), which provided the project leader,
2. Netherlands Institute for Sea Research (NIOZ),
3. Physics and Electronics Laboratory of the Organization for Applied Scientific Research (FEL-TNO),
4. Delft University of Technology (TU-Delft),
5. Rijkswaterstaat, Tidal Water Division,
6. Bedford Institute of Oceanography (BIO, Canada),
7. Scripps Institute of Oceanography (from the US),
8. University of Heidelberg (from the BRD),
9. Istituto per lo Studio della Dinamica delle Grandi Masse (ISDGM, Italy).

The experiment had a twofold purpose: on one hand, in the context of the VIERS-1 program, to make radar, meteorological and oceanographic measurements to find relations between the microwave return from the sea surface and the geophysical situation, on the other, as a preliminary to a program on air-sea gas transfer, to try to measure the vertical flux of carbon dioxide in the atmosphere just above the sea surface with the eddy correlation method.

TU-Delft, FEL-TNO, ISDGM, KNMI and the Scripps/Heidelberg University group were involved in the VIERS-1 experiment; KNMI, NIOZ and BIO in the carbon dioxide flux measurements.

The experiment was supported by the Netherlands Remote Sensing Board (BCRS) and the National Research Program on Global Air-Pollution and Climate (NOP). The support of NOP was in behalf of the CO_2 flux measurements, that of BCRS for VIERS-1.

The following quantities were measured:

- radar backscatter from the sea surface (X-band and C-band),
- mean winds and momentum fluxes,
- waves (wave height, wave direction, wave breaking),
- heat and moisture (mean values and fluxes),
- local currents.

Many of these quantities were measured by two or more separate methods. Of the systems used for wave measurement some should be mentioned specifically in this context, viz.

- an optical system, designed and operated by the Scripps/Heidelberg University group, providing wave height and wave direction of the small waves (cm-length),
- the FEL-TNO SHIRA system that gave the directional wave spectrum of the longer waves and surface currents and
- an image-processing system, operated by KNMI, used to detect whitecaps and to determine their statistical properties.

6.1.1 Course of events

The majority of the instruments and basic equipment, including the 21 meter boom, had been transported to the platform before the experiment proper. Also the boom, which ends in two prongs had already been installed. During the VIERS-1 experiment one prong was used only for the RSSG, the other for the remaining instruments. In figure 6-2 the boom is shown during the mounting of equipment.

The first week was nevertheless needed to connect instruments and data systems and repair the inevitable malfunctioning of a few instruments in a set that has been transported. The most serious problem was encountered with one of the radar systems where a part broke down which was not commercially available anymore, so the problem had to be solved by "cannibalizing" another radar and transporting the borrowed components to the platform.

In the second week (weekends were spent ashore) the measurements were started. The meteorological situation was not always very favorable for the experiment: the wind had the habit of coming from a N to NE-ly direction, which makes the measurements with the eddy

correlation method difficult to interpret, due to flow distortion. Also the wind speed remained below 15 m/s, somewhat lower than had been hoped for.

No serious technical problems were encountered during the remaining part of the experiment. KNMI registered a total of 47 data runs of about one hour duration each.

On December 6 the experiment was finished and due to hard work by the participants and a reasonably quiet sea all instruments could be transported ashore the same day. This greatly restricted the time lost waiting for the instruments to be returned.

Figure 6-2 Instrument boom with RSSG and other instruments

6.2 Wind measurements

Wind and momentum flux measurements were made with two different instruments, a Kayo Denki DAT 300 sonic anemometer and a pressure anemometer (PA), the latter an instru-

ment developed at KNMI [79]. Both instruments measure the three dimensional wind vector. Sampling frequency was 70 Hz, which was adequate for the PA (its 3 dB point is at about 30 Hz) and a substantial oversampling for the sonic, which has an internal sampling frequency of 10 Hz.

The anemometers were mounted at the end of a 21 meter long boom, to reduce flow distortion due to the platform.

During the experiment the sonic was used in an upright position, the PA was used upside down: in this way the sensor head of the PA was closest to the water surface.

The standard wind equipment of MPN, consisting of cup anemometers and vanes, was used to check whether the wind situation justified executing an experiment: wind measurements with an easterly wind direction are not useful, the boom being on the West side of the platform.

The most important data obtained from the anemometers at the boom are the momentum fluxes, measured with the eddy correlation technique.

6.2.1 Momentum flux measurements

The eddy correlation technique is an absolute and - at least in principle - simple method for the measurement of the momentum flux. The only thing needed is a measurement of the average product of the horizontal and vertical turbulent wind velocities.

However, the technique has some exacting requirements. The most important of these is that the orientation of the instrument in space and the structure of the flow around it must be known very precisely, as a small unheaded tilt can cause large errors, e.g. neglecting a tilt of only 1° would lead to a incorrect sign and an order of magnitude error in the momentum flux. The commonly used tilt correction method, in which the sole cause of a mean vertical wind component is assumed to be a tilt of the instrument, is in principle not correct, as shown by Wyngaard [114]. The author also presented a more adequate correction method, but that method can only be applied to situations where the dimensions of the disturbing body are small compared to the measuring height and not to the effects of large structures, such as the main body of a platform. The only way to handle this is to make the platform effect as small as possible.

To obtain trustworthy values of the momentum flux the anemometers were therefore mounted as far as possible from the platform body. To this end a 21 meter long boom was used, attached to one of the risers of MPN.

The length of the boom was based on earlier wind tunnel tests [111], which also gave values for the remaining effect of the platform body on the mean flow. At the end of the boom electronic levels gave the vertical orientation of the boom head and so of the instruments. As stated, the boom ended in two prongs. On one of these the anemometers were mounted, on the other the sensor box of the Reflective Stereo Slope Gauge (RSSG). The remaining flow distortion was mainly due to the boom head and the instruments mounted there and was corrected, using an distortion model developed by Oost [78], a generalization of the model of Wyngaard, mentioned earlier.

Before the experiment both anemometers were subjected to an extensive speed and direction calibration that took care of any "self-distortion", i.e. flow distortion effects of the instruments on their own readings [73].

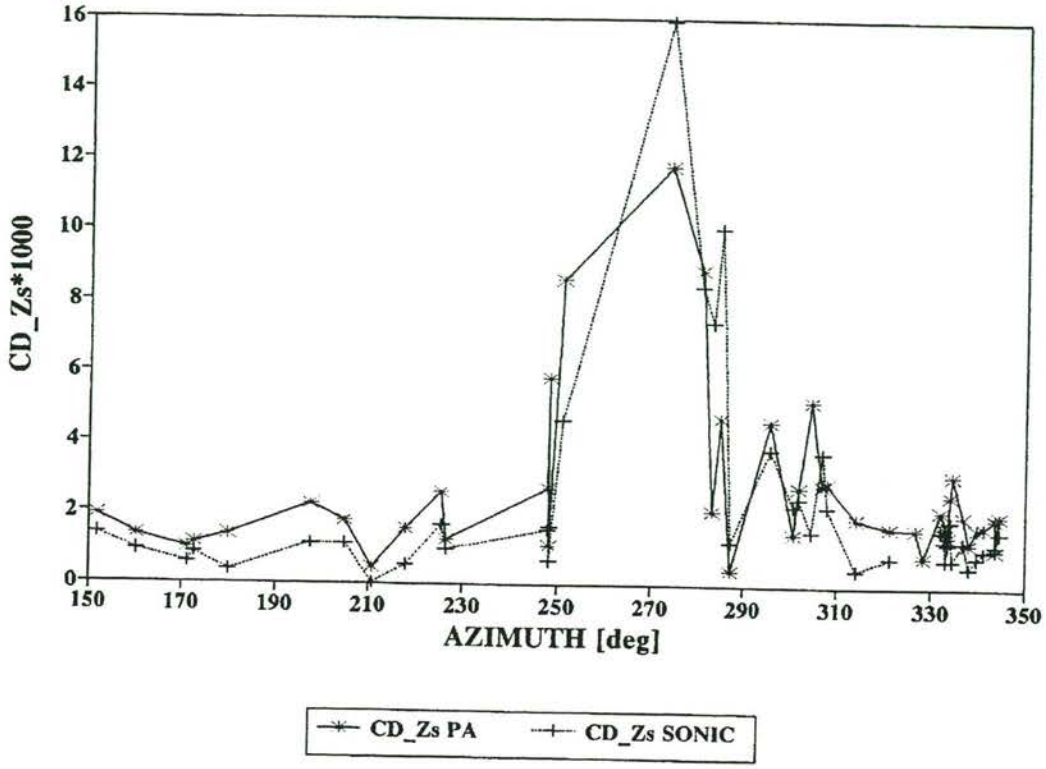

Figure 6-3 Uncorrected local drag coefficient CD_Zs as a function of the azimuth angle of the wind (West is 270°). PA: pressure anemometer; SONIC: sonic anemometer. The large deviations around 270° were caused by strong flow distortion.

It turned out that for flow directions around 270° (westerly) the distortion was so intense that no correction could be made (figure 6-3). These data were excluded from further treatment. The remaining data still showed a large scatter (figure 6-4).

This scatter could partly be attributed to transient effects, like frontal passages (figure 6-5) and rain drops hitting the sensors (figure 6-6). The runs therefore were broken up in clusters of at least three minutes each, in which these transients were absent. This strongly reduced the scatter and also brought the independent measurements of the momentum flux, made with the two anemometers within each others uncertainty range (figure 6-7).

After a promising start the data-analysis has turned out to be more time consuming than expected. A tilt compensation system used in the KNMI pressure anemometer flawed early on during the experiment (this could not be detected at that time), causing the loss of the calibration points of the instrument. Fortunately the data could be reconstructed, using an iteration procedure and the known characteristics of the measurement situation, but this took time. At the time of writing most data had been analyzed.

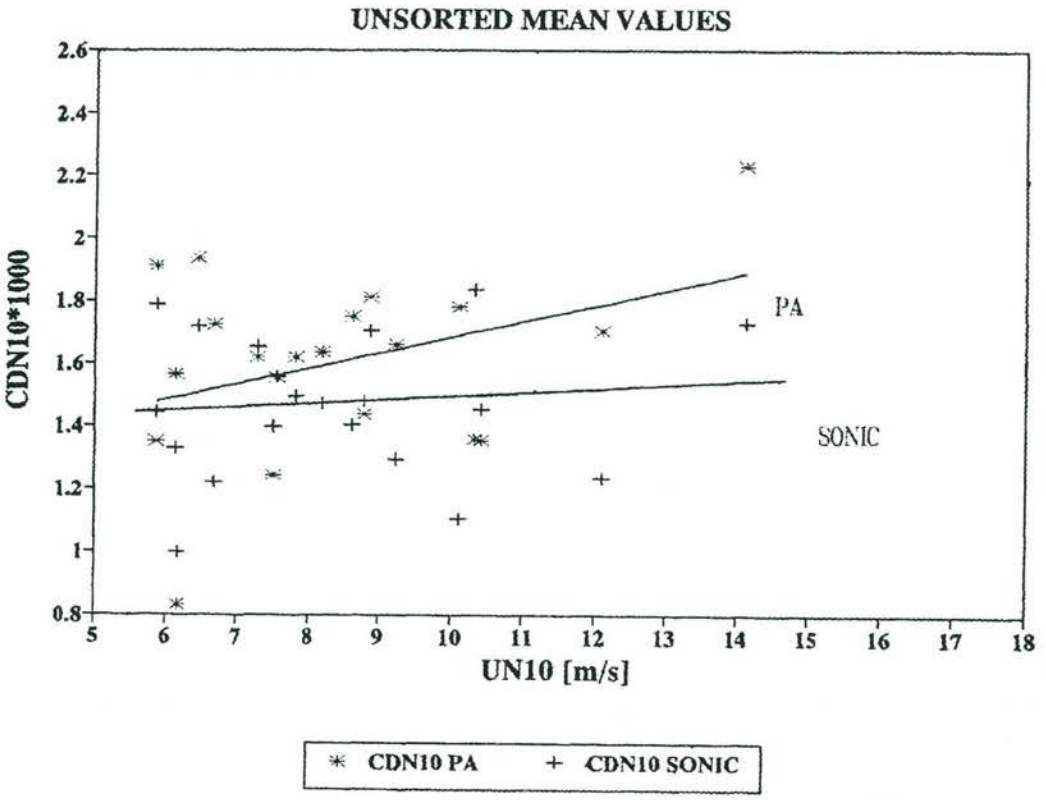

Figure 6-4 Values for the neutral drag coefficient at 10 meter (CDN10) as a function of the neutral 10 meter wind speed (UN10). Results after removal of the strongly disturbed values of figure 6-3 and correction of the data for the remaining flow distortion.

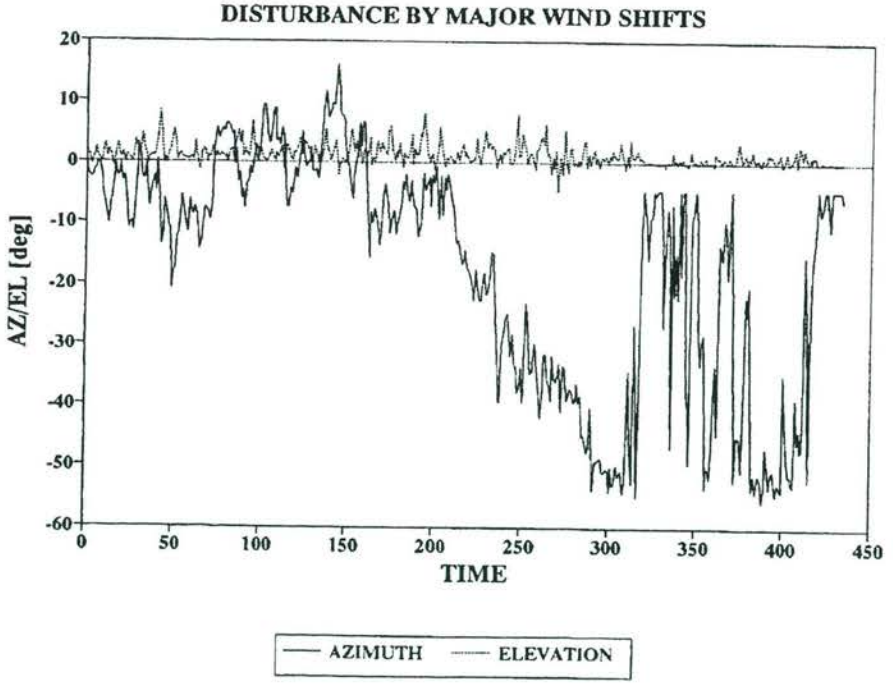

Figure 6-5 The signature of a frontal passage in the wind speed measurements of the sonic anemometer.

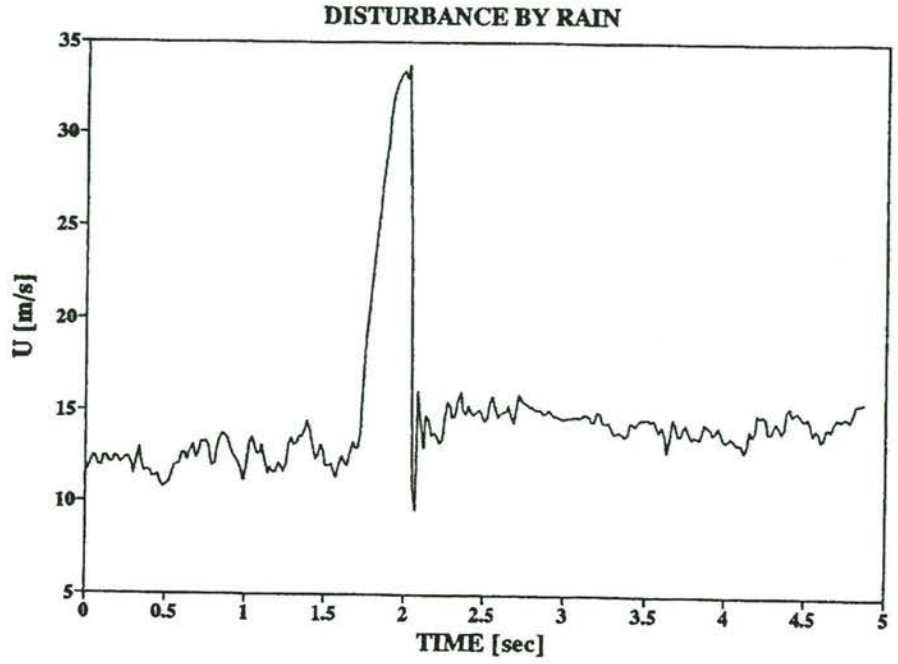

Figure 6-6 Strong fluctuations in the PA signal due to rain drops hitting the sensors.

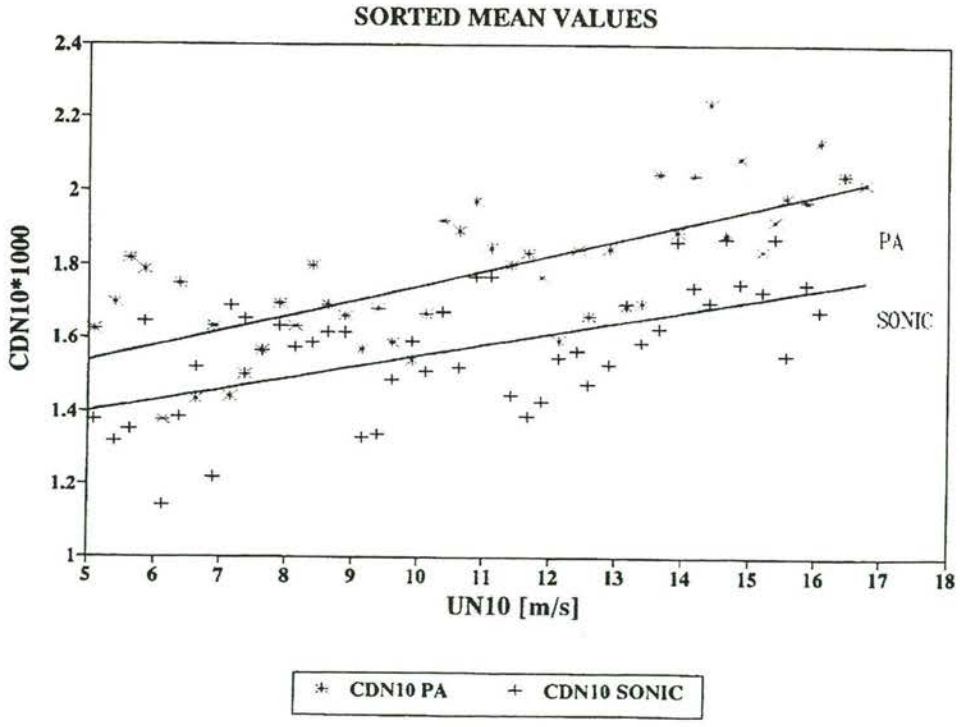

Figure 6-7 As figure 6-4, after removal of all data obtained under non-standard condition.

6.2.2 Analysis of turbulence measurements

The results are presented of the wind and turbulence measurements, done at MPN during the VIERS-1 field campaign. The data were, as already stated, measured with a Kayo Denki DAT-300 sonic anemometer and a pressure anemometer. The sonic anemometer was used upright, the PA upside down, which resulted in a height difference between the centers of the respective sensors of almost 2m (1.93m, to be precise). This height difference should not affect the turbulent momentum flux τ, which is constant throughout the lowest few meters of the atmosphere. τ is calculated as

$$\tau = \rho\, u_\star^2 \tag{6.1}$$

with the friction velocity u_* defined as

$$u_\star^2 = - < u'w' > \tag{6.2}$$

u' and w' are the turbulent components of respectively the horizontal along-wind and vertical wind speed component. u' is found from

$$u' = u - U \tag{6.3}$$

in which u is the instantaneous wind speed component and U its mean value (w' is defined in the same way).

6.2.2.1 Failure in the tilt compensation for the sensors of the PA.

After a number of runs the automatic compensation for the tilt-sensitivity of the pressure sensors in the PA failed. This resulted in an offset of the zero reading, which is obtained while the anemometer is perpendicular to its position during the measurements (boom raised). The problem arose at KNMI run 24, was not intermittent and we could solve it by measuring the offset separately and applying a suitable constant correction for all KNMI runs with a sequence number higher than 24.

6.2.2.2 Flow distortion.

Flow distortion effects are inevitable, although steps were taken to minimize them: the instruments were mounted on a 21m long boom to reduce the effect of the platform body on the flow and the instruments were distributed over two separate "prongs" at the end of the boom to space them as much as possible. The remaining flow distortion must be measured or calculated.

For the mean flow the wind tunnel measurements of Wills [111] could be applied.

For the turbulent quantities the situation is less simple, because the flow distortion effects depend on the relative size of the turbulent eddies and the distorting body. For the VIERS-1 experiment the effect of the main body on the turbulence may be neglected, whereas the effect of the boom head can be treated mathematically, using the assumption that the size of the distorting body is much smaller than the integral length scale of the turbulence. For the actual calculations we successfully applied the ellipsoid model of Oost [78]. Figures 6-8 and 6-9 show the effect of this treatment on u_*. Note the difference in the u_* values from the

sonic anemometer and the PA before the correction calculation and their correspondence thereafter.

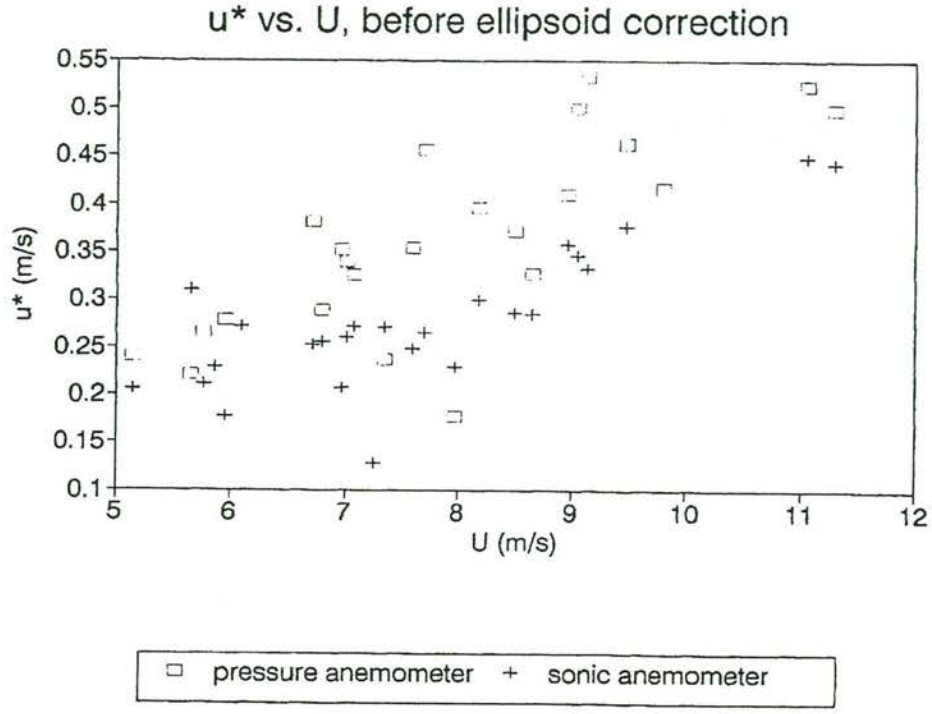

Figure 6-8 u_* vs. U, before ellipsoid correction.

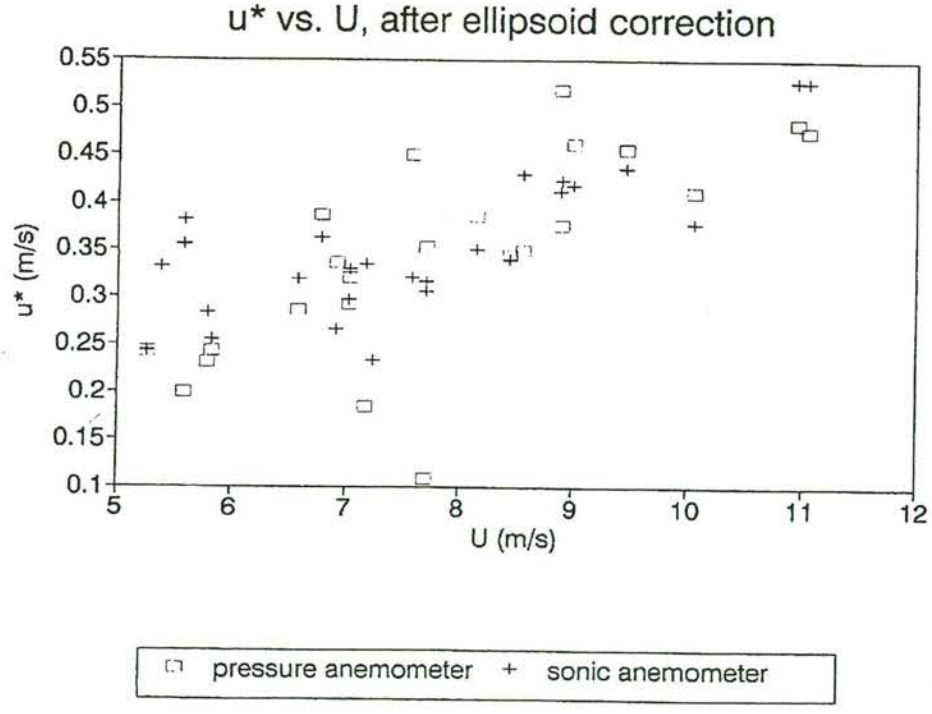

Figure 6-9 u_* vs. U, after ellipsoid correction.

Table 6-1 contains the values used to represent the distorting bodies.

Table 6-1 Values to represent the distorting bodies

Sizes of ellipsoids (m)

Direction → Bluff body ↓	East-West (x)	North-South (y)	Up-Down (z)
Prong	1.04	0.25	0.11
RSSG	0.31	0.93	0.19
Desjardin	0.14	0.14	0.49
Crossbeam	0.28	1.35	0.19
Rotor	0.11	0.11	0.38

Position of the pressure anemometer relative to the ellipsoids (m)

Direction → Bluff body ↓	East-West (x)	North-South (y)	Up-Down (z)
Prong	-0.47	-0.04	-1.10
RSSG	-0.23	-2.04	-1.10
Desjardin	-0.48	0.13	-1.35
Crossbeam	-0.88	-0.90	-1.10
Rotor	0.04	0.00	-1.26

Position of the sonic anemometer relative to the ellipsoids (m)

Direction → Bluff body ↓	East-West (x)	North-South (y)	Up-Down (z)
Prong	-0.51	-0.04	0.78
RSSG	-0.27	-2.04	0.78
Desjardin	-0.52	0.13	0.53
Crossbeam	-0.92	-0.90	0.78
Rotor	0.00	0.00	0.62

6.2.2.3 Regression calculations.

Most of the time during the experiment the wind speed remained in the range 5-7 m/s. To test their validity we compared the data with those of the 1986 HEXMAX experiment, which covered a much larger range of wind speeds. After applying all necessary corrections we found an excellent correspondence between the HEXMAX and the VIERS-1 values for the friction velocity, as figure 6-10 shows.

The regression line in figure 6-10 corresponds to a linear wind speed dependence of the drag coefficient, as used in most publications on that subject:

$$u_\star^2 = C_D \times U^2 = (A \times U + B) \times U^2 = A \times U^3 + B \times U^2 \qquad (6.4)$$

in which C_D is the dragcoefficient and A and B regression coefficients.

For the combined data set (VIERS-1 &HEXMAX) the values for A and B are

$$A = 1.07 \times 10^{-4} \text{ and } B = 4.55 \times 10^{-4}$$

if for U the wind speed reduced to 10m height is used.

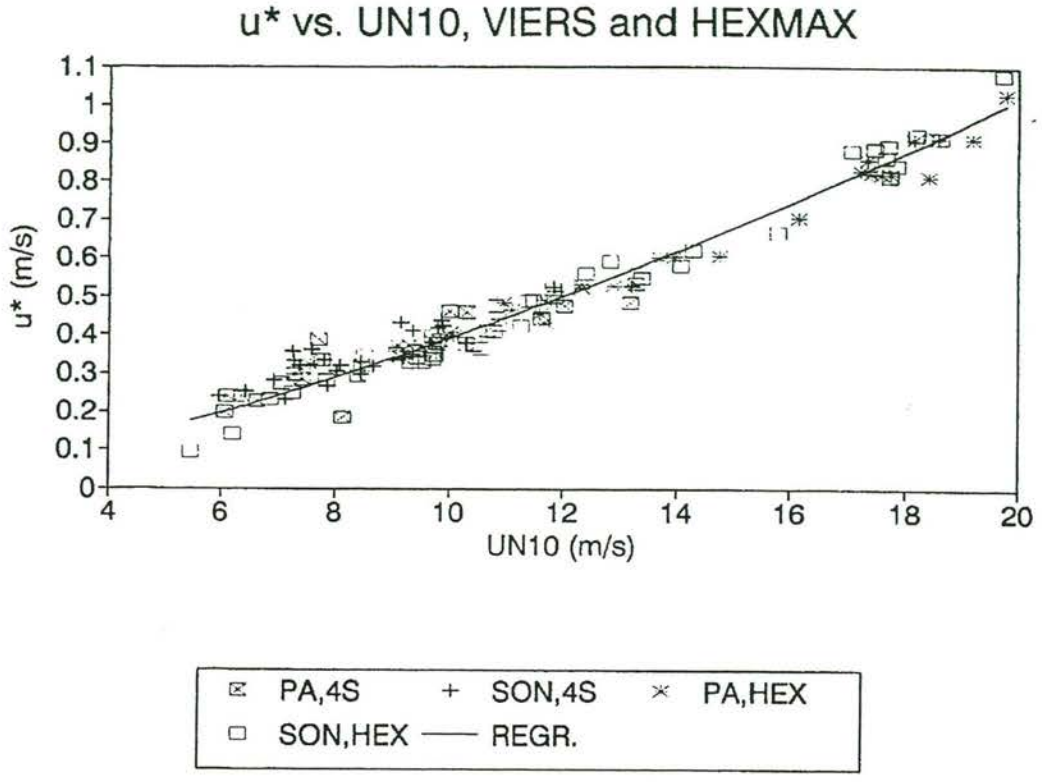

Figure 6-10 u_* vs. UN10, VIERS-1 and HEXMAX

Despite the good correspondence between the HEXMAX and VIERS-1 data it is clear that there is a deviation with respect to the regression curve at the lower wind speeds, where the VIERS-1 data are concentrated. This indicates that we are entering here a wind speed range where other effects, e.g. due to stability, start playing a larger role. We therefore recalculated the regression line using only the VIERS-1 data. The A and B coefficients then have the values

$$A = -1.00 \times 10^{-5} \text{ and } B = 1.75 \times 10^{-3}$$

Due to the strong flow distortion effects mentioned earlier quite a few runs had to be discarded. To make it possible to use them nevertheless in the interpretation of radar data and other purposes, we also did a regression calculation between the u_* values of PA and sonic anemometer and the wind speed measured operationally at the platform, which is available for all runs. The coefficients in this case are

$$A = -3.70 \times 10^{-5} \text{ and } B = 1.93 \times 10^{-3}$$

These last values should only be used if no other possibilities exist and certainly not if the wind is from the land.

6.2.2.4 Results

The results are presented in table 6-2. The following comment can be given by the various columns:

RUN	The KNMI run number
DATE	The date the run was started
START	Start time of the run (local time)
T.LTH	Duration of the run, as used for the calculation. It should be noted that for runs 21, 24, 27 and 72 only the first part of the run has been used, because of a significant change in the weather situation during the run (frontal passages). Indicated is the duration actually used.
QUALITY PREF.	For runs where both PA and sonic data are available the instrument is indicated with the smallest deviation with respect to the regression value. If the PA (or sonic) value did not conform to the Chauvenet criterion for the acceptance of data [12] an indication is given that only the sonic (or PA) value should be used. For three PA runs (36, 61 and 63) u_* values have been "synthesized" using the regression calculation and the wind speed measured by the PA.
PA, AZIM.	Azimuth direction of the wind as measured by the PA, after correction.
PA, U(z)	Wind speed as measured by the PA, after correction
PA, z	Mean height of the PA sensor head above the water level during the full run.
PA, u'w'	Mean value of the correlation of the turbulent parts of the longitudinal horizontal and vertical wind component over the analyzed part of the run, after correction, as measured by the PA.
PA, u*	Friction velocity measured by the PA: $(- u'w')^{1/2}$
PA, z0	Roughness length calculated for the PA.
PA, UN10	Wind speed at the 10 m level under neutral circumstances.
MPN, U	Wind speed measured operationally at a mean height of 27.61 m above mean sea level.
MPN, AZIM.	Wind direction measured operationally
du*	differences in friction velocity values
regr.	values from regression calculations
SONIC, ...	As for the PA

Table 6-2 Wind/Turbulence values VIERS/MPN

WIND/TURBULENCE VALUES VIERS/MPN.
Corrections applied: blocking of mean flow (BMT), ellipsoid correction for turbulent quantities, surface current
QUALITY: *: PA-values obtained from regression calculation
PREF. : "PA" or "Sonic" indicates the sensor with the smallest deviation from the regression value
"... only" indicates that the value of the other sensor didn't conform to the Chauvenet criterion

RUN	DATE	START (hh:mm)	T.LTH (sec.)	QUALITY PREF.	PA AZIM. (degr.)	PA U(z) (m/s)	PA z (m)	PA u'w' (m2/s2)	PA u* (m/s)	PA z0 (m)	PA UN10 (m/s)
2	11/12/90	10:00	3540	PA	248.6	7.19	4.89	-0.1130	0.34	0.000980	7.76
5	11/16/90	09:20	3600	Sonic only	226.8	7.71	5.93	-0.2031	0.45	0.006586	8.25
8	11/16/90	11:00	3480	PA	218.5	8.62	5.78	-0.1222	0.35	0.000311	9.07
11	11/19/90	05:40	4200	Sonic	281.3	12.16	4.69	-0.2334	0.48	0.000182	13.17
14	11/19/90	19:12	3600	Sonic	271.7	7.70	4.85	-0.0857	0.29	0.000104	8.39
18	11/20/90	14:39	4200	PA	308.4	8.98	4.97	-0.1414	0.38	0.000304	9.77
21	11/20/90	16:14	1260	Sonic	338.7	8.85	4.20	-0.2129	0.46	0.001727	9.99
24	11/20/90	19:14	1260	Sonic	330.3	6.74	5.02	-0.1495	0.39	0.003429	7.71
27	11/21/90	09:36	2340	Sonic	248.7	6.02	5.31	-0.0534	0.23	0.000105	6.62
30	11/21/90	11:32	3840	PA	207.7	8.39	5.51	-0.1189	0.34	0.000247	9.14
33	11/21/90	13:59	4020	Sonic	198.9	5.69	5.02	-0.0589	0.24	0.000282	6.35
36	11/21/90	16:19	2460	*	176.5	6.84	4.11	0.2087	0.26	0.000072	7.48
54	11/29/90	08:22	4260	Sonic	252.5	5.49	4.86	-0.0584	0.24	0.000408	6.10
61	11/29/90	11:21	1500	*	334.7	5.32	3.98	3.1064	0.18	0.000032	5.84
63	11/29/90	12:30	2340	*	349.4	5.41	3.74	2.8608	0.19	0.000031	5.94
66	11/29/90	13:33	3360	Sonic only	339.7	7.56	4.53	-0.0118	0.11	2.9E-12	7.83
72	11/29/90	17:33	1980	PA	344.7	9.80	4.83	-0.1693	0.41	0.000320	10.64
77	12/03/90	12:11	3540	PA only	307.3	5.64	4.75	-0.0400	0.20	0.000054	6.06
78	12/03/90	13:58	3300	PA	298.7	6.70	3.95	-0.0822	0.29	0.000321	7.41
79	12/03/90	15:03	3540	Sonic	291.0	7.67	4.15	-0.0342	0.19	0.000000	8.12
82	12/03/90	16:33	3300	PA	269.2	8.41	4.39	-0.1247	0.35	0.000298	9.20
83	12/03/90	17:38	3360	PA	281.6	9.05	4.80	-0.1489	0.39	0.000378	9.82
84	12/03/90	19:05	3480	Sonic	276.0	7.75	4.38	-0.1025	0.32	0.000253	8.47
92	12/04/90	13:49	2640	Sonic	334.2	9.36	4.69	-0.2086	0.46	0.001219	10.29
93	12/04/90	14:56	1560	Sonic only	336.5	8.77	4.12	-0.2679	0.52	0.004513	9.97
97	12/04/90	17:37	3600	PA	330.9	10.99	4.36	-0.2247	0.47	0.000396	12.01

Regression (VIERS only):
(u*)^2 = -1.00E-05 *UN10^3 +1.75E-03 *UN10^2
(u*)^2 = -3.70E-05 *ffMPN^3+1.93E-03 *ffMPN^2

Regression (VIERS + HEXMAX):
(u*)^2 = 1.07E-04 *UN10^3 +4.55E-04 *UN10^2

RUN	MPN U (m/s)	MPN AZIM. (degr.)	d(u*) @ABS PA-sonic	d(u*) @ABS regr.-PA	d(u*) @ABS regr.-SO	SONIC AZIM. (degr.)	SONIC U(z) (m/s)	SONIC z (m)	SONIC u'w' (m2/s2)	SONIC u* (m/s)	SONIC z0 (m)	SONIC UN10 (m/s)
2	8.15	249.2	0.0698	0.0187	0.0553	249.7	7.54	6.82	-0.0710	0.27	0.000074	7.86
5	8.98	230.4	0.1297	0.1134	0.0095	226.3	7.94	7.86	-0.1030	0.32	0.000423	8.08
8	10.09	222.9	0.0805	0.0201	0.0574	217.3	8.90	7.71	-0.1850	0.43	0.002029	9.14
11	13.15	283.8	0.0446	0.0473	0.0042	282.5	12.53	6.62	-0.2785	0.53	0.000447	13.21
14	8.05	272.8	0.0042	0.0500	0.0484	272.3	7.96	6.78	-0.0883	0.30	0.000113	8.46
18	10.47	307.1	0.0476	0.0216	0.0221	311.1	9.29	6.90	-0.1795	0.42	0.000895	9.87
21	8.61	319.9	0.0432	0.0551	0.0196	342.2	9.08	6.13	-0.1749	0.42	0.000851	9.80
24	8.87	305.7	0.0240	0.0710	0.0520	333.6	6.87	6.95	-0.1315	0.36	0.002326	7.58
27	6.90	232.1	0.0527	0.0408	0.0001	246.0	6.38	7.24	-0.0805	0.28	0.000586	6.91
30	8.79	210.4	0.0042	0.0278	0.0336	200.9	8.63	7.44	-0.1161	0.34	0.000207	9.18
33	6.09	204.4	0.0115	0.0185	0.0092	195.1	5.87	6.95	-0.0646	0.25	0.000417	6.41
36	6.89	187.7	0.0246	0.0488	0.0589	182.9	6.55	6.04	-0.0543	0.23	0.000049	7.12
54	5.10	252.9	0.0011	0.0094	0.0027	248.1	5.49	6.79	-0.0589	0.24	0.000540	5.96
61	6.86	349.9	0.1476	0.0558	0.0335	364.8	6.75	5.91	-0.1104	0.33	0.001547	7.29
63	7.14	341.0	0.1666	0.0556	0.0577	355.7	6.61	5.67	-0.1263	0.36	0.002819	7.26
66	8.34	333.2	0.1981	0.2120	0.0220	345.8	7.60	6.46	-0.0940	0.31	0.000280	8.03
72	11.56	184.5	0.0335	0.0204	0.0401	344.1	9.79	6.76	-0.1429	0.38	0.000186	10.29
77	6.06	307.7	0.1811	0.0491	0.1197	309.5	5.92	6.68	-0.1453	0.38	0.012608	6.36
78	8.05	303.7	0.0330	0.0170	0.0174	307.8	6.88	5.88	-0.1022	0.32	0.000980	7.38
79	8.61	299.0	0.1498	0.1471	0.0158	302.8	7.30	6.08	-0.1121	0.33	0.000903	7.79
82	8.30	277.2	0.0358	0.0217	0.0364	275.9	8.21	6.32	-0.1007	0.32	0.000180	8.67
83	9.03	287.4	0.0352	0.0136	0.0302	283.6	8.91	6.73	-0.1229	0.35	0.000233	9.35
84	7.76	279.3	0.0093	0.0257	0.0159	276.0	7.99	6.31	-0.1086	0.33	0.000348	8.46
92	10.50	326.3	0.0202	0.0388	0.0355	335.5	9.32	6.62	-0.1905	0.44	0.001192	9.86
93	9.86	330.2	0.1052	0.1124	0.0314	340.2	8.75	6.05	-0.1701	0.41	0.001149	9.35
97	13.20	325.8	0.0520	0.0112	0.0471	334.7	11.18	6.29	-0.2767	0.53	0.001224	11.85

6.3 Wave measurements

Waves were measured in several ways, using the following instruments:

- the Reflective Stereo Slope Gauge (RSSG), developed and operated by the group of Heidelberg University
- the SHIRA system, developed and operated by FEL-TNO
- a WAVEC buoy, operated by RWS
- a wire wave gauge, attached to the boom head, operated by KNMI
- a wave staff, attached to the platform proper, operated by RWS

6.3.1 The wire wave gauge

The sensor part of the wire gauge consists of a 12 m long Nichrome wire of 0.2 mm diameter, twisted around a passive 1 mm support wire, with a streamlined weight at the lower end and attached to the boom head on the other. The wave wire is connected to a constant (electrical) current source. The resistance of the wire varies with the waves, because the sea water effectively short-circuits the wire at the water level. The voltage variations in combination with the vertical slope of the wire then give the wave height.

The wire slope is measured by a potentiometer, fixed to the boom head by a swiveling joint and with its rotary axis connected to the support wire. The swivel is needed to accommodate variations of the direction of the surface (water) current.

The wire gauge only measures wave heights. Sampling frequency was 20 Hz, which allows measuring waves up to a frequency of 10 Hz, or about 1.5 cm wave length. This wave length is well within the range that can be measured with a 1 mm diameter wire.

The wire gauge functioned without problems. Earlier versions, used at MPN during other experiments, did not have the support wire construction and could carry only a limited weight. This led to problems: Due to the strong tidal currents in the area the slope of the wire sometimes exceeded the technically allowed range and the wire was vibrating in the wind, which led to spurious readings. The new construction allowed a much larger weight to be used, suppressed the vibrations and led to satisfactory, relatively small and well defined slope angles. A survey of the wire gauge results is given in table 6-3.

Table 6-3 Results of some wave measurements

VIERS MPN EXPERIMENT 1990 mean values as at 3/04/92

				SEA WAVES:				CO2/H2O:			BOOM POSITION:		
1	2	3	4	5	6	7	8	9	10	11	12	13	14
run				WAVR Hs	WAVR Tz	WIRE Hs	WIRE Tz	INF.RED H2O STDEV.	CO2	IRGA CO2	WTL LAT	WTL LON	bmhgt
	mo/day	hr:sec	sec	m	sec	m	sec	g/m^3		ppm	°	°	m
2	11/12	10:00	3540	1.26	4.45	1.14	4.02	0.15		345	-0.83	0.084	5.34
5	11/16	09:20	3600	1.32	4.92	1.16	4.3	0.09	0.01	357	-0.15	0.102	6.38
8	11/16	11:00	3480	1.4	4.81	1.14	4.02	0.1	0.01	351	-0.17	0.296	6.23
11	11/19	05:40	4200	2.6	5.32	2.53	5.43			343	-0.75	-0.00	5.14
14	11/19	19:12	3600	1.89	5.23	1.89	5.04	0.19	0.01	337	-0.52	-0.14	5.3
18	11/20	14:39	4200	2.16	4.89	1.95	4.99	0.24	0.01	335	-0.55	0.042	5.42
21	11/20	16:14	3660	2.03	4.92	1.88	4.84	0.22	0.01	334	-0.74	0.062	4.65
24	11/20	19:14	3780	1.62	4.72	1.53	4.6	0.28	0.02	337	-0.59	0.345	5.47
27	11/21	09:36	3900	1.07	4.08	1.05	4.08	0.23	0.01	343	-0.32	-0.00	5.76
30	11/21	11:32	3840	1.08	4.31	1.1	4.22	0.24	0.01	349	0.18	-0.00	5.96
33	11/21	13:59	4020	0.95	4.15	0.95	4.16	0.2	0.01	346	-0.32	-0.01	5.47
36	11/21	16:19	2460	1.13	3.69	1.03	3.77			351	-0.06	-0.26	4.56
42	11/26	17:21	3540	0.98	4.48	0.92	4.76			361	-0.57	-0.37	5.48
45	11/27	17:06	3240	0.86	3.59	0.83	3.78			352	-1.07	-0.76	5.67
48	11/28	15:53	3420	0.71	3.63	0.7	3.72			347	-0.16	0.15	5.48
51	11/28	19:22	3420	0.61	3.33	0.61	3.42			344	-0.16	0.069	5.57
54	11/29	08:22	4260	0.63	3.75	0.56	3.56			346	0.547	0.078	5.31
61	11/29	11:21	1500	0.66	3.52	0.62	3.58			336	0.883	0.103	4.43
62	11/29	11:51	2220	0.69	3.54	0.7	3.43			335	0.734	0.125	4.2
63	11/29	12:30	2340	0.91	3.82	0.88	3.58			335	0.852	0.138	4.19
66	11/29	13:33	3360	1.05	4.02	1.09	3.9	0.21	0.01	339	-0.32	-0.12	4.98
67	11/29	14:33	3180	1.17	3.97	1.22	3.99			347	-0.38	-0.11	5.33
68	11/29	15:33	4140	1.29	4	1.26	3.99			348	-0.37	-0.1	5.68
71	11/29	17:07	1200	1.47	4.16	1.3	3.89			348	-0.31	0.051	5.29
72	11/29	17:33	4380	1.43	4.07	1.4	4.08			348	-0.41	0.098	5.28
73	11/29	19:02	3300	1.5	4.02	1.39	4.11			350	-0.23	0.083	5.45
74	11/29	19:59	3780	1.51	4.13	1.36	4.02			349	-0.23	0.096	5.44
77	12/03	12:11	3540	1.12	4.2	0.96	4.2			358	-0.18	-0.08	5.2
78	12/03	13:58	3300	1.23	4.11	1.03	4.74			357	-0.72	0.117	4.4
79	12/03	15:03	3540	1.31	4.18	1.06	4.19	0.16	0.01	353	-0.64	-0.12	4.6
82	12/03	16:33	3300	1.28	4	0.98	4.15	0.15	0.01	351	-0.73	0.058	4.84
83	12/03	17:38	3360	1.3	4.16	0.93	4.1	0.14	0.01	351	-0.76	0.075	5.25
84	12/03	19:05	3480	1.36	4.44	1.02	4.39	0.12	0.01	353	-0.62	0.027	4.83

COLUMN EXPLANATION:

1,2,3,4 - (1) RUN number, (2) DATE, (3) START time (local), (4) run length
5, 7 - Significant waveheight: (5) waverider, (7) wavewire
6, 8 - Wave period: (6) waverider, (8) wavewire
9, 10 - Standard deviation infrared fluctuation sensor : (9) H2O, (10) CO2
11 - Absolute CO2 quantity
12, 13 - Level signals, indicating tilt of the boom head
14 - Mean run distance between boom and sea level

				SEA WAVES:				CO2/H2O:			BOOM POSITION:		
1	2	3	4	5	6	7	8	9	10	11	12	13	14
run				WAVR Hs	WAVR Tz	WIRE Hs	WIRE Tz	INF.RED H2O STDEV.	INF.RED CO2 STDEV.	IRGA CO2	WTL LAT	WTL LON	bmhgt
	mo/day	hr:sec	sec	m	sec	m	sec	g/m^3		ppm	°	°	m
92	12/04	13:49	2640	1.86	5.03	1.88	5.16	0.22	0.01	347	-0.22	0.199	5.14
93	12/04	14:56	1560	2.01	5.34	1.69	5.21	0.17	0.01	347	-0.21	0.242	4.57
94	12/04	16:08	0										
97	12/04	17:37	3600	2.05	5.02	1.81	5	0.15		347	-1.05	-0.01	4.81
98	12/04	18:39	3600	2.15	5.19	1.9	5.01	0.16	0.01	347	-1.12	0.024	5.21
99	12/04	19:44	3600	2.29	4.98	1.97	5.1	0.18		347	-1.31	0.042	5.63
100	12/04	20:56	3540	2.45	5.02	1.86	5.03	0.18	0.01	311	-1.39	0.052	5.85
101	12/04	22:11	2700	2.49	5.16	2.07	5.25	0.22	0.01	349	-1.36	0.058	5.85
105	12/05	13:29	3540	1.85	5.66	1.55	5.6	0.17	0.01	351	0.438	-0.13	5.76

COLUMN EXPLANATION:

1,2,3,4 - (1) RUN number, (2) DATE, (3) START time (local), (4) run length
5, 7 - Significant waveheight: (5) waverider, (7) wavewire
6, 8 - Wave period: (6) waverider, (8) wavewire
9, 10 - Standard deviation infrared fluctuation sensor : (9) H2O, (10) CO2
11 - Absolute CO2 quantity
12, 13 - Level signals, indicating tilt of the boom head
14 - Mean run distance between boom and sea level

6.3.2 The wave staff

MPN is part of the operational North Sea Monitoring Network and as such has a facility to measure wave heights. This is done with a wave staff, fixed rigidly to the so called "hydro sensor pole" at the South Western corner of the platform. The wave staff has sensor points with mutual vertical distances of 10 cm and is sampled with 4 Hz. The limited resolution in space and time of the instrument and the way it is mounted made it unsuitable for our measurements. Its data, however, provided a very useful check on the performance of the other wave instruments.

6.3.3 The SHIRA system

Long wave measurements are important for the verification of the model, because the gravity waves have influence on the microwave backscatter. This influence is not explicitly modeled in the present ESA ERS-1 algorithm but it is integrated in the VIERS model. For the measurement of waves during the experiment, use was made of waveriders and a pitch and roll buoy (WAVEC). However, the directional information on the waves can be measured in more detail - especially in complicated situations - by the SHIRA system.

SHIRA is a scanning radar, based on a standard ships navigation radar system. With every rotation of the antenna, a new image of the area surrounding the antenna is formed. SHIRA

records a user specified subsection of these images for each rotation in a digital format on a PC. Thus a three dimensional (x,y,t) database is formed of the microwave reflectance of the ocean waves on which further data processing can be performed. This database can be used to monitor ocean waves and obtain a directional wave spectrum. Some of the hardware characteristics are listed in table 6-4, see also reference [34,66,67,68,69].

The SHIRA antenna was placed on a movable mount on the top deck of MPN. The line of sight was obstructed only between 60 and 120 degrees w.r.t. North by a large crane, so a free view was obtained of about 300 degrees. The obstructed view East was not very important for the experiment as the fetch for waves coming from that direction is only a few kilometers. Furthermore meteorological measurements cannot be performed for conditions with winds from the East because of the flow distortion by the platform. The first 750 meter around the platform could not be imaged because the antenna pattern of the system is such that the amplification is very low in this region. The electronic equipment was set up in the large workshop on the lower deck of MPN.

The instrument was operated from November 18 till December 5, 1990. It performed very well with only minor technical problems throughout this period. Measurements were conducted roughly every 30 minutes during the periods in which also the other radar and meteo equipment was operated.

A total of 237 measurements were conducted, yielding about half a Gigabyte of raw data and about four times that amount of FFT intermediate products. As mentioned above, most of the data were processed already on the site, in between the measurements and sometimes during the night. An overview over all measurements conducted with the SHIRA system during the 1990 VIERS-MPN experiment can be found in [34].

Table 6-4 Specifications of the SHIRA system

electromagnetic:	frequency polarization	9.445 GHz HH
geophysical:	wave lengths wave frequencies	15 - 600 m 70 - 400 mHz
measurement window:	dimensions position in range position in azimuth	600 x 600 150 - 5000 m 300 degrees
time resolution:		1 image per 1.2 sec
digitization:	frequency resolution	30 MHz 8 bit
data storage:	primary backup	hard disk optical disk
processing:		PC-based with aid of an array processor

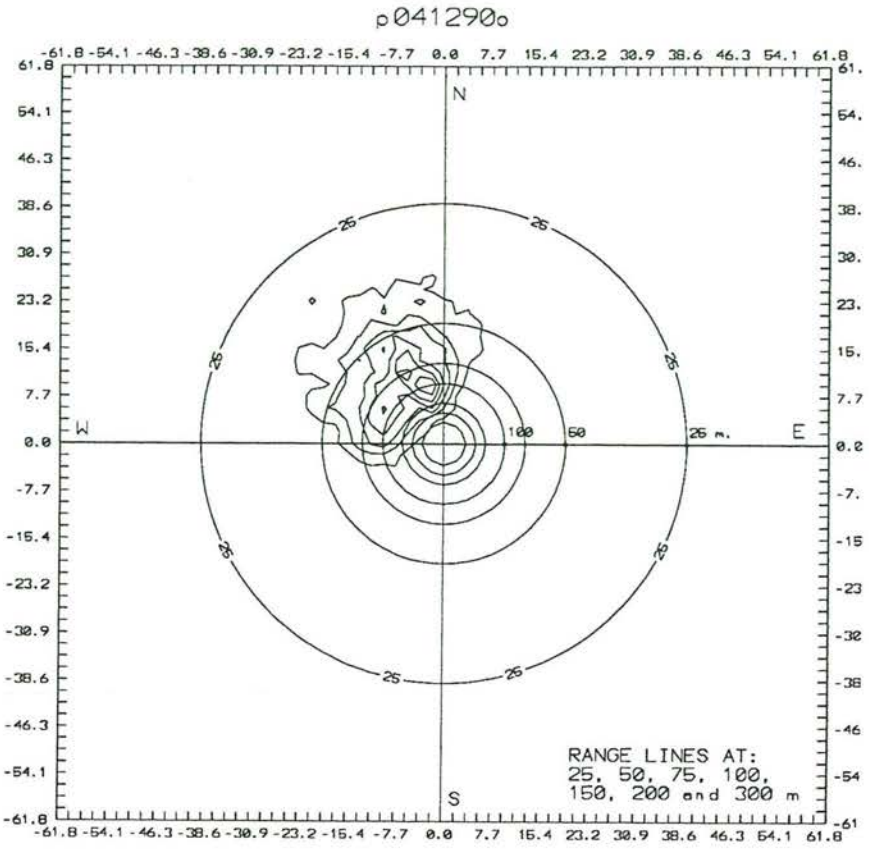

Figure 6-11 An example of a SHIRA measurement

Figure 6-11 gives an example of the data acquired during the experiment. On December 4, 1990 the wind increased from 10 to 14 m/s during the day, from NNW directions. The significant wave height increased from 162 to 255 cm. This strong wave field can be seen beautifully in figure 6-11.

SHIRA turns out to be sensitive enough to image wave fields under very low windspeed conditions (< 5 m/s) and significant wave heights well below 1 m. The complex directional spreading of the wave fields was imaged beautifully by the system. At the moment of finalizing this report the validation of the data could not yet be performed because the directional wave data from the pitch/roll buoy were available only since 1 week. A validation of the SHIRA capacity to measure directional wave spectra is underway.

Because SHIRA measures the propagation speed and direction of the waves, the data can be used, - by applying a priori knowledge of the undistorted (shallow water) phase speed of the waves - to obtain the water current speed and direction. The sensitivity of the system to currents has been reported earlier. However the accuracy could never be established or demonstrated because of a lack of good quality simultaneous SHIRA and current measurements. The data acquired during this campaign is the first complete set of measurements allowing such a verification. The first results are very promising.

6.4 The RSSG measurements

6.4.1 Overview

A direct measurement of the small-scale structure scattering electromagnetic radiation at the ocean surface was of significant importance for the VIERS-1 project, since in all previous investigations no sufficient spatial data about the short waves was obtained. Without spatial wave data, radar backscattering theories can only be investigated indirectly. A clean separation of electromagnetic and hydrodynamic effects or, more generally, a physically-based modeling of the radar return from the sea surface is not possible. Point measuring devices, even if they are capable to resolve the highest frequencies, are not sufficient since it is impossible to derive the spatial wave structures. However, with an instrument which yields either a continuous information of the wave slope or height, two-dimensional wave number spectra can be computed and used to test a wide range of backscatter models in a statistical sense. For an even more detailed study of electromagnetic scattering from the ocean surface and the form and kinematics of the "roughness elements" for the wind field, the actual shape of the water surface can be analyzed from such wave images. Moreover, statistical parameters which cannot be inferred from power spectra, such as the probability density function of wave slope or wave slope and height and which are significant, e.g., for radar altimetry, can also be derived.

Within the VIERS-1 project wave imaging instruments have first been used in the laboratory experiments [14,30]. Based on this experience an instrument could be built, tested and then used in the field campaign at the Noordwijk tower. Here, we report on the field measuring technique. In section 2, a brief overview of spatial measuring technology for short ocean waves is given. It will be shown that the measurement of the small-scale spatial structure of the ocean surface is a special case of the principle to recover the shape of a surface in three dimensions from

1. the shading in a two-dimensional image ("shape from shading")
2. the parallax of image features taken from two different point of views ("shape from stereo").

These methods are extensively explored and used in modern computer vision [45].

The new instrument, named the *Reflective Stereo Slope Gauge* (RSSG), is based on these concepts and discussed in section 6.4.3, while section 6.4.4 describes the technical details of the experimental setup. In section 6.4.5 we turn to the algorithm used for fast and accurate automated processing of the digital stereo images. This is a crucial aspect of any imaging measuring instrument. Without the capability to extract accurate physical information from Gigabytes of image data in reasonable time, imaging techniques are worthless. Therefore, we concentrated our research effort first on optimal algorithms for stereo processing of the kind of images taken by our instrument. Section 6.4.6 finally summarizes the measurements taken and shows some exemplary first results. Because of the importance of the data, we will continue to process the data beyond the end of the VIERS-1 project with funds provided by the Office of Naval Research within the SAXON-FPN project.

6.4.2 Review of imaging wave measuring techniques

In this section, a brief review of imaging wave measuring techniques is given. It is the purpose of this review to provide some background of the technique chosen to be developed

within the VIERS-1 project. Basically three principles can be used to take images from short wind waves:

- stereo
- light reflection
- light refraction.

While stereo measurements yield the *height* of the waves, the latter two techniques measure the *slope* of the waves. In terms of modern computer vision these techniques can be regarded as *shape from shading* techniques [54,55].

6.4.2.1 Stereo photography

Stereo photography is the oldest technique to take two-dimensional spatial measurements of wind waves and has been used by a number of investigators over nearly one century [8,17,29,40,42,43,71,83,90,93,94,95102,103,110]. Despite many efforts only a few images have been analyzed manually; furthermore none of the previous techniques could resolve the short waves, which are of interest for C-Band and higher frequency radar scatterometry (X, K, W bands). Careful analysis [56] showed that for several reasons it will never be possible to resolve the shortest wind waves with conventional stereo techniques. There are three major problems, two of them are of principal nature, the third one of practical nature.

- Insufficient height resolution.
  The height resolution is basically determined by the ratio of the stereo base a to distance from the water surface Z. Even with a large a/Z, the height resolution will not exceed the horizontal resolution. The height of a wave depends on the wavelength and wave slope. Even a wave with a medium steepness of 0.1 will have a crest/trough height of only 0.03 wavelengths. Consequently, even under most favorable conditions, only the height of waves with wavelength larger than several tens of pixels can be resolved. Thus stereo video images with a typical resolution of 512 x 512 pixels cover at most one decade of wave numbers. It is hardly possible to resolve waves with wavelengths smaller than 6 cm just because of these simple geometric facts.
- Correspondence problem.
  More complex problems arise from the fact that the water surface is not a diffusive but a specular reflecting surface. An ideal *diffusive* surface element reflects the incoming light into all directions with equal brightness (Lambertian law). Thus this surface element can be seen from any spatial position, for example from two cameras at different spatial locations, with equal brightness; the brightness depends only on the angle between the light sources and the surface normal and not on the camera direction. However, the water surface is a *specular* reflector. In this case, the light received by two cameras with different orientation in space comes from different directions, depending on the reflection law. Therefore, facets in the stereo images are not equally bright, except for an entirely uniform illumination. Even then, the strong nonlinearity of the reflection coefficient with the angle of reflection, hardly changing for low angles of incidence, makes the detection of a wide range of surface slopes all but impossible and easily biased by small inhomogeneities in the illumination.
- Dependence on natural light conditions.
  Use of natural light effectively limits the use of the instrument. It can be used only in the rare cases when the illumination is sufficiently homogeneous. No measurements are possible during night.

6.4.2.2 Stilwell photography

In contrast to the stereo technique, Stilwell photography [96] measures the slope of waves. Except for resolution restriction, however, this technique is subject to the same problems as stereo photography [56]. A homogeneous sky illumination is required, the relation between wave slope and brightness is highly nonlinear, only a rather limited range of slopes and only one slope component of the waves can be measured. Because of all these difficulties, it is not surprising that over more than 20 years, almost no successful wave measurements have been reported in the literature.

6.4.2.3 Scanning laser slope gauges

Recently, scanning laser slope gauges are evolving from laser slope gauges [46,47]. Although such an instrument allows an accurate measurement of wave slope it has several disadvantages for use in the field. First, the spatial resolution of the instrument is rather limited as compared to instruments with an imaging device. Secondly, the delicate instrument has to be placed on a floating platform which disturbs the flows in air and water and thus possibly biases the measurements of short wind waves. Third, because of the limited distance between the water surface and the optical receiver, the instrument can only be used up to moderate wind speeds.

6.4.2.4 Refraction-based wave slope measurements

This type of instrument is based on refraction as laser slope gauges are. It has delivered the most detailed and accurate area-extended wave slope measurements so far. It has extensively been used in the Delft wind/wave facility within VIERS-1 project. Results from two-dimensional wave number spectra have been reported in [50,59]. Unfortunately, it is very difficult to use this technique in the field because of the bulky submerged light source needed for the operation of this instrument.

6.4.3 Principle of combined slope/height measurement

The discussion in the previous section showed that none of the available techniques is really suitable for field measurements of short wind waves. Consequently, a new type of instrument which combines height and slope measurements in an innovative way was designed within the VIERS-1 project according to the following design goals:

- Compact and rugged sensor head to be mounted on a boom extruding from a platform with no parts submerged in the water. It should be possible to operate the instrument also under rough sea conditions.
- Artificial light source to ensure continuous operation of the instrument independent of daylight and to provide a precise stereo correspondence.
- Recording of image sequences to study the spatio-temporal characteristics of wind waves including long wave/short wave interaction.

We decided to base the new system on light reflection since no part should be submerged in the water. It is obvious that such a technique cannot give a continuous spatial measurement of either wave slope and height but only statistical measurements. By simultaneous measurements of slope and height, however, the new instrument (RSSG) delivers a detailed insight into the properties of short wind waves. Essentially, the RSSG can be regarded as an extension of the classic work of Cox and Munk [18,19] who used sun glitter images to measure the two-dimensional slope distribution.

Instead of the sun, an artificial illumination source, placed close to the cameras and looking straight down onto the water surface, has been used. The system, consisting of two synchronized CCD cameras, takes stereo images from the specular reflections from the same sector of the water surface. In this way *combined slope/height* measurements are obtained.

With a single point light source close to the cameras, a specular reflection is only observed if the normal of the facet at the water surface points into the bisector of the camera. This condition can be met only for one camera. Thus two cameras located at different spatial positions would see different specular reflexes and a height determination would not be possible since no corresponding points exist in the right and left stereo image. The problem of different reflexes in the two images can be overcome if a special arrangement with *two* light sources is used as shown in figure 6-12. By the use of polarization filters one camera receives light only from the corresponding light source. Figure 6-13 shows some typical stereo image pairs. The reflexes in both images are the same. Thus an accurate stereo correspondence is obtained. This special illumination setup is a significant advantage over all previous stereo instruments.

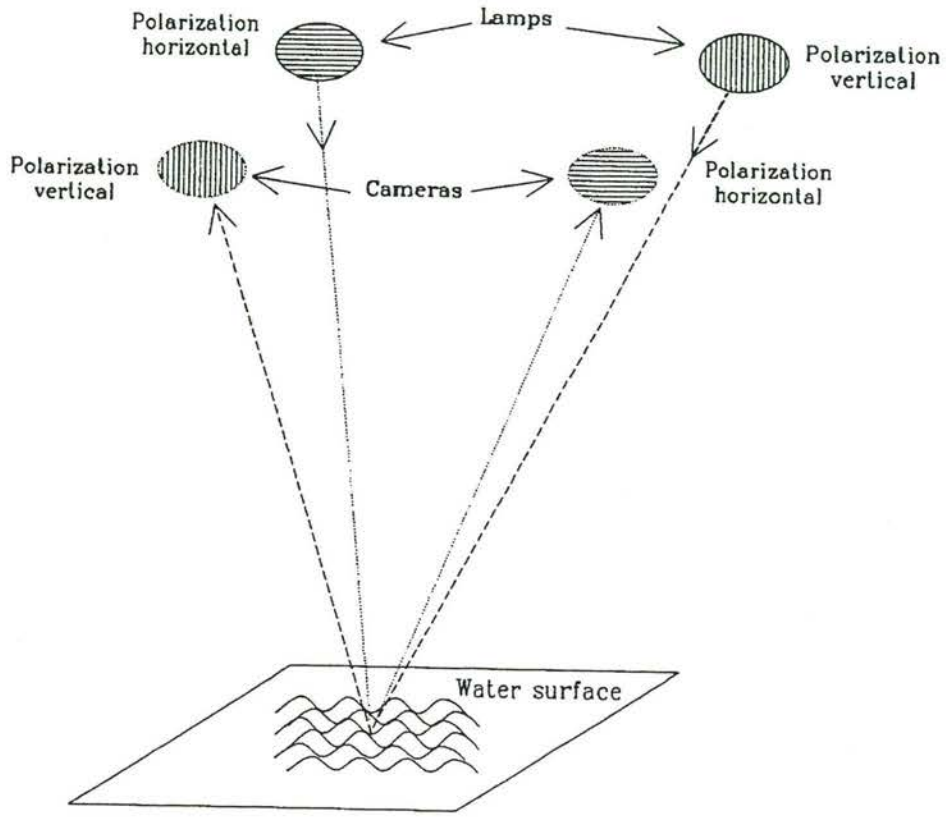

Figure 6-12 Illustration of the principle of the RSSG in top view

Because of the more precise stereo correspondence, we chose a rather small stereo base of only 30 cm at a distance of 5 m to the water surface which led to a compact and rugged sensor head. We also used a telelens in order to take images of a small sector of the water surface with high resolution. Thus with a system looking straight down, the reflexes reveal two pieces of information. They mark the positions at the water surface with slope zero. From the stereo evaluation, we also obtain their height.

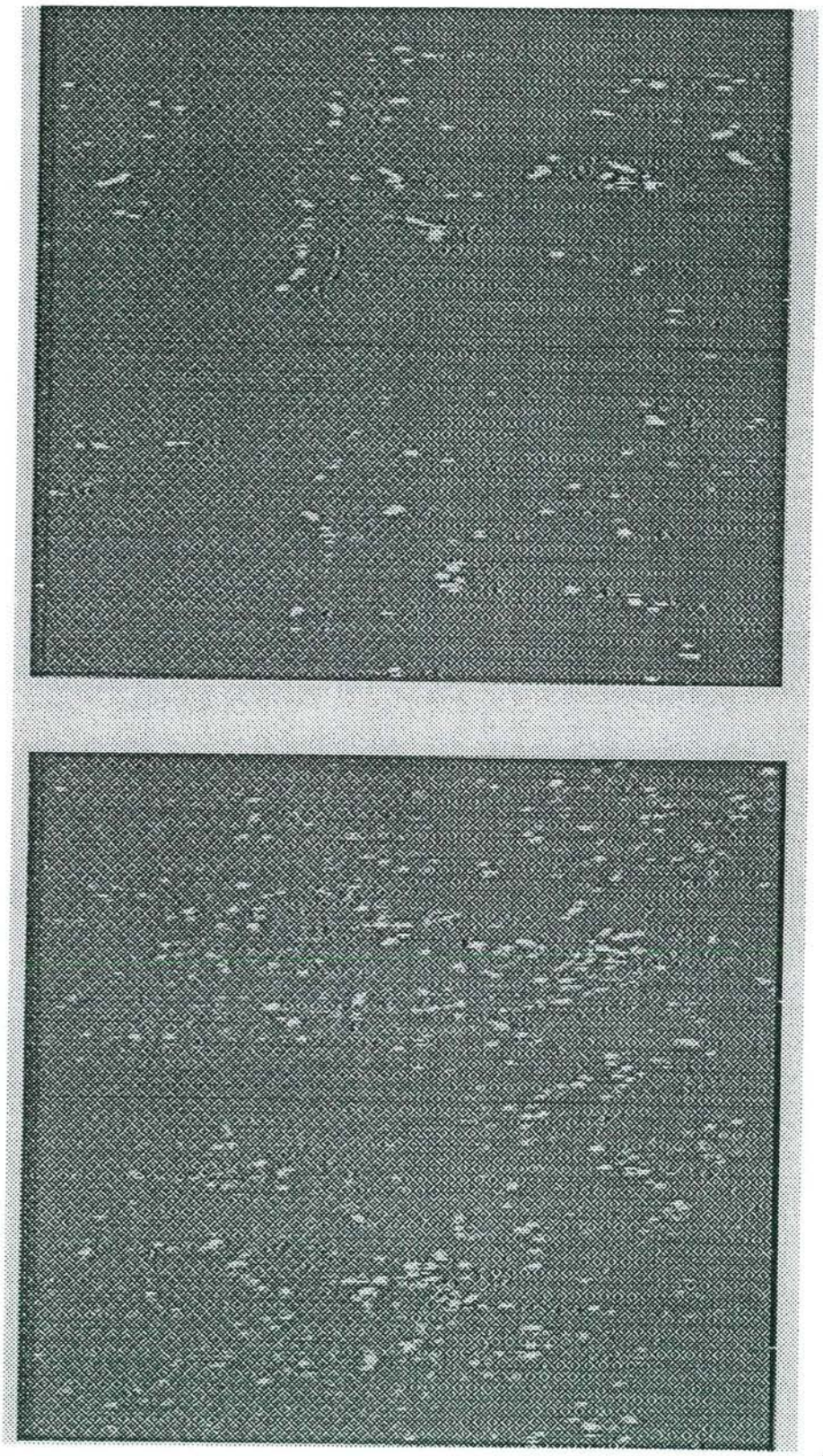

Figure 6-13 Examples of RSSG images; the image sector is 27x36cm^2; wind speeds 2.4 m/s (top) and 6.4 m/s (bottom). The top half of each image represents the first field, the bottom half the second field (time difference 17 ms); bright reflexes correspond to the left image, gray ones to the right image

6.4.4 Experimental setup

The technical details of the setup of the RSSG are outlined in figure 6-14. The two CCD-cameras and the light source, a 300 Watt Xe arc lamp are placed in a compact box of about 1 m x 0.25 m x 0.2 m. A stereo base length of 30 cm was chosen. The cameras are equipped with a remotely controlled electronic shutter (1/60s to 0.1ms) and diaphragm. In order to suppress upwelling radiation, the RSSG operates in the near infrared in a wavelength range between 840 and 1000 nm which is strongly absorbed by water (penetration depth for radiation between 800 to 1000 nm: 40-2.5cm [21]). The surface elevation below the cameras was sensed by an ultra-sonic distance meter which sampled the water height every 1/7s. Although this is only a rough height estimate, it is a useful cross-check of the stereo height measurements.

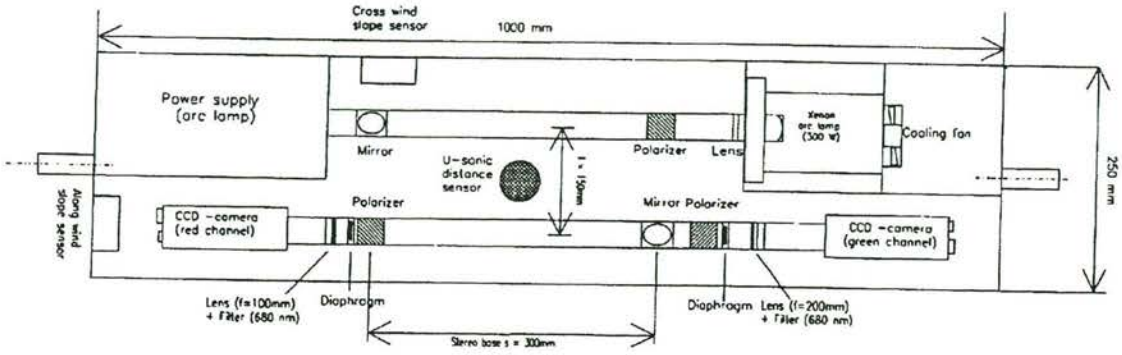

Figure 6-14 Sketch of the RSSG in top view

Table 6-5 Characteristics of the RSSG as used at the Scripps pier and MPN

Height above mean water level	H	5 m
Stereo base(s)	s	0.3 m
Distance lamp - camera	d	0.15 m
Diameter lamp	d_{lamp}	25 mm
Base/height ratio	s/H	0.067
Video cameras		Pulnix TM740
Image size		6.6 mm x 8.8 mm
Focal length	f	100 mm
Depth of focus	Δg	±1 m
Resolution (height)		2 - 4 mm
Range of angle (one image) (tilt of instrument)	ϕ	±2.56/1.89° ≈ ±30/30°
Observed area on water surface		0.36 x 0.27 m^2

Table 6-5 summarizes the characteristics of the RSSG as it was operated at the Scripps pier and the Noordwijk Research Platform (MPN). In order to record long time sequences the stereo images are recorded analogously on a real time laser video recorder (Sony LVR 5000). This WORM (write once, read multiple) device allows high quality recording of component color images (RGB); the red and green channel are used for the stereo images. Each side of an optical disk holds about 40000 stereo images, corresponding to 24 min. of continuous recording or about 20 GByte of digitized stereo image data. Recording and playback of the LVR 5000 is computer controlled via a serial interface. Random access to any image on the disk takes at most 0.5 s and playback of still images does not involve any loss in quality. These features allow the recorder to be used as a huge and fast frame store memory for automatic processing of the stereo images.

6.4.5 Stereo image processing

A successful use of the RSSG entirely depends on a fast and automatic processing of the stereo images. The most difficult problem is the determination of the parallax between the two stereo images. While this task has been performed manually for most previous wave stereo instruments, we have developed an automatic algorithm using advanced techniques from computer vision. Although stereo image processing is generally a difficult task, the special illumination technique and the physical properties of the wave field facilitate the stereo processing considerably:

- The specular reflexes constitute small features on the water surface. Their position can be determined accurately. Therefore also the stereo parallax can be calculated precisely. Using sky light with a gradual change in intensity does not result in such features in the stereo images.
- Except for breaking waves occlusions do not occur.
- Except for breaking waves the height does not show any discontinuities over the whole image sector.

These conditions ensure an unambiguous correspondence between the features in both images. First, an algorithm which has been developed for orientation and motion analysis [51,52] was applied to stereo image processing. The algorithm is analogous to an eigenvalue analysis of the inertia tensor. The lack of depth discontinuities allow the use of a fast multigrid algorithm with a coarse-to-fine strategy. For this purpose, a Laplacian pyramid of the images is calculated. The processing starts in the smallest image (lowest resolution) and works towards the finest resolution. The only drawback of this algorithm is that it takes about one minute on an 40 MHz i860 to evaluate one 256 x 512 stereo image. The accuracy is well in the subpixel range.

Later, a faster algorithm has been developed which is based on a fast correspondence algorithm. The image is segmented and the individual reflexes are found by a fast label algorithm. Then a correlation technique is used to find corresponding reflexes in the two images. Since the correlation is restricted to the small fraction of the image sector covered by specular reflexes, the algorithm is about 10-100 times faster than a standard correlation algorithm covering the whole image sector. In the end, only about 10 s are needed to process one stereo image. The image processing algorithms are described in detail in [106].

Development of an appropriate stereo algorithm was tedious and time consuming and took basically the whole time of the VIERS-1 project. But in the end we believe that this approach was worthwhile since we are now able to process large numbers of stereo images.

Without all the effort in image processing we would have been able to process only a very small fraction of the images. Then no physical relevant data could have been extracted at all. Additional funds are available from the Office of Naval Research within the SAXON-FPN program. They ensure that the valuable wave image data of the VIERS-1 project can be processed beyond the end of the project.

6.4.6 Performed measurements and first results

Figure 6-13 shows two examples of stereo images taken with the RSSG. During the MPN experiment from November 16 to December 4, 1990 about 300,000 stereo images have been recorded. The images were taken simultaneously with the radar measurements of Delft University of Technology and the meteorological measurements of KNMI. Two types of recordings were performed:

1. Continuous records with 30 frames/sec. Such a recording was taken for 8 min. and includes 14,000 frames. Synchronization with radar is accurate within 1/60 s.
2. Statistical records with 1 frame/sec. over 25 min. (1500 frames).

As an example for the potential of the RSSG, the evaluation of a sequence of 1000 stereo images from the Scripps Pier is shown. Figure 6-15 shows the mean horizontal shift within the image sector for 500 images taken at a rate of 2 frames/s. The vertical shift (perpendicular to the stereo base) is constant within one pixel indicating that the stereo algorithm is very stable. The horizontal shift along the stereo basis is proportional to the mean height in the image sector. The time series shows the height variations due to the gravity waves.

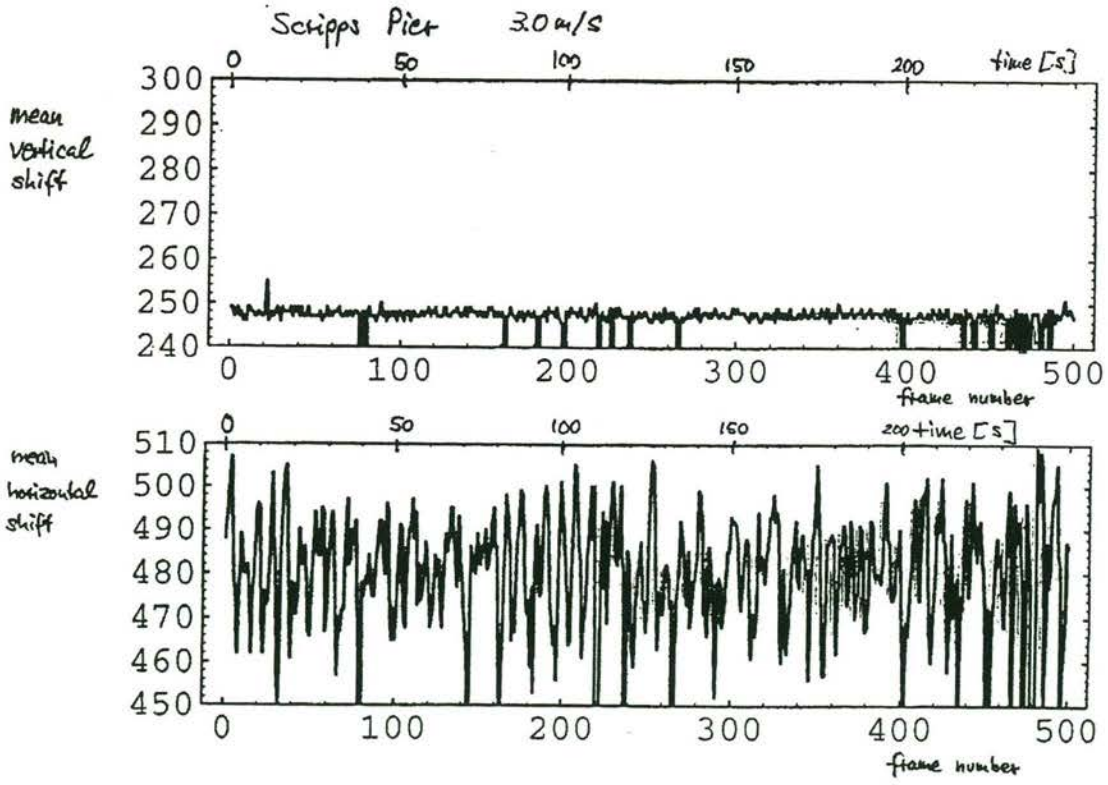

Figure 6-15 Mean vertical and horizontal shift between the stereo images (in bits modulo 512 and 256, respectively) for a time series of 500 stereo images taken at a rate of 2 frames/s. While the vertical shift is constant, the horizontal shift (along the stereo base) indicates the mean height in the image sector

Two possibilities to evaluate slope data are shown in figure 6-16 and figure 6-17.

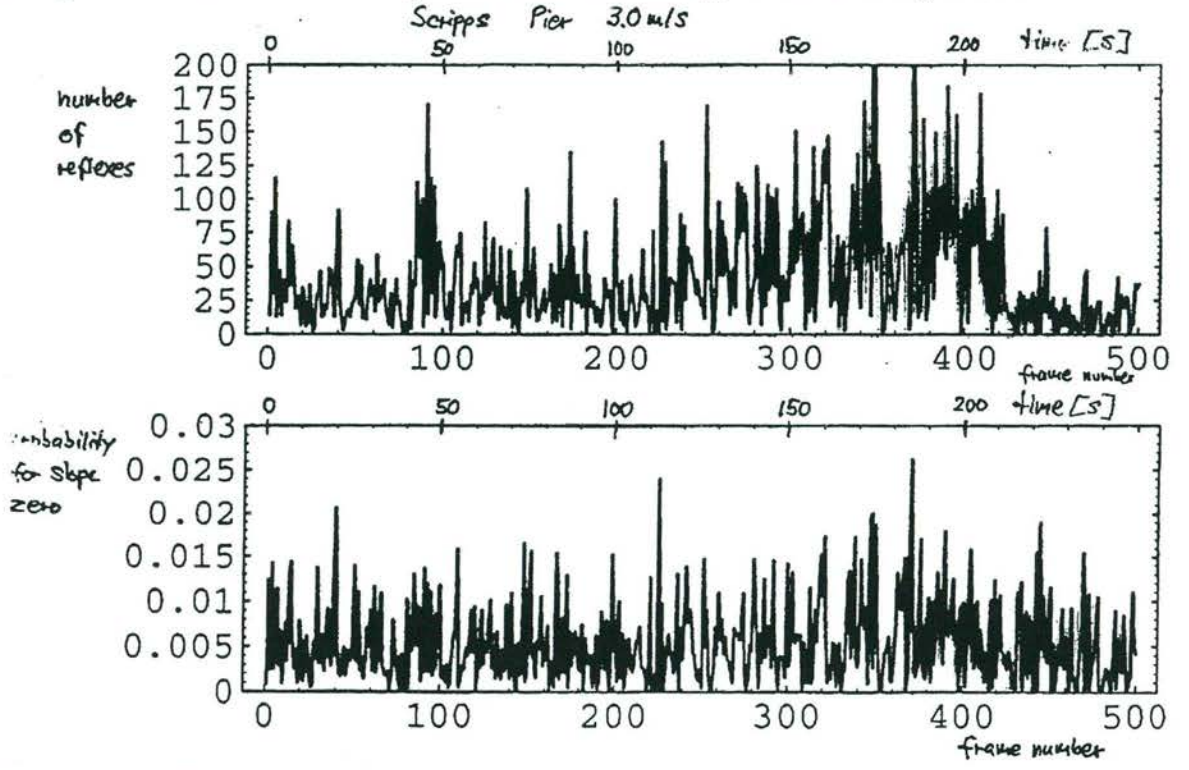

Figure 6-16 Evaluation of the specular reflexes in the stereo images; top: number of reflexes, bottom: probability for slope zero. A slick entered the image sector at about frame 420 causing a drastic reduction in the number of reflexes while the probability for slope zero is only slightly increasing. Continuation of the time series in figure 6-17.

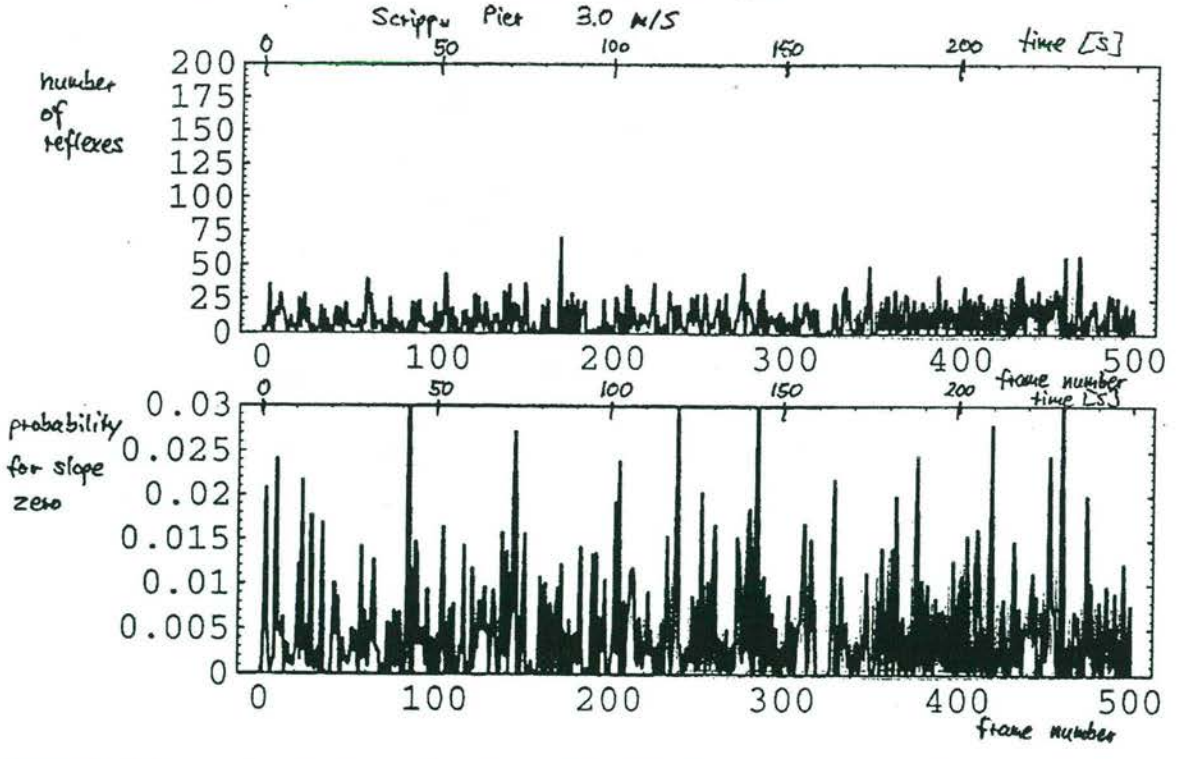

Figure 6-17 Continuation of figure 6-16 with 500 more stereo images

The top time series shows the total number of reflexes. This figure is a good measure for the spectral density of the smallest scale waves. The bottom time series shows the mean probability for slope zero. This quantity is inversely proportional to the mean square slope of the waves integrated over *all* wavelengths. Both quantities show large fluctuations in conjunction with the height of the gravity waves.

A striking event appeared at about frame 420 in figure 6-16. The number of reflexes is drastically reduced, while the probability of the mean square slope is only slightly decreased. This event is caused by a slick entering the image sector, significantly damping the capillary waves. The total mean square slope is only slightly effected, since the capillary waves account only for a small fraction (at most a couple of 10 %) of the wave slope at the low wind speeds encountered in this experiment.

Together with the test measurements at Scripps pier, the measurements cover a wide range of wind speeds from 0–15 m/s (Figures 6-18 and 6-19). A summary of all measurements performed at MPN is contained in figure 6-20. The figure indicates the wind speed, wind direction, and tide for all days at which the RSSG has been used. The shaded vertical bars indicate the measuring period.

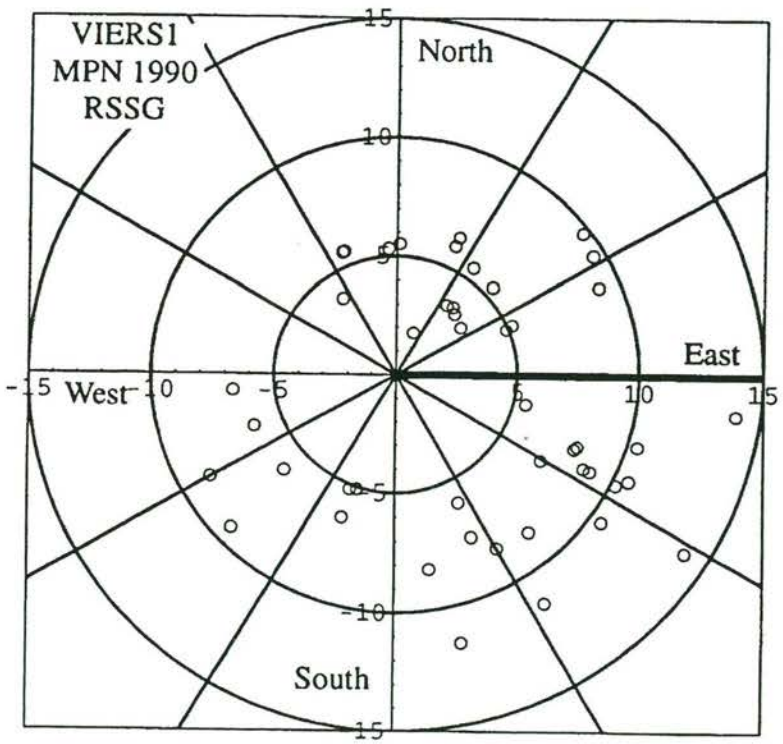

Figure 6-18 Statistics of the wind speed and direction for the measurements at Meetpost Noordwijk. The black bar indicates the boom direction.

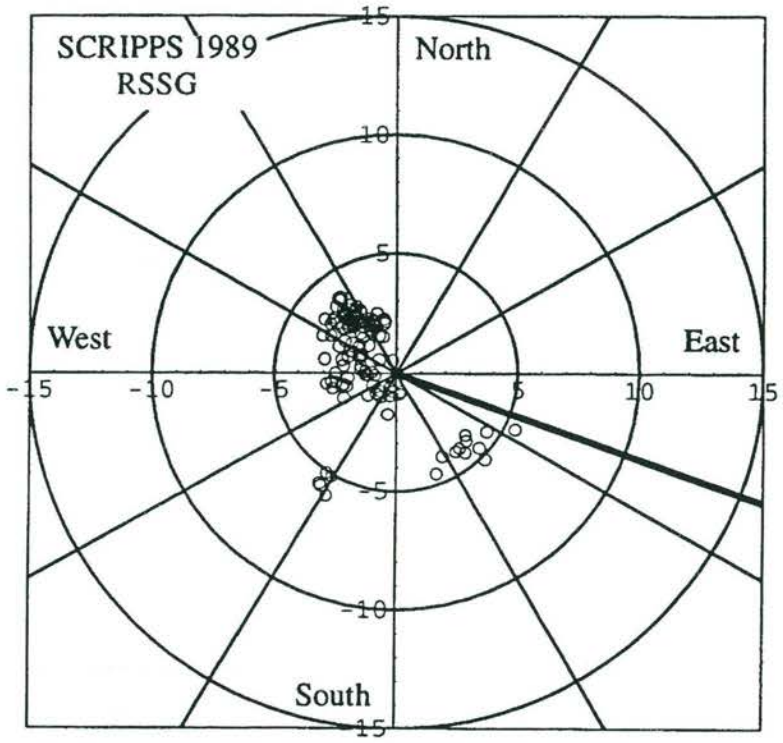

Figure 6-19 Statistics of the wind speed and direction for the measurements at the Scripps Pier 1989. The black bar indicates the pier direction.

6.4.7 Conclusions

Concerning measurements of short wind waves, two significant advances could be achieved during the VIERS-1 project. First, the first simultaneous measurements of radar backscatter and 2D wind-wave measurements were performed in the large Delft wind wave facility. These comparative measurements were the basis for the VIERS-1 radar backscatter model. Secondly, a new instrument, the RSSG, could be developed, tested, and used to perform measurements of properties of short wind waves in the field. Equally important, we could succeed in developing the necessary image processing algorithms to extract the physically important information from the huge amount of image data. Although routine data analysis has not started so far, we can regard the wave measurements of the VIERS-1 project as a full success. After several decades of various and largely unsuccessful attempts to measure the fine-scale structure of the ocean surface, finally reliable optical techniques are coming along both for laboratory and field measurements. Data evaluation will be continued after the end of the VIERS-1 project and further papers will be published.

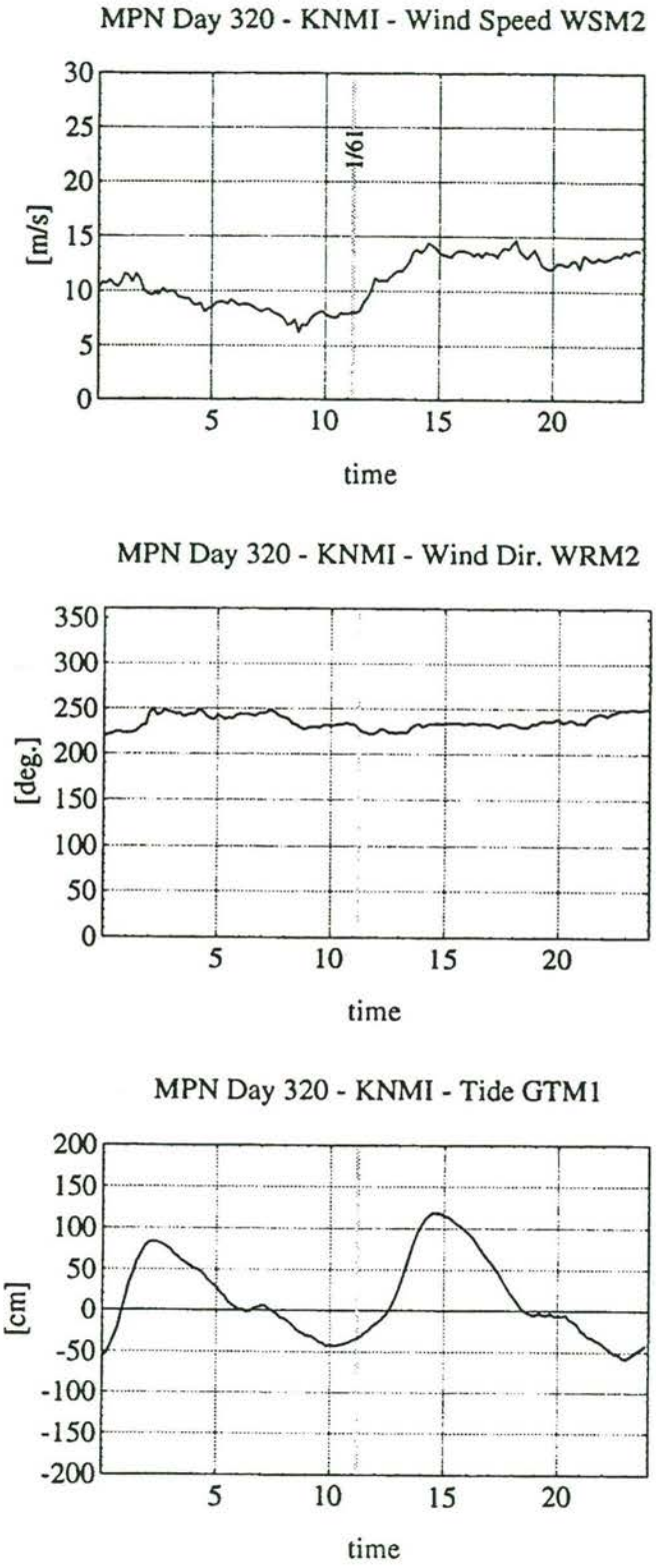

Figure 6-20 **Summary of the measurements performed from November 16 to December 4 at the Noordwijk research platform. The graphs indicate the following data for each measuring day: wind speed, wind direction, tide, and (with shaded vertical bars) the times at which measurements have been obtained.**

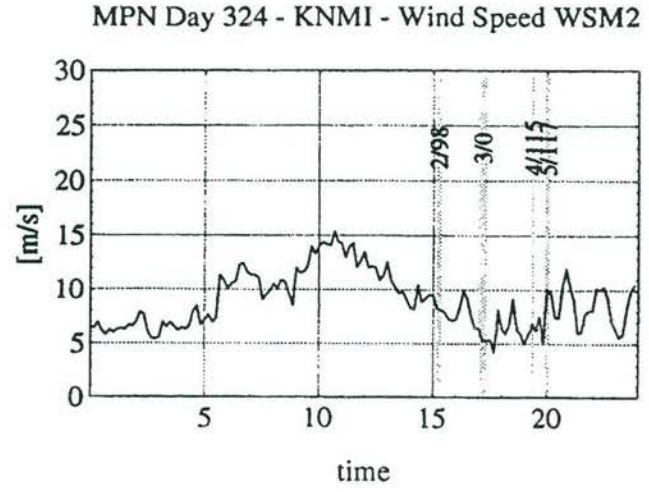

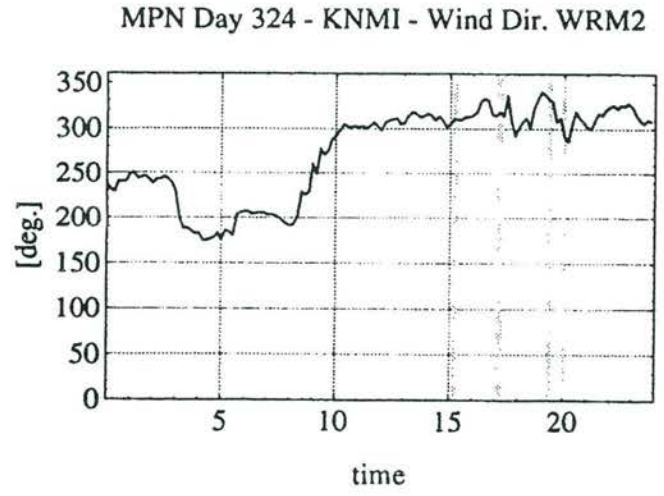

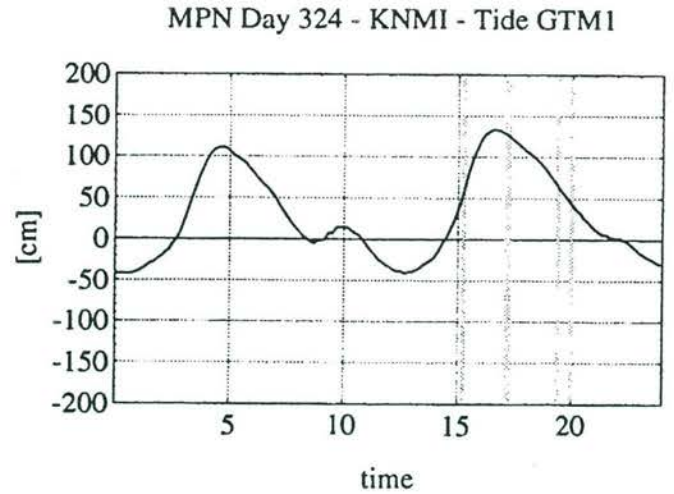

Figure 6-20 continued

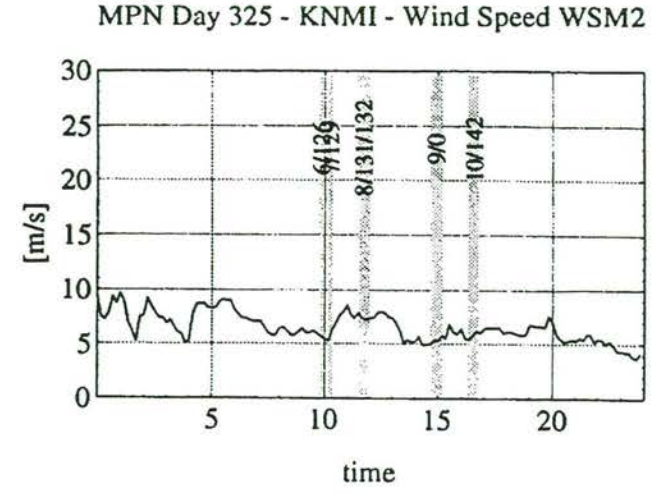

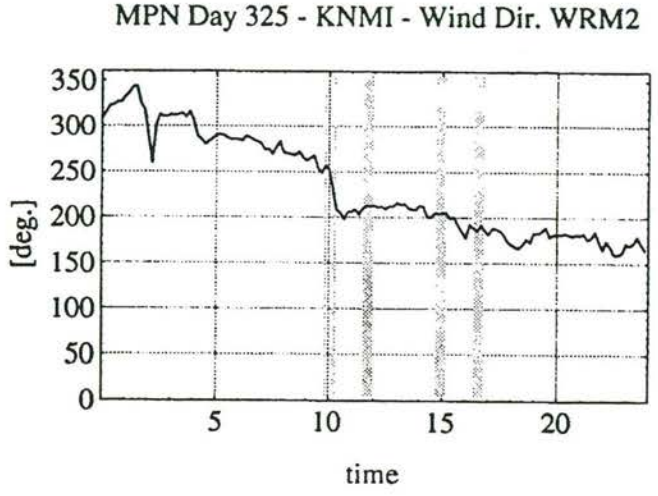

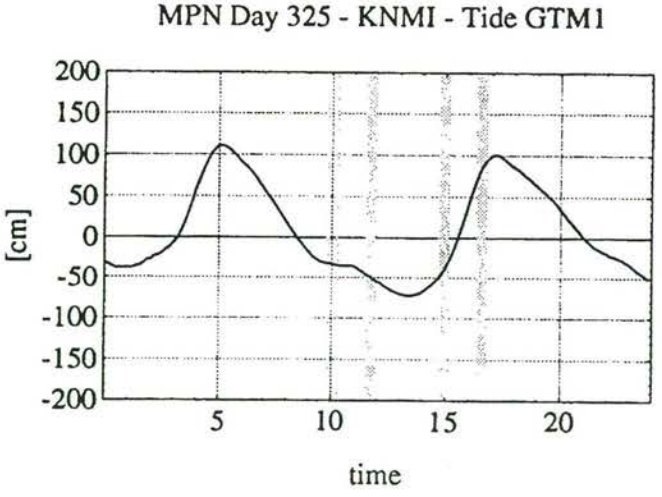

Figure 6-20 continued

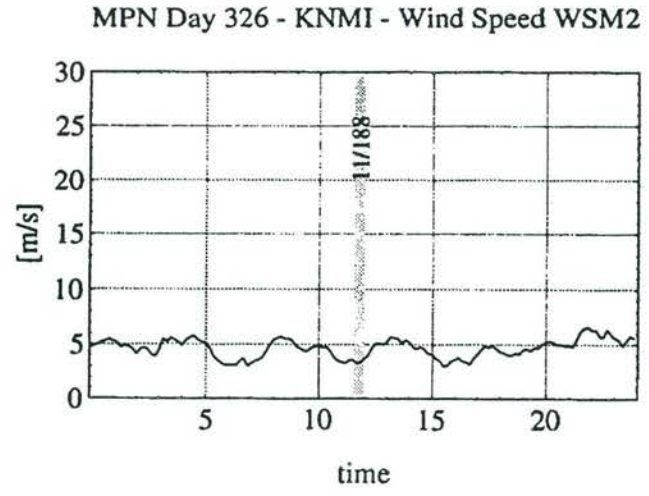

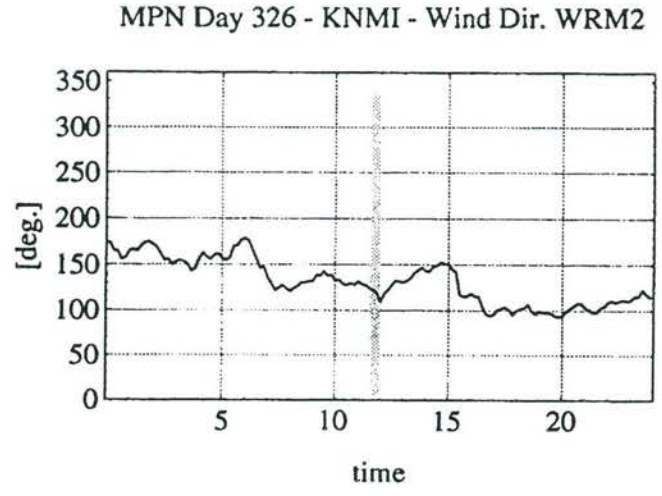

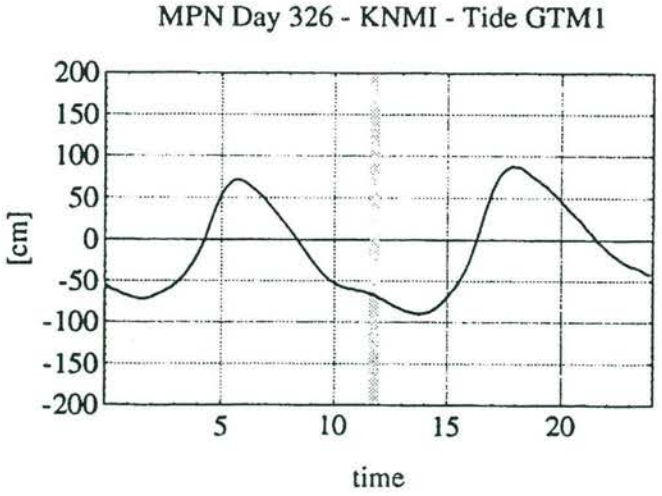

Figure 6-20 continued

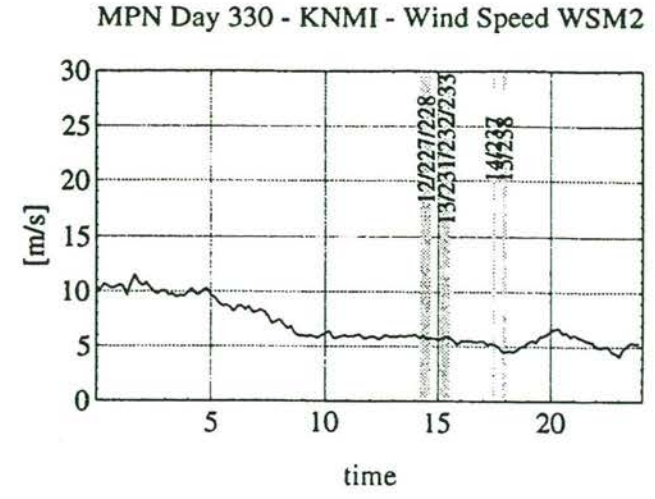

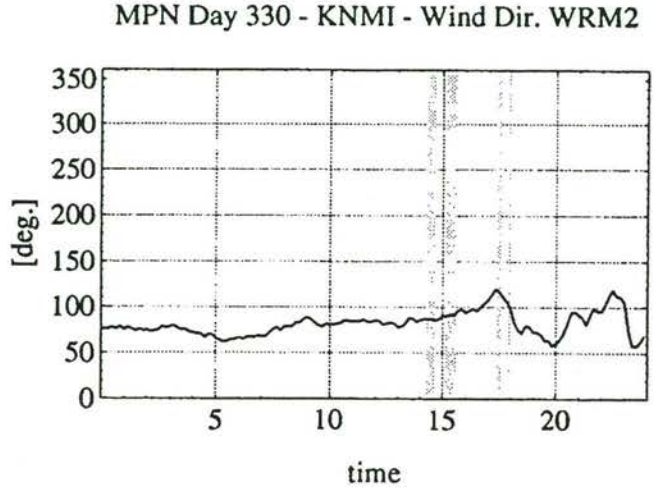

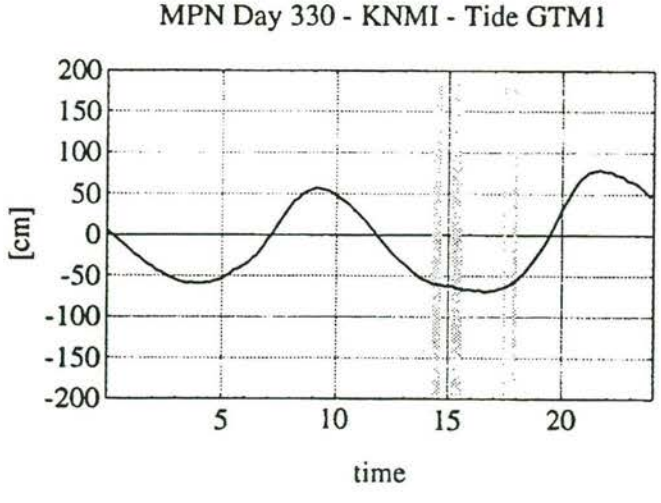

Figure 6-20 continued

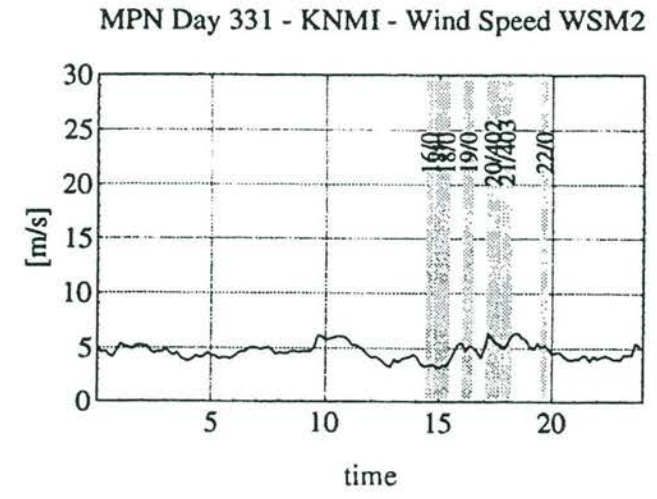

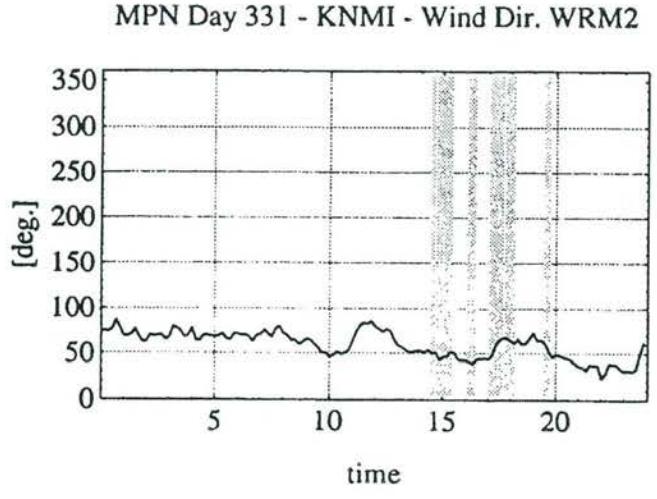

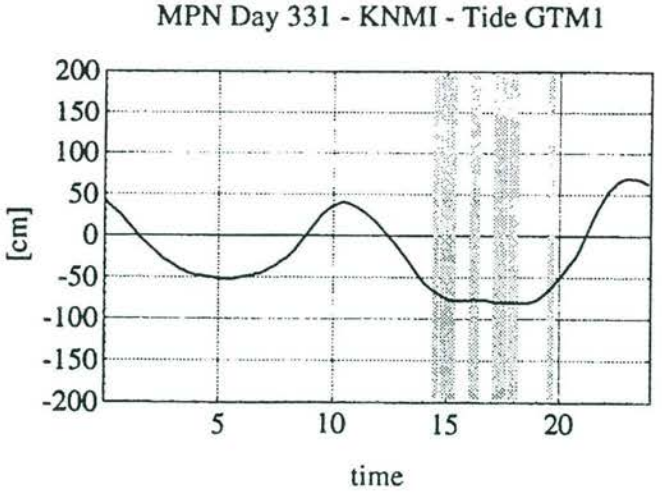

Figure 6-20 continued

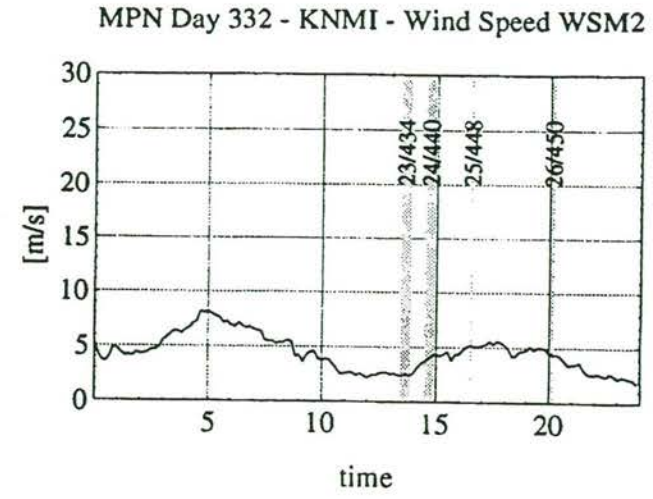

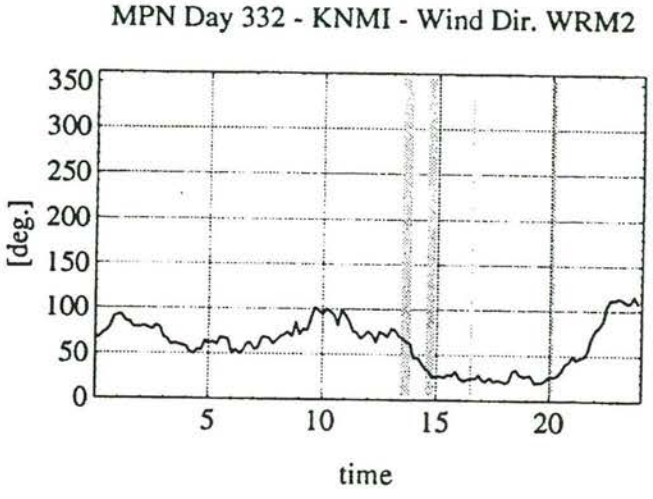

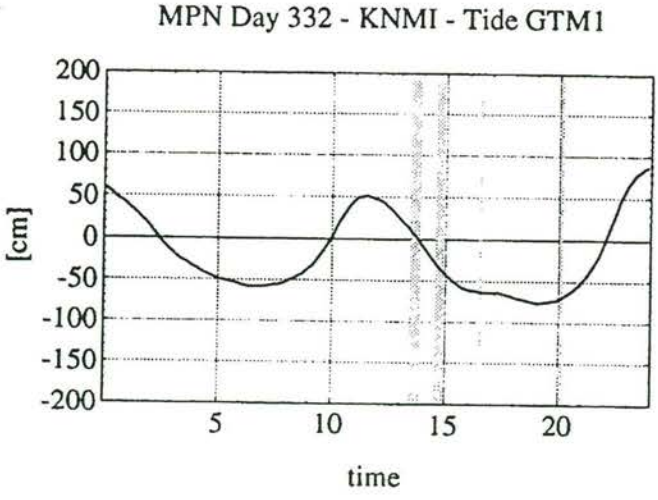

Figure 6-20 continued

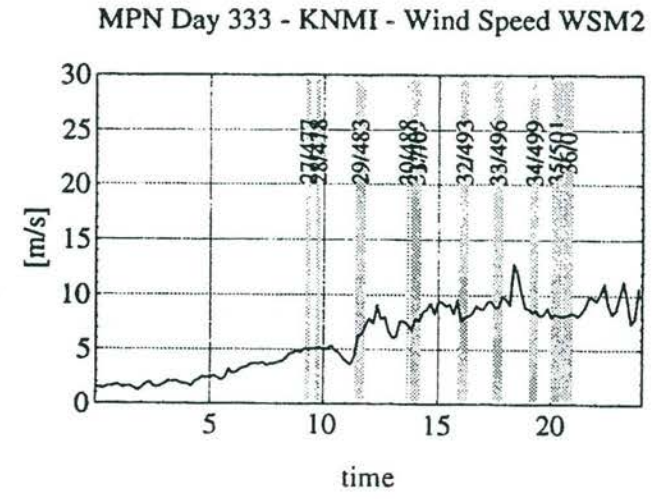

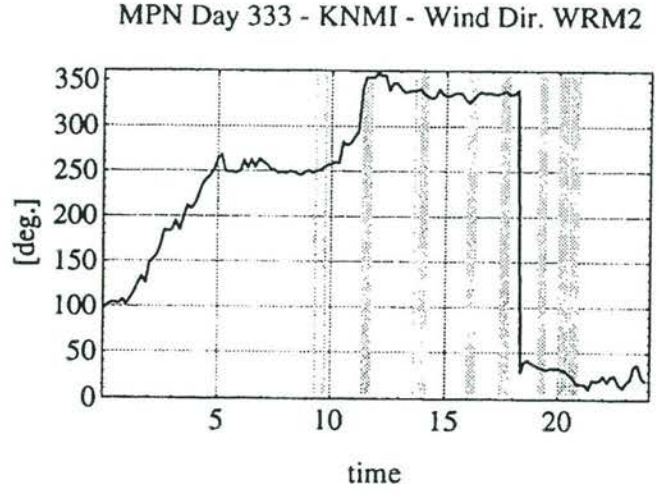

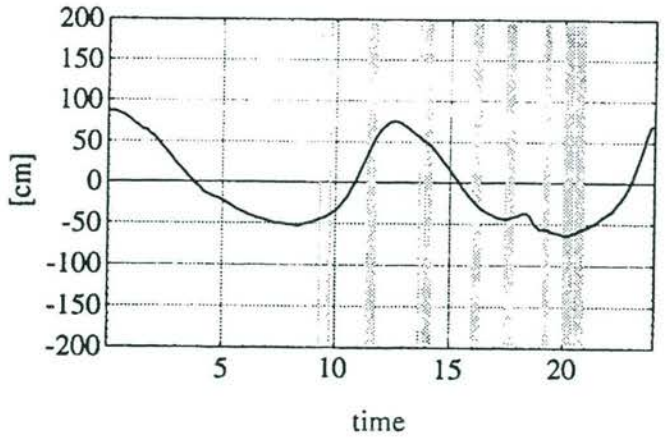

Figure 6-20 continued

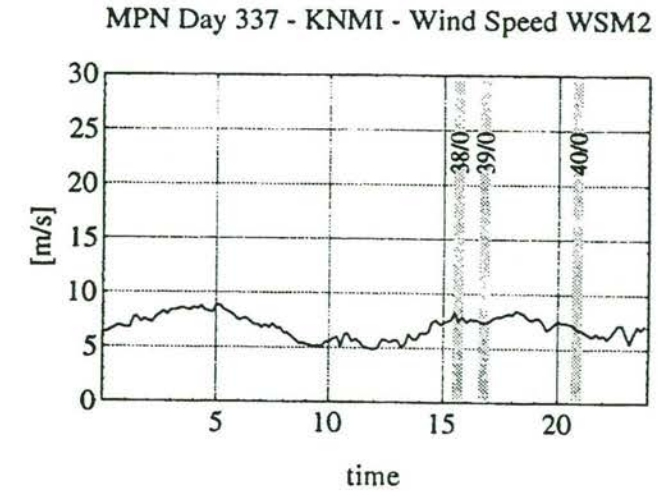

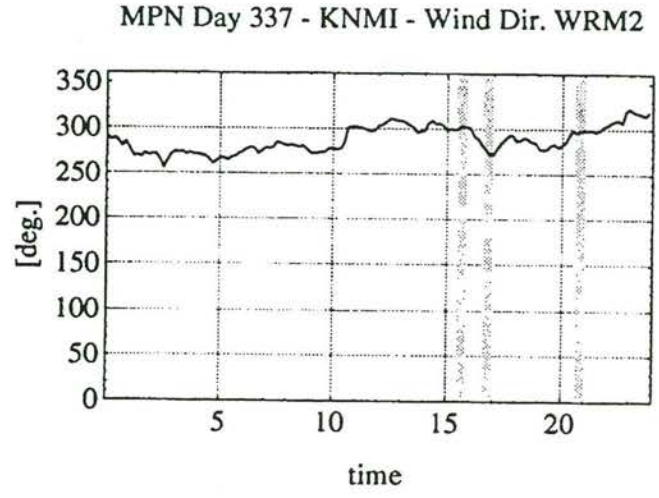

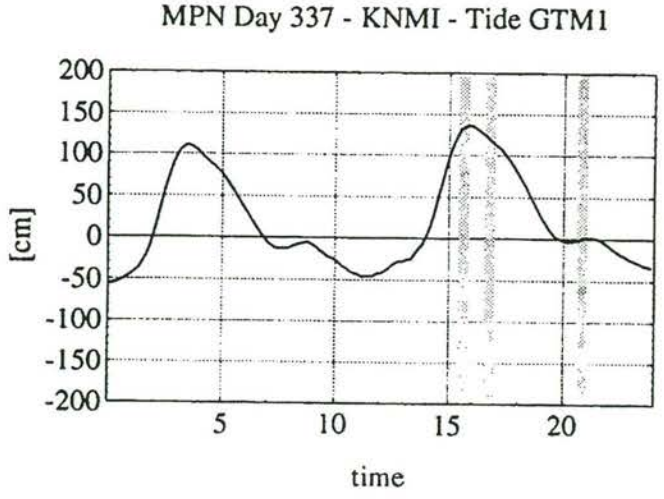

Figure 6-20 continued

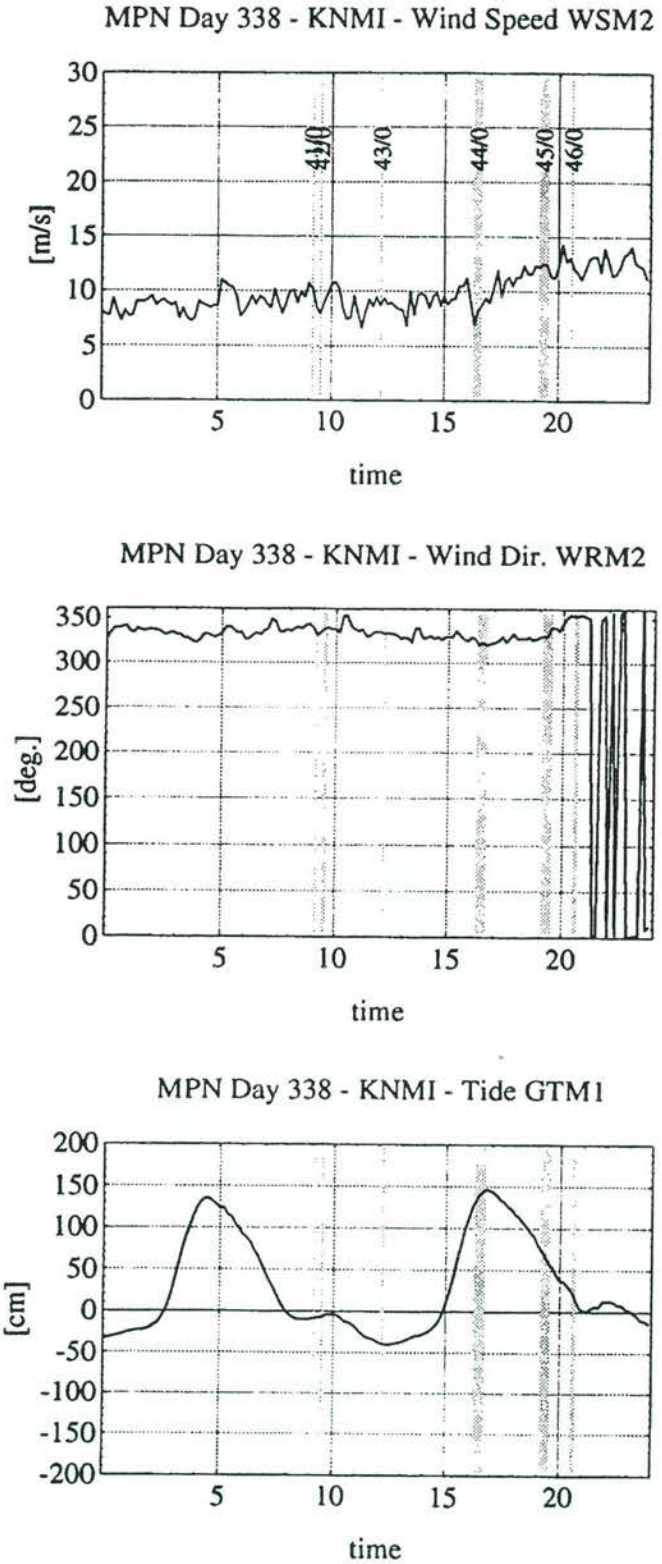

Figure 6-20 continued

6.5 The VIERS-1 microwave data

6.5.1 Outline of the X-band scatterometer

In all the experiments the microwave backscatter measurements were performed with an FM-CW X-band scatterometer. In the Delft wind/wave tank experiment one parabolic reflector antenna was used for both transmitter and receiver, while in the Delta tank experiment separate parabolic reflector antenna's for transmitting and receiving were used. For the platform experiment major changes were incorporated in the radar hardware to improve stability and sensitivity; also the antenna's were replaced by dielectric lens type antenna's. Figure 6-21 shows the VIERS-scatterometer mounted on a measuring deck of MPN.

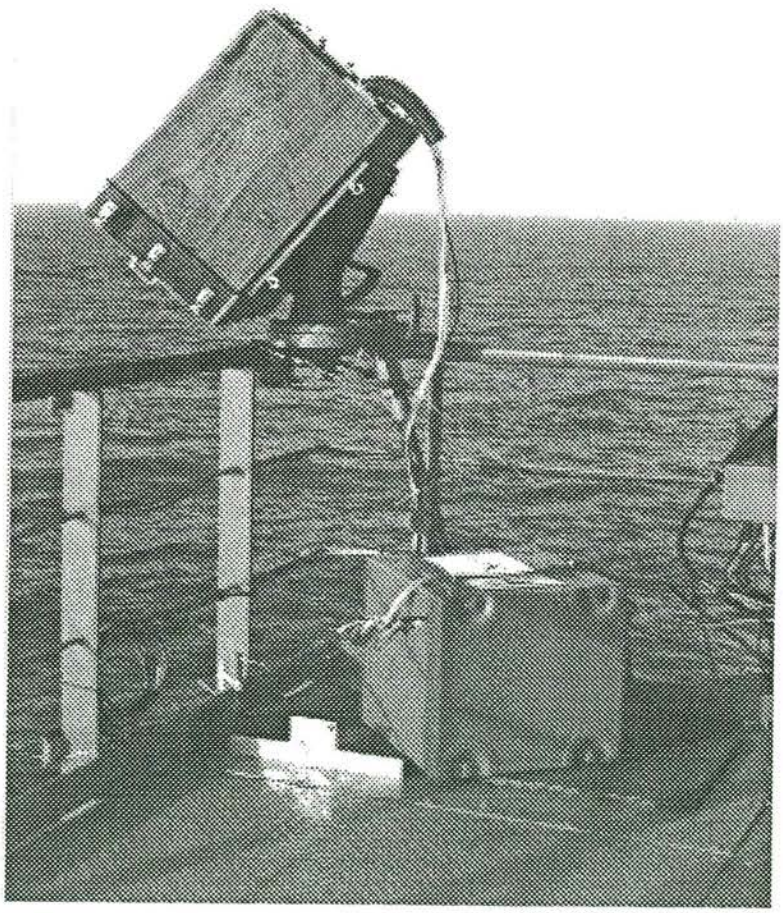

Figure 6-21 The FM-CW X-band scatterometer at MPN

A simplified block diagram of the VIERS-scatterometer is presented in figure 6-22.

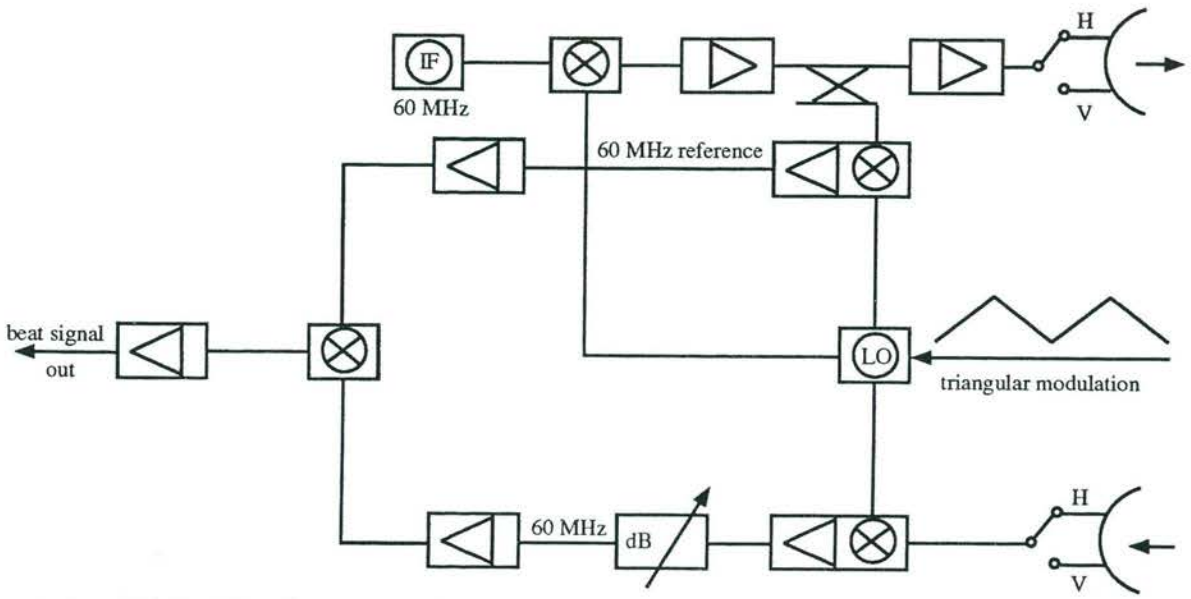

Figure 6-22 Block diagram of the MPN-VIERS scatterometer

Some characteristics of this system are listed in table 6-6.

Table 6-6 Specifications of the X-band FM/CW scatterometer

Radar type	FM/CW
Frequency	9.6 GHz
Modulation	50 Hz triangular, 100 MHz sweep
Polarization	HH, HV, VH and VV
Range resolution	1.5 m
Antenna	dielectric lens
Azimuth angle	210° - 90° with respect to the North
Angle of incidence	30° - 90°

The system uses a stable IF and a YIG tuned LO source to generate the signals needed by the transmitter and receiver. The output of the LO source is mixed with the output of the IF source to produce the RF signal. The RF signal is amplified in the output stage by a solid-state medium-power amplifier to produce an average output of 1 Watt.

The output of the receiving antenna is directly connected to the mixer RF port. The output of the receiver mixer is fed into the IF section. The IF section uses an attenuator-amplifier pair to bring the received signals in the dynamic range of the detector. The frequency difference between the two oscillators is kept constant by an automatic frequency control system. To eliminate amplitude variations of the reference signal both 60 MHz-channels are provided with an automatic gain control (not shown in figure 6-22). Finally the beat signal is

found at the output of the IF mixer.

All control functions e.g. the choice of polarization states, and the setting of the attenuator to bring the received signals into the dynamic range of the detector, are performed by a PC. Also the digital chirp generation, data acquisition and synchronization with other equipment are done by means of the PC.

During a flank of the triangular modulation, the beat frequency was digitized using 12 bits to produce 64 samples per flank , which was increased to 128 samples per flank for detailed measurements. The raw data was stored on disk and after the measurement transferred to an optical disk. The analog beat signal was also recorded on a DAT recorder.

During a measurement day the scatterometer was calibrated several times. For this calibration a Luneberg lens with a radar cross section of 10 m^2 was mounted an a boom outside the tower (figure 6-23).

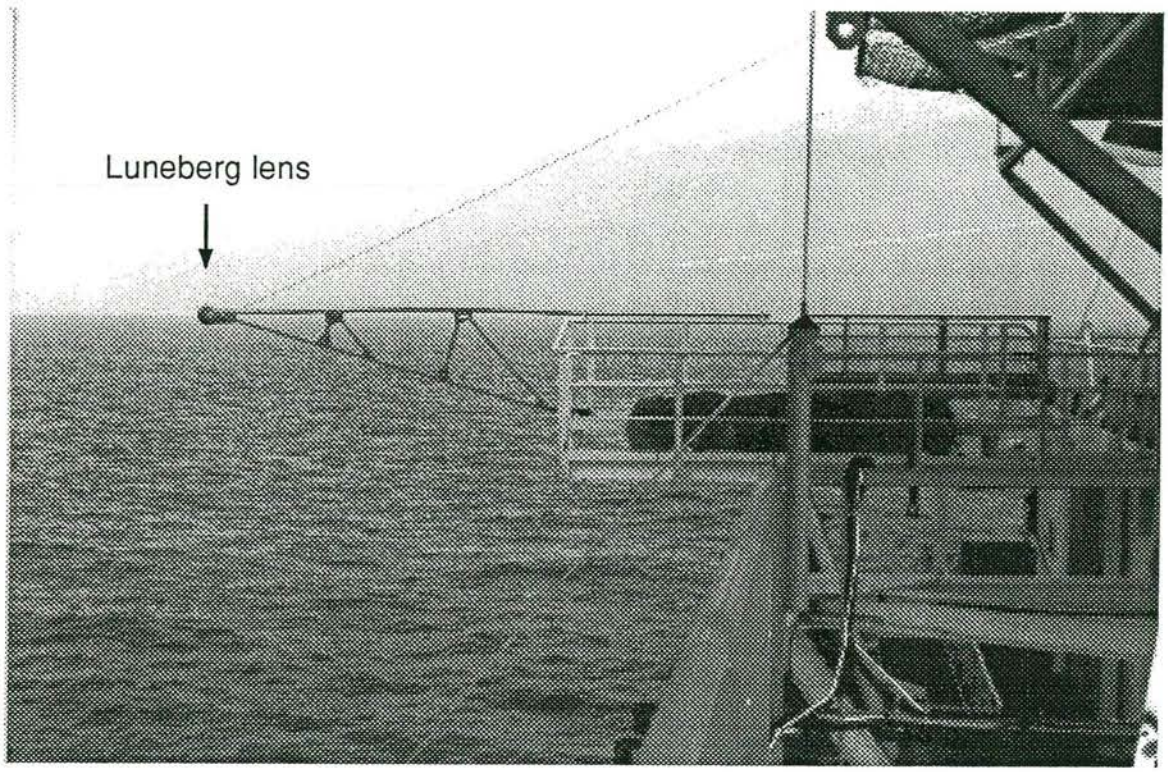

Figure 6-23 X-band scatterometer calibration setup at MPN

In figure 6-24 and figure 6-25 the results of the calibration measurements for HH- respectively VV-polarization are given. The vertical axis is the relative received power, while the horizontal axis represents the calibration sequence number. Two regions can be seen, on the left the calibration measurements made during the initial test phase are shown, while on the right the calibration results obtained during the actual campaign can be seen. Unreliable measurements due to heavy wind or rain conditions are indicated.

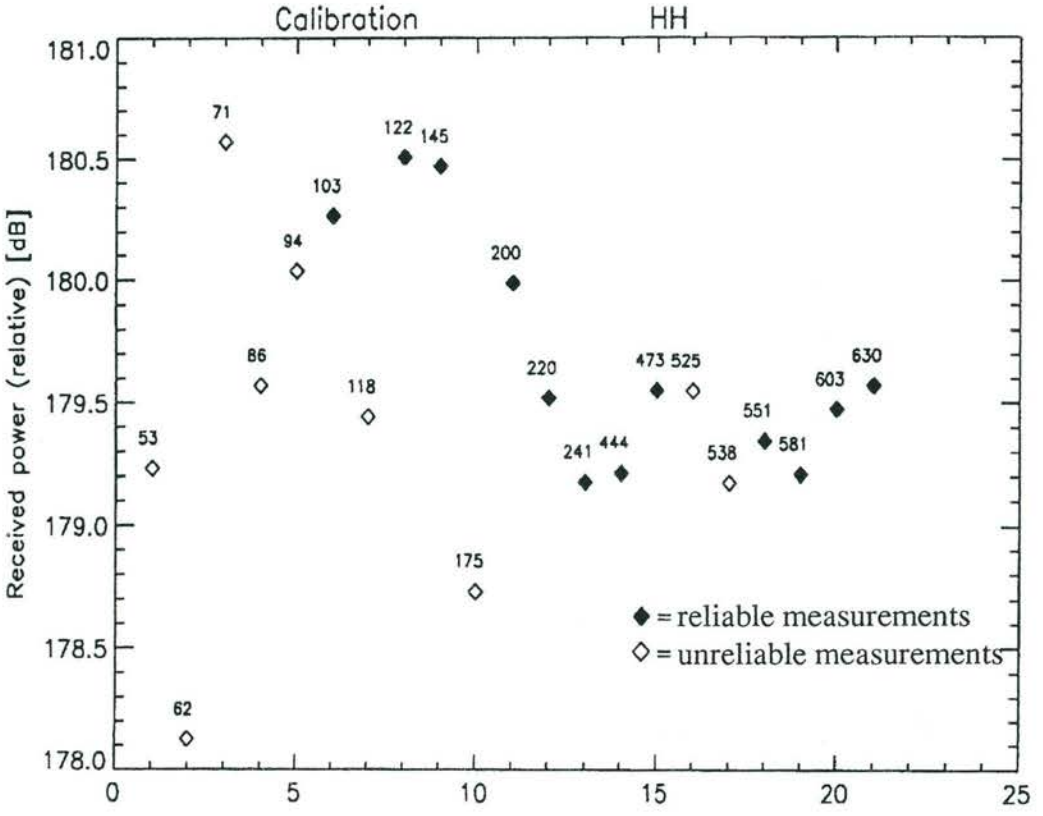

Figure 6-24 HH-polarization calibration results

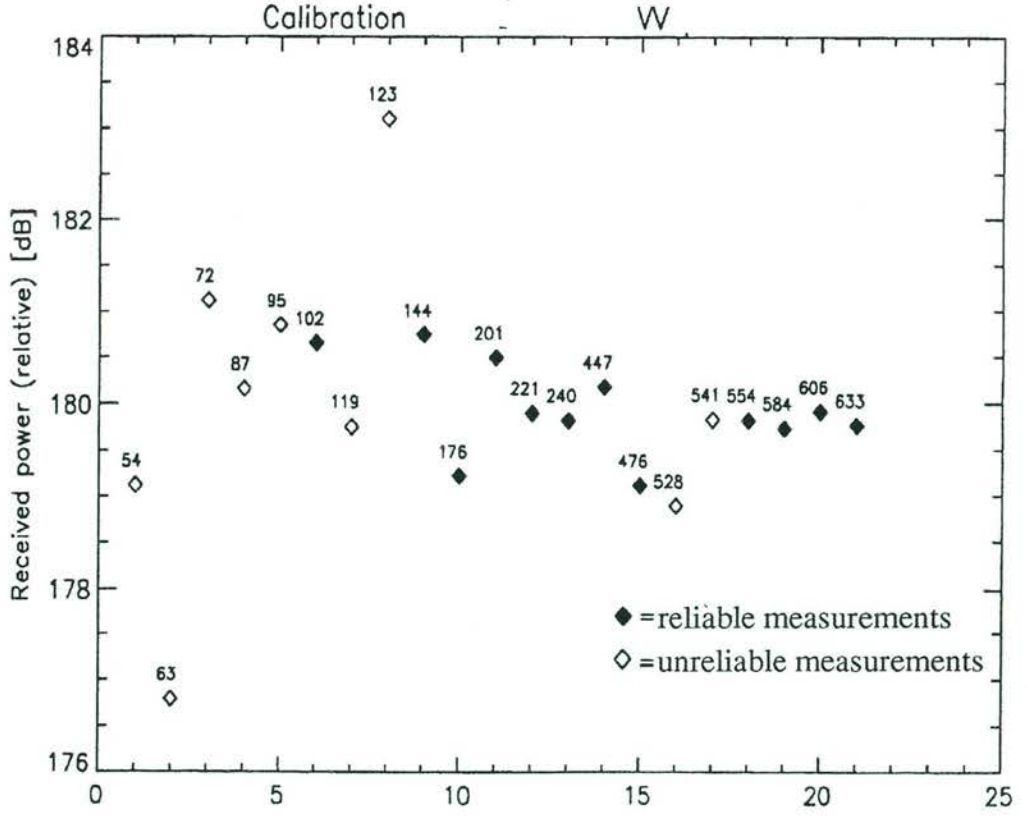

Figure 6-25 VV-polarization calibration results

The same calibrator was used to measure the combined antenna pattern of the scatterometer (figure 6-26 and figure 6-27).

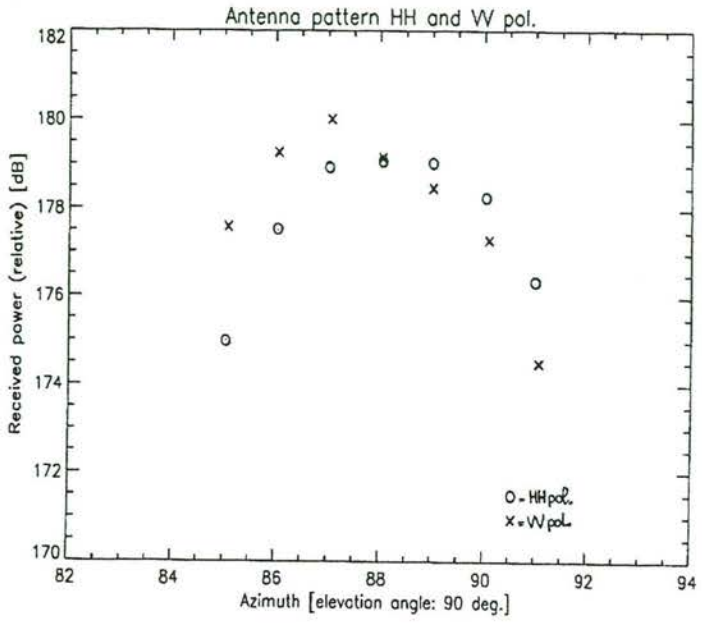

Figure 6-26 Measured azimuth patterns at MPN

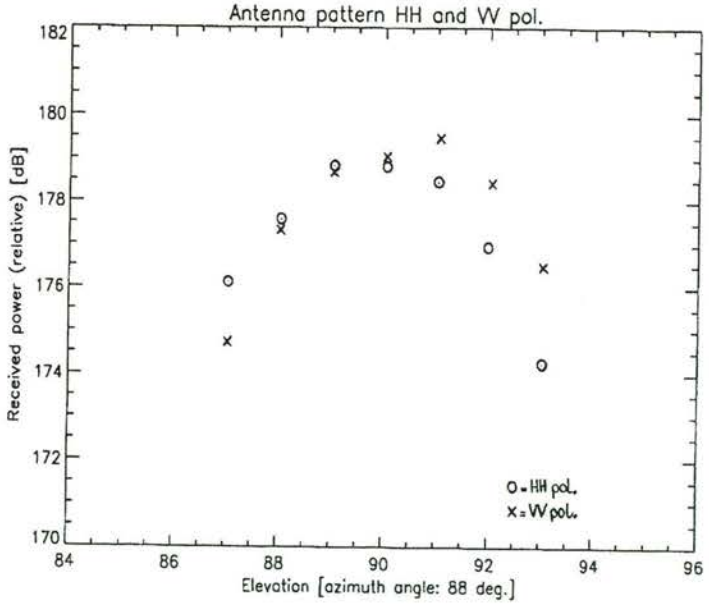

Figure 6-27 Measured elevation patterns at MPN

The antenna patterns were also separately measured outdoor on the roof of the building of the department of Electrical Engineering of the Delft University of Technology. Both types of measurements are in good agreement as is shown in table 6-7.

Table 6-7 Two way -3dB beamwidth (deg), outdoor versus MPN experiment

Polarization	Outdoor	MPN
HH	5.5	6.1
VV	5.3	5.9
HV	5.4	5.9
VH	5.5	6.0

6.5.2 Some results of the tower experiment

In the tower experiment measurements of the microwave backscatter have been performed, together and simultaneously with wind speed, wind direction, wave spectrum and the directional wave slope spectrum measurements as a function of azimuth angle, incidence angle and polarization.

As a reference radar measurements were made with the footprint as close as possible to the area below the wind and wave slope measurement equipment mounted on the outrigger.

In figure 6-28 the measured incidence angle dependence is shown for a downwind condition. The data were partially calibrated at that moment so care has to be taken with interpreting the absolute levels.

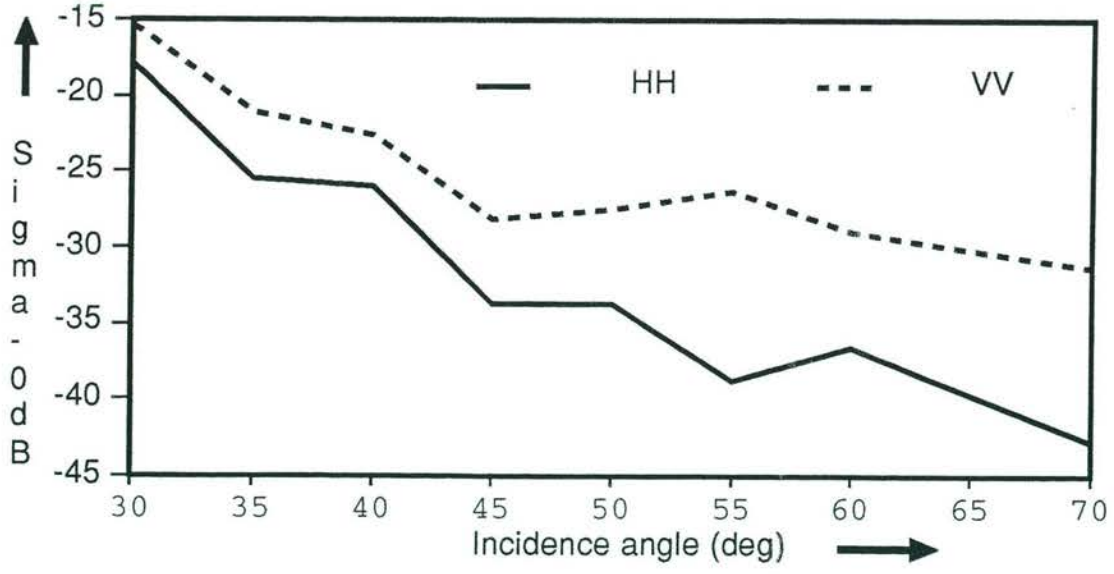

Figure 6-28 σ^0 as a function of incidence angle for HH and VV pol. Downwind.

In figure 6-29 the difference between the response for VV and HH polarization for looking

downwind is shown as a function of incidence angle.

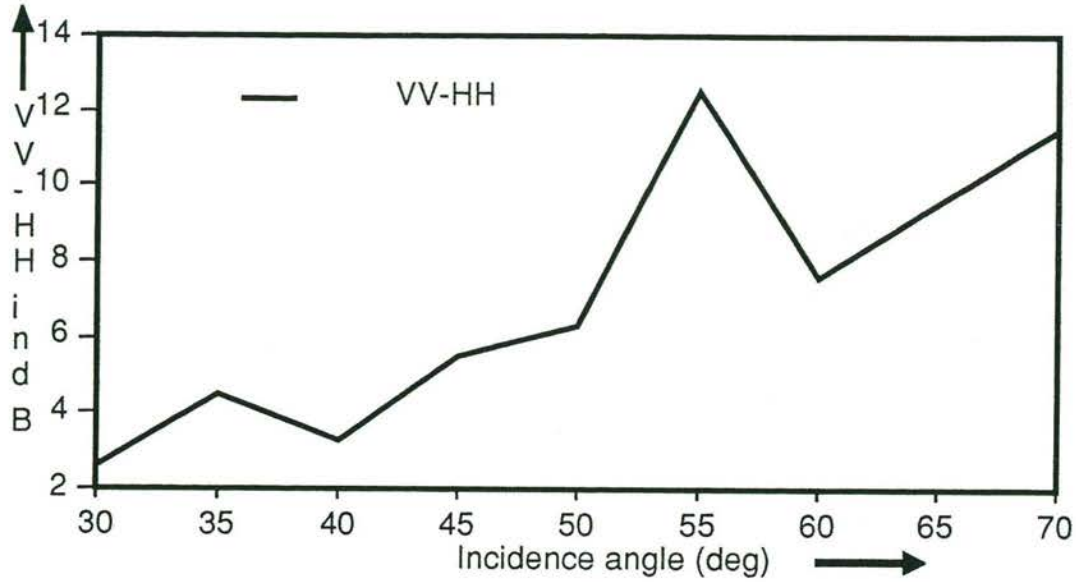

Figure 6-29 Difference between the VV and HH polarization as a function of incidence angle. Looking downwind.

The discrepancy between the measured and expected values can be explained by taking into account that there is a time difference of about 3 hours between the first and last measurement and there is a change in for example the windspeed during this time as can be seen in figure 6-30.

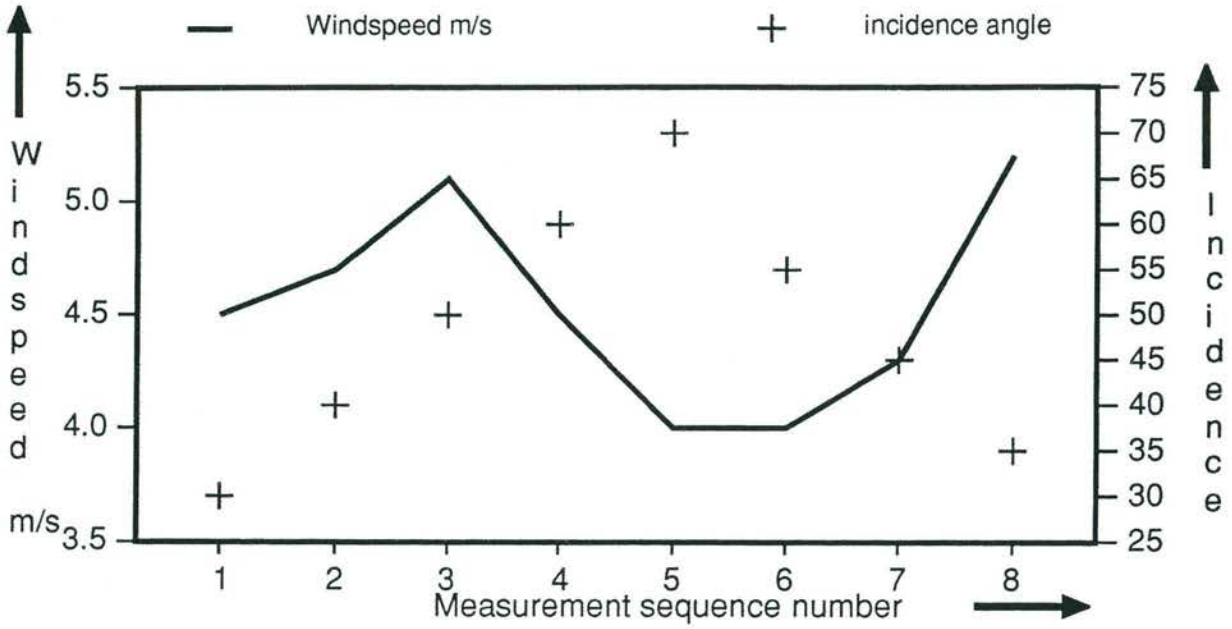

Figure 6-30 Windspeed changes during the measurement time. Same conditions as in figures 6-28 and 6-29.

A first comparison of the X-band data has been made with two models:

- an empirical model developed by G.P. de Loor, based upon all available measurements in literature and from earlier measurements made from 'Noordwijk'. The model is a parameterization of the well known cosine model with an exponential wind dependency,
- a first version of the model developed within the VIERS-1 group and at that moment based upon the two scale principle and tuned with the measurements performed in earlier stages of the VIERS-1 project in the wind/wave tank [14,30]. It is noted that the model as described in previous chapters is quite different from the first version used in this comparison.

The results presented show the windspeed dependency for an upwind looking radar and for three different incidence angles. The windspeed used for this comparison was converted by the KNMI to a neutral stability wind at a height of 10 meter. For a more detailed comparison the wind speed and direction as measured on the outrigger close to the sea surface will be used in combination with the directional wave slope spectrum measurements.

In figure 6-31, 6-32 and 6-33 the comparison between the field measurements and the two models is shown for respectively 35, 40 and 50 degrees incidence angle, VV polarization.

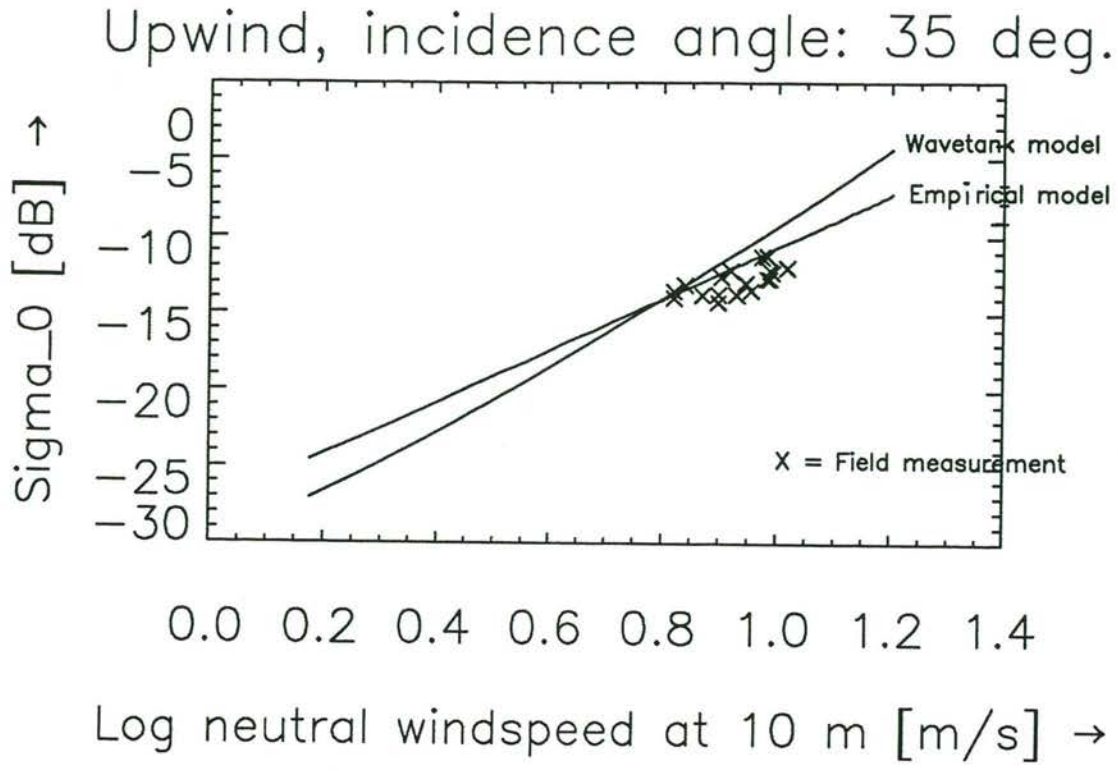

Figure 6-31 Windspeed dependence, upwind, 35 deg., VV pol.

The number of measurements at an incidence angle of 35 degrees and VV polarization under upwind conditions is small and concentrated around a windspeed of 8 m/s. The model predictions are close to the measurements, but the wavetank model overestimates at higher wind speeds.

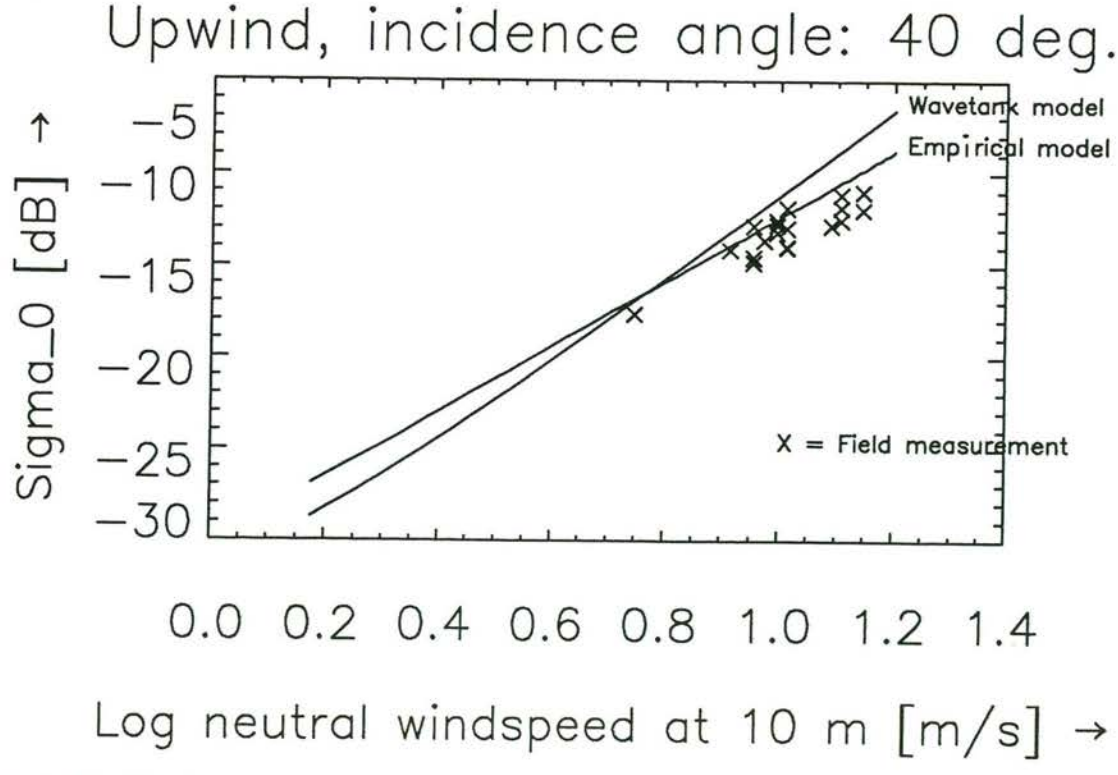

Figure 6-32 Windspeed dependence, upwind, 40 deg., VV pol.

At 40 and 50 degrees incidence angle the measurements are spread over the windspeed range. Both models overestimate the backscatter values and in general the predictions of the wavetank model are lower than the empirical model at low windspeeds and higher than the empirical model at high windspeeds, with a cross-over point at about 6 m/s. This cross-over point seems to be independent of the incidence angle.

The presented backscatter measurements are calibrated values with a remaining total error (due to calibration and speckle) of less then 1 dB.

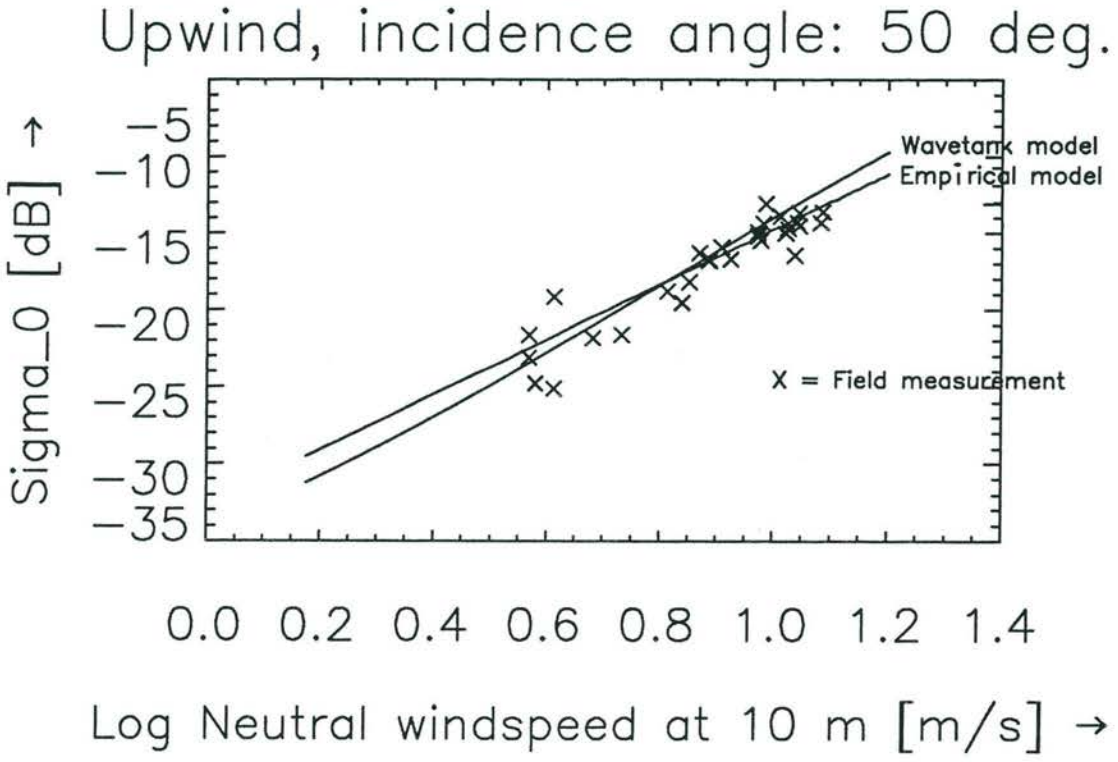

Figure 6-33 Windspeed dependence, upwind, 50 deg., VV pol.

Assuming an exponential windspeed dependency, the exponent can be calculated from both model results and the measurement. In table 6-8 an overview is given of the windspeed exponent for VV-polarization and three incidence angles as derived from the measurements and the models. The wavetank model gives a much too large exponent as compared with the empirical model and the measurements. The difference between the measurements and the empirical model can be explained from the limited number of measurements and a limited range of windspeeds.

Table 6-8 Windspeed exponent for VV polarization

	Incidence angle in degrees		
	35	**40**	**50**
Measurements	0.64	1.43	1.93
Empirical model	1.70	1.76	1.79
Wavetank model	2.27	2.21	2.15

6.6 The VEERS-1 microwave data

The ISDGM group VEERS-1 was involved in the MPN experiment for two weeks, from the 19th to the 30th of November. During this period a C-band coherent and pulsed scatterometer was operated together with the Delft University of Technology (TU-Delft) X-band scatterometer to get simultaneous backscatter measurements from the sea. The technical characteristics of the radar are reported in Table 6-9.

The C-band radar is "self calibrating" because it is possible to control the amount of the emitted power by measuring of the calibration signal and the inside sensor temperature. Because the radar is of the pulsed type and the antenna acts as transmitter and receiver, the receiving gate (depending on the radar-sea distance) must be set before the measurements. The sequence of the operational modes of the radar is the following:

- acquisition of the calibration and the sensor temperature signals,
- setting of the receiving gate (steps of 25 ns, corresponding to 3.75 m of range),
- data acquisition.

The acquisition of the calibration and the sensor temperature signals is then carried out time to time during the measurements (typically every 100 s). The setting of the receiving gate is instead performed once. Unfortunately this resulted almost always in incorrect data, due to a wrong indication of the manufacturer; the range was displaced by ± 3.75 m. As a consequence the resulting data were biased low in their absolute values. Nevertheless they may be corrected according to theoretical computations for 20, 30, 40 and 50 degrees of incidence angle. This shortcoming does not prevent the use of data in the computation of the quantities independent from the absolute value of the RCS, such as the Modulation Transfer Function (MTF) and the parameters describing the gravity waves characteristics (orbital velocity, HS).

Table 6-9 Characteristics of the C-band radar

Frequency	5.4 GHz	
Antenna gain	30.5 dB	
Transmitted power	10 mW	
Pulse length	50 ns	
PRF	150 kHz	
Polarization	VV or HH	
Radiation lobes	Azimuth HH	5.6
	Elevation HH	4.0
	Azimuth VV	4.0
	Elevation VV	5.6
Range of operation	15 - 600 m	
Output signal amplitude	±4 V differential	
Output signal frequency band	0 - 150 Hz	
Power supply	220 V, 50 Hz	
Antenna diameter	0.7 m	
Antenna weight	6 kg	
Sensor dimensions	60 x 31 x 18 cm	
Sensor weight	28 kg	

6.6.1 The structure of the radar data records

The complex backscatter output signal was sampled at 660 Hz (1.54 s for 1024 complex data sequences) and then recorded on a PC hard disk. The writing took about 0.15 s. Then, every 100 seconds or so, an acquisition of the internal calibration signal and the system noise was performed. The data structure is shown in figure 6-34.

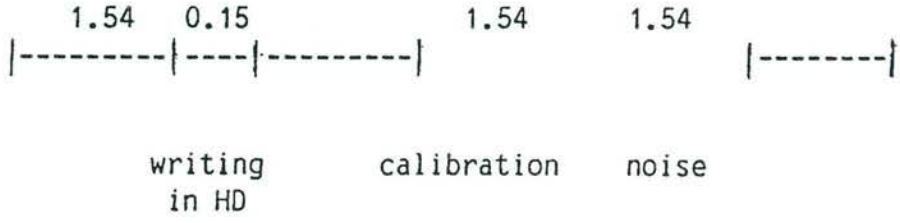

Figure 6-34 Data structure of the VEERS radar

Typically, two kinds of records were obtained during the campaign, the 300 seconds records with the radar looking upwind and the 1200 seconds records with the radar looking towards the boom where the anemometers and the RSSG were installed. A total of 40 upwind and 9 "boom" records were obtained (Table 6-10), almost all in coincidence with the measurements of the TU-Delft X-band radar.

Table 6-10 Data records available for investigation

Upwind (degrees)	Records	
0	1 VV	
10	4 VV	2HH
20	3 VV	2 HH
30	3 VV	2 HH
40	8VV	2 HH
50	4 VV	1 HH
60	4 VV	2 HH
70	1 VV	1 HH
	---	---
total	28 VV	12 HH
Boom (degrees)	**Records**	
40	6 VV	4 HH

6.6.2 The data processing

For each sequence of data (i .e. 1.54 seconds), four complex power spectra were calculated, each one obtained from 256 complex data. From this analysis it was possible to get:

- the time series of the Doppler frequency Fd (the peak frequency of each complex spectrum)
- the time series of the Radar Cross Section
- the average complex spectrum

The power spectra of the Doppler frequency and the RCS time series, computable after resampling of the data, constitute the first step in studying the modulation induced on RCS by the large gravity wave system.

In figure 6-35 an example is given of the Fd and RCS time series.

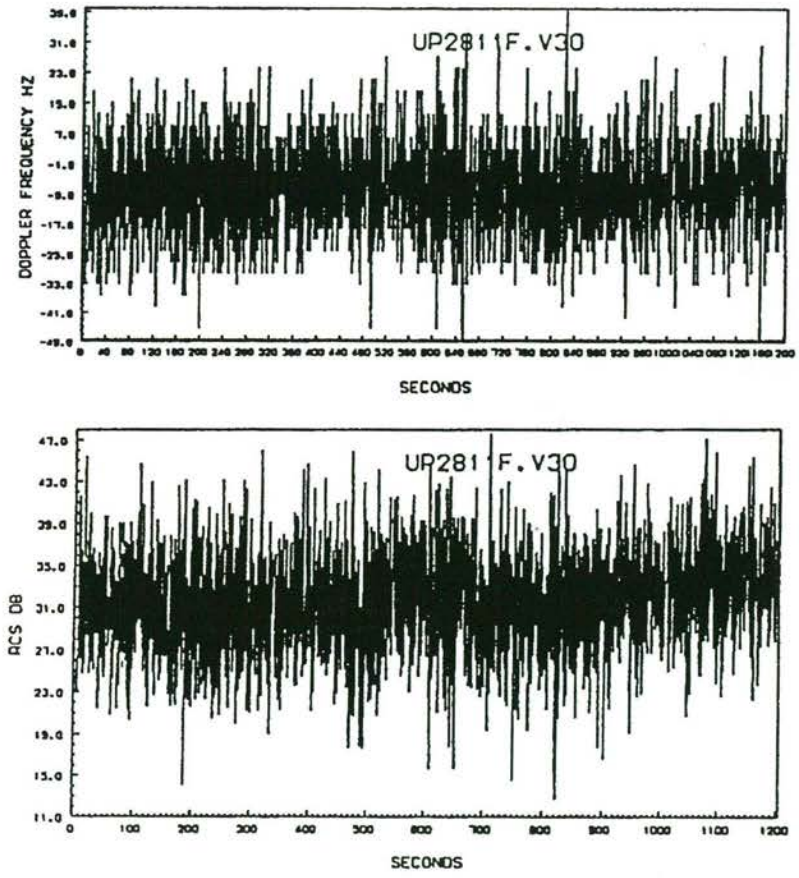

Figure 6-35 C-band time series of Fd (top) and RCS (bottom)

The respective power spectra, after normalization, are shown in figure 6-36 and the average RCS power spectrum in figure 6-37.

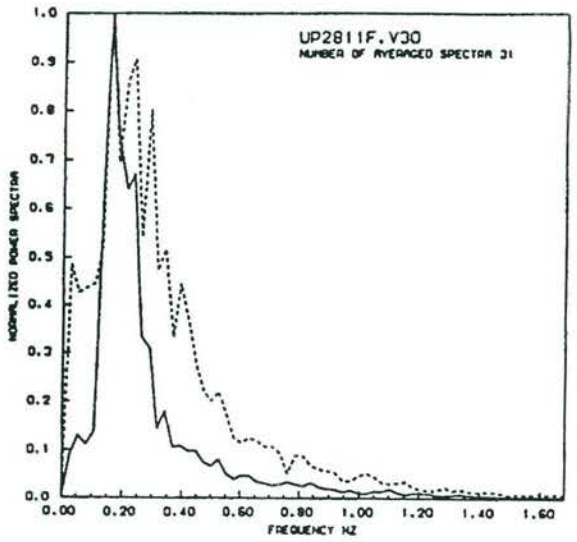

Figure 6-36 Normalized power spectra

Note in figure 6-36 the correspondence of the peak of the spectra, indicating the wave induced modulation that, however, is not so clear in all records. Note also, in figure 6-37, that the peak of the spectrum does not coincide with the Bragg frequency, indicated by the vertical dashed lines, due to the effect of the wave motion and because the radar backscattering is not the same at the crest and at the through of the large waves.

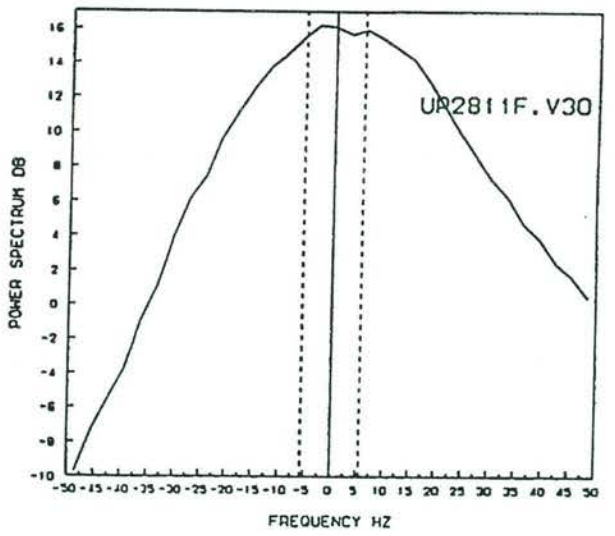

Figure 6-37 Average RCS power spectrum

Another kind of analysis is represented by the identification of "single events" in the data. A "single event" is defined as an unusually high or low value of the RCS and Fd and is normally associated with nonlinear phenomena occurring at the sea surface like breaking waves. An example of this is given in figure 6-38, where spikes around 800 seconds are evi-

dent. A blow up of the signal in this surrounding confirms the correspondence between the behavior of the RCS and Fd.

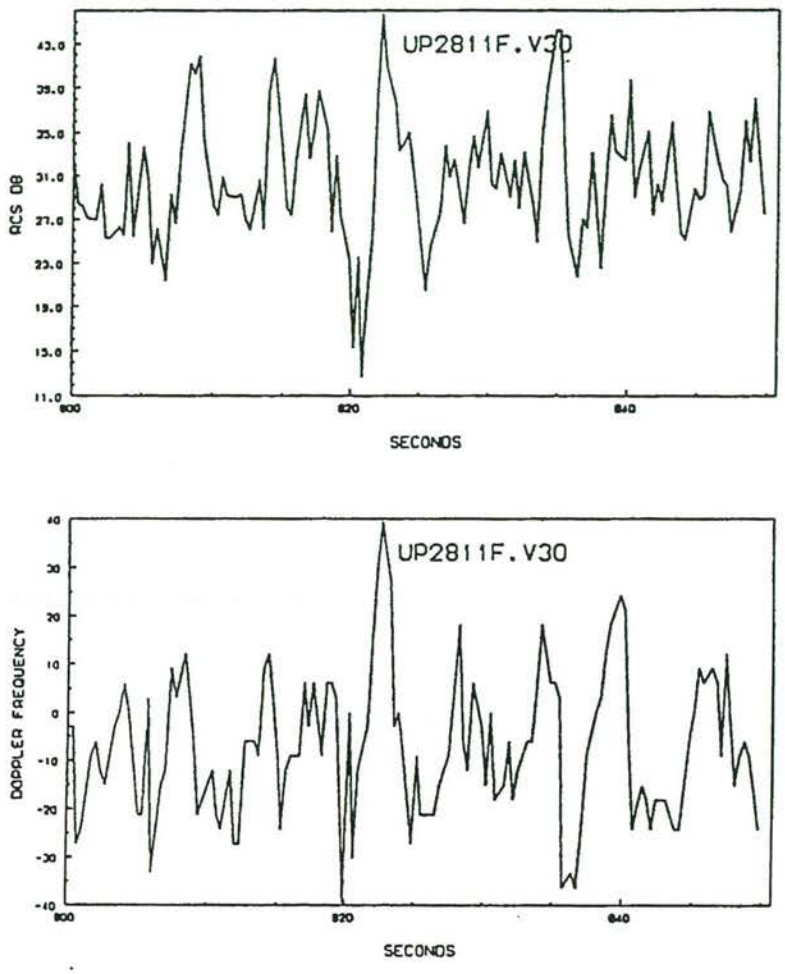

Figure 6-38 Time series of an example of an event, RCS (top), Fd (bottom)

6.6.3 Next steps in the analysis

At the present level of processing, the C-band radar data are ready to be exchanged with those of the other experimenters, in the form of the RCS and Doppler frequency time series (re-sampled) and of the average RCS power spectrum.

The correction of RCS data for the bias introduced by the incorrect setting of the radar range will be done soon, but it may not be completely successful.

A study of the MTF is underway at the Institute.

The investigation of the low frequency gravity wave information (Hs, orbital motion) obtainable from the radar data is foreseen in the coming months.

Finally, the exchange of data among experimenters shall allow a complete and exhaustive study of the RCS-wind stress-high frequency wave spectrum relationships.

6.7 Conclusions

The data processing of the measurements has just been completed and a first analysis was done. Some results were presented to indicate that a very valuable data set has been acquired. The preliminary results clearly demonstrate the potential for evaluating different backscatter models.

A complete list of all X-band radar measurements including the most important environmental parameters is included in Appendix B. The friction velocity listed in Appendix B is based upon a parameterization using the MPN reference wind speed as input. The high quality friction velocity measurements from KNMI are listed elsewhere.

7 CONCLUSION

In this report the progress made in the VIERS-1 project has been described. The activities during the last phase were mainly focused on the development of the VIERS model. Much progress has been made with the modeling.

In chapter 2 the main principles of the short wave model TESTWA were given. Together with a long wave (gravitation) model, TESTWA forms the wind/wave interaction module of the total VIERS model. Results using this module in the Delft wind/wave flume were promising. However, the adjusted long wave model used in the flume can not be used at sea. It turned out that the wind/wave module needs a very accurate modeling of the long waves. Errors in e.g. the estimation of the dominant wave peak, lead to erroneous levels of the short waves and thus to wrong backscattering cross sections. Several options can be chosen for the long wave spectrum at sea, but the best option probably will be to use the output of the WAM model as input for the VIERS model.

The short wave model TESTWA was tested using the Delft wind/wave flume data and proved to be able to accurately reproduce the measured spectra. Validation of TESTWA at sea is a much more difficult task to perform. At the moment of writing the essential input for this validation: information on the short wave spectrum measured with the Reflective Stereo Slope Gauge, is not yet available. As long as this fails only the overall model can be tested and validated at sea.

Several backscattering models which were published in the open literature have been implemented and subjected to a comparison. Data from the Delft wind/wave experiment were execellently suited for this purpose. The test revealed that the best backscattering model at the moment is the improved two-scale model. This model performs better than the -more sophisticated in terms of physics- "IEM" and "Full Wave" models. The two-scale model has already been implemented on the ECMWF computer to be used in a validation using ERS-1 data. However the modular structure of the VIERS model permits a swapping of backscattering modules. So, in case progress is reported on one of the other scattering models, a change of module still will be possible.

In November and December 1990 an experiment was conducted from the Meetpost Noordwijk, 9 kilometers off the Dutch coast near the sea resort Noordwijk. Radar measurements at two frequencies: X-band and C-band were performed together with measurements of the friction velocity and waves. A new wave measuring instrument was tested for the first time in 'open' sea: the Reflective Stereo Slope Gauge. A detailed description of this instrument is given in chapter 6. Data of all sensors, except the RSSG is available now and the testing of the VIERS algorithms using these data started recently.

In the near future the validation of the algorithms at sea will be performed. Following this validation recommendations for changes of the algorithms, if necessary, will be followed up by upgrading the models. Then the second generation model will be extensively tested and made operational for the use at the ECMWF using ERS-1 data. Coupling of the VIERS model to other models like WAM will be considered.

REFERENCES

[1] Abramowitz, M. and I.A. Stegun, I.A.,
Handbook of mathematical functions.
Dover Publications, Inc, New York, USA, 1970.

[2] Bahar, E.,
Depolarization of electromagnetic waves excited by distributions of electric and magnetic sources in inhomogeneous multilayerd structures of arbitrary varying thickness: generalized field transforms.
J. Math. Phys. 14, 1502-1509, 1973.

[3] Bahar, E.,
Depolarization of electromagnetic waves excited by distributions of electric and magnetic sources in inhomogeneous multilayerd structures of arbitrary varying thickness: full wave solutions.
J. Math. Phys. 14, 1510-1515, 1973.

[4] Bahar, E.,
Scattering cross sections for random rough surfaces: full wave analysis.
Radio Science 16(3), 331-341, 1981.

[5] Bahar, E.,
Scattering cross sections for composite random surfaces: full wave analysis.
Radio Science 16(6), 1327-1335, 1981.

[6] Bahar, E.,
Full-wave solutions for the depolarization of the scattered radiation fields by rough surfaces of arbitrary slope.
IEEE Trans. Antennas and Propagation 29(3), 443-454, 1981.

[7] Bahar, E., D.E. Barrick and M.A. Fitzwater,
Computations of scattering cross sections for composite surfaces and the specification of the wavenumber where spectral splitting occurs.
IEEE Trans. Antennas and Propagation 31(5), 698-709, 1983.

[8] Banner, M. L., I. S. F. Jones and J.C. Trinder,
Wavenumber spectra of short gravity waves.
J. Fluid Mech. 198, 321-344, 1989.

[9] Barrick, D.E. and W.H. Peake,
A Review of Scattering from Surfaces with Different Roughness Scales.
Radio Science 3(8), 865-868, 1968.

[10] Barrick, D. E., and B. J. Lipa,
Analysis and interpretation of altimeter sea echo.
Adv. Geophys. 27, 60-99, 1985.

[11] Beckmann, P. and A. Spizzichino,
The Scattering of Electromagnetic Waves from Rough Surfaces.
MacMillan, 1963.

[12] Brooks, C.E.P. and N. Carruthers,
Handbook of statistical methods in meteorology.
Her Majesty's Stationery Office, 1953.

[13] Brown, G.S.,
Backscattering from a Gaussian distributed perfectly conducting rough surface.
IEEE Trans. Antennas and Propagation 26(3), 472-482, 1978.

[14] Calkoen, C. J., et al.,
Viers-1 progress report part-2,
Technical Report bcrs 90-27, BCRS, 1990.

[15] Calkoen, Ch., P. Snoeij, D. van Halsema, J. Vogelzang, W.A. Oost, B. Jähne,
Evaluation of a two-scale model using extensive radar backscatter and wave measurements in a large wind-wave flume.
Proceedings IGARSS 91, 885-888, 1991.

[16] Chen, K.S. and A.K. Fung,
A Scattering Model for Ocean Surface.
Proc. IGARSS'91, Remote Sensing: Global Monitoring for Earth Management,
Espoo, Finland, June 3-6, 1991, IEEE, 1991.

[17] Cote, L. J. et al.,
The directional spectrum of a wind generated sea as determined from data obtained by the Stereo Wave Observation Project.
Meteorological Papers, 2, No. 6, N.Y. N.Y. Univ.-College of Engineering, New York, 1-88, 1960.

[18] Cox. C., and W. Munk,
Statistics of the sea surface derived from sun glitter.
J. Marine Res. 13, 198-227, 1954.

[19] Cox C., and W. Munk,
Measurement of the roughness of the sea surface from photographs of the sun's glitter.
J. Opt. Soc. America, 44, No. 11, 838-850, 1954.

[20] Davidson, R. C.
Methods in Nonlinear Plasma Theory.
Academic. 1972.

[21] Defant A.,
Physical Oceanography.
Pergamon Press, New York, 1961.

[22] Donelan, M. A., J. Hamilton and W.H. Hui
Directional spectra of wind-generated waves.
Phil. Trans. R. Soc. Lond. A315, 509-562, 1985.

[23] Donelan, M. A. and W.J. Pierson,
Radar Scattering and Equilibrium Ranges in Wind-Generated Waves with Application to Scatterometry.
J. Geophys. Res. 92, 4971-5029, 1987.

[24] Ebuchi N., H. Kawamura, and Y. Toba,
Fine structure of laboratory wind-wave surfaces studied using an optical method.
Boundary-Layer Meteorology 39, 133-151, 1987.

[25] Fu, L. L., and R. Glazman,
The effect of the degree of wave development on the sea state bias in radar altimetry measurement.
J. Geophys. Res. 96, 829-834, 1991.

[26] Fung, A.K. and G.W. Pan,
A Scattering Model for Perfectly Conducting Random Surfaces,
I Model Development.
Int. J. Remote Sensing 8(11), 1579-1593, 1987.

[27] Fung, A.K. and K.S. Chen,
Kirchhoff model for skewed random surface.
J. Electromagn. Waves and Appl. 5(2), 205-216, 1991.

[28] Fung, A.K., Z.Q. Li and K.S.Chen,
Backscattering from a Randomly Rough Dielectric Surface.
IEEE Trans. Geosci. Remote Sensing 30(2), 356-369, 1992.

[29] Gienapp H.,
Visuelle stereoskopische Ermittlung der Wellenhöhen und -längen des Seegangs.
Deutsche Hydrographische Zeitschrift 26, Heft 4, S. 171-176, 1973.

[30] Halsema, D. van, et al.,
Progress report on the VIERS-1 project.
Technical Report bcrs 89-24, BCRS, 1989.

[31] Halsema, D. van, B. Jähne, W. A. Oost, C. Calkoen, and P. Snoeij,
First results of the VIERS-1 experiment.
Radar Scattering from Modulated Wind Waves, edited by G. Komen and W. Oost, 49-57, Kluwer, Boston, 1989.

[32] Halsema, D. van, Ch. Calkoen, W.A. Oost., P. Snoeij, J. Vogelzang, and B. Jähne,
Dual-polarized scatterometer measurements of wind and mechanically generated waves in a very large wind/wave flume.
Proceedings of the 5th Int. Coll. Physical Measurements and Signatures in Remote Sensing,
Courchevel, France, 14-18 January 1991, 247-252, 1991.

[33] Halsema, D. van, P. Snoeij, Ch. Calkoen, W.A. Oost, J. Vogelzang, B. Jähne,
Modulation of the microwave backscatter by long gravity waves as measured in a very large wind/wave flume.
Proceedings IGARSS 91, 885-888, 1991.

[34] Halsema, D. van and J.H.M. Teeuwen,
SHIRA measurements from MPN during the VIERS-1 experiment from November 12 till December 6, 1990.
FEL-TNO report no. FEL-91-C310, 1991.

[35] Hansen, R.C. and L.L. Bailin,
A new method of near field analysis.
IRE Trans. Ant. & Prop. 7, 458-467, 1959.

[36] Hasselmann, K.,
On the non-linear energy transfer in a gravity wave spectrum. Part 1.
J. Fluid Mech. 12, 481-500, 1962.

[37] Hasselmann, K.,
On the non-linear energy transfer in a gravity wave spectrum. Part 2 and 3.
J. Fluid Mech. 15, 273-281 and 385-398, 1963.

[38] Hasselmann, K. et al.,
Measurements of wind-wave growth and swell decay during the Joint North Sea Wave Project (JONSWAP).
Deutch. Hydr. Zeit. A12, 1973.

[39] Heras, M. M. de las and P.AE.M. Janssen,
Comparison of hindcast results of low-frequency swell with the WAM and the coupled WAM model.
KNMI memo OO-91-06, 1991.

[40] Hidaka, Koji,
A stereophotogrammetric survey of waves and swells in the ocean.
Me. Imp. Mar. Obs. Kobe 7, Nr.3, 231-368, 1941.

[41] Holliday, D., G. St-Cyr and N.E. Woods,
A radar ocean imaging model for small to moderate incidence angles.
Int. J. Remote Sensing, Vol. 7, No. 12, 1809-1834, 1986.

[42] Holthuijsen, L. H.,
The directional energy distribution of wind generated waves as inferred from stereophotographic observations of the sea surface.
Commun. Hydraul., Rep. No. 81-2, Dept. Civ. Eng., Delft University of Technology, 1981.

[43] Holthuijsen, L. H.,
Stereophotography of Ocean Waves.
Appl. Ocean Res. 5, 204-209, 1983.

[44] Holthuijsen, L. H.,
Observations of the directional distribution of ocean-wave energy in fetch-limited conditions.
J. Phys. Oceanogr. 13, 191-207, 1983.

[45] Horn, B. K. P.,
Robot Vision.
MIT Press, Cambridge, 1986.

[46] Hwang, P. A.,
Radar Backscatter and Surface Fine Structure at the Air-Water Interface, Part I. Measurement System and Calibration.
STC Technical Report 4010, Science and Technology Corp., Hampton VA, 1990.

[47] Hwang, P. A.,
Surface Fine Structure at the Air-Water Interface, Part IV. Scanning Slope Sensor and Instrument Platform for Field Deployment.
Technical Report,Quest Integrated Inc., Kent WA., in preparation, 1992.

[48] Jähne, B.,
Energy balance in small-scale waves - an experimental approach using optical slope measuring technique and image processing.
Radar Scattering from Modulated Wind Waves,
edited by G. Komen and W. Oost, 105-120, Kluwer, Boston, 1989.

[49] Jähne, B., and S. Waas,
Optical measuring technique for small-scale water surface waves.
Advanced Optical Instrumentation for Remote Sensing of the Earth's Surface,
SPIE conference proceedings 1129, 122-128, Washington, 1989.

[50] Jähne, B. and K.S. Riemer,
Two-Dimensional Wave Number Spectra of Small-Scale Water Surface Waves.
J. Geophys. Res. Oceans 95, 11531-11546, 1990.

[51] Jähne, B.,
Motion determination in space-time images.
Image Processing III, SPIE Conf. Proceedings 1135, Washington, 1990.

[52] Jähne, B.,
Motion determination in space-time images.
1990 Proceedings Computer Vision - ECCV 90, Antibes, France, Springer Verlag, Berlin, 1990.

[53] Jähne, B.,
Digital Image Processing.
Springer Verlag, Berlin, 1991.

[54] Jähne, B., J. Klinke, P. Geißler, and F. Hering,
Image sequence analysis of ocean wind waves.
Proceedings International Seminar in Transport Processes,
May 25-29, Athens, Greece, in press, 1992.

[55] Jähne, B., S. Waas, and J. Klinke,
Shape from shading techniques for short ocean waves.
Proceedings International Seminar in Transport Processes,
May 25-29, Athens, Greece, in press, 1992.

[56] Jähne, B., S. Waas, and J. Klinke,
A critical theoretical review of optical techniques for short ocean wave measurements.
Proceedings of Conference on Optics of the Air-Sea Interface, Theory and Measurements,
L. Estep ed., SPIE Conference Proceedings 1749, SPIE's Annual Meeting, 19-24 July 1992, San Diego, in press, 1992.

[57] Jähne, B., and H. Schultz,
Calibration and accuracy of optical slope and height measurements for short wind waves.
Proceedings of Conference on Optics of the Air-Sea Interface, Theory and Measurements,
L. Estep ed., SPIE Conference Proceedings 1749, SPIE's Annual Meeting, 19-24 July 1992, San Diego, in press, 1992.

[58] Jähne, B., and J. Klinke,
Imaging of short ocean wind waves with shape from shading techniques.
submitted to JOSA A, 1992.

[59] Jähne, B., and J. Klinke,
Wave number spectra of short wind waves - a comparative study from different wind-wave facilities.
to be submitted to *J. Geophys. Res.*, 1992.

[60] Janssen, P. A. E. M.,
Quasilinear approximation for the spectrum of wind-generated water waves.
J. Fluid Mech. 117, 493-506, 1982.

[61] Janssen, P. A. E. M.,
The initial evolution of gravity-capillary waves.
J. Fluid Mech. 184, 581-597, 1987.

[62] Janssen, P. A. E. M.,
Wave-Induced Stress and the Drag of Air Flow over Sea Waves.
J. Phys. Oceanogr. 19, 745-754, 1989.

[63] Kawai, S., K. Okuda, Y. Toba,
Field data support of threeseconds power law and $gu_*\sigma^{-4}$ spectral form for growing wind waves.
J. Oceanogr. Soc. Japan 33, 137-50, 1977.

[64] Kinsman, B.,
Wind Waves - Their Generation and Propagation on the Ocean Surface.
Prentice Hall, Englewood Cliffs N.Y., 1965.

[65] Kitaigorodskii, S. A.,
On the theory of the equilibrium range in the spectrum of wind-generated gravity waves.
J. Phys. Oceanogr. 13, 816-827, 1983.

[66] Kleijweg, J.C.M. and P. Hoogeboom,
A mobile radar system for monitoring waves.
Proc. of Signature Problems in Microwave Remote Sensing of the Surface of the Earth, 15-17 May 1990, Sheraton Hyannis, Hyannis, MA, USA, URSI, 1990.

[67] Kleijweg, J.C.M.,
SHIRA: a mobile radar system for monitoring waves.
UDT '91 conference proceedings, Paris, France, 23-25 April 1991, 993-998.
Microwave Exhibitions and Publishers Ltd., 1991.

[68] Kleijweg, J.C.M.,
SHIRA systeem beschrijving en eerste meetresultaten.
FEL-TNO report, no. FEL-91-B103, 1991.

[69] Kleijweg, J.C.M. and J.H.M. Teeuwen,
Metingen met SHIRA in de rehearsal campagne van de ERS-1.
BCRS report no. BCRS 91-03, 1991.

[70] Klinke, J., and B. Jähne,
2D wave number spectra of short wind waves - results from wind-wave facilities and extrapolation to the ocean.
Proceedings of Conference on Optics of the Air-Sea Interface, Theory and Measurements,
L. Estep ed., SPIE Conference Proceedings 1749, SPIE's Annual Meeting, 19-24 July 1992, San Diego, in press, 1992.

[71] Kohlschütter, E.,
Die Forschungsreise S.M.S. "Planet" Band 2, Stereophotogrammetrische Aufnahmen.
Ann. d. Hydrographie 34, 1906.

[72] Komen, G. J. et al.,
WAM book.
to be published.

[73] Kraan, C. and W. A. Oost,
A new way of anemometer calibration and its application to a sonic anemometer.
J. Atm. Oceanic Techn. 6, 516-524, 1989.

[74] Kwoh, D. S. and B. M. Lake,
The nature of microwave backscattering from water waves.
The Ocean Surface, edited by Y. Toba and H. Mitsuyasu, 249-256, Reidel Publishing Co., 1985.

[75] Lamb, H.,
Hydrodynamics.
6th ed., Dover, New York. 1945.

[76] Matlab 1990

[77] Mitzner, K.M.,
Effect of small irregularities on electromagnetic scattering from an interface of arbitrary shape.
J. Math. Phys. 5, 1776-1786, 1964.

[78] Oost,W.A.,
Flow distortion by an ellipsoid and its application to the analysis of atmospheric measurements.
J. Atm. Oceanic Techn. 8, 331-340, 1991.

[79] Oost, W.A., E.H.W. Worell, J.W. Schaap, C. van Oort and C. Kraan,
An improved version of the pressure anemometer.
J. Atm. Oceanic Techn. 8, 575-584, 1991.

[80] Oost, W.A.,
The wind profile in a wave flume.
J. Wind Eng. Ind. Aerodyn. 37, 113-121, 1991.

[81] Pan, G.W. and A.K. Fung,
A Scattering Model for Perfectly Conducting Random Surfaces,
II Rang of Validity.
Int. J. Remote Sensing 8(11), 1595-1605, 1987.

[82] Phillips, O. M.,
Spectral and statistical properties of the equilibrium range in the wind-generated gravity waves.
J. Fluid Mech. 156, 505-531, 1985.

[83] Pierson, W. J.(ed.),
The Directional Spectrum of a Wind Generated Sea as Determined by the Stereo Wave Observation Project.
Coll. Engng., N.Y.U. Met. Pap. 2, no. 6, 1962.

[84] Pierson, W. J. and L. Moskowitz,
A proposed spectral form for fully developed wind sea based on the similarity theory of S. A. Kitaigorodskii.
J. Geophys. Res. 69, 5181-5190, 1964.

[85] Plant, W. J.,
On the steady-state energy balance of short gravity wave systems.
J. Phys. Oceanogr. 10, 1340-1352, 1980.

[86] Rice, S.O.,
Reflection of electromagnetic waves from slightly rough surfaces.
Comm. Pure Appl. Math. 4, 351-378, 1951.

[87] Riemer, K., T. Scholz, und B. Jähne,
Bildfolgenanalyse im Orts-Wellenzahl-Raum.
Proc. 13. DAGM-Symposium Mustererkennung 1991,
B. Radig, ed., 223-230, Springer, Berlin, 1991.

[88] Riemer, K., T. Scholz, und B. Jähne,
Analysis of image sequences from water surface waves in the space wave number domain.
in preparation, 1992.

[89] Sancer, M.I.,
Shadow corrected electromagnetic scattering from randomly rough surfaces.
IEEE Trans. Antennas and Propagation 17, 577-589, 1969.

[90] Schuhmacher, A.,
Untersuchung des Seegangs mit Hilfe der Stereophotogrammetrie.
Jahrbuch 1936 Lilienthal-Gesellschaft f. Luftfahrtforschung, S. 239 ff., Berlin, 1936.

[91] Schuhmacher, A.,
Stereophotogrammetrische Wellenaufnahmen.
Wissenschaftliche Ergebnisse der Deutschen Atlantischen Expedition auf dem Forschungs- und Vermessungsschiff "Meteor" 1925-1927, 1939.

[92] Schuhmacher, A.,
Stereophotogrammetrische Wellenaufnahmen mit schneller Bildfolge.
Dtsch. Hydrogr. G., 3, 78, 1950.

[93] Shemdin O. H., H. M. Tran, and S. C. Wu,
Directional measurements of short ocean waves with stereophotography.
J. Geophys. Res. 93, 13891-13901, 1988.

[94] Shemdin O. H., and H.M. Tran,
Measuring short surface waves with stereophotography.
Photogr. Eng. & Remote Sensing 58, 311-316, 1992.

[95] Simpson, L.S.,
Preliminary investigation of the directional spectrum of ocean wave height as obtained from stereo wave photographs.
Ocean Dynamics Branch, Exploratory Oceanography Division, Research and Development Department, U.S. Naval Oceanographic Office, Washington, DC,
Informal Manuscript No. 67.1, 1967.

[96] Stilwell, D. Jr.,
Directional energy spectra of the sea from photographs.
J. Geophys. Res. 74, 1974-1986, 1969.

[97] Stolte, S.,
Dynamik kurzwelligen Seegangs und Seegangsbrechens.
Forschungsanstalt der Bundeswehr für Wasserschall- und Geophysik.
Forschungsbericht 1990-4.

[98] Stratton, J.A.,
Electromagnetic theory.
McGraw-Hill inc, New York, USA, 1941.

[99] Toba, Y.,
Local balance in the air-sea boundary processes, III. On the spectrum of wind waves.
J. *Oceanogra. Soc. Japan* 39, 209-220, 1973.

[100] Ulaby, F.T., R.K. Moore and A.K. Fung,
Microwave Remote Sensing, volume II.
Addison-Wesley Publ. Comp., 1981.

[101] Valenzuela, G.R.,
Theories for the interaction of electromagnetic and oceanic waves - a review.
Boundary-Layer Meteorology 13, 612-85, 1978.

[102] Vliet, G. J. v. d.,
Stereofotografie van Zeegolven.
Rep. No. 720013, Central Electronic Service Dept.,
Delft University of Technology, 1972.

[103] Vliet, G. J. v. d.,
Stereofotografie van Zeegolven 2.
Rep. No. 740022, Central Electronic Service Dept.,
Delft University of Technology, 1974.

[104] Waas, S.,
Entwicklung eines Verfahrens zur Messung kombinierter Höhen- und Neigungsverteilungen von Wasseroberflächenwellen mit Stereoaufnahmen.
Diplomarbeit, Univ. Heidelberg, 1988.

[105] Waas, S., and B. Jähne,
Combined slope/height measurements of water surface waves: part I: instrument design.
to be submitted to *Optical Engineering*, 1992.

[106] Waas, S., and B. Jähne,
Combined slope/height measurements of water surface waves: part II: image processing and first results.
to be submitted to *Optical Engineering*, 1992.

[107] Waas, S., and B. Jähne,
Combined slope-height measurements of short wind waves: first results from field and laboratory measurements.
Proceedings of Conference on Optics of the Air-Sea Interface, Theory and Measurements,
L. Estep ed., SPIE Conference Proceedings 1749, SPIE's Annual Meeting, 19-24 July 1992, San Diego, in press, 1992.

[108] Walsh, E. J., and F. C. Jackson,
Observations on Electromagnetic Bias in Radar Altimeter Sea Surface Measurements.
J. Geophys. Res. 94, 14575-14584, 1989.

[109] Walz, A.,
Strömungs- und Temperaturgrenzschichten.
Karlsruhe, 259 pp, in German,
Verslag G.Braun, 1966.

[110] Weinblum, G., and W. Block,
Stereophotogrammetrische Wellenaufnahmen.
Schiffbautechn. Ges. 36. Ord. Haufptvers., Berlin, 1935.

[111] Wills, J.A.B.,
HEXOS model tests on the Noordwijk tower.
NMI Report R184, 56 pp., 1984.

[112] Wolfe, W. L., and G. J. Zissis (eds.),
The Infrared Handbook.
The Infrared Information Analysis Center, Environmental Research Institute of Michigan, 3rd printing, 1989.

[113] Wright, J.W.,
A new model for sea clutter.
IEEE Trans. Antennas and Propagation 16, 217-223, 1968.

[114] Wyngaard, J.C.,
The effects of probe-induced flow distortion on atmospheric turbulence measurements.
J.Appl.Meteor. 20, 784-794, 1981.

[115] Yaplee, B. S., A. Shapiro, D. L. Hannond, B. B. Au, and E. A. Uliana,
Nanosecond radar observation of the ocean surface from a stable platform.
IEEE Trans. Geosci. Electron. GE-9, 170-174, 1971.

APPENDIX A Backscatter models

Appendix A.1 Jacobi-Anger expansion

First define the polar coordinates

$$\begin{aligned} \vec{x} &= \vec{e_x} r\cos(\alpha) + \vec{e_y} r\sin(\alpha) \\ \vec{q} &= \vec{e_x} q\cos(\beta) + \vec{e_y} q\sin(\beta) \end{aligned} \tag{A.1}$$

with r = |x | and q = |q |. The unit vectors in x- and y-direction are given by e_x and e_y. From (A.1) one finds :

$$q \cdot x = qr[\cos(\beta)\cos(\alpha) + \sin(\beta)\sin(\alpha)] = qr\cos(\beta - \alpha) \tag{A.2}$$

Suppose now that the wave spectrum W is separable into a radial part, W_r, and an angular distribution, W_a, as is the case in many parameterizations

$$W(q) = W_r(q)W_a(\beta) \tag{A.3}$$

For the moment we assume that the angular distribution is the same over the complete wave number range. Substitution of the preceding equations in the definition of the autocorrelation function Φ, yields

$$\Phi(r,\alpha) = \int_0^{\infty} dq\, q\, W_r(q) \int_0^{2\pi} d\beta\, W_a(\beta)\cos[qr\cos(\beta - \alpha)] \tag{A.4}$$

The awkward looking double cosine can be expanded in the form (Abramowitz and Stegun, 9.1.44) [1]:

$$\cos[qr\cos(\beta - \alpha)] = J_0(qr) + 2\sum_{m=1}^{\infty}(-1)^m J_{2m}(qr)\cos[m(\beta - \alpha)] \tag{A.5}$$

where $J_n(z)$stands for the Bessel function of integer order n. (A.5) is one of the forms of the so called Jacobi-Anger expansion, which can be easily derived from the generating function of the Bessel functions. Substitution of (A.5) in (A.4) and changing the order of summation and integration gives

$$\begin{aligned} \Phi(r,\alpha) = & \int_0^{\infty} dqqW_r(q)J_0(qr)\int_0^{2\pi} d\beta W_a(\beta) \\ & + 2\sum_{m=1}^{\infty}\{(-1)^m \int_0^{\infty} dqqW_r(q)J_{2m}(qr) \\ & \times [\cos(2m\alpha)\int_0^{2\pi} d\beta w_a(\beta)\cos(2m\beta) \\ & + \sin(2m\alpha)\int_0^{2\pi} d\beta W_a(\beta)\sin(2m\beta)]\} \end{aligned} \tag{A.6}$$

where use has been made of the well known identity

$$\cos(a-b) = \cos(a)\cos(b) + \sin(a)\sin(b) \tag{A.7}$$

To write (A.6) in a more compact form we define

$$\begin{aligned} A_n &= \int_0^{2\pi} d\beta W_a(\beta)\cos(n\beta)\,,\ n \geq 0 \\ B_n &= \int_0^{2\pi} d\beta W_a(\beta)\sin(n\beta)\,,\ n > 0 \\ R_n(r) &= \int_0^{\infty} dqqW_r(q)J_n(qr)\,,\ n \geq 0 \end{aligned} \tag{A.8}$$

The coefficients A_n and B_n are, up to a factor π, equal to the Fourier expansion coefficients of W_a. Suppose that the wind is directed along the x-axis. In this case, W_a is an even function of the angle β. Therefore B_n equals zero. The coefficients R_n are the coefficients of the expansion of W_r into Bessel functions. These coefficients are a function of r. Note that only the even coefficients appear in (A.6).

Substitution of (A.8) into (A.6) yields, with B_n equal to zero :

$$\Phi(r,\alpha) = A_0R_0(r) + 2\sum_{m=1}^{\infty}(-1)^m A_{2m}R_{2m}(r)\cos(2m\alpha) \tag{A.9}$$

Note that $\Phi(r,\alpha)$ is an even function of α.

If r = 0, (A.9) reduces to

$$\Phi(0,\alpha) = A_0R_0(0) = A_0\int_0^{\infty} dqqW_r(q) = A_0N \tag{A.10}$$

since $J_0(0) = 1$ and $J_n(0) = 0$ for $n > 0$. Now define

$$U(r,\alpha) = \Phi(0,\alpha) - \Phi(r,\alpha) \tag{A.11}$$

From the preceding equations one finds

$$U(r,\alpha) = A_0[N - R_0(r)] - 2\sum_{m=1}^{\infty}(-1)^m A_{2m}R_{2m}(r)\cos(2m\alpha) \tag{A.12}$$

For simple angular distributions only the first few terms in (A.12) survive. For instance, Holliday, St-Cyr and Woods [41] take for the angular distribution

$$\begin{aligned} W_a(\beta) &= \tfrac{1}{\pi} \quad |\beta| \leq \tfrac{\pi}{2} \\ W_a(\beta) &= 0 \quad |\beta| > \tfrac{\pi}{2} \end{aligned} \tag{A.13}$$

which gives $A_0 = 1$ and $A_{2m} = 0$ for $m > 0$. An angular distribution of the form

$$W_a(\beta) = \tfrac{1}{\pi}\cos^2(\beta) \tag{A.14}$$

(a cosine-squared distribution, which is widely used) yields $A_0 = 1$ and $A_2 = ½$, all other angular coefficients being equal to zero.

It will be shown in appendix A.3 that only the first two or three expansion coefficients contribute to the autocorrelation function. Therefore the angular coefficients can be calculated without problems.

Appendix A.2 Calculation of the radial coefficients

The radial coefficients were defined as

$$R_{2m}(r) = \int_0^\infty dq\, qW_r(q)J_{2m}(qr) \quad m \geq 0 \tag{A.15}$$

$J_{2m}(qr)$ is an even function of q. If W_r is a simple, odd function of q, the integral can be extended over the complete real axis and evaluated using contour integration. However, for a spectrum with a k^{-4} asymptotic behavior, W_r will be even. Still this integral can be evaluated using contour integration for a class of functions W_r.

Suppose now that W_r is an even function. First write the Bessel function in (A.15) in terms of Hankel functions :

$$J_n(z) = \tfrac{1}{2}[H_n^{(1)}(z) + H_n^{(2)}(z)] \tag{A.16}$$

This must be done anyway, since only the Hankel functions stay finite in one infinite semicircle of the complex plane. The Hankel function of the first kind, $H_n^{(1)}(z)$, is finite in the upper semi circle, the Hankel function of the second kind, $H_n^{(2)}(z)$, is finite in the lower semi circle. From (A.15) and (A.16) one easily finds

$$R_{2m}(r) = \tfrac{1}{2}\int_0^\infty dq\, q\, W_r(q)\,[H_{2m}^{(1)}(qr) + H_{2m}^{(2)}(qr)] \quad m \geq 0 \tag{A.17}$$

When substituting p = -q in the term with $H^{(2)}$, equation (A.17) yields

$$\begin{aligned} R_{2m}(r) = {} & \tfrac{1}{2}\int_0^{+\infty} dq\, q\, W_r(q)\, H_{2m}^{(1)}(qr) \\ & + \tfrac{1}{2}\int_0^{-\infty} dp\, p\, W_r(p)\, H_{2m}^{(2)}(-pr)] \quad m \geq 0 \end{aligned} \tag{A.18}$$

since W_r is an even function of q. The Hankel functions are interrelated by the identity (Abramowitz and Stegun, 9.1.39)

$$H_{2n}^{(2)}(-z) = -H_{2n}^{(1)}(z) \tag{A.19}$$

Now substitute (A.19) in the second term of (A.18), exchange the integration limits in this

term and substitute q = p. Summing the two integrals results in

$$R_{2m}(r) = \frac{1}{2}\int_{-\infty}^{+\infty} dq\, q\, W_r(q) H_{2m}^{(1)}(qr) \quad m \geq 0 \tag{A.20}$$

If |z| approaches infinity, the Hankel function of the first kind approaches zero for $0<\arg(z)<\pi$. If W_r has poles in the upper complex plane (preferably not on the real axis) and falls off faster than 1/q, the radial coefficients can be calculated analytically using contour integration.

However, for z = 0 the Hankel function of the first kind has a singularity of the form ln(z) for order zero and z^{-n} for order n. Therefore the radial coefficients are given by

$$\begin{aligned} R_{2m}(r) = \pi\imath \sum_{j=1}^{n} Res\{qW_r(q)H_{2m}^{(1)}(qr) \quad ; q = q_j\} \\ + \tfrac{1}{2}\pi\imath Res\{qW_r(q)H_{2m}^{(1)}(qr) \quad ; q = 0\} \end{aligned} \tag{A.21}$$

In the first term the residues of all n (non-real) poles q_j of W_r in the upper complex plane are summed. The second term gives the contribution of the pole in the first Hankel function at the origin. It must be multiplied with ½ since the pole is located on the line of integration (Cauchy principal value). Due to the specific form of the integrand, the second term only contributes for m > 0, since for m = 0 the logarithmic singularity is balanced by the factor q.

For the octupole spectrum, defined in the next section, the singularities in the Hankel function cancel.

Appendix A.3 The octupole spectrum

Several forms of the radial spectrum with k^{-4} asymptotic behavior were considered. A spectrum that appeared to be particularly suitable for analytic integration is the so called octupole spectrum

$$W_r(q) = B\frac{q^4}{q^8+a^8} \tag{A.22}$$

with a and B parameters determining the peak position and the strength, the peak being located at q = a. The octupole spectrum has eight poles of first order

$$q_j = a\exp\frac{\imath\pi(2j-1)}{8} \quad j = 1,2,\ldots,8 \tag{A.23}$$

Its radial coefficients are given by

$$R_{2n}(r) = \frac{\imath\pi B}{4a^2}\sum_{j=1}^{4}\exp\frac{-\imath\pi(2j-1)}{4} H_{2n}^{(1)}[ar\exp\frac{\imath\pi(2j-1)}{8}] \tag{A.24}$$

Holliday, St-Cyr and Woods [41] consider a radial spectrum of the form

$$W_r(q) = Bq^{-4}\exp(\frac{-q_0}{q}) \tag{A.25}$$

where B stands for the Phillips constant (B = 0.006) and q_0 for the peak wave number defined by

$$q_0 = \frac{g}{U^2} \tag{A.26}$$

with g the gravitational acceleration and U the wind speed. With these definitions the peak is located at $q = q_0/4$.

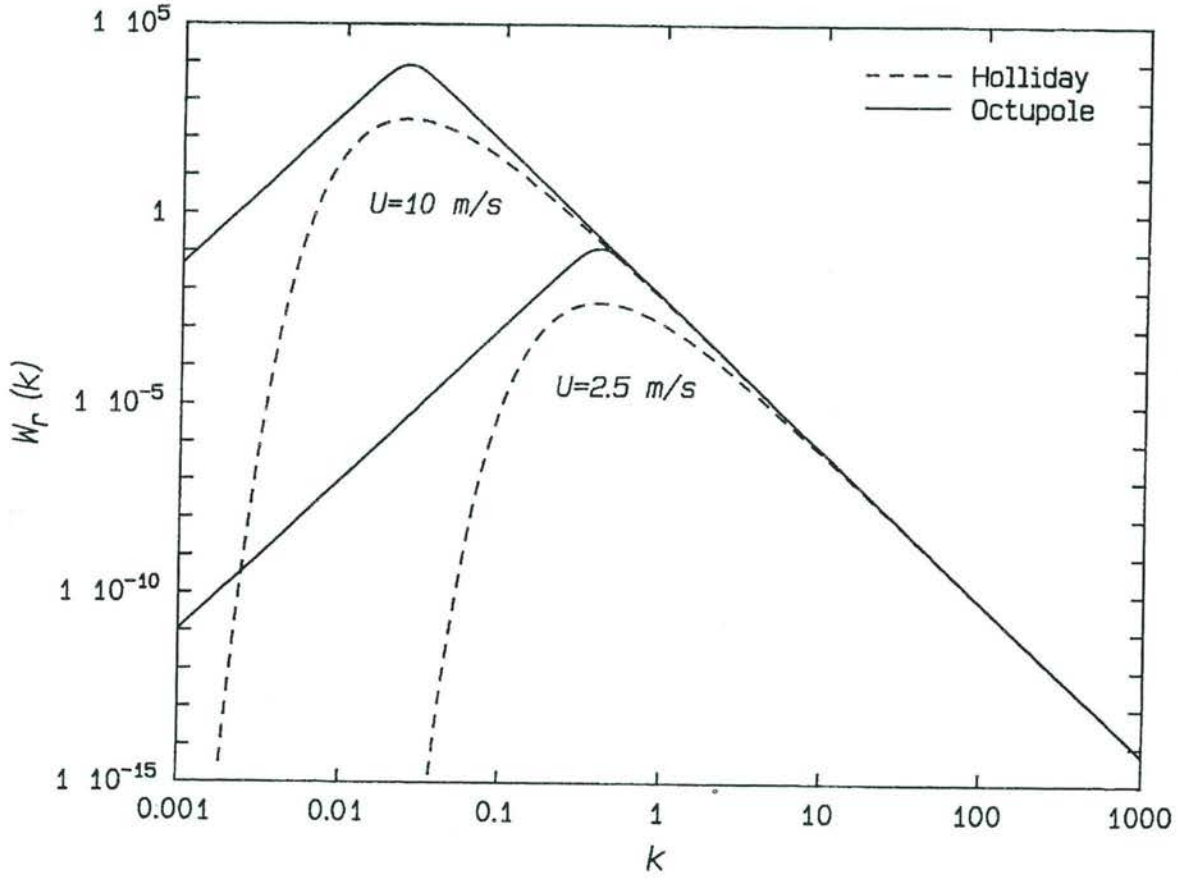

Figure A-1 Holliday and Octupole radial spectrum

Figure A-1 shows the two radial spectra defined above for two wind speeds, 2.5 m/s and 10 m/s. The value of B is 0.006 for both spectra, while the value of a for the octupole spectrum was chosen such that the peak position is the same for both spectra ($a = g/(4U^2)$). The octupole spectrum behaves behave like k^4 for small wave numbers and like k^{-4} for the tail of the spectrum. At the low wave number range, the octupole spectrum is much higher than that of Holliday, St. Cyr and Woods. It must be investigated how this affects the cross section.

The radial coefficients R_{2n} of the octupole spectrum are shown in figure A-2 for n = 0 to 4 at L-band (1.275 MHz). R_0 is finite at r = 0 while all other coefficients vanish. The radial coefficients show an oscillatory behavior around value zero due the Hankel functions. The higher coefficients rise very slowly as r increases.

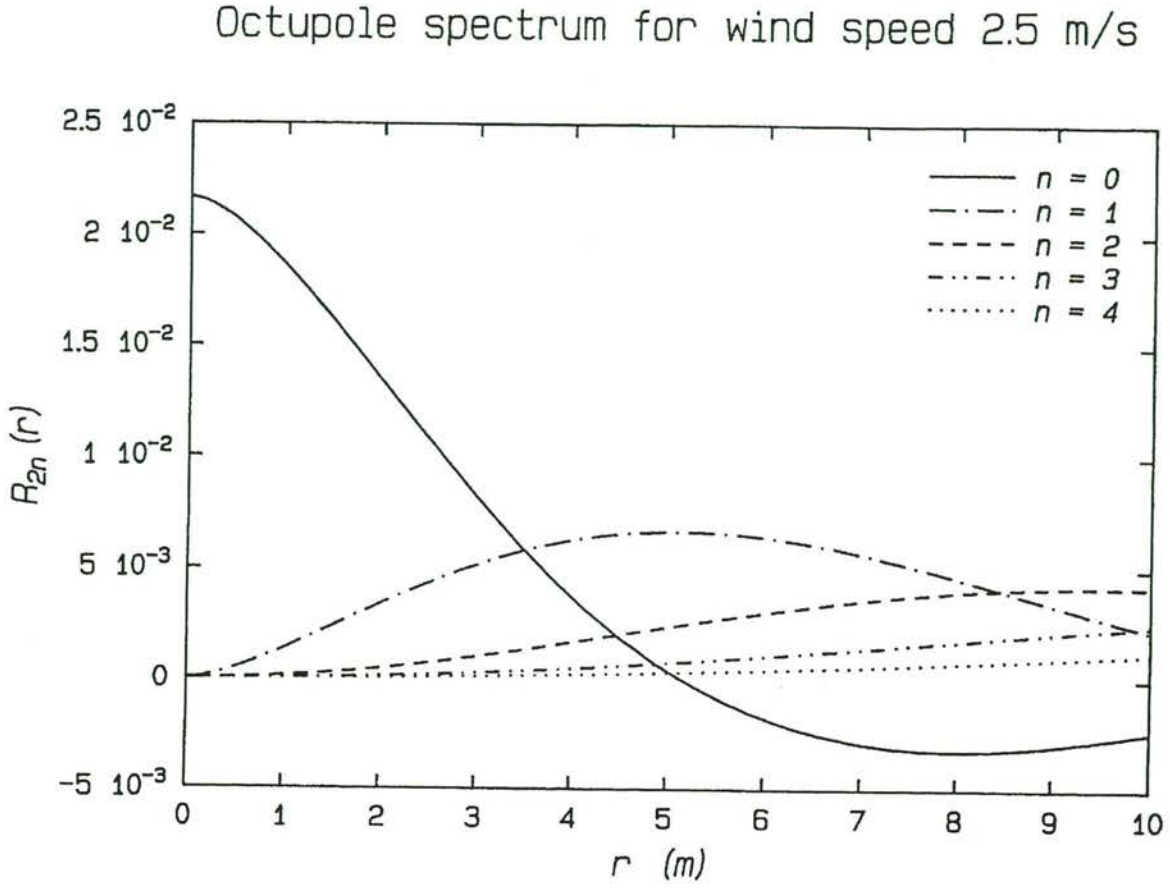

Figure A-2 The radial coefficients for the octupole spectrum at L-band for a wind speed of 2.5 m/s

To get an impression of the relative importance of the radial coefficients, figure A-3 shows the function F (see equation (9)) for $\alpha = 0°$. The angular coefficients were all set equal to one. The radar frequency is again 1.275 MHz, while the incidence angle equals 23°. F falls off rapidly as observed by Holliday, St-Cyr and Woods. The dotted line shows F when only R_0 is included; the dot-dashed line when also R_2 is taken into account. This gives already a good approximation : inclusion of R_4 (solid line) makes very little difference, whereas the higher coefficients make no significant contribution at all. This shows that the expansion of the autocorrelation function converges rapidly, two or at most three terms being significant.

Equation (A.24) shows that the radial coefficients for the octupole spectrum are the product of a factor containing a and B and a factor which is a function of ar. Since only the first two or three coefficients are significant, the latter factor can be tabulated once and interpolated with a spline. This is a very efficient way to obtain the radial coefficients.

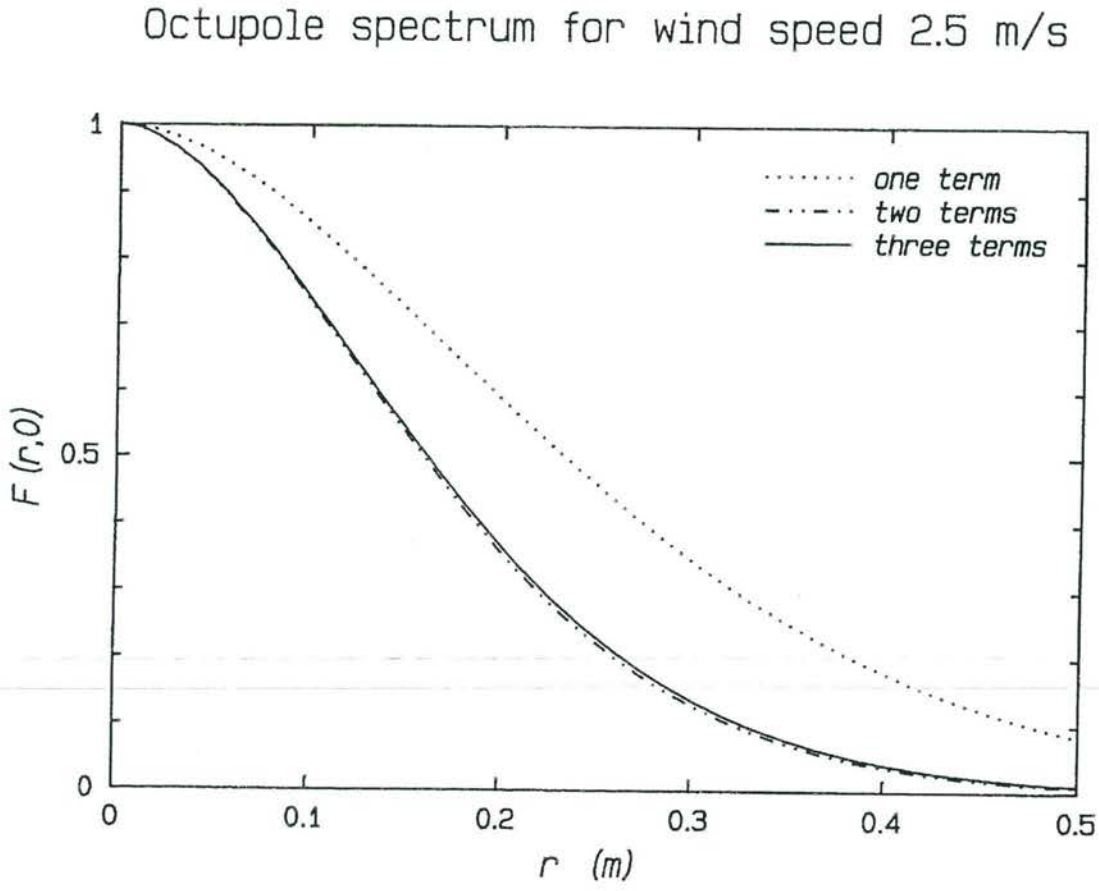

Figure A-3 The function F(r,α) for α=0° at L-band, wind 2.5 m/s, inc angle 23°

Appendix A.4 Residues for the octupole spectrum

The octupole spectrum was defined as

$$W_r(q) = B\frac{q^4}{q^8+a^8} \tag{A.27}$$

with a and B real parameters. The octupole spectrum has eight poles of first order

$$q_j = a\exp\frac{\imath\pi(2j-1)}{8} \quad j = 1,2,\ldots,8 \tag{A.28}$$

The first four poles, j = 1, 2, 3, 4, are located in the upper part of the complex plane. Integrating along the contour shown in figure A-4, with R_c approaching infinity, the radial coefficients are given by (see (A.21))

$$R_{2n}(r) = \imath\pi B\sum_{j=1}^{4} Res[(q-q_j)\frac{q^5}{q^8+a^8}H_{2n}^{(1)}(qr)]_{q=q_j} \tag{A.29}$$

$$+\frac{1}{2}\imath\pi B Res[\frac{q^5H_{2n}^{(1)}(qr)}{q^8+a^8}]_{q=0}$$

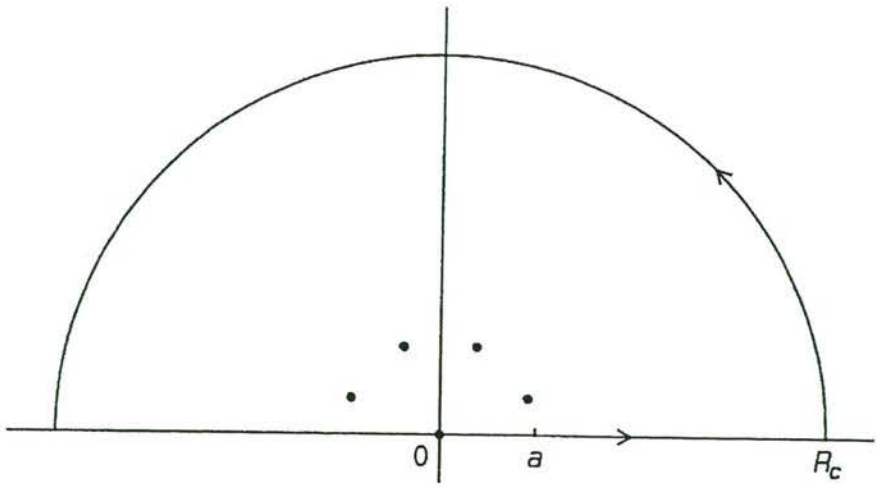

Figure A-4 Integration contours for the octupole spectrum

Note that the singularity at the origin is located on the contour. By taking the Cauchy principal value, its contribution is half of what it would have been if it were located within the contour. First we will consider the first term in (A.29). Define

$$d(q,q_j) = \frac{q-q_j}{q^8+a^8} = \frac{q-q_j}{(q-q_1)(q-q_2)...(q-q_8)} \tag{A.30}$$

Now $q_{j+8m} = q_j$ for all integer m. All poles show up in the denominator of (A.30), except the pole on which the residue is calculated. Counting from the first pole after the one on which the residue is calculated one finds

$$D(q,q_j) = \frac{1}{(q-q_{j+1})(q-q_{j+2})...(q-q_{j+7})} \tag{A.31}$$

Substituting $q=q_j$ and using the relation

$$q_{j+k} = a\exp\frac{\imath\pi(2j+2k-1)}{8} = q_j\exp\frac{\imath\pi k}{4} \tag{A.32}$$

yields

$$D(q_j,q_j) = \frac{1}{q_j^7(1-\exp\frac{\imath\pi}{4})(1-\exp\frac{\imath\pi}{2})(1-\exp\frac{3\imath\pi}{4})...(1-\exp\frac{7\imath\pi}{4})} = \frac{1}{8q_j^7} \tag{A.33}$$

Then (A.29), (A.30) and (A.33) give

$$R^1_{2n}(r) = \frac{\imath\pi B}{8a^2}\sum_{j=1}^{4}\exp(\frac{-\imath\pi(2j-1)}{4})H^{(1)}_{2n}[ar\exp\frac{\imath\pi(2j-1)}{8}] \tag{A.34}$$

where the superscript 1 indicates the first term of (A.29). The residue can be calculated directly from (A.34) far away from the singularity where ar is large. If ar is small, singularities in the Hankel function may play a role. To investigate this, the series expansion of the Han-

kel function is needed. The Hankel function of the first kind is defined as (Abramowitz and Stegun, 9.1.3)

$$H_{2n}^{(1)}(z) = J_{2n}(z) + \imath Y_{2n}(z) \tag{A.35}$$

with Y_{2n} the Bessel function of the second kind. With the series expansions J_{2n} of and Y_{2n} (Abramowitz and Stegun, 9.1.10 and 9.1.11) one finds for the Hankel function of the first kind

$$\begin{aligned} H_{2n}^{(1)}(z) = & \sum_{k=0}^{\infty}\{1 + \imath\tfrac{2}{\pi}\ln(\tfrac{1}{2}z) - \tfrac{\imath}{\pi}[\Psi(k+1) + \Psi(2n+k+1)]\}\frac{(-1)^k(\frac{1}{2}z)^{2n+2k}}{k!(2n+k)!} \\ & + \sum_{k=0}^{2n-1}\frac{-\imath(2n-k-1)!}{\pi k!}(\tfrac{1}{2}z)^{-2n+2k} \end{aligned} \tag{A.36}$$

where Ψ is the digamma function. For n = 0 the Hankel function has a logarithmic singularity at the origin, while for n > 0 it has a z^{-2n} singularity. For the residues $z = q_j r$ one has

$$z = ar\exp\frac{\imath\pi(2j-1)}{8} \tag{A.37}$$

$$(\tfrac{1}{2}z)^m = (\tfrac{1}{2}ar)^m\exp\frac{\imath\pi m(2j-1)}{8} \tag{A.38}$$

$$\ln(\tfrac{1}{2}z) = \ln(\tfrac{1}{2}ar) + \frac{\imath\pi(2j-1)}{8} \tag{A.39}$$

Substitution of (A.37) to (A.39) in (A.36) yields

$$\begin{aligned} H_{2n}^{(1)}[ar\exp(\tfrac{\imath\pi(2j-1)}{8})] = & \sum_{k=0}^{\infty}[1 - \tfrac{(2j-1)}{4} - \tfrac{\imath}{\pi}[\Psi(k+1) + \Psi(2n+k+1)]] \\ & \times \frac{(-1)^k(\frac{ar}{2})^{2n+2k}}{k!(2n+k)!}\exp(\tfrac{\imath\pi(n+k)(2j-1)}{4}) \\ & + \sum_{k=0}^{\infty}\frac{2\imath\ln(\frac{ar}{2})}{\pi}\frac{(-1)^k(\frac{ar}{2})^{2n+2k}}{k!(2n+k)!}\exp(\tfrac{\imath\pi(n+k)(2j-1)}{4}) \\ & + \sum_{k=0}^{2n-1}\frac{-\imath(2n-k-1)!}{\imath 1!}(\tfrac{ar}{2})^{-2n+2k}\exp(\tfrac{\imath\pi(-n+k)(2j-1)}{4}) \end{aligned} \tag{A.40}$$

This is written in the form

$$\begin{aligned} & H_{2n}^{(1)}ar\exp\frac{\imath\pi(2j-1)}{8} = \\ & \sum_{k=0}^{\infty}f_1(ar;n,k)r_1(j,n+k) \\ & + \sum_{k=0}^{\infty}f_2(ar;n,k)r_2(j,n+k) \\ & + \sum_{k=0}^{\infty}f_3(ar;n,k)r_1(j,n+k) \\ & + \sum_{k=0}^{2n-1}f_4(ar;n,k)r_1(j,k-n) \end{aligned} \tag{A.41}$$

where

$$f_1(ar;n,k) = 1 - \frac{\imath}{\pi}\Psi(k+1) + \Psi(2n+k+1)\, f_2(ar;n,k) \tag{A.42}$$

$$f_2(ar;n,k) = \frac{(-1)^k(\frac{ar}{2})^{2n+2k}}{k!(2n+k)!} \tag{A.43}$$

$$f_3(ar;n,k) = \imath \ln(\tfrac{ar}{2})\, f_2(ar;n,k) \tag{A.44}$$

$$f_4(ar;n,k) = \frac{-\imath(2n-k-1)!}{\pi k!}(\tfrac{ar}{2})^{-2n+2k} \tag{A.45}$$

and

$$r_1(j,m) = \exp(\frac{\imath\pi(2j-1)m}{4}) \tag{A.46}$$

$$r_2(j,m) = -\frac{(2j+1)}{4}\exp(\frac{\imath\pi(2j-1)m}{4}) \tag{A.47}$$

Substituting (A.41) in (A.34) yields

$$\begin{aligned} R^1_{2n}(r) = \frac{\imath\pi B}{8a^2}[&\sum_{k=0}^{\infty} f_1(ar;n,k)s_1(n+k) + \sum_{k=0}^{\infty} f_2(ar;n,k)s_2(n+k) \\ &+ \sum_{k=0}^{\infty} f_3(ar;n,k)s_1(n+k) + \sum_{k=0}^{2n-1} f_4(ar;n,k)s_1(k-n)] \end{aligned} \tag{A.48}$$

with f_1, f_2, f_3 and f_4 defined in (A.42, A.43, A.44 and A.45), and with s_1 and s_2 defined as

$$s_1(m) = \sum_{j=1}^{4}\exp(\frac{\imath\pi(m-1)(2j-1)}{4}) \tag{A.49}$$

$$s_2(m) = -\sum_{j=1}^{4}\frac{2j-1}{4}\exp(\frac{\imath\pi(m-1)(2j-1)}{4}) \tag{A.50}$$

Since $\exp(\pm i\pi(2j-1)) = -1$, it follows that

$$s_i(m \pm 4) = -s_i(m) \qquad i = 1,2 \tag{A.51}$$

Direct evaluation of (A.49) and (A.50) yields

$$\begin{aligned} s_1(1) &= 4 \\ s_1(2) &= 0 \\ s_1(3) &= 0 \\ s_1(4) &= 0 \\ s_2(1) &= -4 \\ s_2(2) &= \imath\sqrt{2} \\ s_2(3) &= \imath \\ s_2(4) &= \imath\sqrt{2} \end{aligned} \tag{A.52}$$

If n=0, the only singular term in (A.48) is the logarithmic one in f_3 for k=0, since for k>1 this singularity is removable. However, $f_3(ar;0,0)$ is multiplied with $s_1(0)$ which equals zero. Therefore expression (A.48) is regular for n = 0.

For $n > 0$ the singularities are poles arising from f_4 when $k<n$ and having the form $(\frac{1}{2}ar)^{-2(n-k)}$. If $n = 1$ and $k = 0$ it has the form $(\frac{1}{2}ar)^{-2}$. This term is to be multiplied with $s_1(-1)$ which equals zero. If $n = 2$ poles arise from the terms with $k = 0$ and $k = 1$. These are to be multiplied with $s_1(-2)$ and $s_1(-1)$ which both are equal to zero.

The situation is a bit more complicated when $n > 2$. For $n = 3$ and $k = 0$ the contribution of f_4 to the residue equals

$$\begin{aligned} f_4(ar;3,0)s_1(-3) &= -4\frac{-\imath 5!}{\pi}(\frac{ar}{2})^{-6} \\ &= 480\frac{\imath}{\pi}(\frac{ar}{2})^{-6} \end{aligned} \tag{A.53}$$

and the contribution to the radial coefficient equals

$$-\frac{60B}{a^2}(\frac{ar}{2})^{-6} \tag{A.54}$$

This clearly diverges if r approaches zero.

So far, no attention was paid to the second term of (A.29), the residue at $q = 0$. Its contribution to the radial coefficient is

$$R_{2n}^2(r) = \frac{\pi\imath B}{2} Res[\frac{q^5 H_{2n}^{(1)}(qr)}{q^8+a^8}]_{q=0} \tag{A.55}$$

For $n = 0$, the singularity in the Hankel function is logarithmic and of the form $\ln(\frac{1}{2}qr)$, as can be seen from the series expansion of the Hankel function in (A.40). However, the factor q^5 in (A.55) removes this singularity. Therefore the residue at $q = 0$ does not contribute to the radial coefficient for $n = 0$.

For $n > 1$ the singularity is a pole, arising from the last summation in the series expansion of the Hankel function, equation (A.40), all other terms being regular now. Substituting only the leading term in this last summation (the one with $k = 0$; all other terms will not contribute to the residue) into (A.55) yields after some rewriting

$$R_{2n}^2(r) = \frac{B}{2}\frac{(2n-1)!}{(\frac{r}{2})^{2n}} Res[\frac{1}{q^{2(n-k)-5}(q^8+a^8)}]_{q=0} \tag{A.56}$$

If $n = 1$ or $n = 2$ the poles are again balanced by the factor q^5 and the contribution of the residue at $q = 0$ to the radial coefficient vanishes.

For $n = 3$ the residue in (A.56) becomes

$$Res[\frac{1}{q(q^8+a^8)}]_{q=0} = \frac{1}{a^8} \tag{A.57}$$

From (A.56) and (A.57) one readily finds

$$R_6^2(r) = \frac{60B}{a^2}(\frac{ar}{2})^{-6} \tag{A.58}$$

which exactly cancels the divergent contribution from the poles at $q = q_j$ in (A.54).

For n = 4, the divergent contribution from the poles at $q = q_j$ comes from

$$f_4(ar;4,1)s_1(-3) = -4\frac{-\imath 6!}{\pi}\left(\frac{ar}{2}\right)^{-6} = 2880\,\frac{\imath}{\pi}\left(\frac{ar}{2}\right)^{-6} \tag{A.59}$$

and the contribution to the radial coefficient equals

$$-\frac{360B}{a^2}\left(\frac{ar}{2}\right)^{-6} \tag{A.60}$$

The residue of the leading term in the divergent part of the series expansion of the Hankel function (the one with k = 0) equals

$$Res\left[\frac{1}{q^2(q^8+a^8)}\right]_{q=0} = 0 \tag{A.61}$$

since the first derivative of the factor between the brackets equals zero at q = 0. The contribution to the radial coefficient of the second term in the divergent part of the series expansion of the Hankel function (the one with k = 1) is

$$R_8^2(r) = \frac{B\,6!}{2\left(\frac{r}{2}\right)^6} Res\left[\frac{1}{q(q^8+a^8)}\right]_{q=0} = \frac{360B}{a^2}\left(\frac{ar}{2}\right)^{-6} \tag{A.62}$$

Again the contribution of the pole at q = 0 cancels the divergent part of the contribution of the poles at $q = q_j$. This holds for all n.

It has been shown in this appendix that the radial expansion coefficients R_{2n} for the octupole spectrum are regular when r approaches zero. It has also been shown earlier that only R_0, R_2 and maybe R_4 contribute to the autocorrelation function. Therefore the contribution of the pole at q = 0 can be neglected in practice, since this pole only contributes for R_6 and higher coefficients. Nevertheless, one must still be careful applying (A.34) to calculate the radial coefficients R_0, R_2 and R_4 using some numerical routine for the Hankel function of the first kind. One must be sure that the result is sufficiently accurate since in the summation over the residues large terms (the singular parts which arise from the Bessel function of the second kind) cancel for small values of ar. This may spoil the precision of the final results.

A safer, but more elaborate procedure to calculate the radial coefficients is to use (A.48), with the singular terms in the series expansion of the Hankel function removed.

R_0 equals N in the limit that r goes to zero (see equation (20). From (A.48) one finds, with n = k = 0

$$N = R_0(0) = \frac{\imath\pi B}{8a^2} f_2(0;0,0)\, s_2(0) = \pi\sqrt{2}\frac{B}{8a^2} \tag{A.63}$$

since $f_2(0;0,0) = 1$ and $s_2(0) = -s_2(4) = -i\pi\sqrt{2}$.

It is interesting to notice that (A.63) can also be found from contour integration of the octupole spectrum along the infinitely large quarter circle in the first quadrant of the complex plane. The integral along the positive imaginary axis equals the one along the positive real axis.

APPENDIX B The MPN 1990 X-band scatterometer measurements

In this appendix a complete list of the X-band scatterometer measurements including most of the environmental parameters are given.

The friction velocity listed is based upon a parameterization using the MPN reference wind speed as input. The high quality friction velocity measurements are listed in section 6.

NO	scatterometer measurement code
RCS	normalized radar cross section
INC	incidence angle (deg)
AZI	azimuth angle (degN)
POL	polarization
WS	MPN wind velocity, cup 2 (m/s)
UST	friction velocity based on MPN wind and parameterization (m/s)
WD	wind direction (degN)
FP	peak frequency waves
SWH	significant wave height (m)
Tair	air temperature (deg C)
Tsea	bulk sea water temperature (deg C)

Table B-1 List of the X-band measurements

NO	DT	TI	RCS	INC	AZI	POL	WS	UST	WD	FP	SWH	Tair	Twater
98	21-Nov	02:52 PM	-13.1	40	255	HH	9.6	0.381	302	0.14	196	8.4	11.0
99	21-Nov	03:19 PM	-13.3	40	255	VV	8.2	0.331	310	0.16	187	8.8	11.0
106	21-Nov	04:57 PM	-14.1	40	330	VV	6.4	0.263	316	0.14	187	8.3	10.9
109	21-Nov	05:19 PM	-17.3	40	330	HH	5.3	0.221	314	0.15	172	8.4	10.9
110	21-Nov	05:38 PM	-23.3	60	330	HH	4.2	0.177	308	0.14	168	8.1	10.9
113	21-Nov	06:00 PM	-18.2	60	330	VV	6.4	0.263	301	0.15	160	6.4	10.9
114	21-Nov	06:51 PM	-19.3	60	330	VV	5.9	0.244	332	0.15	150	5.9	10.9
115	21-Nov	07:28 PM	-13.9	40	255	VV	6.2	0.256	330	0.15	141	7.3	10.8
117	21-Nov	08:04 PM	-13.5	40	255	HH	10.1	0.398	292	0.15	127	6.7	10.8
126	21-Nov	09:55 AM	-16.1	40	255	VV	5.7	0.236	257	0.17	98	8.1	10.8
128	21-Nov	10:20 AM	-19.3	40	255	HH	6.3	0.260	208	0.17	98	7.3	10.7
129	21-Nov	10:23 AM	-18.6	40	255	HH	6.3	0.260	208	0.17	98	7.3	10.7
131	21-Nov	11:29 AM	-16.0	45	275	VV	7.9	0.320	210	0.17	95	6.8	10.6
132	21-Nov	11:36 AM	-20.7	45	275	HH	7.9	0.320	210	0.17	95	6.8	10.6
133	22-Nov	12:20 PM	-15.5	45	275	VV	7.9	0.320	212	0.17	88	6.8	10.7
134	22-Nov	12:27 PM	-20.6	45	275	HH	7.9	0.320	212	0.17	88	6.8	10.7
135	22-Nov	01:22 PM	-19.9	45	275	VV	6.1	0.252	215	0.18	100	7.2	10.6
136	22-Nov	01:29 PM	-23.4	45	275	HH	5.0	0.209	210	0.16	87	7.2	10.6
137	22-Nov	02:29 PM	-22.5	45	275	VV	4.9	0.205	200	0.17	79	7.4	10.6
138	22-Nov	02:38 PM	-26.1	45	275	HH	5.0	0.209	205	0.16	93	7.4	10.6
139	22-Nov	03:22 PM	-19.7	45	275	VV	5.5	0.229	199	0.17	82	7.2	10.6
140	22-Nov	03:28 PM	-20.3	45	275	HH	6.8	0.279	201	0.17	92	7.2	10.6
142	22-Nov	04:21 PM	-21.5	45	275	VV	5.4	0.225	189	0.18	97	7.0	10.6
143	22-Nov	04:29 PM	-22.6	45	275	HH	5.8	0.240	185	0.17	95	7.0	10.6
148	22-Nov	05:23 PM	-20.3	40	275	VV	6.5	0.267	188	0.18	96	7.0	10.6
149	22-Nov	05:53 PM	-20.7	40	275	VV	6.0	0.248	174	0.17	84	7.0	10.4
150	22-Nov	06:23 PM	-21.7	40	275	VV	6.0	0.248	167	0.17	77	6.9	10.4
151	22-Nov	06:53 PM	-19.9	40	275	VV	5.9	0.244	173	0.17	75	7.1	10.6
152	22-Nov	07:23 PM	-19.3	40	275	VV	6.6	0.271	185	0.17	75	7.1	10.7
153	22-Nov	07:53 PM	-18.5	40	275	VV	7.6	0.309	182	0.16	81	6.8	10.7
154	22-Nov	08:23 PM	-19.3	40	275	VV	5.5	0.229	183	0.18	75	7.0	10.7
155	22-Nov	08:53 PM	-19.5	40	275	VV	5.4	0.225	182	0.16	76	7.1	10.7
156	22-Nov	09:23 PM	-19.9	40	275	VV	5.4	0.225	176	0.17	79	7.3	10.7
157	22-Nov	09:53 PM	-21.9	40	275	VV	5.2	0.217	174	0.15	75	7.2	10.7
158	22-Nov	10:23 PM	-22.9	40	275	VV	5.0	0.209	168	0.16	72	7.0	10.7
159	22-Nov	10:53 PM	-25.6	40	275	VV	4.4	0.185	162	0.16	61	7.0	10.7
160	22-Nov	11:31 PM	-28.6	40	275	VV	3.9	0.165	180	0.15	64	7.0	10.6
161	22-Nov	12:01 AM	-25.0	40	275	VV	4.7	0.197	174	0.14	64	7.0	10.6
162	22-Nov	12:31 AM	-25.0	40	275	VV	5.2	0.217	165	0.15	61	6.8	10.6
163	22-Nov	01:01 AM	-24.6	40	275	VV	5.3	0.221	165	0.14	64	6.7	10.5
164	22-Nov	01:31 AM	-24.9	40	275	VV	4.9	0.205	171	0.15	62	6.6	10.5
165	22-Nov	02:01 AM	-24.5	40	275	VV	4.1	0.173	172	0.15	70	6.4	10.5
166	22-Nov	02:31 AM	-24.1	40	275	VV	4.5	0.189	155	0.16	68	6.2	10.5
167	22-Nov	03:01 AM	-21.0	40	275	VV	4.5	0.189	153	0.17	69	6.1	10.5
168	22-Nov	03:31 AM	-20.1	40	275	VV	5.6	0.232	151	0.15	76	6.0	10.5
169	22-Nov	04:01 AM	-18.5	40	275	VV	4.9	0.205	157	0.18	73	5.8	10.5
170	22-Nov	04:31 AM	-21.2	40	275	VV	5.8	0.240	156	0.15	71	5.6	10.1
171	22-Nov	05:01 AM	-20.5	40	275	VV	5.1	0.213	157	0.15	66	5.7	10.2
172	22-Nov	05:31 AM	-25.6	40	275	VV	3.6	0.153	170	0.15	60	5.7	10.3
173	22-Nov	06:01 AM	-27.1	40	275	VV	3.1	0.132	179	0.14	53	5.6	10.3
174	22-Nov	06:31 AM	-23.2	40	275	VV	3.5	0.149	157	0.12	58	5.6	10.4
179	22-Nov	09:38 AM	-18.0	30	315	HH	4.4	0.185	143	0.16	51	4.6	10.3
182	22-Nov	10:02 AM	-23.3	40	315	VV	4.9	0.205	133	0.19	49	4.5	10.2
183	22-Nov	10:25 AM	-33.8	50	315	HH	4.8	0.201	129	0.16	51	4.4	10.0
185	22-Nov	10:45 AM	-36.7	60	315	HH	3.8	0.161	130	0.16	51	4.4	10.0
186	22-Nov	10:53 AM	-29.7	60	315	VV	3.5	0.149	128	0.16	51	4.6	10.1
187	22-Nov	11:28 AM	-42.8	70	315	HH	3.6	0.153	128	0.17	48	5.3	10.4
188	22-Nov	11:35 AM	-31.9	70	315	VV	3.6	0.153	125	0.16	50	5.6	10.5
189	22-Nov	11:47 AM	-38.8	55	315	HH	3.3	0.140	122	0.15	49	5.5	10.5
190	22-Nov	11:53 AM	-27.0	55	315	VV	3.4	0.144	119	0.15	52	5.6	10.5

Table B-1 continued

NO	DT	TI	RCS	INC	AZI	POL	WS	UST	WD	FP	SWH	Tair	Twater
191	23-Nov	12:05 PM	-33.8	45	315	HH	3.7	0.157	110	0.15	46	5.7	10.4
192	23-Nov	12:11 PM	-28.9	45	315	VV	4.0	0.169	119	0.16	51	5.7	10.5
193	23-Nov	12:21 PM	-25.5	35	315	HH	4.7	0.197	123	0.17	48	5.8	10.5
194	22-Nov	10:32 AM	-22.4	35	315	VV	4.4	0.185	128	0.17	51	4.4	10.0
195	23-Nov	12:33 PM	-21.7	35	315	VV	5.1	0.213	128	0.16	53	5.8	10.5
196	23-Nov	02:54 PM	-24.1	50	240	VV	4.1	0.173	151	0.14	50	7.2	10.4
197	23-Nov	03:00 PM	-26.1	50	240	HH	4.1	0.173	151	0.15	48	7.3	10.3
198	23-Nov	03:30 PM	-30.0	50	330	VV	3.0	0.128	117	0.14	47	7.6	9.9
199	23-Nov	03:52 PM	-35.7	50	330	HH	3.5	0.149	116	0.14	46	7.5	10.0
224	27-Nov	01:42 PM	-17.4	50	45	VV	6.0	0.248	88	0.17	93	4.1	9.7
226	27-Nov	02:14 PM	-22.3	50	45	HH	5.8	0.240	87	0.16	102	4.3	9.8
227	27-Nov	02:16 PM	-22.6	50	45	HH	5.8	0.252	87	0.16	102	4.3	9.8
229	27-Nov	02:46 PM	-27.1	70	45	HH	5.8	0.240	86	0.15	98	4.6	9.7
230	27-Nov	02:58 PM	-20.7	70	45	VV	5.8	0.240	87	0.15	101	4.7	9.7
231	27-Nov	03:09 PM	-19.7	60	45	VV	5.6	0.232	91	0.16	93	5.0	9.7
237	27-Nov	05:31 PM	-25.3	40	255	VV	5.2	0.217	117	0.14	96	5.6	9.5
238	27-Nov	05:54 PM	-22.8	40	255	HH	4.5	0.189	106	0.13	98	5.8	9.5
239	27-Nov	06:04 PM	-22.4	40	255	HH	4.5	0.189	99	0.13	101	6.0	9.5
244	27-Nov	08:01 PM	-19.5	40	315	VV	6.5	0.267	60	0.11	98	5.6	9.5
245	27-Nov	08:31 PM	-17.1	40	315	VV	6.2	0.256	82	0.12	98	5.9	9.5
247	27-Nov	09:31 PM	-19.1	40	315	VV	5.6	0.232	90	0.12	105	6.2	9.5
248	27-Nov	10:01 PM	-20.8	40	315	VV	5.0	0.209	95	0.13	89	6.3	9.6
249	27-Nov	10:31 PM	-23.8	40	315	VV	5.0	0.209	119	0.13	87	6.2	9.6
250	27-Nov	11:01 PM	-22.1	40	315	VV	4.1	0.173	105	0.12	90	6.2	9.8
251	27-Nov	11:31 PM	-20.1	40	315	VV	5.4	0.225	58	0.13	92	5.8	9.6
252	27-Nov	12:01 AM	-19.9	40	315	VV	5.0	0.209	75	0.13	92	5.7	9.5
253	27-Nov	12:31 AM	-21.0	40	315	VV	4.3	0.181	77	0.13	93	5.9	9.6
254	27-Nov	01:01 AM	-20.0	40	315	VV	5.4	0.225	69	0.14	90	6.1	9.6
255	27-Nov	01:31 AM	-20.1	40	315	VV	4.9	0.205	77	0.14	98	6.0	9.6
256	27-Nov	09:01 PM	-19.1	40	315	VV	6.1	0.252	92	0.12	89	6.7	9.5
257	27-Nov	02:31 AM	-20.7	40	315	VV	4.5	0.189	70	0.15	92	5.7	9.6
258	27-Nov	03:01 AM	-20.1	40	315	VV	5.0	0.209	68	0.14	103	6.1	9.6
259	27-Nov	03:31 AM	-21.1	40	315	VV	4.6	0.193	75	0.15	99	6.2	9.7
260	27-Nov	04:01 AM	-22.4	40	315	VV	3.8	0.161	78	0.14	100	6.1	9.6
261	27-Nov	04:31 AM	-21.7	40	315	VV	4.1	0.173	70	0.14	100	6.0	9.6
262	27-Nov	05:01 AM	-21.6	40	315	VV	4.3	0.181	68	0.13	109	5.8	9.6
263	27-Nov	05:31 AM	-21.9	40	315	VV	4.1	0.173	66	0.14	105	5.8	9.5
264	27-Nov	06:01 AM	-21.0	40	315	VV	4.2	0.177	71	0.14	96	5.9	9.5
265	27-Nov	06:31 AM	-21.0	40	315	VV	4.7	0.197	68	0.14	93	5.8	9.4
402	28-Nov	05:19 PM	-17.0	40	255	VV	6.4	0.263	48	0.16	92	7.2	9.6
403	28-Nov	05:53 PM	-20.8	40	255	HH	5.0	0.209	67	0.17	92	6.9	9.6
406	28-Nov	08:02 PM	-20.0	40	255	VV	4.5	0.189	49	0.16	83	6.2	9.7
407	28-Nov	08:31 PM	-23.0	40	255	VV	4.3	0.181	45	0.16	74	6.2	9.7
408	28-Nov	09:01 PM	-23.2	40	255	VV	4.0	0.169	36	0.14	78	6.3	9.7
409	28-Nov	09:31 PM	-27.0	40	255	VV	4.3	0.181	38	0.13	84	6.3	9.7
410	28-Nov	10:01 PM	-22.5	40	255	VV	4.0	0.169	23	0.14	72	6.4	9.6
411	28-Nov	10:31 PM	-22.3	40	255	VV	4.2	0.177	38	0.13	87	6.4	9.6
412	28-Nov	11:01 PM	-22.5	40	255	VV	3.9	0.165	31	0.14	87	6.3	9.7
413	28-Nov	11:31 PM	-20.6	40	255	VV	4.4	0.185	33	0.13	84	6.4	9.8
414	28-Nov	12:01 AM	-19.7	40	255	VV	5.3	0.221	67	0.13	88	6.2	9.9
415	28-Nov	12:31 AM	-20.5	40	255	VV	3.6	0.153	74	0.13	88	6.1	10.0
416	28-Nov	01:01 AM	-18.9	40	255	VV	4.8	0.201	92	0.13	95	5.3	10.0
417	28-Nov	01:31 AM	-20.3	40	255	VV	4.2	0.177	85	0.14	101	5.2	10.1
418	28-Nov	02:01 AM	-19.7	40	255	VV	4.3	0.181	79	0.14	107	5.0	10.0
419	28-Nov	02:31 AM	-19.8	40	255	VV	4.7	0.197	76	0.15	88	4.9	10.0
420	28-Nov	03:01 AM	-18.8	40	255	VV	5.5	0.229	68	0.15	94	4.8	10.0
422	28-Nov	09:14 AM	-25.1	50	45	HH	3.6	0.153	78	0.15	83	2.3	9.7
423	28-Nov	09:21 AM	-20.8	50	45	VV	4.2	0.177	76	0.16	72	2.5	9.7
424	28-Nov	09:40 AM	-30.5	60	45	HH	4.5	0.189	89	0.16	84	2.7	9.8
425	28-Nov	09:47 AM	-24.0	60	45	VV	4.6	0.193	102	0.14	84	2.7	9.8
426	28-Nov	10:30 AM	-35.1	50	0	HH	3.8	0.161	97	0.14	75	3.0	9.9
427	28-Nov	10:38 AM	-27.9	50	0	VV	3.4	0.144	94	0.14	71	3.0	9.9

Table B-1 continued

NO	DT	TI	RCS	INC	AZI	POL	WS	UST	WD	FP	SWH	Tair	Twater
428	28-Nov	10:56 AM	-32.8	50	315	HH	2.5	0.107	99	0.13	73	3.3	9.9
429	28-Nov	11:03 AM	-27.0	50	315	VV	2.6	0.111	94	0.14	78	3.4	9.9
430	28-Nov	11:57 AM	-34.4	50	270	HH	2.4	0.103	71	0.14	80	3.8	10.1

Table B-1 continued

NO	DT	TI	RCS	INC	AZI	POL	WS	UST	WD	FP	SWH	Tair	Twater
431	29-Nov	12:04 PM	-25.9	50	270	VV	2.2	0.095	75	0.14	83	4.0	10.1
432	29-Nov	12:19 PM	-33.9	50	285	HH	2.4	0.103	72	0.13	75	4.1	10.1
433	29-Nov	12:28 PM	-25.7	50	285	VV	2.4	0.103	63	0.14	72	4.1	10.2
434	29-Nov	01:27 PM	-34.2	50	300	HH	2.4	0.103	70	0.14	77	4.9	10.3
435	29-Nov	01:34 PM	-27.3	50	300	VV	2.4	0.103	68	0.14	76	4.9	10.3
436	29-Nov	01:47 PM	-35.0	50	330	HH	2.6	0.111	64	0.14	74	5.1	10.2
437	29-Nov	01:54 PM	-28.6	50	330	VV	2.4	0.177	62	0.16	76	5.2	10.2
438	29-Nov	02:12 PM	-31.3	50	345	HH	3.1	0.132	47	0.14	75	5.3	10.2
439	29-Nov	02:18 PM	-25.5	50	345	VV	3.1	0.132	47	0.14	75	5.3	10.2
440	29-Nov	02:33 PM	-26.2	50	15	HH	3.7	0.157	35	0.14	69	5.5	10.2
441	29-Nov	02:40 PM	-21.6	50	15	VV	3.7	0.157	35	0.14	69	5.5	10.2
442	29-Nov	02:54 PM	-24.4	50	30	HH	4.2	0.177	25	0.15	73	5.7	10.2
443	29-Nov	03:01 PM	-19.5	50	30	VV	4.4	0.185	26	0.16	71	5.7	10.2
448	29-Nov	04:35 PM	-18.9	40	255	VV	5.2	0.217	24	0.17	74	6.5	10.1
450	29-Nov	08:01 PM	-21.6	50	30	VV	4.9	0.205	23	0.18	65	7.2	10.0
451	29-Nov	08:31 PM	-21.8	50	30	VV	4.4	0.185	28	0.17	68	7.3	10.1
452	29-Nov	09:01 PM	-23.1	50	30	VV	3.4	0.144	43	0.16	58	7.4	10.1
453	29-Nov	09:31 PM	-25.1	50	30	VV	3.7	0.157	48	0.15	57	7.3	10.1
454	29-Nov	10:01 PM	-30.5	50	30	VV	2.6	0.111	70	0.15	58	7.3	10.1
455	29-Nov	10:31 PM	-36.6	50	30	VV	2.5	0.107	89	0.14	56	7.5	10.1
456	29-Nov	11:01 PM	-35.5	50	30	VV	2.5	0.107	112	0.14	57	7.1	10.2
457	29-Nov	11:31 PM	-33.6	50	30	VV	2.3	0.099	109	0.13	62	7.1	10.2
458	29-Nov	12:01 AM	-33.4	50	30	VV	1.8	0.078	108	0.13	60	7.2	10.2
459	29-Nov	12:31 AM	-34.5	50	30	VV	1.4	0.061	104	0.14	62	7.4	10.3
460	29-Nov	01:01 AM	-34.6	50	30	VV	1.7	0.073	108	0.14	56	7.4	10.3
461	29-Nov	01:31 AM	-38.9	50	30	VV	1.6	0.069	116	0.14	53	7.3	10.4
462	29-Nov	02:01 AM	-41.8	50	30	VV	1.2	0.052	126	0.13	63	7.1	10.4
463	29-Nov	02:31 AM	-32.5	50	30	VV	2.0	0.086	157	0.14	60	6.9	10.4
464	29-Nov	03:01 AM	-32.2	50	30	VV	1.6	0.069	183	0.14	64	6.9	10.4
465	29-Nov	03:31 AM	-32.5	50	30	VV	2.0	0.086	184	0.14	67	6.7	10.4
466	29-Nov	04:01 AM	-31.3	50	30	VV	1.8	0.078	208	0.15	66	6.6	10.4
468	29-Nov	05:01 AM	-30.2	50	30	VV	2.4	0.103	252	0.16	60	7.0	10.4
469	29-Nov	05:31 AM	-30.2	50	30	VV	2.4	0.103	250	0.15	61	7.1	10.3
470	29-Nov	06:01 AM	-27.5	50	30	VV	3.2	0.136	248	0.16	61	7.2	10.3
471	29-Nov	06:31 AM	-26.9	50	30	VV	3.2	0.136	253	0.16	57	7.3	10.3
477	29-Nov	09:24 AM	-17.7	40	255	VV	5.0	0.209	250	0.17	59	8.1	10.2
478	29-Nov	09:50 AM	-19.8	40	255	HH	5.1	0.213	254	0.17	60	8.2	10.1
479	29-Nov	09:57 AM	-20.8	40	255	HH	5.2	0.217	257	0.16	55	8.2	10.1
482	29-Nov	11:10 AM	-12.8	30	270	HH	3.9	0.165	288	0.17	64	8.1	10.1
483	29-Nov	11:24 AM	-11.1	30	270	VV	4.4	0.185	341	0.17	58	8.8	10.1
484	29-Nov	11:42 AM	-10.8	30	270	VV	6.4	0.263	353	0.16	58	9.4	10.2
485	29-Nov	11:49 AM	-11.6	30	270	HH	6.4	0.263	353	0.16	58	9.4	10.2
486	30-Nov	12:19 PM	-12.7	35	0	VV	7.4	0.301	355	0.17	55	9.0	10.2
487	30-Nov	12:42 PM	-15.9	35	0	HH	8.0	0.323	347	0.18	70	8.6	10.3
488	30-Nov	01:35 PM	-15.1	40	0	VV	7.6	0.309	339	0.18	89	9.5	10.3
489	30-Nov	02:05 PM	-15.1	40	0	VV	7.9	0.320	336	0.19	90	9.2	10.4
490	30-Nov	02:35 PM	-13.4	40	0	VV	8.7	0.349	332	0.18	89	9.7	10.4
491	30-Nov	03:05 PM	-14.2	40	0	VV	9.4	0.374	333	0.18	115	9.6	10.4
492	30-Nov	03:35 PM	-14.5	40	330	VV	9.2	0.367	336	0.17	117	9.5	10.4
493	30-Nov	04:05 PM	-14.8	40	330	VV	7.7	0.312	326	0.18	123	8.9	10.4
494	30-Nov	04:55 PM	-14.0	40	330	VV	8.8	0.352	337	0.18	124	9.1	10.4
495	30-Nov	05:05 PM	-14.0	40	330	VV	8.8	0.352	336	0.18	129	9.2	10.4
496	30-Nov	05:35 PM	-12.9	40	330	VV	8.9	0.356	338	0.17	158	9.1	10.4
497	30-Nov	06:05 PM	-14.2	40	330	VV	9.7	0.384	336	0.18	131	9.2	10.3
498	30-Nov	06:35 PM	-14.2	40	330	VV	12.0	0.463	41	0.18	154	8.2	10.3
499	30-Nov	07:04 PM	-13.7	50	30	VV	8.8	0.352	37	0.17	155	8.7	10.3
500	30-Nov	07:34 PM	-14.5	50	30	VV	8.1	0.327	32	0.17	143	9.0	10.3
501	30-Nov	08:01 PM	-14.3	50	30	VV	8.9	0.356	33	0.17	140	9.2	10.3
502	30-Nov	08:31 PM	-14.7	50	30	VV	8.2	0.331	31	0.17	145	9.2	10.3
503	30-Nov	09:01 PM	-15.2	50	30	VV	8.3	0.334	17	0.16	141	9.3	10.2

Table B-1 continued

NO	DT	TI	RCS	INC	AZI	POL	WS	UST	WD	FP	SWH	Tair	Twater
504	30-Nov	09:31 PM	-14.4	50	30	VV	8.5	0.342	11	0.17	133	9.5	10.2
505	30-Nov	10:01 PM	-14.3	50	30	VV	9.8	0.388	21	0.16	151	9.5	10.2
506	30-Nov	10:31 PM	-14.3	50	30	VV	11.1	0.433	25	0.16	149	9.2	10.2
507	30-Nov	11:01 PM	-13.1	50	30	VV	8.7	0.349	12	0.16	150	9.4	10.2
508	30-Nov	11:31 PM	-16.4	50	30	VV	9.6	0.381	36	0.16	144	8.9	10.2
509	30-Nov	12:01 AM	-13.6	50	30	VV	10.7	0.078	20	0.13	156	9.0	10.2
510	30-Nov	12:31 AM	-13.9	50	30	VV	9.1	0.363	24	0.14	154	8.8	10.2
511	30-Nov	01:01 AM	-15.0	50	30	VV	9.3	0.370	19	0.14	140	8.9	10.2
512	30-Nov	01:31 AM	-14.9	50	30	VV	8.3	0.334	22	0.14	142	9.0	10.3
513	30-Nov	02:01 AM	-15.5	50	30	VV	8.5	0.342	23	0.14	149	9.0	10.3
514	30-Nov	02:31 AM	-16.7	50	30	VV	7.6	0.309	26	0.13	139	8.9	10.3
515	30-Nov	03:01 AM	-16.8	50	30	VV	6.9	0.282	30	0.14	131	8.8	10.3
516	30-Nov	03:31 AM	-16.3	50	30	VV	6.8	0.279	29	0.14	137	8.8	10.3
517	30-Nov	04:01 AM	-15.9	50	30	VV	7.2	0.294	34	0.14	137	8.8	10.3
518	30-Nov	04:31 AM	-16.7	50	30	VV	6.9	0.282	36	0.14	136	8.7	10.3
519	30-Nov	05:01 AM	-18.2	50	30	VV	6.5	0.267	38	0.14	128	8.5	10.3
520	30-Nov	05:31 AM	-18.8	50	30	VV	6.0	0.248	46	0.15	130	8.3	10.3
521	30-Nov	06:01 AM	-19.5	50	30	VV	5.5	0.229	56	0.14	135	8.0	10.3
522	30-Nov	06:31 AM	-21.3	50	30	VV	4.7	0.197	61	0.14	132	7.5	10.2
523	30-Nov	07:01 AM	-22.0	50	30	VV	4.6	0.193	63	0.14	124	7.5	10.2
529	30-Nov	10:01 AM	-24.8	50	30	VV	3.8	0.161	47	0.13	135	7.0	10.1

Table B-1 continued

NO	DT	TI	RCS	INC	AZI	POL	WS	UST	WD	FP	SWH	Tair	Twater
530	01-Dec	02:01 PM	-19.1	50	30	VV	3.9	0.165	24	0.13	126	8.1	10.1
531	01-Dec	06:01 PM	-17.6	50	30	VV	7.3	0.297	87	0.16	127	5.6	10.2
532	01-Dec	10:01 PM	-16.7	50	30	VV	7.2	0.294	65	0.15	121	4.9	10.0
542	04-Dec	01:23 PM	-16.1	40	255	VV	5.1	0.213	307	0.15	110	9.3	9.6
543	04-Dec	02:32 PM	-15.7	40	255	HH	6.4	0.263	309	0.16	94	9.1	9.6
546	04-Dec	03:29 PM	-13.7	35	315	VV	7.6	0.309	299	0.16	122	9.1	9.7
547	04-Dec	04:03 PM	-14.2	35	315	VV	7.9	0.320	302	0.16	133	9.2	9.7
548	04-Dec	04:36 PM	-14.2	35	315	VV	7.6	0.309	283	0.16	121	9.0	9.7
549	04-Dec	05:03 PM	-13.2	35	315	VV	7.4	0.301	272	0.16	111	8.9	9.7
550	04-Dec	05:38 PM	-12.7	35	315	VV	7.9	0.320	289	0.16	118	9.1	9.7
555	04-Dec	07:16 PM	-14.1	40	255	VV	7.8	0.316	277	0.16	120	9.0	9.7
556	04-Dec	07:39 PM	-17.2	40	255	HH	6.7	0.275	282	0.16	115	9.1	9.7
559	04-Dec	08:36 PM	-13.0	35	315	VV	7.3	0.297	299	0.16	132	9.0	9.7
560	04-Dec	09:06 PM	-13.8	35	315	VV	6.8	0.279	299	0.16	129	9.0	9.7
561	04-Dec	09:36 PM	-13.9	35	315	VV	6.1	0.252	297	0.16	126	9.1	9.7
562	04-Dec	10:06 PM	-13.5	35	315	VV	6.3	0.260	304	0.16	136	9.4	9.7
563	04-Dec	10:36 PM	-13.1	35	315	VV	6.7	0.275	310	0.16	132	9.6	9.7
564	04-Dec	11:06 PM	-13.7	35	315	VV	6.3	0.260	323	0.16	133	9.6	9.7
565	04-Dec	11:36 PM	-12.6	35	315	VV	7.1	0.290	317	0.16	129	9.6	9.6
566	04-Dec	12:06 AM	-13.4	35	315	VV	8.2	0.331	325	0.17	131	9.6	9.6
567	04-Dec	12:36 AM	-13.8	35	315	VV	9.3	0.370	338	0.17	128	9.5	9.6
568	04-Dec	01:06 AM	-13.9	35	315	VV	8.3	0.334	335	0.17	120	9.5	9.6
569	04-Dec	01:36 AM	-13.5	35	315	VV	9.0	0.360	336	0.17	125	9.4	9.6
570	04-Dec	02:06 AM	-13.8	35	315	VV	9.2	0.367	336	0.16	139	9.2	9.6
571	04-Dec	02:36 AM	-11.3	35	315	VV	9.0	0.360	331	0.16	132	9.3	9.6
572	04-Dec	03:06 AM	-12.1	35	315	VV	8.7	0.349	331	0.16	122	9.3	9.6
573	04-Dec	03:36 AM	-12.1	35	315	VV	8.5	0.342	327	0.16	126	9.3	9.6
574	04-Dec	04:06 AM	-13.0	35	315	VV	7.6	0.309	325	0.15	143	9.3	9.6
575	04-Dec	04:36 AM	-12.7	35	315	VV	8.7	0.349	330	0.16	135	9.4	9.6
576	04-Dec	05:06 AM	-11.2	35	315	VV	8.7	0.349	333	0.15	135	9.5	9.6
577	04-Dec	05:36 AM	-12.0	35	315	VV	10.4	0.409	336	0.15	160	9.2	9.6
578	04-Dec	06:06 AM	-12.0	35	315	VV	7.7	0.312	326	0.16	137	9.1	9.6
579	04-Dec	06:36 AM	-12.3	35	315	VV	9.6	0.381	333	0.15	145	9.2	9.6
585	04-Dec	09:13 AM	-16.8	40	255	VV	10.7	0.419	339	0.15	178	8.9	9.6
586	04-Dec	09:37 AM	-18.8	40	255	HH	8.0	0.323	338	0.16	163	8.8	9.6
589	04-Dec	10:47 AM	-13.4	40	330	VV	7.5	0.305	341	0.14	187	8.2	9.5
590	04-Dec	11:17 AM	-15.0	40	330	HH	8.0	0.323	337	0.14	191	8.7	9.5
591	04-Dec	11:47 AM	-12.8	40	330	VV	9.3	0.370	334	0.14	172	8.9	9.5

Table B-1 continued

NO	DT	TI	RCS	INC	AZI	POL	WS	UST	WD	FP	SWH	Tair	Twater
592	05-Dec	12:17 PM	-14.6	40	330	HH	8.7	0.349	332	0.14	184	9.0	9.5
593	05-Dec	01:10 PM	-13.6	40	330	VV	8.4	0.338	328	0.13	182	8.7	9.5
594	05-Dec	01:17 PM	-15.5	40	330	HH	8.3	0.334	328	0.13	169	8.8	9.5
595	05-Dec	01:47 PM	-11.9	40	330	VV	7.9	0.320	339	0.13	175	8.4	9.5
596	05-Dec	02:17 PM	-15.7	40	330	HH	9.6	0.381	330	0.13	183	8.6	9.5
597	05-Dec	02:47 PM	-13.2	40	330	VV	9.9	0.391	326	0.14	166	8.1	9.5
598	05-Dec	03:17 PM	-15.8	40	330	HH	8.8	0.352	329	0.13	160	8.7	9.5
599	05-Dec	03:47 PM	-12.8	40	330	VV	10.5	0.412	326	0.12	179	8.7	9.5
600	05-Dec	04:17 PM	-17.3	40	330	HH	9.0	0.360	327	0.13	192	8.6	9.5
601	05-Dec	04:47 PM	-12.6	40	330	VV	8.8	0.352	320	0.13	168	8.9	9.5
602	05-Dec	05:17 PM	-14.7	40	330	HH	10.4	0.409	325	0.14	181	9.1	9.5
607	05-Dec	06:01 PM	-12.8	40	330	VV	11.3	0.439	333	0.14	163	8.9	9.5
608	05-Dec	06:31 PM	-11.1	40	330	VV	11.3	0.439	327	0.14	203	9.1	9.5
609	05-Dec	07:01 PM	-12.5	40	330	VV	11.6	0.449	327	0.13	202	9.0	9.6
610	05-Dec	07:31 PM	-11.8	40	330	VV	12.5	0.479	330	0.13	224	9.0	9.6
611	05-Dec	08:01 PM	-11.0	40	330	VV	11.2	0.436	336	0.14	191	8.4	9.5
612	05-Dec	08:31 PM	-12.0	40	330	VV	12.7	0.485	354	0.14	227	9.0	9.6
613	05-Dec	09:01 PM	-11.5	40	330	VV	11.7	0.453	354	0.14	213	8.7	9.5
614	05-Dec	09:31 PM	-10.2	40	330	VV	13.0	0.495	1	0.14	212	8.3	9.5
615	05-Dec	10:01 PM	-10.6	40	330	VV	11.8	0.456	353	0.14	236	8.2	9.5
616	05-Dec	10:31 PM	-10.9	40	330	VV	11.4	0.443	3	0.13	263	8.0	9.5
617	05-Dec	11:01 PM	-10.0	40	330	VV	13.3	0.504	1	0.13	242	8.5	9.5
618	05-Dec	11:31 PM	-10.3	40	330	VV	12.6	0.482	1	0.14	230	8.3	9.4
619	05-Dec	12:01 AM	-12.1	40	330	VV	11.2	0.436	13	0.14	254	7.8	9.4
620	05-Dec	12:31 AM	-12.9	40	330	VV	11.3	0.439	9	0.13	239	6.5	9.4
621	05-Dec	01:01 AM	-10.1	40	330	VV	10.1	0.398	15	0.12	277	7.7	9.4
622	05-Dec	01:31 AM	-12.0	40	330	VV	11.0	0.429	5	0.13	251	7.9	9.4
623	05-Dec	02:01 AM	-11.0	40	330	VV	11.9	0.459	7	0.12	255	7.7	9.4
624	05-Dec	02:31 AM	-10.6	40	330	VV	11.7	0.453	7	0.12	255	8.2	9.4
625	05-Dec	03:01 AM	-12.9	40	330	VV	10.3	0.405	354	0.12	241	7.0	9.4
626	05-Dec	03:31 AM	-11.7	40	330	VV	11.2	0.436	356	0.12	247	7.2	9.4
627	05-Dec	08:18 AM	-20.8	40	300	VV	6.2	0.256	30	0.12	173	7.2	9.3
628	05-Dec	08:48 AM	-16.2	40	300	VV	6.7	0.275	19	0.12	160	6.4	9.3
629	05-Dec	09:18 AM	-18.0	40	300	VV	10.6	0.416	14	0.12	176	0.0	9.4
634	05-Dec	11:01 AM	-16.1	40	255	VV	10.0	0.395	34	0.13	196	6.9	9.3
635	05-Dec	11:27 AM	-19.4	40	255	HH	6.0	0.248	26	0.13	182	7.3	9.3

The National Remote Sensing Programme 1990-2000, (NRSP-2) is implemented under the responsibility of the Netherlands Remote Sensing Board (BCRS) and coordinated by the Ministry of Transport and Public Works.

The objectives of the NRSP-2 are: to secure the long-term integration of the operational use of remote sensing through temporary stimulation in the user-sectors of government and industry, to strengthen the development of remote sensing applications and the expansion of the national infrastructure.

Publication of:

Netherlands Remote Sensing Board (BCRS)
Programme Bureau
Rijkswaterstaat Survey Department

P.O. Box 5023
2600 GA Delft
The Netherlands
tel.: + 31 15 691111
Fax: 618962